Investigation on Conformal Planar High-Gain Antennas: Corrugated Antennas and Fabry-Pérot-Type Cavity Antennas

by

Mohammad Mahdi Honari Kalateh

A thesis submitted in partial fulfillment of the requirements for the degree of

Doctor of Philosophy

In

Engineering Management

Department of Mechanical Engineering
University of Alberta

Abstract

There are many applications such as radar, space, and satellite communication, which require antenna with high gain while maintaining low profile, planar structure, and low fabrication cost. In this thesis, two techniques are presented to design high-gain antennas with planar structures, numerically, and experimentally. Corrugated structures and miniaturized-element frequency selective surfaces (MEFSSs) are used to improve the radiation gain of corrugated antennas, and Fabry-Pérot-type cavity (FPC) antennas, respectively.

First, for high power applications, TM_{01} to TE_{11} mode converters are required to convert the undesired mode of high power source to the desired mode for corrugated antennas. These mode converters are designed for the purpose of achieving high conversion efficiency over wide operational bandwidth. Using 3D printing technology, these mode converters are printed and their performance is experimentally studied.

Conventional corrugated antennas are fabricated on metallic sheets and are fed by open-ended waveguides. In order to reduce the fabrication expense and to easily integrate them with other planar structures, the realization of corrugated antennas on laminates using SIW technology is presented. Due to the large structure of corrugated antennas, the simulation and optimization process are time-consuming. Design and analysis of these antennas based on surface susceptance of corrugated structure are presented in this work. General radiation performance of corrugated antennas such as resonant frequency, spectral bandwidth, and directivity is estimated using a unit-

cell analysis of corrugated surface. The effect of width and height of corrugations and the permittivity of material inside corrugations on directivity and surface susceptance is parametrically studied.

The design of dual-band high-gain antennas is a challenging problem, especially if the antennas are required to be planar and fabricated with cheap fabrication processes. In the study of corrugated antennas, it is shown that a dual-band operation can be achieved by using two different corrugations. To improve the front-to-back ratio of the antenna, two dual-band cavity back feeder antennas are proposed to feed the dual-band corrugated structure. The dual-band feeder antennas and dual-band corrugated antennas are fabricated and measured.

Using MEFSS structures in FPC antennas may enhance the antenna gain. This technique is proposed in this work to enhance the radiation of on-chip antenna by utilizing a MEFSS cover on top of it. This is absolutely essential in radio frequency integrated circuits (RFICs) due to the restrictions on the thickness of metallic layers, substrate loss, and the limitations in a real estate. Due to using MEFSS structure, the height of the FPC antenna composed of the MEFSS cover, high impedance surface (HIS), and the a single proximity patch antenna can be designed to be very small. A scaled MEFSS cover is designed and fabricated and the measurement results demonstrate a gain enhancement of 9 dBi. A wideband MEFSS cover is then designed with two MEFSS layers to solve the problem of narrow bandwidth of single-layer MEFSS structure. These MEFSS structures can be used for radiation gain enhancement off of the on-chip antenna.

Preface

This work presents the design and analysis of high-gain planar antennas. This thesis is an original work by Mohammad Mahdi Honari as the main contributor. The detailed contributions are as follows:

I performed all designs, analyses, simulations, and measurement in this work. Prof. Pedram Mousavi provided strong supervisory advice and discussions during all steps of this work. Dr. Rashid Mirzavand, Prof. Ashwin K. Iyer, Prof. Kamal Sarabandi, Dr. Jordan Melzer, Mrs. S. Aslanzadeh and Mr. Saghlatoon helped with some aspects of the work.

Chapter 3 of this thesis has been accepted as M. M. Honari, R. Mirzavand, S. Aslanzadeh, H. Saghlatoon, and P. Mousavi, "Wideband Printed TM_{01} to TE_{11} Mode Converters," *IEEE Access*. In this part, S. Aslanzadeh helped with 3D printing fabrication, and Dr. Mirzavand and H. Saghlatoon, helped with the measurement part.

Chapter 4 was published in two papers. In one paper , the fabrication of the corrugated antennas using SIW technology was published as M. M. Honari, R. Mirzavand, J. Melzer and P. Mousavi, "A New Aperture Antenna Using Substrate Integrated Waveguide Corrugated Structures for 5G Applications," *IEEE Antennas and Wireless Propagation Letters*, vol. 16, pp. 254-257, 2017. Dr. Mirzavand and Dr. Melzer helped in revising the manuscript. In the other paper , the size reduction of corrugated antennas was published as M. M. Honari, R. Mirzavand and P. Mousavi, "A High-Gain Planar Surface Plasmon Wave Antenna Based on Substrate Integrated Waveguide Technology with Size Reduction," *IEEE Transactions on Antennas and Propagation*, vol. 66, no. 5, pp. 2605-2609, May 2018. Dr. Mirzavand helped with measurement of the antenna. Moreover, the design and analysis of corrugated antennas is ready for submission as M. M. Honari, K. Sarabandi, and P. Mousavi, "Design and Analysis of Corrugated Antennas Based on Corrugations' Surface Susceptance," *IEEE Transactions on Antennas and Propagation*. Prof. K. Sarabandi, helped in developing initial ideas and analyzing this work.

A part of chapter 5 which is about a dual-band corrugated antenna was published as M. M. Honari, R. Mirzavand, H. Saghlatoon and P. Mousavi, "A Dual-Band Low-Profile Aperture Antenna With Substrate-Integrated Waveguide Grooves," *IEEE Transactions on Antennas and Propagation*, vol. 64, no. 4, pp. 1561-1566, April 2016. Dr. Mirzavand, and Mr. Saghlatoon helped with fabrication and measurement of the antenna. The discussion about the feeder antennas was published as M. M. Honari, R. Mirzavand, J. Melzer, A. K. Iyer and P. Mousavi, "Dual-Band Open-Ended Waveguide Feeder Antennas with Collinear Feed Design," *IEEE Transactions on Antennas and Propagation*, vol. 66, no. 11, pp. 6358-6363, Nov. 2018. I took advantage of precious discussions with Prof. A. K. Iyer while preparing the material for this part of the paper. Also, Prof. A. K. Iyer and Dr. Melzer helped in revising the manuscript. Another part of chapter 5 regarding dual-band high-gain corrugated antenna integrated with feeder antenna is prepared to be submitted as M. M. Honari, K. Sarabandi and P. Mousavi, "Dual-Band High-Gain Planar Corrugated Antennas with Integrated Feeding Structure," *IEEE Transactions on Antennas and Propagation.* Prof. K. Sarabandi furnished useful pieces of advice for preparing the manuscript.

Chapter 6 is partially submitted as M. M. Honari, P. Mousavi, and K. Sarabandi " Miniaturized-Element Frequency Selective Surface Metamaterials: A Solution to Enhance Radiation Off of RFICs," *IEEE Transactions on Antennas and Propagation.* Prof. Sarabandi helped in developing the idea and revising the manuscript. He also provided practical advices. The section related to wideband MEFSS cover is prepared to be submitted as M. M. Honari, P. Mousavi, and K. Sarabandi "Wideband Radiation Enhancement of RFICs Using Multi-layer Miniaturized-Element Frequency Selective Surface Covers," *IEEE Transactions on Antennas and Propagation.*

To my loving wife, Parinaz

and my dear Parents

whose support has resulted in my success

Acknowledgments

This thesis is a product of the work, guidance, and love from great people that have helped me during the journey through my Ph.D. program. First and foremost, I take immense pleasure to extend my sincere and deep sense of gratitude to my supervisor, Prof. Pedram Mousavi, for his sustained enthusiasm, creative suggestions, motivation and exemplary guidance throughout the course of my doctoral research. He had a paramount influence on different aspects of my life because he treated me like his son and taught me a new lesson every day. He has built a solid foundation for my educational and professional career. I am also grateful to my advisory committee Prof. Ashwin K. Iyer, and Vien Van for reviewing my dissertation and supplying me with their invaluable insights. My special thanks go to Prof. Iyer, and Prof. K. Sarabandi for guiding me with their keen advice, critical insight, and confidence throughout some parts of the thesis.

Most importantly, I would like to thank my parents for their dedication, boundless love and continuous support which enhanced my ambition throughout my educational life. I could not have been where I am today without your support. Words cannot describe all my gratitude and love for you. I would also like to thank my loving wife, Parinaz, for her invaluable support, endless patience and understanding, and for always being there for me. Your energy and inspiration motivated me in every step I took along this journey. Thanks for making my life so beautiful!

I would like to take this opportunity to thank all the individuals, colleagues and friends who assisted me during this research project. My special thanks go to my friend, Rashid Mirzavand, for sharing his knowledge, experience, and for supporting this research project. Thank you for all the support and insight that enabled me to reach this milestone in my academic achievement. I would also like to express my gratitude to all my friends, who were of great assistance to me during this journey.

The financial support provided by University of Alberta, Natural Science and Engineering Research Council (NSERC), Alberta Innovates Technology Futures (AITF), is gratefully acknowledged. Moreover, Personal financial assistance in the form of scholarships/awards from the University of Alberta is highly appreciated.

Contents

List of Figures

List of Tables

List of Acronym

1D	One dimensional
2D	Two dimensional
3D	Three dimensional
AMC	Artificial Magnetic Conductor
EBG	Electromagnetic BandGap
EOT	ExtraOrdinary Transmission
FPC	Fabry-Pérot Cavity
FSS	Frequency Selective Surface
HIS	High Impedance Surface
HPBW	High-Power BeamWidth
HPM	High Power Microwave
IC	Integrated Circuit
MEFSS	Miniaturized-Element Frequency Selective Surface
OEW	Open-Ended Waveguide
PCB	Printed Circuit Board
PRS	Partially Reflecting Surface
RF	Radio Frequency
TEM	Transverse ElectroMagnetic
TEN	Transverse-Equivalent Network
TE	Transverse Electric
TM	Transverse Magnetic

List of Symbols

ε_0	Free-space Permittivity
ε_r	Relative Permittivity
μ_0	Free-space Permeability
μ_r	Relative Permeability
α	Attenuation Constant
β	Propagation Constant
k	Complex Propagation Constant
k_0	Free-space Propagation Constant
λ	Wavelength
ω	Angular Frequency
Z_0	Characteristic Impedance
f_r	Resonant Frequency
f	Frequency
D	Directivity
L	Inductance
C	Capacitance

Chapter 1

Introduction

Along with the advances in technology over the past decades, we have experienced a remarkable growth in investigation on and development of new wireless communication systems. In many applications, those systems need to have several features such as high gain, high efficiency, wide bandwidth, and high power. For instance, high-gain antennas are essential for many wireless applications in which a high path loss in medium weakens the transmitted signal. Therefore, there is a need to improve the antenna gain, especially where there is a limitation on power amplifiers' stage in transmitting site or where a high signal-to-noise ratio is desired in receiving site.

Antenna arrays are one of the most straightforward methods to increase the gain of systems. But, they add complexity to the antenna structure requiring the design of a large feed network which itself increases the loss in the system and degrades the antenna efficiency. Although horn and reflector antennas as conventional medium- to high-gain antenna structures used to play an important role in many applications, their heavy weight, high profile and non-planar structures limit their applicability in modern communication systems. As a result, it is required to propose planar antennas with high gain, lower profile, light weight, and inexpensive fabrication cost.

Being Planar for antennas is very vital for integration with the rest of the system. This requirement favors planar antennas which are manufactured using commodity printed circuit board (PCB) or integrated circuits (IC) processes. The capability to manufacture the antennas on PCB or IC makes the integration of radio frequency (RF) systems with antennas feasible resulting in circuit miniaturization. This would be of value in integrating RF transceivers or RFICs.

1.1 Motivation

This work presents two techniques for designing high-gain antennas based on corrugated structures and miniaturized element frequency selective surfaces (MEFSS) structures. The main motivation behind this work arises from the requirement for high gain antennas with planar structure, low profile, and cheap fabrication expense. The corrugated structure technique is used for the applications of space and satellite communications where a planar antenna structure is required to embed in a CubeSat [1]. The technique of using MEFSS structure as a gain boosting cover on top of an on-chip antenna, which is proposed in this thesis, can find applications in on-chip communication and radar systems.

In some specific applications, high power is required for the system. In this case, a waveguide mode converter is needed to convert an undesired mode of High power microwave (HPM) source to a desired output mode for propagation. HPM sources normally generate axially symmetric modes such as the transverse electromagnetic (TEM) mode or the TM_{01} circular waveguide mode. These modes produce a doughnut-shaped far-field radiation pattern with a null at boresight if they directly radiate from an open-ended waveguide or a horn antenna [2]. In this work, several mode converters are designed and printed for high power antenna applications.

The conventional structure of corrugated antennas is composed of a central aperture surrounded by symmetric 1D (rectangular) or 2D (bull's-eye) corrugations patterned on a metallic sheet. Although these corrugated antennas in literature have provided favorable radiation characteristics, they have considerable drawbacks that prevent them from being used in many applications. In addition to high cost of making metallic structures, they are bulky and hard to be integrated with other parts of the system, especially planar devices. Therefore, development of these antennas in a planar structure with inexpensive fabrication methods is a challenge.

There are some works in literature that analyzed corrugated antennas. For example, 1D corrugated antennas are investigated using Eigenfunction expansion, Fourier transform and mode matching method [3]. Furthermore, in [4], authors studied corrugated antennas utilizing the singular integral equation approach in a rigorous manner. Although, these methods give a full perspective view of the problem, it is hard to do a fast rough estimation of a general radiation

performance of an antenna. In many works, different types of corrugations along with their dimensions are optimized to get the best antenna performance [5]. However, due to a large antenna size, this process is very time consuming. It seems that a fast approach to designing and analyzing corrugated antennas, and estimating their radiation performance is required. This can avoid the time consuming approach of optimization process for designing corrugated antennas.

Dual-band antennas can be used in many applications where both receiving and transmitting sites are required in one package. In this case, the antenna can be used as a transmitter in one band and as receiver in the other band. Designing high-gain low-profile dual-band corrugated antennas with planar structures poses several challenges which are investigated in this work.

Design of fully integrated RF systems that are able to generate enough radiation power to mitigate high propagation loss is critical in millimeter and submillimeter-wave frequencies. At such high frequencies, the antenna size is approximately a few millimeters, which facilitates their practical implementation and integration on a chip. Besides, a co-design of all parts including the antenna can improve the efficiency and decrease the input power level [6]. However, antenna integration on chip has its own set of challenges. One of the main issues is that silicon material deteriorates on-chip antenna performance since it introduces a thick substrate with low resistivity and high relative permittivity which launches surface waves in a lossy medium [7, 8]. Although many techniques such as using a thin metasurface [9], and artificial magnetic conductor [10] inside the chip have been proposed as a solution to poor radiation of on-chip antennas, due to limitations in the number, the thickness, and conductivity of metallic layers on CMOS process, as well as limited real estate, fabrication of on-chip antenna with high efficiency is still not practically feasible.

To shield an on-chip antenna and prevent the propagated waves from coupling into silicon layer, an incorporated ground plane can be used. However, in this case, due to the small distance between the antenna and ground plane, which creates strong inter-coupling, the radiation resistance is very small resulting in the antennas' poor efficiency. To improve the radiation characteristics of an on-chip antenna, silicon micromachining can be used. However, micromachining and CMOS

processes are not directly compatible and many additional steps are required [11]. Using a silicon lens on the backside of the chip is reported in [12] to mitigate the surface wave loss of the silicon substrate. However, the level of complexity and fabrication limitations make the realization of this approach difficult. One of the current technologies for enhancing the radiation performance of RFICs is based on the incorporation of a relatively thick superstrate over which the antenna can be placed [13, 14]. The drawback of thick superstrates is the reduction in radiation efficiency due to dielectric loss and power loss in surface waves. Launching surface waves in thick superstrates can also increase mutual coupling among radiating elements of an array. To improve the radiation efficiency, dielectric resonators can also be integrated on top of the chip [15, 16]. However, the alignment of the dielectric resonator with the excitation underneath may be difficult especially at submillimeter-wave frequencies. In addition, the height of the structure becomes larger when dielectric resonators are added on top. This increase in height may not be suitable for many applications. As a result, a technique for radiation gain enhancement of an active CMOS circuit is necessary for on-chip communications. It is shown that the gain enhancement in on-chip antenna can be achieved using MEFSS structures added as a cover on top of the IC.

1.2 Objectives

The followings are the main objectives of this work:

1. To design and print high-performance TM_{01} to TE_{11} mode converters that are necessary to be used in high power antenna applications.
2. To design and fabricate a planar corrugated antenna on laminates using substrate integrated waveguide (SIW) technology.
3. To analyze corrugated antennas with surface susceptance of the corrugated structure and estimate the radiation performance based on a unit-cell analysis that would reduce the design of a corrugated antenna to the design of a corrugated unit-cell.
4. To investigate the effect of corrugations' dimensions on the resonant frequency, spectral bandwidth, and directivity of corrugated antennas.
5. To design and investigate dual-band corrugated structures

6. To design, and fabricate dual-band feeder antennas to be used at the center of dual-band corrugated structures creating dual-band corrugated antennas.
7. To provide a solution in order to improve radiation performance off of on-chip antennas using MEFSS structures and design, and fabricate a prototype at 10 GHz.
8. To design a wideband MEFSS cover, and use it as a solution in wideband on-chip antennas.

1.3 Outline

In chapter 2, a background on corrugated surfaces, MEFSS structures, and theory of leaky wave is provided. Moreover, a brief review of literature about advances in corrugated antennas, and FSS structures with their applications in antenna theory is presented. Chapter 3 introduces three categories of TM_{01} to TE_{11} mode converters that can generate the desired modes to feed the cavity in corrugated antennas for high power applications. These wideband mode converters are printed and successfully measured demonstrating a high TM_{01} to TE_{11} mode conversion. Chapter 3 presents corrugated antenna structure realized on laminate by SIW technology. It is shown that by coupling mechanism, the feed line, grooves, and cavity can be designed and fabricated on PCBs. Then, a simple approach for design and analysis of corrugated antennas based on surface susceptance is proposed which estimates their general radiation performance. The relation between resonant frequency, spectrum bandwidth, and directivity of the antenna with unit-cell's corrugation susceptance is analytically approximated which reduces the design a corrugated antenna into the design of a single unit-cell. This is followed by an investigation on the effect of corrugations' width, height, and the materials' permittivity inside corrugations on unit-cell's susceptance and antenna directivity. A 2D corrugated (bull's-eye) antenna with 3 corrugations is designed with this method and implemented that could achieve a measured gain of 17.4 dBi. Chapter 4 discusses the possibility of design and fabrication of planar dual-band corrugated antennas. It is shown that by using two different corrugations, dual-band operation may be achieved. To solve the problem of back radiation of transmission line feed, two classes of dual-band open-ended circular waveguide feeder antennas with a compact collinear end-launcher-type feed is proposed. The proposed feeder structures can generate a mixed mode close to TE_{11} on the aperture of the open-ended waveguide

in both bands resulting in stable broadside gains over each band of interest. For the integration purposes and due to having a thick substrate in the structure of dual-band feeder antenna, it is required that the height of the corrugations be increased. It is shown that in this case, the corrugated structure with anti-resonance that satisfies the resonance condition can be used. A dual-band corrugated structure integrated with feeder antenna is implemented which demonstrates a measured gain of 15.8 and 17.5 dBi at frequencies of 9.7 GHz and 13.85 GHz, respectively, and can be used in satellite communications. Chapter 6 presents a technique to improve the radiation characteristics of an on-chip antenna in an active CMOS circuit. A MEFSS cover is utilized on top of an on-chip antenna to provide gain enhancement, which is essential for many applications such as radar and communication systems. This is important due to restrictions on thickness of metallic layers, losses in substrate, and limitations in a real estate. The MEFSS cover consists of partially reflecting surface (PRS) and high impedance surface (HIS) creating a Fabry-Pérot-type cavity (FPC). Because of using MEFSS structure, the height of FPC can be reduced without any deterioration of antenna radiation. A proximity patch antenna is embedded in the HIS layer which is fed by a small metallic trace on the last layer of chip using coupling mechanism. By utilizing the transverse-equivalent network of the structure and imposing the resonance condition, the geometrical parameters of the MEFSS unit-cell are calculated. For demonstration purposes, a scaled MEFSS cover for gain enhancement at the center frequency of 10 GHz is designed, fabricated and measured. A wideband multi-layer MEFSS cover is proposed and designed to solve the problem of narrow bandwidth of single-layer MEFSS structure. This wideband MEFSS cover is then used on top of an on-chip antenna to improve the antenna gain. In chapter 7, a brief conclusion of the work is presented and several suggestions for the future work are given.

Chapter 2

Background and Review of Literature

There are various techniques to enhance the gain of an antenna structure. Antenna arrays or conventional high-gain antennas are not desired in many applications due to their complex lossy feed network and non-planar structures, respectively. In this thesis, corrugated structures and frequency selective surfaces are used as approaches of gain enhancement in radar, space and satellite communications, and on-chip antenna applications. Therefore, in this chapter, a brief background and literature review related to these techniques is provided.

2.1 Transverse Resonance Technique

The electromagnetic fields in spectral domain in two dimensional (2D) structures with a homogenous transverse cross-section may be expressed as superposition of transverse magnetic and (TM) transverse electric (TE) modes. In this case, it can be shown that these modes are traveling in an equivalent transmission line model [17] which is the solution of Maxwell equations. As a result, all the techniques known in transmission line theory can be used to face the problem. For instance, Fig. 2.1 shows a grounded dielectric slab with a thickness of h and its transverse equivalent transmission line model. If a propagation along X-direction is considered, the transverse equivalent transmission line for TE and TM modes will be along Z-direction as shown in Fig. 2.1, where the slab and free space are shown by transmission lines with the characteristic impedance of $Z_1^{TM/TE}$, and $Z_0^{TM/TE}$, and propagation constant of k_{z1}, and k_{z0}, respectively. One of the techniques that is valid in the model is transverse resonance technique which results in the dispersion equation. The transverse resonance equation in Fig. 2.1 is expressed as the follows:

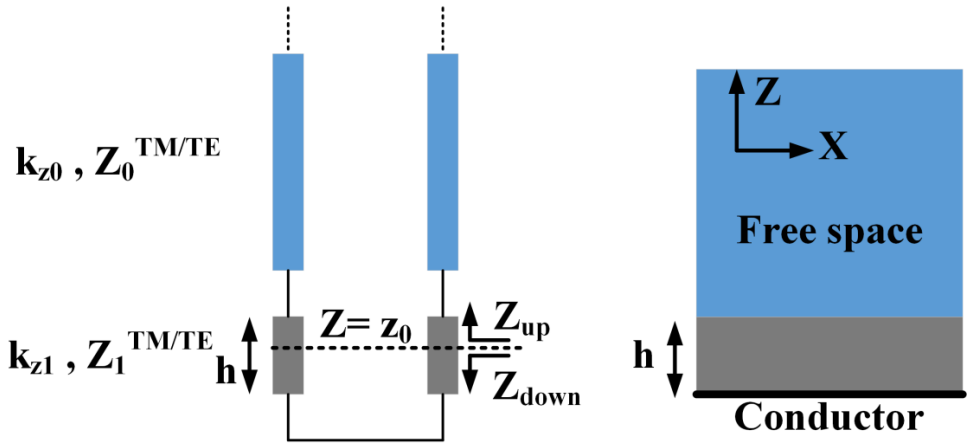

Fig. 2.1. A grounded dielectric slab and its transverse equivalent transmission line model.

$$Z_{up}(z_0) + Z_{down}(z_0) = 0 \tag{2.1}$$

where Z_{up}, and Z_{down} are the impedance looking upward and the impedance looking downward from an arbitrary point z_0, respectively. Note that the resonance condition of (2.1) is not dependent on z_0. The same resonance condition can be verified for admittances and reflection coefficients with the following equations:

$$Y_{up}(z_0) + Y_{down}(z_0) = 0 \tag{2.2}$$

$$\Gamma_{up}(z_0) \cdot \Gamma_{down}(z_0) = 1 \tag{2.3}$$

For a complicated circuit, by obtaining the transverse equivalent transmission line model or transverse-equivalent network (TEN), the dispersion equation can be calculated by calculating the resonance condition of the model.

2.2 Waves Excited on Planar Structures

For a general geometry, both transverse and normal propagation constants can be complex variables (i.e. $k_z=\beta_z-j\alpha_z$, $k_x=\beta_x-j\alpha_x$). Then, two components of propagation constant vector satisfy the following equation:

$$k_x^2 + k_z^2 = k_0^2 \tag{2.4}$$

By substituting the complex values of propagation constant components in (2.4), two

independent equations are obtained:

$$(\beta_x^2 + \beta_z^2) - (\alpha_x^2 + \alpha_z^2) = |\overline{\beta}|^2 - |\overline{\alpha}|^2 = k_0^2 \quad (2.5)$$

$$\alpha_x\beta_x + \alpha_z\beta_z = \overline{\alpha} \cdot \overline{\beta} = 0 \quad (2.6)$$

where $\overline{\alpha} = \alpha_x \overline{a}_x + \alpha_z \overline{a}_z$ and $\overline{\beta} = \beta_x \overline{a}_x + \beta_z \overline{a}_z$ are attenuation and propagation vectors, respectively. To find out the possible modes travelling on a planar structure, an arbitrary geometry is taken into account. Assume in a point z_0 which is on top of the geometry, the upward medium is free space with characteristic impedance of Z_0, and the downward medium is the arbitrary geometry with an impedance of $Z_{down} = R_{down} - jX_{down}$, where R_{down} and X_{down} are impedance and reactance of the downward medium, respectively. Now, the resonance condition for the TM mode can be written as:

$$Z_{down} + Z_0^{TM} = Z_{down} + \frac{k_z}{\omega\varepsilon_0} = 0 \quad (2.7)$$

The similar resonance condition can be written for TE mode as well. We can simplify (2.7) as:

$$\omega\varepsilon_0(R_{down} + jX_{down}) = -\beta_z + j\alpha_z \quad (2.8)$$

For $z > z_0$, the possible plane waves in free space above the structure depend on the signs of the impedance R_{down} and reactance X_{down}. Fig. 2.2 shows all possible TM modes excited on an arbitrary planar structure. The signs of R_{down} and X_{down} determine the direction of propagation constant and attenuation, respectively, according to (2.8). Each of six categories, depicted in Fig. 2.2, shows a specific guided wave on the surface as follows: (1) surface wave, (2) improper surface wave, (3) surface wave traveling in lossy surface, (4) improper wave growing away from the structure, (5) complex wave decaying away from the surface, (6) improper leaky wave.

As demonstrated, when both impedance and reactance of the structure are negative, a leaky wave emerges which radiates in the forward direction. It is worth mentioning that, as shown in Fig. 2.2 and presented in (2.6), the vectors $\overline{\alpha}$ and $\overline{\beta}$ are always perpendicular to each other.

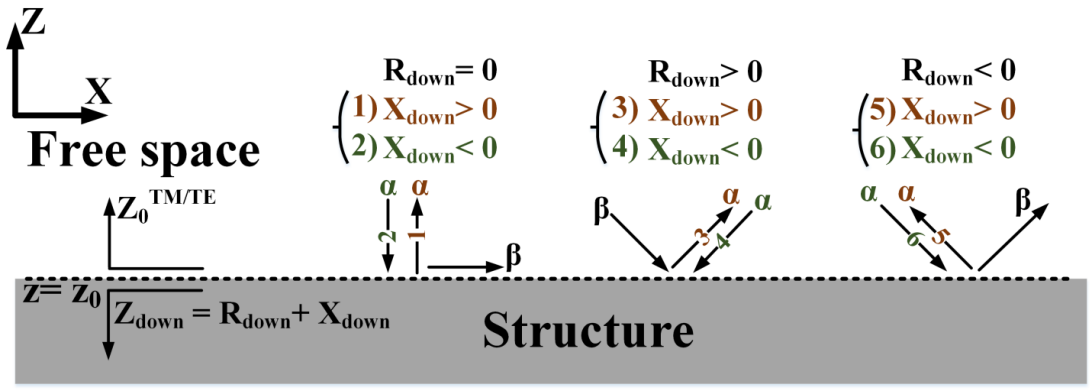

Fig. 2.2. Possible TM modes excited on an arbitrary planar structure.

2.3 Frequency Selective Surfaces

Frequency selective surface (FSS) structures are 1D or 2D periodic elements designed to exhibit frequency selectivity or filtering. Fig. 2.3 shows typical geometries for FSS elements [18]. They have been used as an alternative to electromagnetic band-gap (EBG) structures with the advantages of planarity and easy realization in millimeter- and submillimeter-wave communication [19]. They have many applications in radar instruments and satellite communications. These periodic structures can perform spatial filtering [20], polarization converting [21], and antenna gain boosting [22]. Over the past few decades, FSS structures have been widely investigated as a part of many devices such as artificial magnetic conductors (AMC), transmitarrays [23], and reflectarrays [24]. The size of the elements and their spacing in traditional resonant FSS structures are comparable to wavelength at frequency of operation. To observe a desired frequency selective behavior, the structure must contain a large number of the resonant unit-cells resulting in an electrically large surface. Therefore, for many applications, FSS unit-cells with smaller electrical dimensions and less sensitivity to the incidence angle are required. A new class of FSS structure called miniaturized-element frequency selective surface (MEFSS) has recently been introduced [25]. This new class consists of a multilayer periodic array of metallic structures; as equivalent inductor and capacitor; with dimensions much smaller than wavelength at frequency of interest. One of the most attractive features of MEFSS structures is that the interaction of MEFSS surface with incident TEM wave can be simplified with a model of lumped

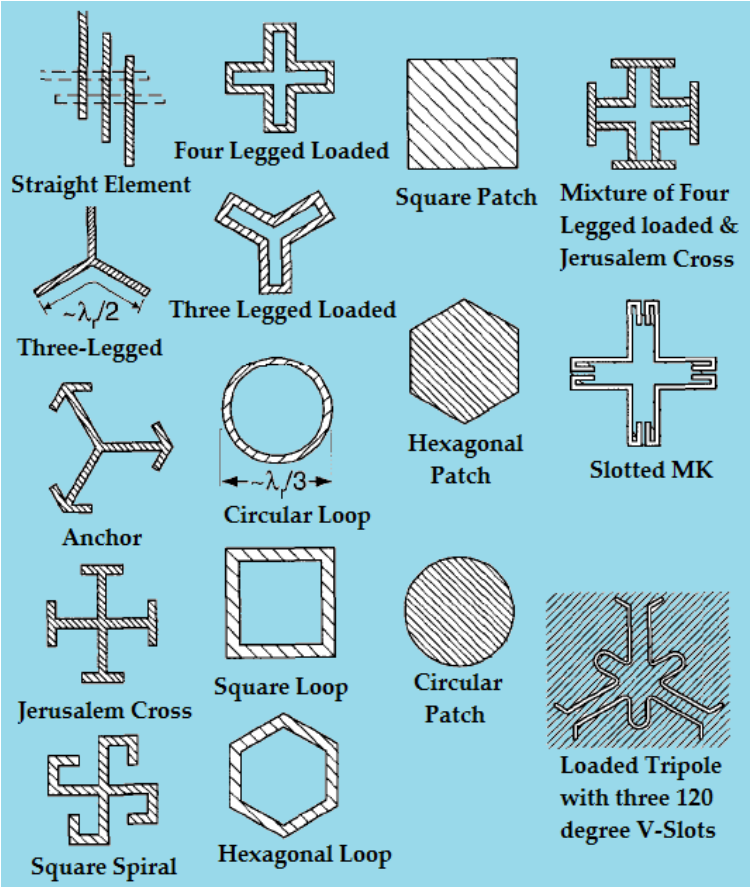

Fig. 2.3. Typical geometries for FSS elements [18].

inductors and capacitors [26]. In fact, using their equivalent circuit model, the design and tuning of MEFSS structures with desired frequency response becomes much easier. Multi-pole filters with arbitrary number of transmission zeros and poles can be designed to realize wideband bandpass, band-stop, and multi-bandpass filtering response [27, 28].

2.4 Fabry-Pérot Cavity Antennas

Fabry-Pérot cavity (FPC) antennas consist of a cavity with partially-reflective-surfaces (PRSs) or frequency selective surfaces on top and a ground plane at the bottom, and a radiating element inside the cavity as shown in Fig. 2.4. Using the cavity which embeds the main radiator

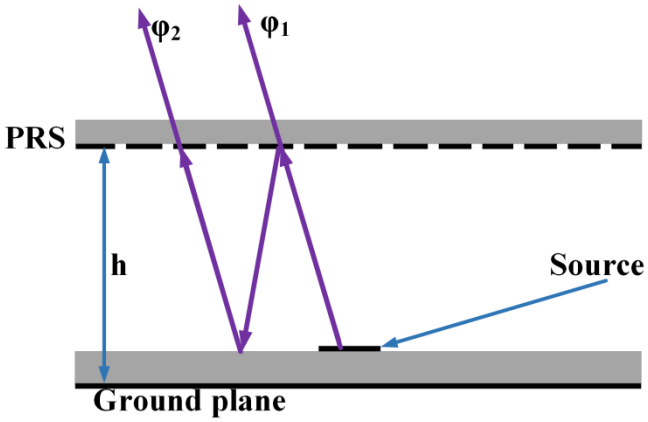

Fig. 2.4. Conventional Fabry-Pérot cavity antenna.

is an effective way to improve the antenna gain without the need to design a feeding network [29]. However, the PRS is required to be placed at a certain distance from the ground plane. The mechanism of operation of FPC antennas is based on multi-reflection of waves inside the cavity. Due to in-phase propagation of waves, transmitted through PRS, into free space, the FPC antennas have a high gain. These antennas have some disadvantages such as high manufacturing cost, and mechanical stability issues [30]. Using ray tracing, it can be easily proved that the directivity of the antenna at boresight can be calculated by [31]:

$$D = \frac{1 - R^2}{1 + R^2 - 2R\cos(\Delta\varphi)} \tag{2.9}$$

where $\Delta\varphi = \varphi_2 - \varphi_1$, and $Re^{j\varphi_R}$ are the complex reflection coefficient of the PRS. The resonance appears when the phase difference between the rays $\Delta\varphi$ is a multiple of 2π. Therefore, the resonance condition necessitates the height of the cavity to be chosen as:

$$h = (\frac{\varphi_R}{\pi} - 1)\frac{\lambda}{4} + N\frac{\lambda}{2} \tag{2.10}$$

Also, the maximum directivity at this resonance condition is given by:

$$D_{\max} = \frac{1 + R}{1 - R} \tag{2.11}$$

2.5 Extraordinary Transmission

Several decades ago, Bethe proved that the power transmitted through a small aperture with radius of R at a certain wavelength of λ is proportional to $(R/\lambda)^4$ [32]. However, Ebbesen et al. [33] and wood [34], and Rayleigh [35] demonstrated that the extraordinary optical transmission (EOT), and wood-rayleigh anomaly may appear for an array of holes on a metallic plate or a slit surrounded by corrugations. This EOT was related to the excitation of surface plasmons (SPs) which are bound modes on the surface of the structure and cannot be excited by an external incident wave. However, the periodic structure can provide necessary conditions to excite them.

From that time on, many 1D and 2D holes with different geometries have been investigated as shown in Fig. 2.5. The study of different structures proves that the electromagnetic coupling depends primarily on the period of grooves rather than on their 1D or 2D geometries [36]. This results in the conclusion that the corrugations do not propagate themselves; however, they contribute to the maximum peak of transmission efficiency by helping out the coupling of electromagnetic waves to surface plasmons [37].

In [38], the authors theoretically analyzed the transmission of light not only through periodic hole gratings (transmission gratings), but also through an aperture on a metallic structure surrounded by periodic corrugations (reflection gratings). In both cases, the coupling of incident photons to surface plasmons is the reason for the extraordinary optical transmission. In the reflection gratings case, it was shown that for a structure with periodic corrugations with a periodicity of p, two possible electromagnetic resonances can satisfy the resonance conditions: one located at a wavelength close to surface plasmon condition ($\lambda \approx p$), and the other one at much longer wavelength ($\lambda \gg p$). According to the electric field distribution, it was shown in [38] that the latter is a cavity mode in which the electric field is extremely concentrated inside the grooves, while for the resonance with smaller wavelength, the electric field intensity over grooves is due to coupling of electromagnetic waves to surface plasmon polaritons.

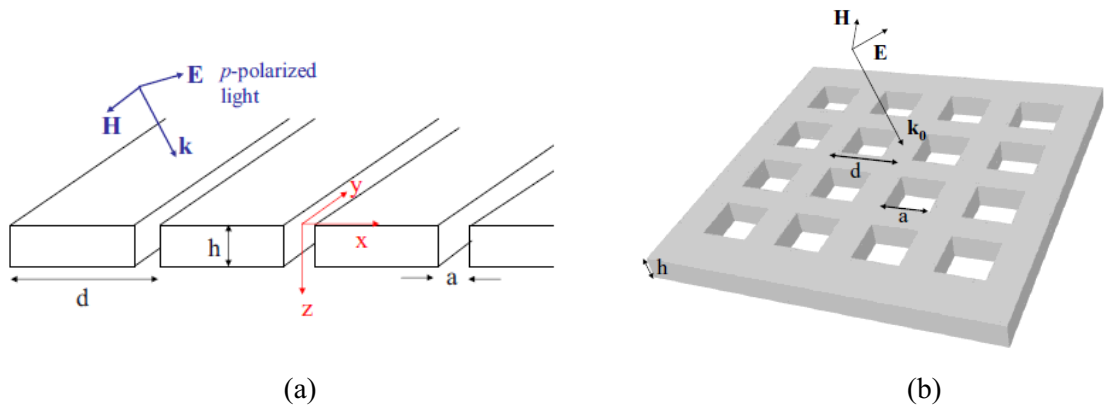

(a) (b)

Fig. 2.5. 1D and (b) 2D of hole arrays perforated on a metallic sheet [36].

For reflection gratings case, 1D and 2D structures were studied in [39] as shown in Fig. 2.6. It is indicated that the diffraction limitation can be overcome by creating periodic texture on either input of exit side of a single aperture in a metal film in 1D or 2D structures. The corrugations on the input side harvest the power more efficiently and the corrugations on the exit side create a more directive beam, both resulting in a high transmission efficiency.

It is theoretically and experimentally demonstrated that to have the maximum transmission, three mechanisms need to occur: slit waveguide mode excitation (adjusted by the thickness of metallic sheet), resonance of the grooves (adjusted by the grooves' dimensions), and in-phase groove reemission (adjusted by the period of the grooves) [40].

Enhanced transmission, later on, was demonstrated by periodic corrugations at microwave and millimeter wave frequencies [41, 42]. Using attractive characteristics of EOT, an interesting family of antennas came to existence. In fact, if the energy is fed by the aperture, the periodic corrugations can increase the antenna gain. These antennas have many important applications in communication technologies and space communications since compared to high profile structures such as horn and parabolic antennas, they can provide comparable radiation characteristics. Using the leaky wave analysis in antenna theory is another perspective to analyze this kind of corrugation structures.

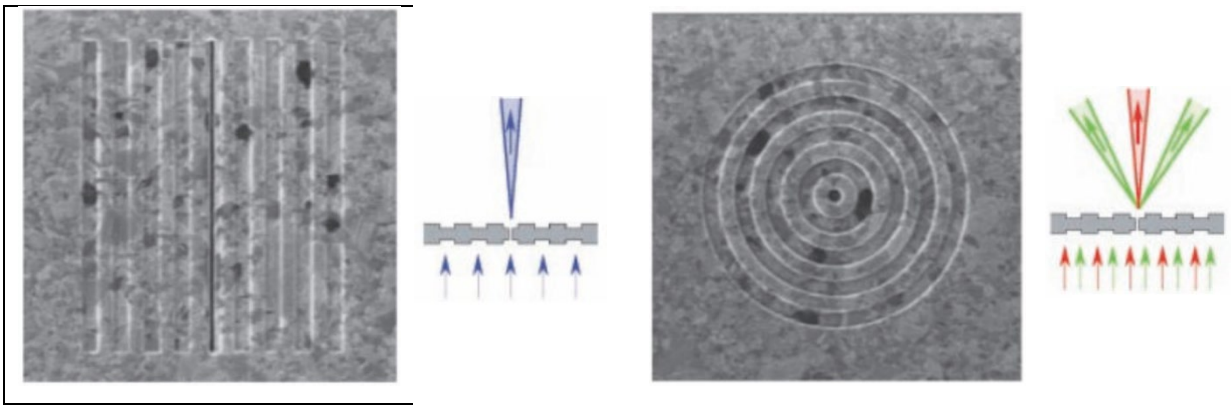

(a) (b)

Fig. 2.6. 1D and (b) 2D structures of single aperture surrounded by corrugations on a metallic sheet [39].

2.6 Array Factor of Corrugated Antennas

To estimate the radiation pattern, the array factor of the corrugated structure can be calculated based on leaky plasmon wave analysis [43]. With the assumption that leaky plasmon waves are propagating along Y-direction as shown in Fig. 2.7, the complex propagation wave-number would be as follows:

$$k_{LW,y} = \beta_{LW} - j\,\alpha_{LW} \tag{2.12}$$

where β_{LW} and α_{LW} are the propagation and attenuation constants. If we assume that each groove is a radiating element with a current determined by the leaky plasmon mode and the distance between elements is p, the array factor of the structure is given by [44]:

$$AF = \sum_{n=1}^{\infty} I_n e^{jk_0 \sin(\theta)(nd-d/2)} + \sum_{n=-1}^{-\infty} I_n e^{jk_0 \sin(\theta)(nd+d/2)} \tag{2.13}$$

In (2.13), it is assumed that there is no direct propagation from the aperture and by symmetry $I_n = I_{-n}$. Based on the leaky plasmon wave with a complex wave-number in the Y-direction, the associated current for each element is:

$$I_n = e^{-jk_{LW,y}(nd-d/2)} \qquad n > 0 \tag{2.14}$$

$$I_n = e^{+jk_{LW,y}(nd+d/2)} \qquad n < 0 \tag{2.15}$$

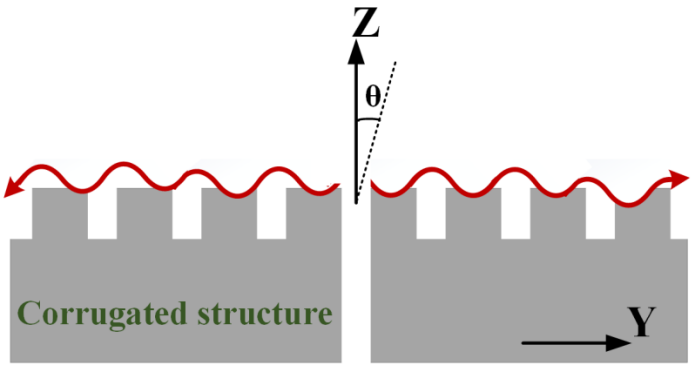

Fig. 2.7. The model of leaky plasmon wave propagating along Y direction.

Substituting (2.14) and (2.15) into (2.13) gives the array factor of the corrugated antenna:

$$AF = \sum_{n=1}^{\infty} e^{j[k_0 \sin(\theta) - k_{LW,y}](nd - d/2)} + \sum_{n=-1}^{-\infty} e^{j[k_0 \sin(\theta) + k_{LW,y}](nd + d/2)} \quad (2.16)$$

Then, this array factor can be simplified as:

$$AF(\theta) = Z_1^{-\frac{1}{2}} \sum_{n=1}^{\infty} Z_1^n + Z_2^{-\frac{1}{2}} \sum_{n=1}^{\infty} Z_2^n = \left(\frac{Z_1^{1/2}}{1 - Z_1}\right) + \left(\frac{Z_2^{1/2}}{1 - Z_2}\right) \quad (2.17)$$

where:

$$Z_1 = e^{jd[k_0 \sin(\theta) - k_{LW,y}]} \quad (2.18)$$

$$Z_2 = e^{-jd[k_0 \sin(\theta) + k_{LW,y}]} \quad (2.19)$$

Although, the array factor of corrugated antenna can be estimated using (2.17), the accuracy of the surface plasmon model determines how accurate (2.17) is as an array factor of corrugation structures.

2.7 Leaky Wave Propagation of Corrugated Antennas

The theory of enhanced transmission in corrugated structures, which is a narrow beamwidth in antenna point of view, can be analyzed using leaky wave theory [45, 46]. It has been indicated that a metallic sheet loaded with corrugations supports the excitation of leaky waves if the periodicity is selected large enough with respect to the wavelength [47]. The periodic

modulation of the guiding geometry provides the existence of space harmonics of the dominant surface mode with the wave-number presented by:

$$k_n = k_0 + 2\pi n/d \qquad n=\ldots,-2,-1,0,1,2,\ldots \tag{2.20}$$

According to the theory for periodic structures, the surface modulation due to existence of surface wave is in a way that n=-1 space harmonic of the TM surface wave is a fast wave with $|k_{-1}| < |k_0|$ in a frequency band. Therefore, the whole structure propagates in that range of frequencies.

The corrugated structure shown in Fig. 2.7 consists of two leaky wave beams for each half of the whole structure. If we just consider one half of the structure, the angle of propagation with respect to the broadside can be achieved by:

$$\beta_{LW,-1} = \beta_0 - 2\pi/d \approx k_0 \sin(\theta_{-1}) \tag{2.21}$$

which shows how the periodicity affects the direction of the propagation. The beam direction of the half corrugated structure is swept with the change in frequency as presented in (2.21). If there is no periodic structure on the metallic sheet, the surface wave would be a bound surface wave whose propagation constant at optical frequencies is given by [48]:

$$\beta_p \approx k_0 \sqrt{\frac{\varepsilon_r}{\varepsilon_r+1}} \tag{2.22}$$

where ε_r is the relative permittivity of the metallic structure at optical frequencies. Depending on the amount of the loading that the corrugations exert on TM surface mode, β_0 and β_p may be close to each other or a bit different. Generally, it is a good approximation to assume $\beta_p \approx k_0 \approx \beta_0$. Therefore, the angle of propagation can be simplified as:

$$\sin(\theta_{-1}) \approx 1 - \lambda/d \tag{2.23}$$

It is seen that the angle of beam at a certain frequency in corrugated structures depends on the periodicity. According to (2.23), for $\lambda \approx d$, the leaky wave structure will propagate at broadside. However, pure broadside radiation ($\beta_{LW,-1}=0$) is not feasible since the attenuation constant goes to zero and the leaky mode becomes a standing wave. In fact, the propagation in this point is close to zero due to the existence of a stop-band null point [12] as shown in Fig. 2.8.

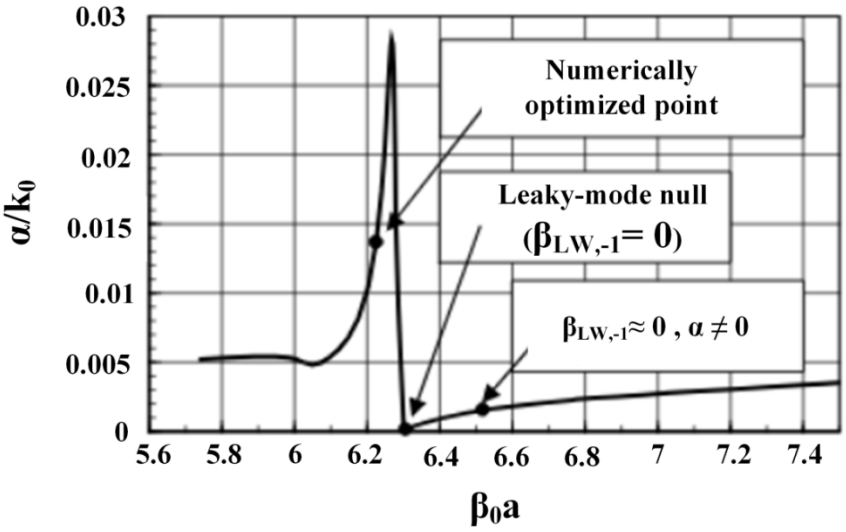

Fig. 2.8. Normalized attenuation constant versus normalized periodic $\beta_0 a$ of the leaky plamon wave [44].

However, there have been solutions such as using double-strip gratings [49] in leaky wave structures that overcome the broadside radiations' problem.

For the whole two-sided corrugated antenna shown in Fig. 2.7, if $d \neq \lambda$ ($\beta_{LW,-1} \neq 0$), there are two beams propagating in ±Y direction as a result of travelling surface wave of each half of the structure. It can be illustrated that there is an optimum point for maximum broadside radiation in which the periodicity is close to a wavelength. This maximum point happens when two beams merge together in a way that a maximum broadside radiation appears [50]. This optimum point corresponds to the following condition [51] (see Appendix A):

$$|\beta_{LW,-1}| = \alpha \tag{2.24}$$

The sharp and directive beam of the corrugated structure is the result of the propagation of the surface modulated elements (grooves) due to superposition of electric field inside corrugations rather than the direct propagation of the center aperture [52]. Other types of analysis, in addition to leaky wave theory, can be done on the corrugated structures. One of the more rigorous studies is by using the singular integral equation approach.

2.8 Various Types of Radiation Pattern of Corrugated Structures

The physical mechanisms of the corrugated structures were studied in [4] using the singular integral equation approach to form different possible radiation patterns. The periodicity of the corrugations (p) and their width (w) and depth (h) affect the radiation pattern of the antenna. Here, depending on d, w, and h, the antennas' radiation pattern can be categorized into two categories:

1. The periodicity is $p< \lambda_0/2$ and the depth of the grooves is $h\leq h_0\leq \lambda_0/4$ where h_0 depends on the width of the grooves. In this category, the structure supports surface wave and the power is transmitted from the center aperture to the grooves without radiation (attenuation constant close to zero). The grooves are considered as discontinuities in the way of surface wave and make it to radiate into a cylindrical wave or to reflect back as a reflection loss. A typical radiation pattern of this type is shown in Fig. 2.9(a). However, if the periodicity is $p< \lambda_0/2$ and the depth of the grooves is $h_0\leq h\leq \lambda_0/4$., the structure supports surface wave, the attenuation constant is very large, and the corrugations operate in the stopband regime. Therefore, a few grooves close to the center aperture affect the radiation pattern of the antenna. A typical radiation pattern of this type is shown in Fig. 2.9(b). The choke ring horn antennas and GPS antennas work in this regime.

2. If the periodicity is $p> \lambda_0/2$, the structure supports a leaky wave. Depending on the values of w, and h, the attenuation and propagation constants differ. This results in having three states of backward proper, forward improper, and improper leaky waves.

A typical radiation pattern of each state is shown in Fig. 2.10. The radiation pattern of the backward proper leaky wave is depicted in Fig. 2.10(a). There are two separate beams with opposite direction with respect to the broadside as expected. The radiation pattern of a half corrugated structure is also shown in this case. For improper leaky wave mode, a flat radiation pattern with a low gain is created. This mode is neither forward nor backward [53]. Finally, the typical radiation pattern of the forward improper leaky wave mode as shown in Fig. 2.10(c) demonstrates that a highly directive beam can be created if the dimensions of the grooves and the periodicity of the corrugation are selected appropriately.

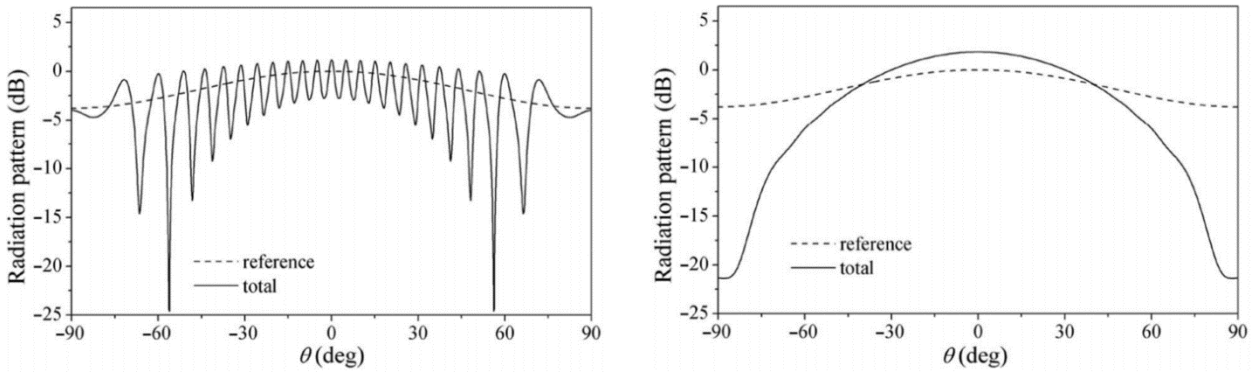

Fig. 2.9. Typical radiation patterns of the corrugated structure with $d < \lambda_0/2$ for the grooves' depth of (a) $h \leq h_0 \leq \lambda_0/4$, and (b) $h_0 \leq h \leq \lambda_0/4$ [4].

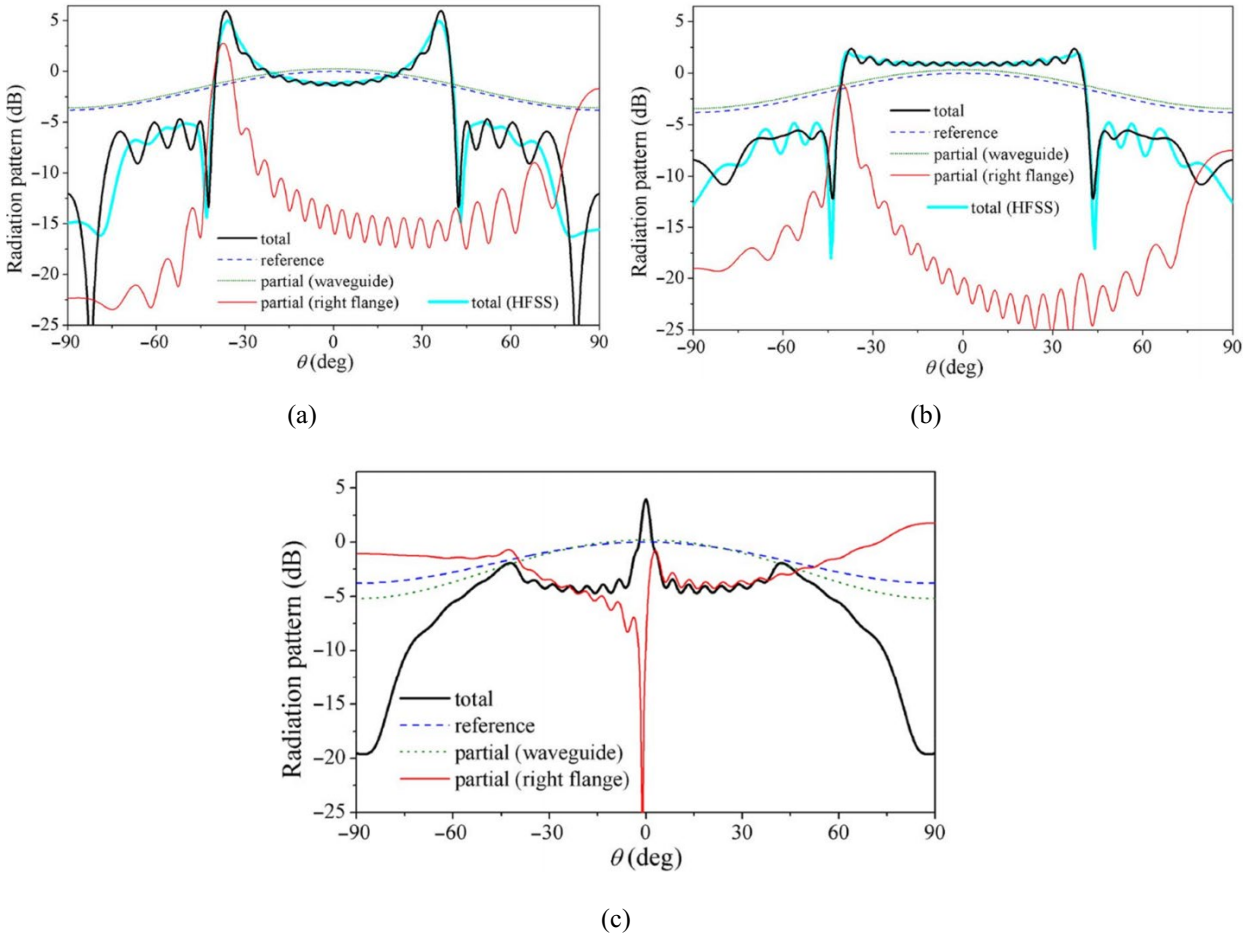

Fig. 2.10. Typical radiation patterns of (a) backward proper, (b) improper, and (c) forward improper leaky wave modes in the corrugated structure [4].

2.9 Corrugated Structures with Off-Axis Beaming

It was shown in [54] that it is possible to focus the beam in an off-broadside angle by the proper modification of the corrugations. The idea is to arrange the corrugations asymmetrically in order to have a directive beam at off-broadside. For this purpose, both upper and lower half of the corrugated structures have to be designed in a way that both radiate in the same direction. This happens when the upper half of the antenna supports a forward leaky wave mode and the lower half supports backward leaky wave mode [53] as shown in Fig. 2.11.

For a certain d_0 shown in Fig. 2.11, it can be analytically proved that the path functions $\rho = d^{(n)}(\varphi)$ for the corrugations n=0,1,2,.., P are:

$$d^{(n)}(\varphi) = (d_0 + n\lambda)/(1 - \sin\theta'\sin\varphi) \qquad \varphi \in (0,2\pi) \qquad (2.25)$$

which implies an offset for each corrugation from the center aperture. For a certain beam direction θ', the path functions of the corrugations are determined. As shown in Fig. 2.12, by using this modification of the structure, the beam direction can be shifted from broadside to a desired angle. A similar structure can be designed for 1D corrugated structure, i.e. a center aperture surrounded by straight corrugations at both sides. This idea of pointing the beam to a desired angle has been previously discussed using holographic artificial impedance surfaces [55].

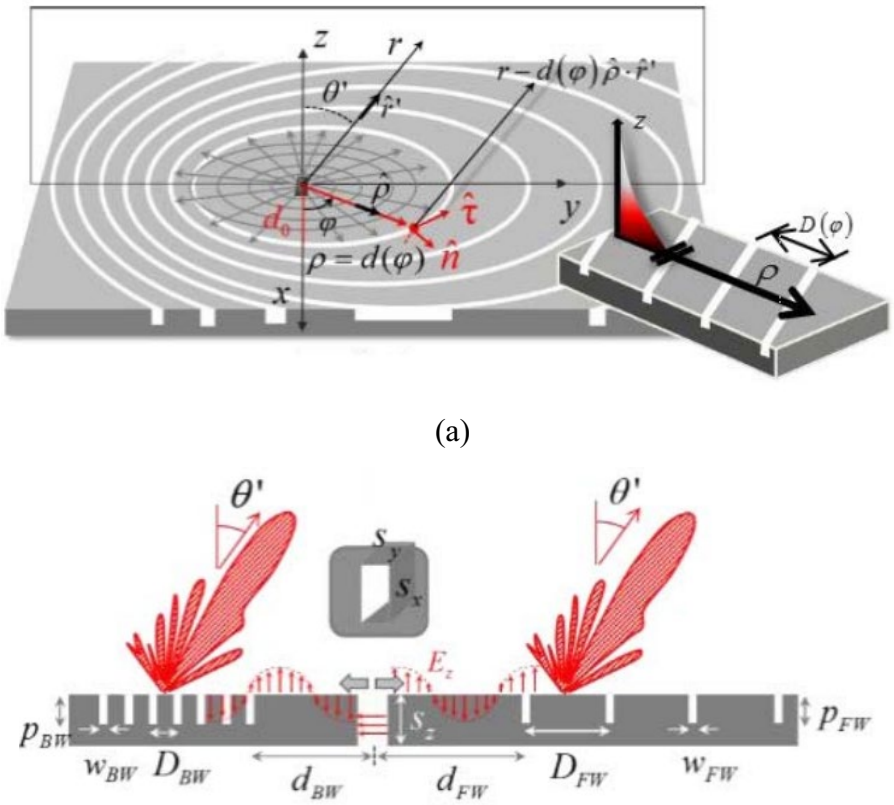

Fig. 2.11. Geometry of the corrugated antenna with off-axis beaming, (a) 3D view, and (b) cross-sectional view [53].

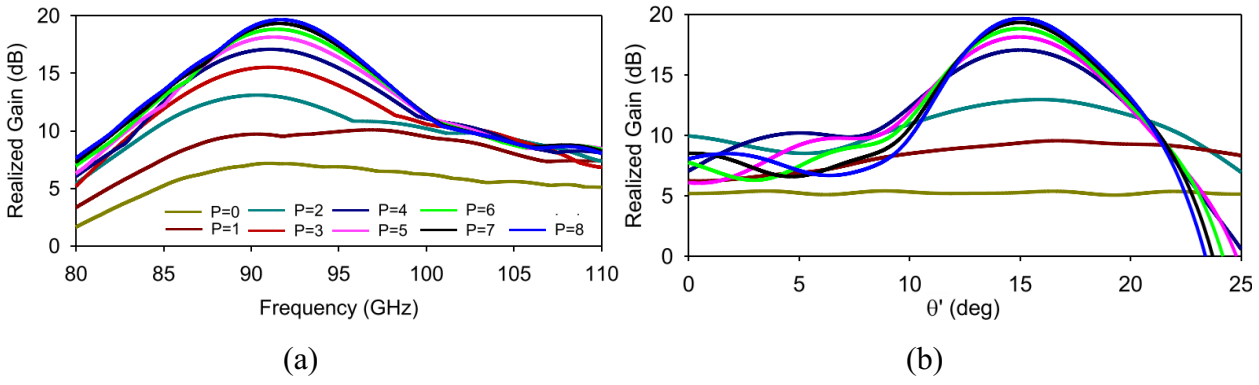

Fig. 2.12. (a) Realized gain versus frequency at $\theta' = 15^{o}$ for different number of corrugations, (b) E-plane at the center frequency for different number of corrugations [53].

2.10 Advances on Corrugated Antennas

Corrugated antennas are a good candidate to be used in high gain applications such as space and satellite communications. There are many works that aim to improve the characteristics of these types of antennas. We briefly review some works in literature in this section.

2.10.1 Basic 1D and 2D corrugated antennas

The basic structure of corrugated antennas consists of an aperture surrounded by 1D [56, 57], or 2D [58] corrugated metallic sheet. The 2D corrugated antenna is called bull's eye antenna. In these antennas, the aperture is fed by a conventional waveguide. Fig. 2.13 shows the structures of 1D and 2D corrugated antennas. The aperture must be designed in such a way that it resonates at the operational frequency. The dimensions of the cavity slot can be designed to have two resonances (transversal and longitudinal) [59]. Therefore, in the design of the corrugated antennas, the metallic sheet has to have a minimum thickness. This makes the structure heavy, high-profile, and expensive. For bull's eye antenna with 6 corrugations reported in [58], a narrow beamwidth in E-plane has been achieved as shown in Fig. 2.14.

2.10.2 Corrugated Antennas with Size Reduction

Due to high volume structure, it is always a need to reduce the size of corrugated antennas as much as possible. In [60], the transversal slot resonance was used instead of the longitudinal one to reduce the antenna thickness. Also, as shown in Fig. 2.15(a), by inserting a material with a permittivity bigger than 1, the thickness of the structure was further reduced. Fig. 2.15(b) shows that in addition to size reduction, the antenna gain of the structure with inserted dielectric material increased about 1.3 dBi compared to that of conventional one.

In another study reported in [61], by integrating additional subwavelength periodic corrugated grooves and adjusting the depth of the grooves, the antenna size was reduced as shown in Fig. 2.16. The excitation of surface modes at microwave frequencies in this case improved the performance of this surface wave antenna. Although the antenna size diminished, due to having

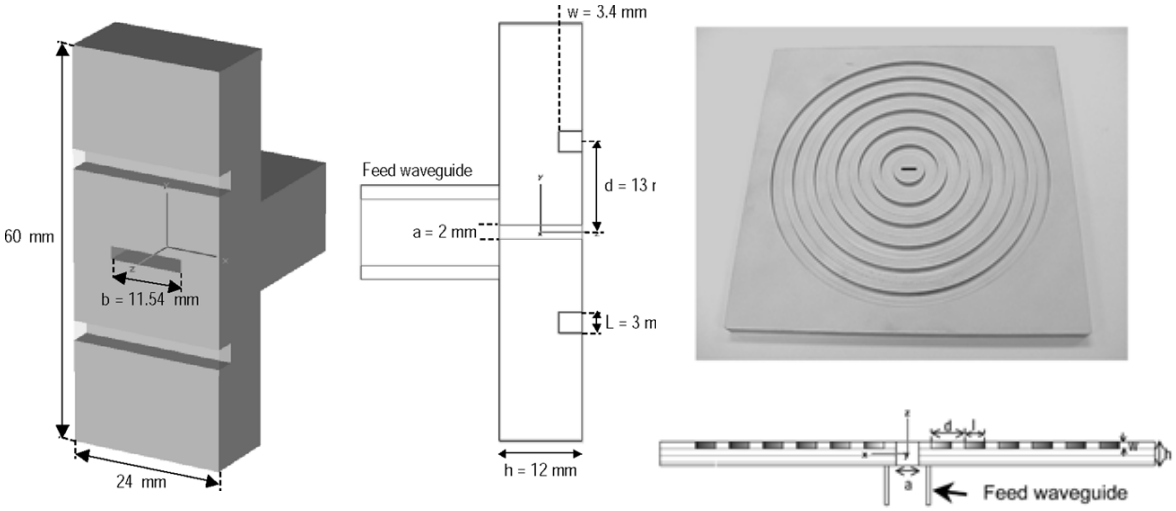

(a) (b)

Fig. 2.13. Basic structures of (a) 1D corrugated antennas [58], (b) 2D corrugated (bull's eye) antennas [58].

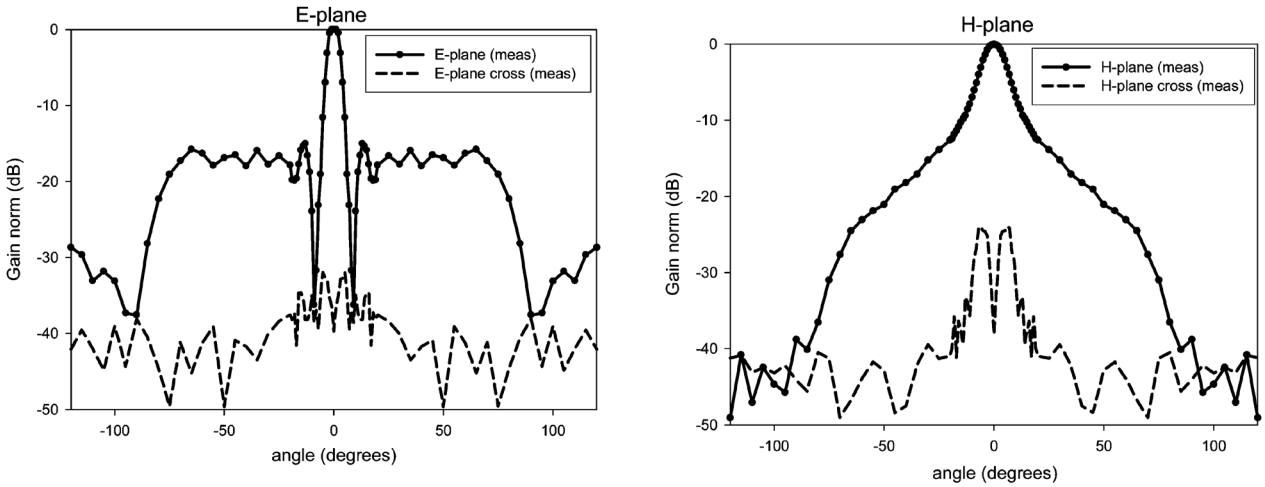

(a) (b)

Fig. 2.14. Radiation pattern of the bull's eye antenna reported in [58] (a) E-plane, (b) H-plane.

a thick metallic structure, the antenna has still high volume.

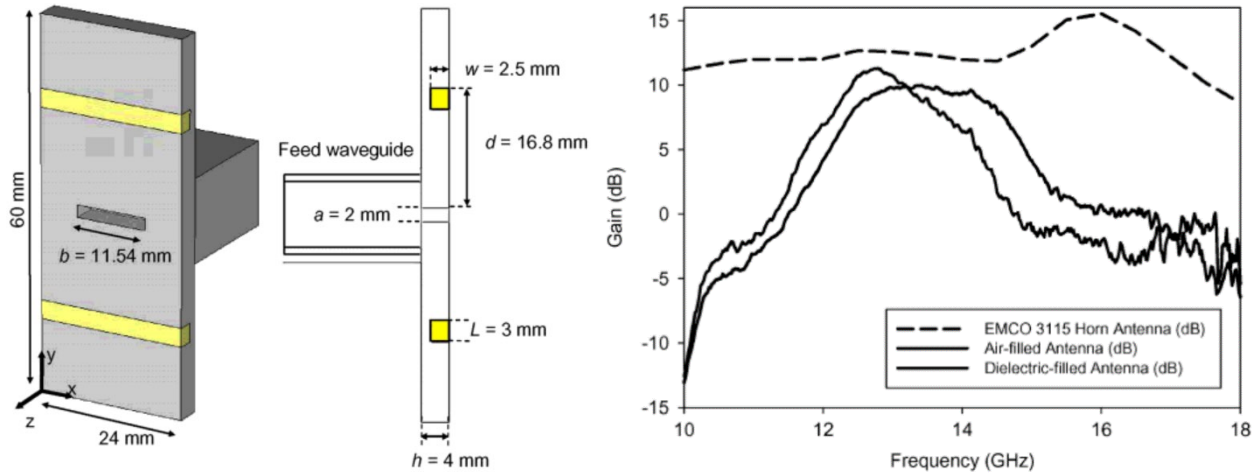

(a) (b)

Fig. 2.15. (a) The corrugated antenna with reduced size, and (b) its corresponding gain compared to the conventional structure [60].

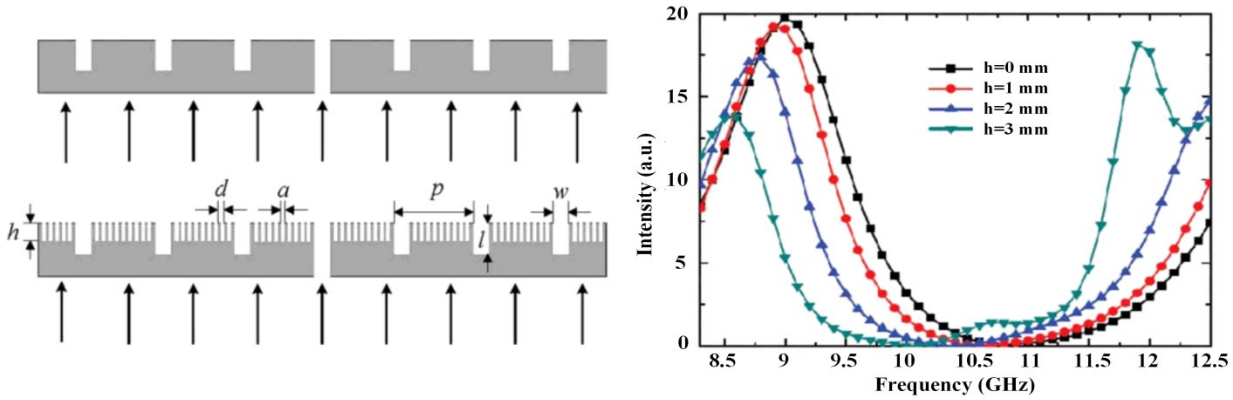

(a) (b)

Fig. 2.16. (a) The antenna with two kinds of corrugation for size reduction, and (b) its intensity diagram for different corrugations' height [61].

2.10.3 Corrugated Antennas for High Gain Applications

There are many applications in millimeter wave and terahertz frequencies that need high gain antennas. In [62], using silicon micromachining, a pyramidal horn and four V-grooves were integrated and designed for terahertz frequencies as shown in Fig. 2.17. The grooves significantly increase the antenna gain, even though; the structure is still low profile. The dimensions of the horn were designed in such a way that a low side-lobe-level was achieved.

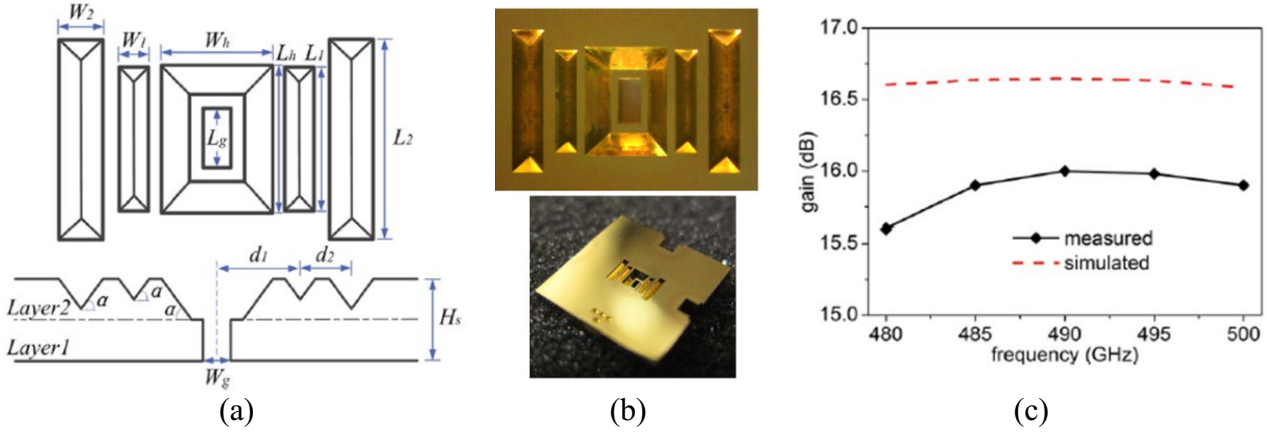

(a) (b) (c)

Fig. 2.17. (a) The geometry of the horn antenna with V-grooves, (b) its fabricated sample, and (c) the corresponding antenna gain [62].

Generally, increasing the number of grooves does not guarantee a higher gain accordingly. This depends on the attenuation constant of the leaky mechanism of the antenna. If grooves are such that a high attenuation constant is achieved, a few number of grooves are enough in the design since the wave attenuates very fast and the energy delivered to the outer grooves is very low. On the opposite side, if the attenuation is low, more grooves can be used in antenna design and as a result, probably, a higher gain can be achieved. A high gain bull's eye antenna with 20 periods of corrugations presented a gain of 29.3 dBi in [63]. The antenna configuration, the antenna gain, and the directivity and beamwidth versus the number of periods are shown in Fig. 2.18. It can be seen that the rate of directivity increase decreases with an increase in the number of periods. The investigation on different shapes of grooves such as triangular and square shapes in corrugated antennas shows that for a high number of grooves, the gain and reflection coefficient are not dependent on the shapes of the grooves if the dimensions are optimized adequately [64]. This is very important especially in terahertz regime where corrugations with high aspect ratio are impossible to fabricate.

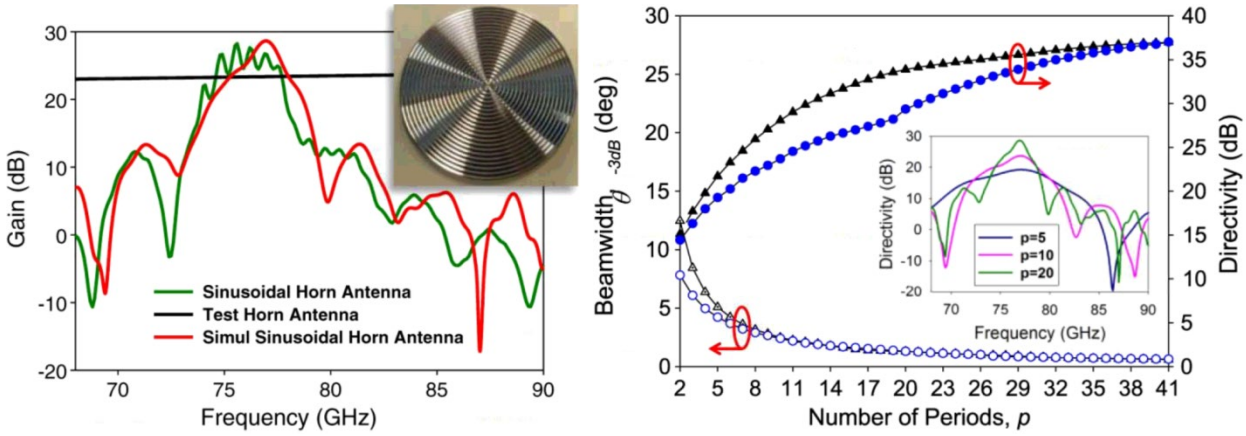

(a) (b)

Fig. 2.18. (a) Gain versus frequency for the high gain bull's eye antenna reported in [63], and (b) the directivity and beamwidth versus the number of periods (line with triangles and line with circles show the square-groove and sinusoidal corrugations respectively).

To increase the antenna gain, double-layer corrugated structures [65] or an array of two slot elements [66] can be used as shown in Fig. 2.19. Due to a high attenuation constant of both structures, few numbers of corrugations have been used. However, the antenna gain of almost 16 dBi has been obtained for both cases.

2.10.4 Corrugated Antennas with High Aperture Efficiency

Using wider grooves can lead to gain improvement since they suppress higher order resonances as reported in [67] and shown in Fig. 2.20(a). It was demonstrated that using annular soft structures of grooves placed on the edge of the antenna results in an increase in gain, a decrease in side-lobe-level, and a reduction in endfire and backfire radiations. This results in having an antenna with higher gain and smaller size and therefore an antenna with higher aperture efficiency. One of the problems of the corrugated structures is diffraction of the surface wave at the edges. This problem can be solved by using soft structures since this diffraction degrades the antenna pattern and antenna efficiency. The excitation of TE_{11} mode in small grooves and TM_{11} mode in big grooves as shown in Fig. 2.20 (b) result in a high aperture efficiency enhancement.

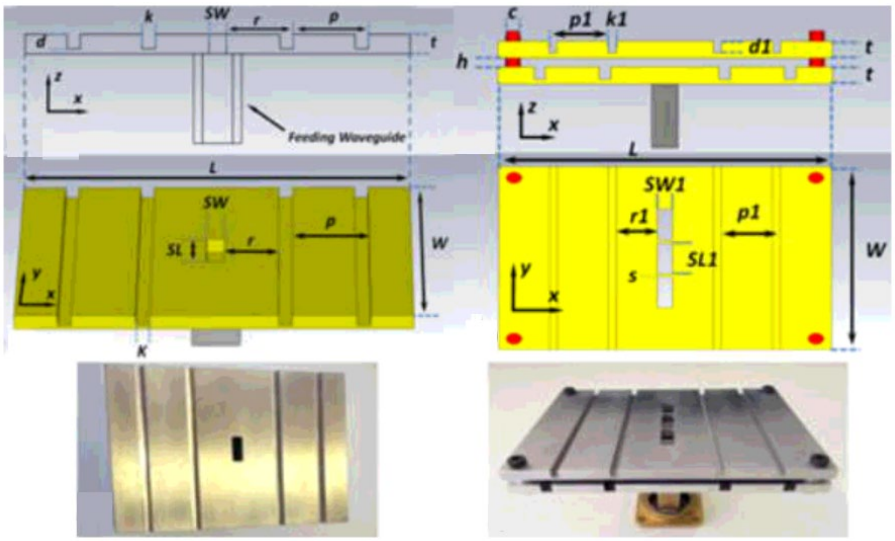

(a)

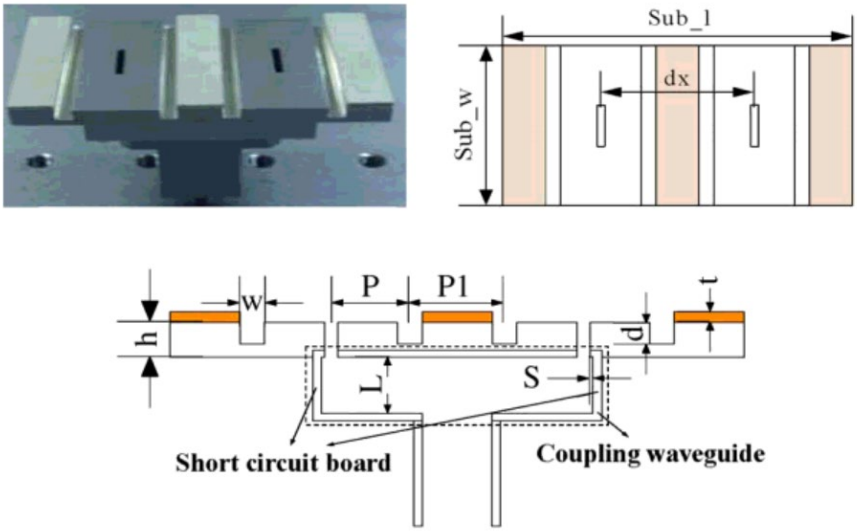

(b)

Fig. 2.19. (a) The geometries for antenna gain improvement (a) double-layer corrugated structure [65], (b) an array of 2 slot elements [66].

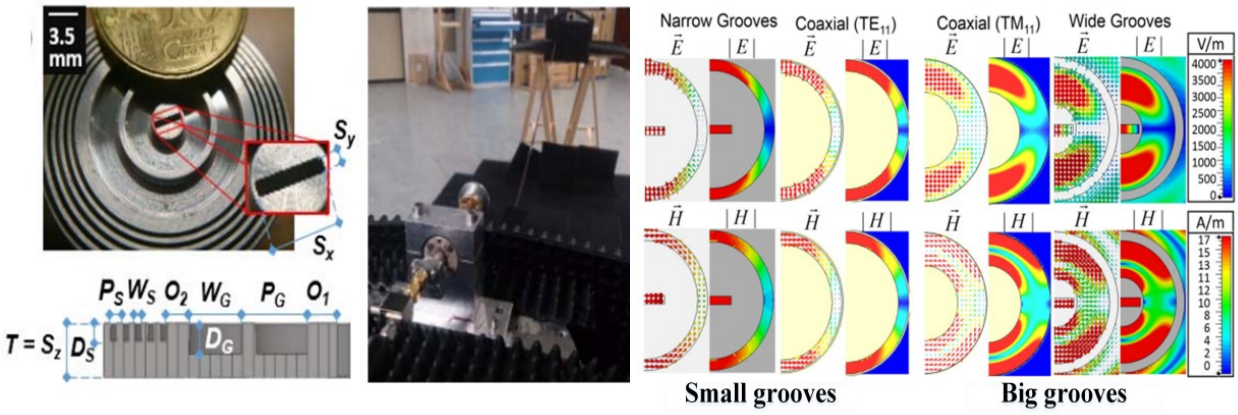

(a) (b)

Fig. 2.20. (a) The geometry proposed in [67] to increase the aperture efficiency, (b) the mode inside big and small grooves.

2.11 Advances on Fabry-Pérot Cavity Antennas

The radiation gain enhancement of simple radiating sources, such as microstrip patches and waveguide apertures, using FPC antennas is an effective gain enhancing method which eliminates the feeding network. There are quite a few works in literature studying the resonant cavity and the possibility of its miniaturization in FPC antennas. Here, we briefly discuss the two main works on FPC antennas.

2.11.1 Miniaturization of FPC Antennas with Artificial Magnetic Conductors (AMCs)

Artificial magnetic conductors (AMCs) fully reflect the incident waves with a reflection phase close to zero degrees as opposed to perfect electric conductor with a reflection phase close to 180 degrees [68]. Metallic patch arrays on a grounded dielectric substrate, which are connected to ground by vias and create mushroom-shape structure, have been proposed as AMCs [69]. Although for each fabrication, AMC structures have been also proposed without connecting vias. In [70], it was shown that using AMC structure in FPC antennas can reduce the height of the antenna by 50%, as shown in Fig. 2.21.

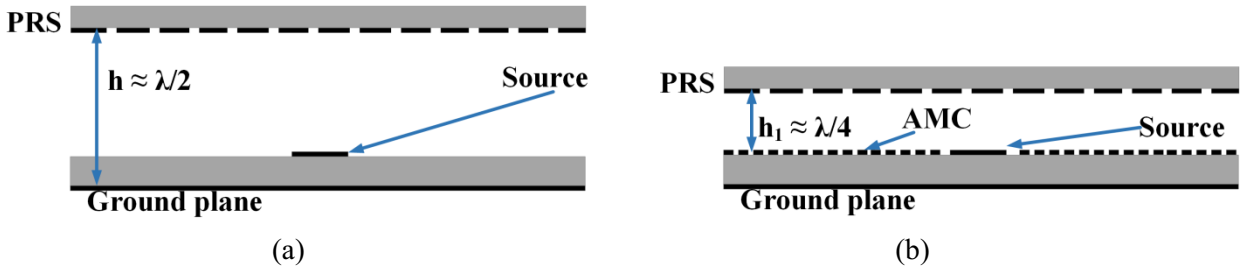

(a) (b)

Fig. 2.21. (a) Conventional FPC antenna, (b) FPC antenna with AMC for size reduction [70].

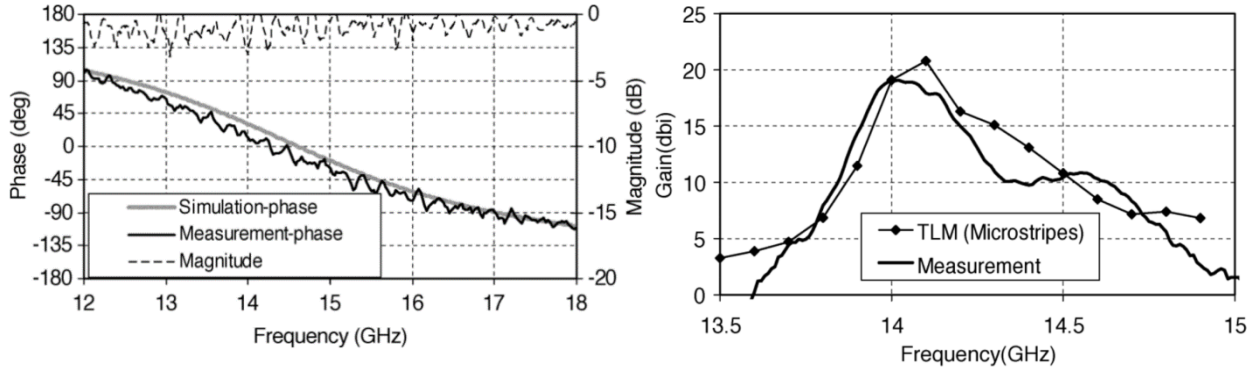

(a) (b)

Fig. 2.22. (a) Reflection magnitude and phase of the AMC, (b) gain of the FPC antenna with AMC [70].

Using ray tracing method, it can be easily shown that the height of FPC can be calculated by:

$$h = \frac{\varphi_R \lambda}{4\pi} + N\frac{\lambda}{2} \tag{2.26}$$

where φ_R is the reflection phase of the PRS. Fig. 2.22 shows the reflection magnitude and phase of the AMC surface for an incident wave, and the corresponding gain for the FPC antenna with AMC structure. As it is shown, when the reflection phase is zero (an ideal AMC), the cavity resonates and a high gain is achieved.

2.11.2 Wideband FPC Antennas

Due to multiple reflection between the ground plane and the PRS, the directivity of FPC antennas increases significantly. However, since the resonance condition occurs in a single

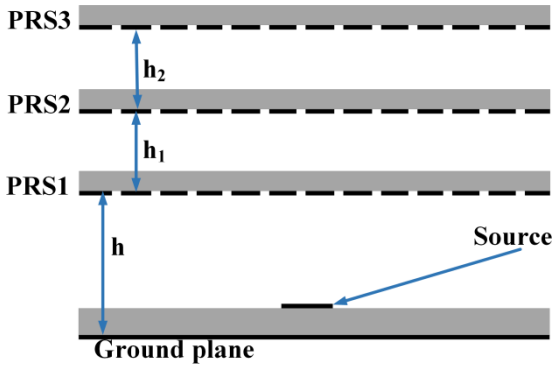

Fig. 2.23. A FPC antenna with three PRS layers.

frequency, this type of antenna has narrow operational bandwidth. One method to make the FPC antennas wideband is to employ multiple PRS layers. To enhance the radiation bandwidth, one effective method is to use PRS with positive reflection phase gradient over a wide bandwidth [71]. This can be done using multiple superstrates or PRS structures. The multiple PRS structures stacked on top of each other with optimized distance from each other may provide multiple resonances. Designing the FSS structures so as to have those resonances close to each other results in a wideband FPC antenna [72]. Fig. 2.23 shows the configuration of a FPC antenna with three PRS layers. As shown in Fig. 2.24, a FPC antenna with two and three PRS layers is designed in [72]. Each PRS layer can add a positive phase gradient which can increase the number of resonances of the cavity. Therefore, the antenna with three PRS layer would provide wider radiation bandwidth. The directivity of the antenna with two and three PRS layers is shown in Fig. 2.25 which demonstrates a wider bandwidth for antenna with three PRS layers.

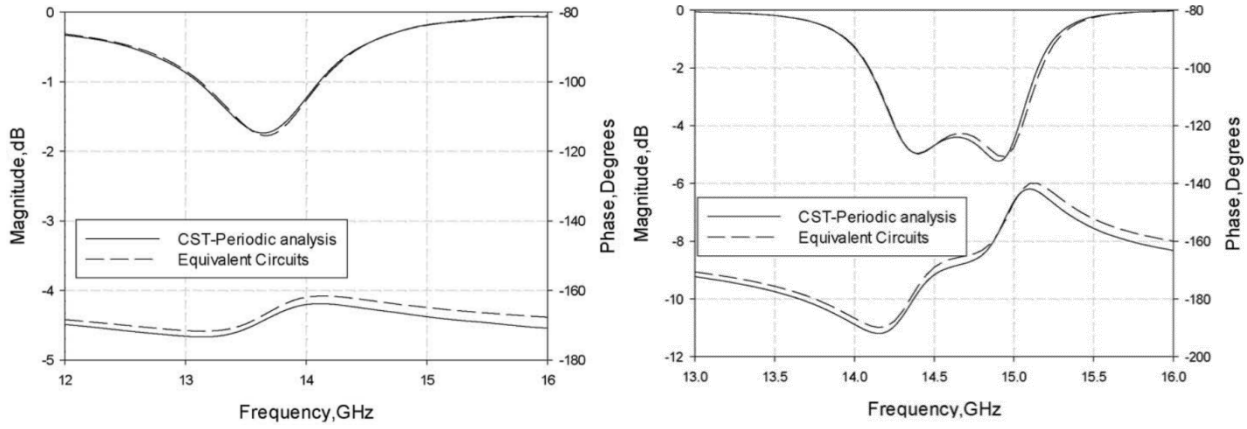

Fig. 2.24. Reflection magnitude and phase of FPC antenna with (a) two PRS layers, and (b) three PRS layers [72].

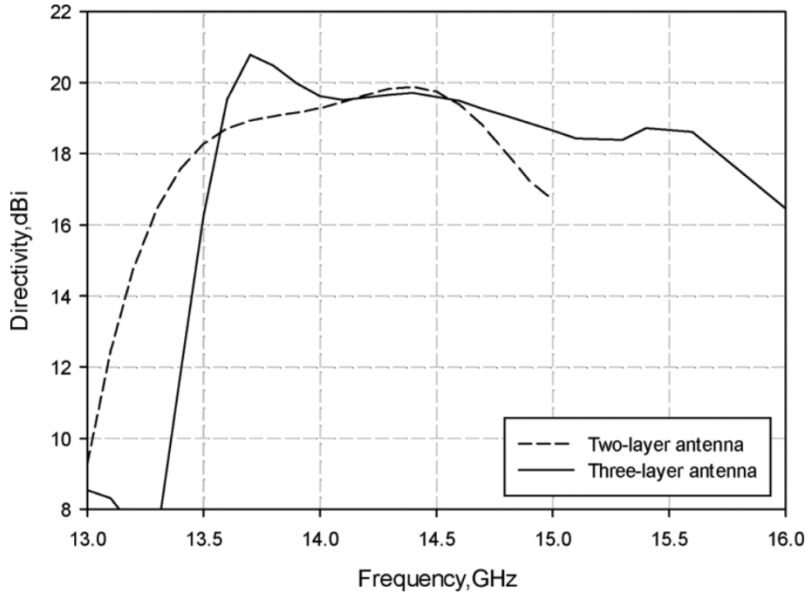

Fig. 2.25. Directivity of FPC antenna with two and three PRS layers [72].

Chapter 3

High-Performance Printed TM01 to TE11 Mode Converters

In this chapter, three categories of the TM_{01}-TE_{11} mode converters; i.e. dielectric loaded based, metallic septum based, and mode converter with intermediate modes; that can be used in corrugated antennas for high power applications are proposed and investigated. The mode converters are designed to achieve high conversion efficiency and wide operational bandwidth. Since high power microwave (HPM) sources generate TM_{01} mode which produces a doughnut-shaped far-field radiation pattern with a null at boresight if it feeds corrugated antennas, the TM_{01}-TE_{11} mode converters are required to build a constructive broadside radiation pattern. The principles of operation of all mode converters are explained in detail. The conventional fabrication of these mode converters is difficult due to the complexity of the structures. Therefore, the feasibility of economical 3D printing fabrication is explored in this chapter.

3.1 Mode Converters

Mode converters are structures that convert an undesired mode to a desired one [2, 73, 74]. Among them, TEM-TE_{11} and TM_{01}-TE_{11} mode converters have been of interest for many researchers to transform radial electromagnetic modes to the mode with a definite polarization and converged radiation pattern [75]. A dual-bend circular waveguide is a conventional structure for TM_{01}-TE_{11} mode converters [76]. Although analytical methods are proposed for these mode converters, unaligned input and output ports and bulky structure make them expensive and hard to realize [77]. Therefore, mode converters with linear axis are more preferable such as a cross-

shaped TM_{01}-TE_{11} mode converter [78], mode converters using intermediate modes [79, 80], dielectric loaded based mode converters [81], and metallic septum based mode converters [82]. The cross-shaped mode converter is not easy to fabricate, and its power-handling efficiency is not sufficient like linear TEM-TE_{11} mode converters. Many mode converter structures use intermediate modes such as the TEM mode [83] for the TM_{01}-TE_{11} mode conversion to increase the maximum conversion efficiency or the conversion efficiency bandwidth. Creating a 180^o phase shift in half of the TM_{01} pattern using different shapes of a dielectric material is another method of TM_{01} to TE_{11} conversion [84, 85]. The mode converters can be integrated with antennas to produce broadside radiation pattern. For example, as reported in [86], the integration of dielectric loading and correcting phase lens in a horn aperture resulted in a stepped lens that converts the TM_{01} mode to the circular polarized TE_{11} mode.

Although many works have been done on TM_{01}-TE_{11} mode converters, the fabrication restrictions always have been an issue. Furthermore, the mode converters are designed so as to be realizable and cost effective. As a result, in many cases, the conversion efficiency and the bandwidth are limited. However, the development of additive manufacturing [87-92] has made the fabrication of mode converters with complex design and even their integration with the rest of the system easy.

3.2 TM_{01}-TE_{11} Mode Converter Design and Analysis

HPM sources mainly generate TM_{01} mode which produces a doughnut-shaped radiation pattern if they are use as the feed of corrugated antennas. As a result, a mode converter is needed to convert the TM_{01} to TE_{11} mode which has a constructive radiation pattern at the broadside. Three categories of high-performance TM_{01}-TE_{11} mode converters are proposed and designed for the X band.

3.2.1 Dielectric-Loaded Mode Converters

The TM_{01} mode has a radial electric field distribution in the circular waveguide. Hence, the upper and lower half cylinders are out of phase which produces a null at the broadside. However, in the TE_{11} mode, the upper and lower half cylinders are in-phase which create a

constructive radiation at broadside in an open-ended waveguide propagation. In dielectric-loaded mode converters, by using two different materials at upper and lower half cylinder and a thin layer of a metallic sheet to separate them, one can create the required 180^o phase shift and convert the TM_{01} mode to TE_{11} mode. However, the dielectric constant and the geometry of the material determine the conversion efficiency, the length of the structure and the operational frequency bandwidth (which is defined as the frequency range within which the conversion efficiency remains within 10% range from its maximum possible value).

Conventionally, if one half of the cylinder is entirely filled with a dielectric material homogeneously, and the other half remains empty, with a certain length, a TM_{01}-TE_{11} is made. In this case, if the dielectric constant of the used material is very low, the operational frequency bandwidth of mode converter is higher; however, the structure is lengthy. On the other hand, if the dielectric constant of the material is high, the bandwidth of mode converter is lower since the reflection increases; however, the structures' size reduces. For a certain material with a certain dielectric constant, to increase the bandwidth, partially filled structures can be used. Fig. 3.1 shows two structures of partially dielectric-loaded mode converters that can increase the operational frequency bandwidth [93]. The structures consisted of 3 dielectric slabs (radially and flat) with a 60^o angle with respect to each other and a flat thin metallic isolator between the upper and lower half cylinders. The metallic isolator length is equal to the dielectric slab. The mode converters are designed for the X-band. To design the structure at the center frequency of 10 GHz, the radius of the waveguide is selected to be 13.3 mm to have the cut-off frequencies of TE_{11} and TM_{01} at 8.75 GHz and 11 GHz, respectively, as shown in Fig. 3.1(d) and therefore support only TE_{11} (desired) and TM_{01} (excitation) modes from 8.75 to 11 GHz.

The Markforged 3D printer which uses Nylon as a filament material is used to print the mode converters. We have characterized the printed Nylon filament to extract its dielectric constant and loss tangent using two back-to-back WR90 waveguides. The Nylon which is used has the dielectric constant and loss tangent of 2.8 and 0.03 respectively at the frequencies around 10 GHz. For a certain value of T or θ in the mode converters shown in Fig. 3.1, the length L is such that the 180^o phase shift is made between the upper and lower sections. This can be expressed

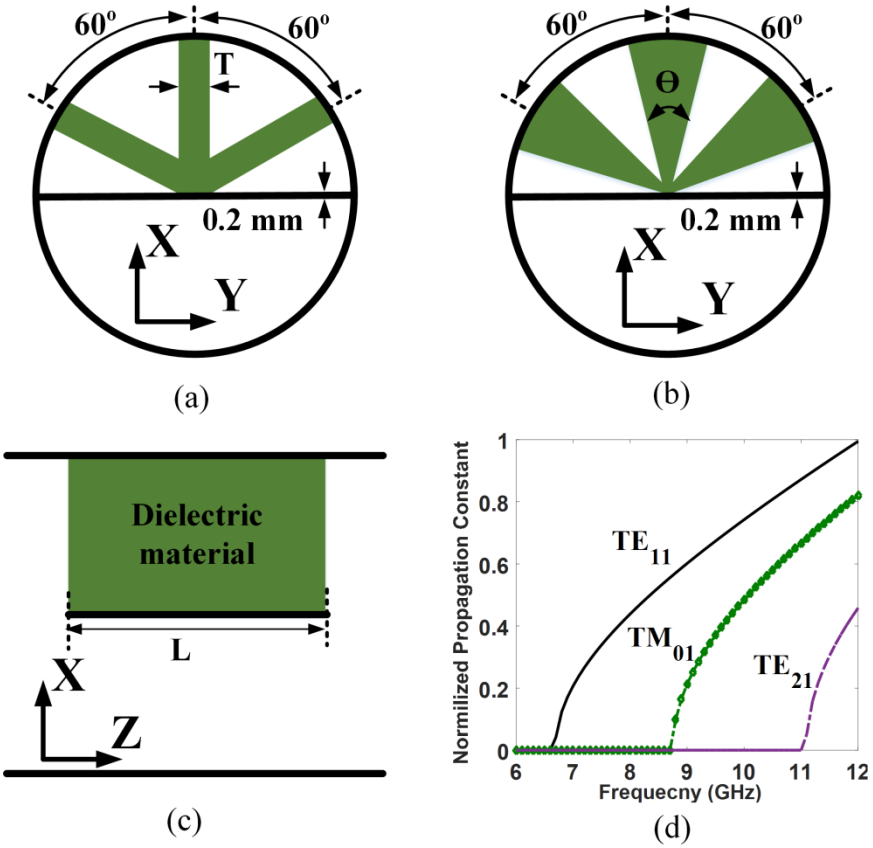

Fig. 3.1. a) Partially filled configurations for the dielectric-loaded mode converters: (a) top view of the flat dielectric slab (FDS) mode converter, (b) top view of the radial dielectric slab (RDS) mode converter, (c) side view of the mode converters, and (d) the normalized propagation constant of the different mode excited in an air-filled circular waveguide with the radius of 13.3 mm.

by:

$$(\beta_d - \beta_0)\, L = \pi \qquad (3.1)$$

where β_d and β_0 are the effective propagation constant of partially dielectric-loaded and the propagation costant of air, respectively, at the desired frequency. The odd multiple of the length (i.e. 3L, 5L,…) also makes an 180° phase shift; however, those lengths make the structure lengthy and create more loss.

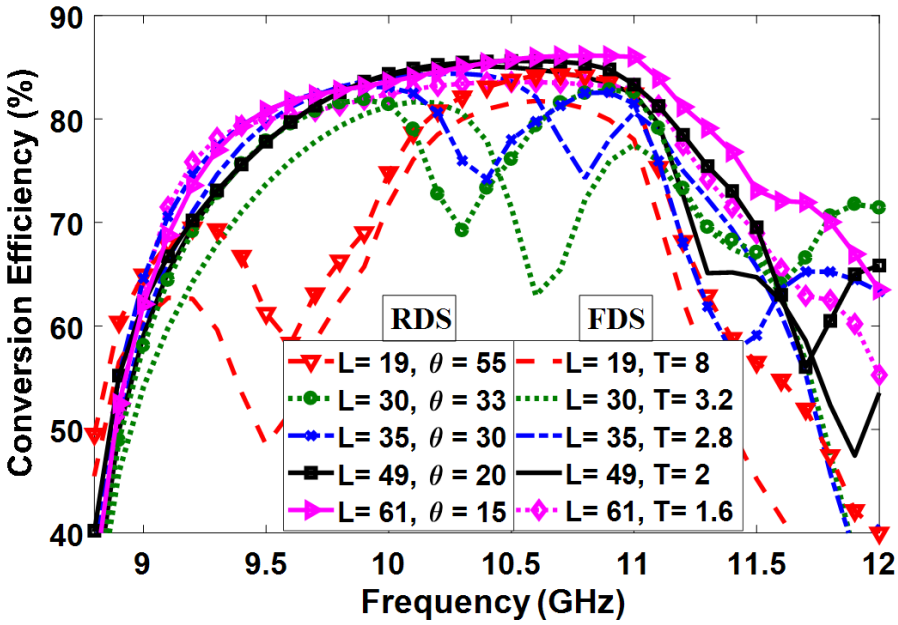

Fig. 3.2. Conversion efficiency of the radially and flat dielectric slab mode converters for different θ and T (The unit for L and T is millimeter and the unit for θ is degree).

The conversion of different input modes to different reflected/transmitted modes can be obtained using HFSS simulator. Fig. 3.2 demonstrates the effect of θ and T on the bandwidth, and maximum value of the conversion efficiency in the radial and flat dielectric slab mode converters, respectively. For different values of length L, the best θ in the RDS case and the best T in the FDS case are achieved for maximum conversion efficiency around 10 GHz using ANSYS HFSS. As shown, for the shortest length L=19 mm, in both mode converters, the dielectric slab is more voluminous (higher θ and T); however, the conversion operational bandwidth is significantly lower. Also, for L= 19 mm, the RDS mode converter has a wider bandwidth with higher efficiency compared to FDS mode converter. Increase in the length of dielectric slab results in lower θ and T, and a higher operational bandwidth. The reason is having a lower reflection due to lower perturbation and discontinuity in the dielectric-filled medium. Finally, for the large length of L= 61 mm, the maximum conversion efficiency and bandwidth are extremely high for both converters. However, in this case, again, the performance of RDS mode converter is better than FDS mode converter. The maximum achievable conversion efficiency cannot exceed 86% as shown in

TABLE 3.1
Four Different Cases of Mode Converters

Case no.	Type	Length	Thickness
#1	FDS	L= 49 mm	T= 2 mm
#2	FDS	L= 19 mm	T= 8 mm
#3	RDS	L= 61 mm	θ= 15 deg
#4	RDS	L= 35 mm	θ= 30 deg

Fig. 3.2 since the utilized Nylon has a loss tangent of 0.03 around 10 GHz. If we use better materials such as Teflon with a loss tangent lower than 0.001, the maximum conversion efficiency would be more than 98%. However, those materials need specialized printer to which we do not have access.

Although the conversion to TE_{11} mode at the output is done with a good efficiency in a wide bandwidth when an input TM_{01} mode is excited, it is interesting to find out to what extend the reflected TM_{01} and TE_{11} modes at the input, transmitted TM_{01} mode at the output, and the reflected/transmitted TE_{21} mode create loss in the system.

Fig. 3.3 shows different mode conversions of the FDS and RDS converters for four cases listed in TABLE 3.1. As shown, for a short length of L= 19 mm (Case #2), there is a high reflection of TM_{01} mode (high $\eta_{1:TM_{01},1:TM_{01}}$) and high transmission of TM_{01} mode (high $\eta_{2:TM_{01},1:TM_{01}}$). Therefore, the conversion efficiency ($\eta_{2:TE_{11},1:TM_{01}}$) of case #2 is not so high and its operational bandwith is limited. For the RDS mode converter with large length L= 61 mm (case #3), we still have a good conversion efficiency compared to the other cases due to mainly having a low $\eta_{2:TM_{01},1:TM_{01}}$ at higher frequencies. For this case, a bandwidth of 20.8% is achieved from 9.27 GHz to 11.42 GHz. According to Fig. 3.3 (c), it is obvious that the cut-off of the TE_{21} mode is at 11 GHz.

In conventional dielectic-filled structures due to a high sudden discontinuity, the performance of the mode converter decreases. However, with a smooth transition, a better efficiency over a wider bandwidth can be achieved. Based on this assumption, we propose a half cone-shaped dielectric-loaded (HCDL) mode converter in Fig. 3.4. To make the transition

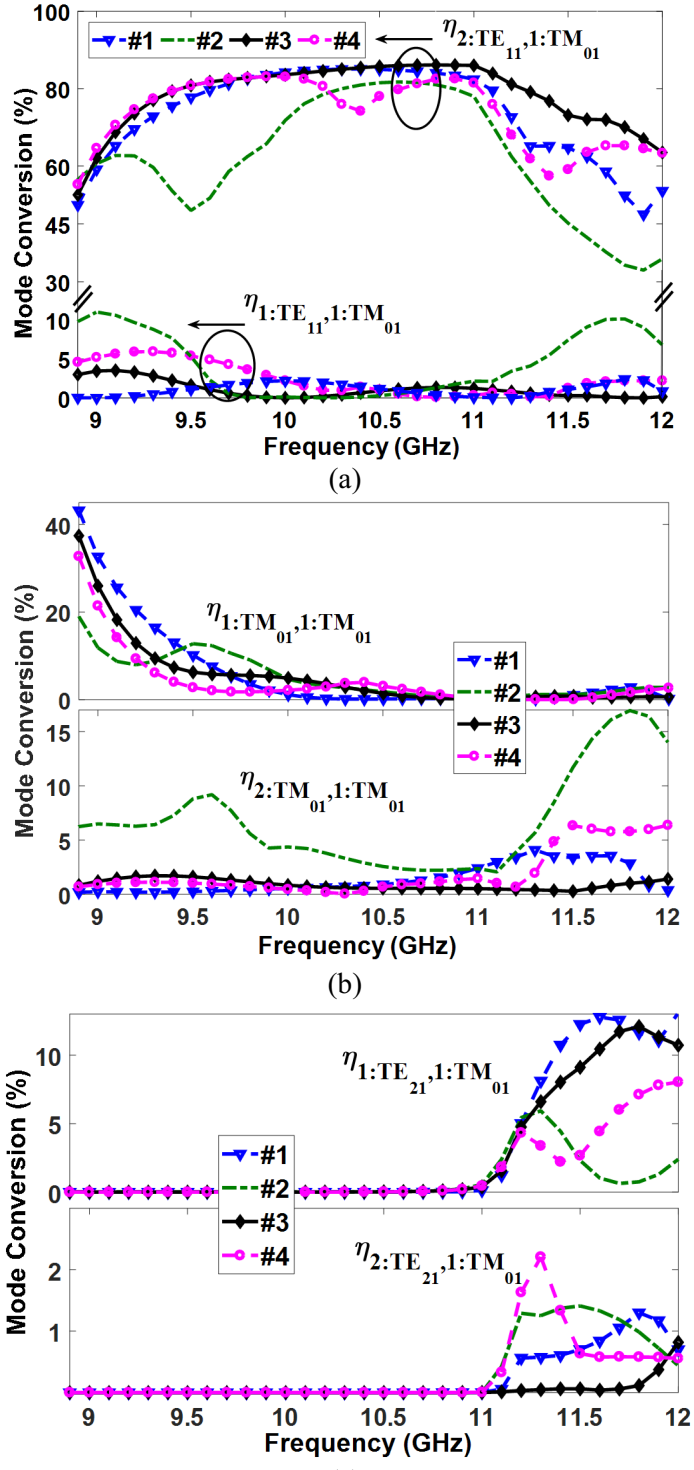

Fig. 3.3. a) Different mode conversions for cases #1, #2, #3, and #4, (a) $\eta_{1:TE_{11},1:TM_{01}}$, and $\eta_{2:TE_{11},1:TM_{01}}$, (b) $\eta_{1:TM_{01},1:TM_{01}}$, and $\eta_{2:TM_{01},1:TM_{01}}$, (c) $\eta_{1:TE_{21},1:TM_{01}}$, and $\eta_{2:TE_{21},1:TM_{01}}$.

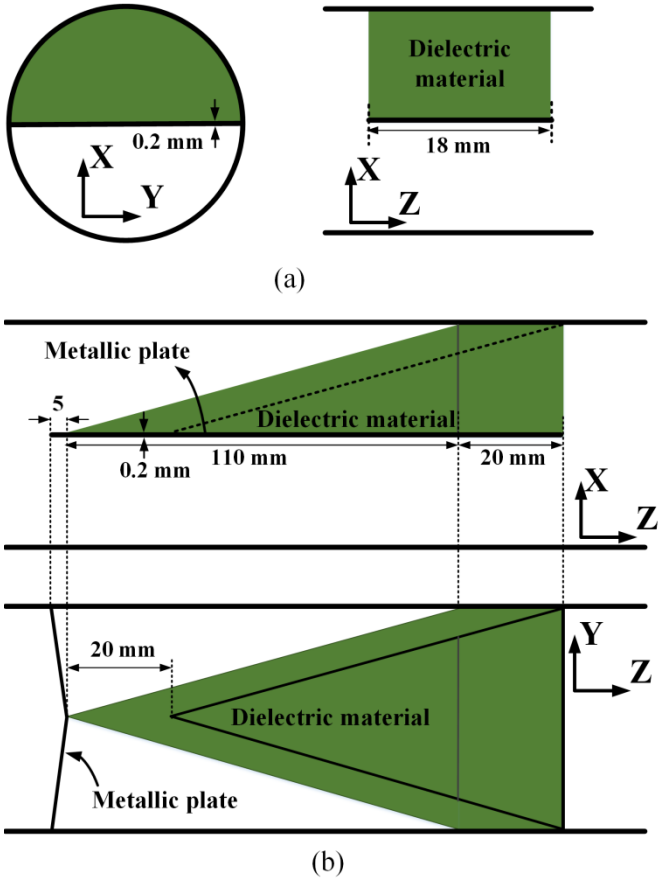

Fig. 3.4. Configuration of (a) conventional (case #5) and (b) proposed half cone-shaped dielectric-loaded (case #6) mode converters.

TABLE 3.2.
Dimension of the Conventional and HCDL Mode Converters

Case no.	Type	Length
#5	Conventional	L = 18 mm
#6	HCDL	L = 135 mm

smooth, the dielectric material fills the space between two half cone-shaped structures. A thin metallic sheet seperates the upper and lower half cylinders. The designed conventional and HCDL mode converters are studied as cases #5 and #6 respectively listed in TABLE 3.2.

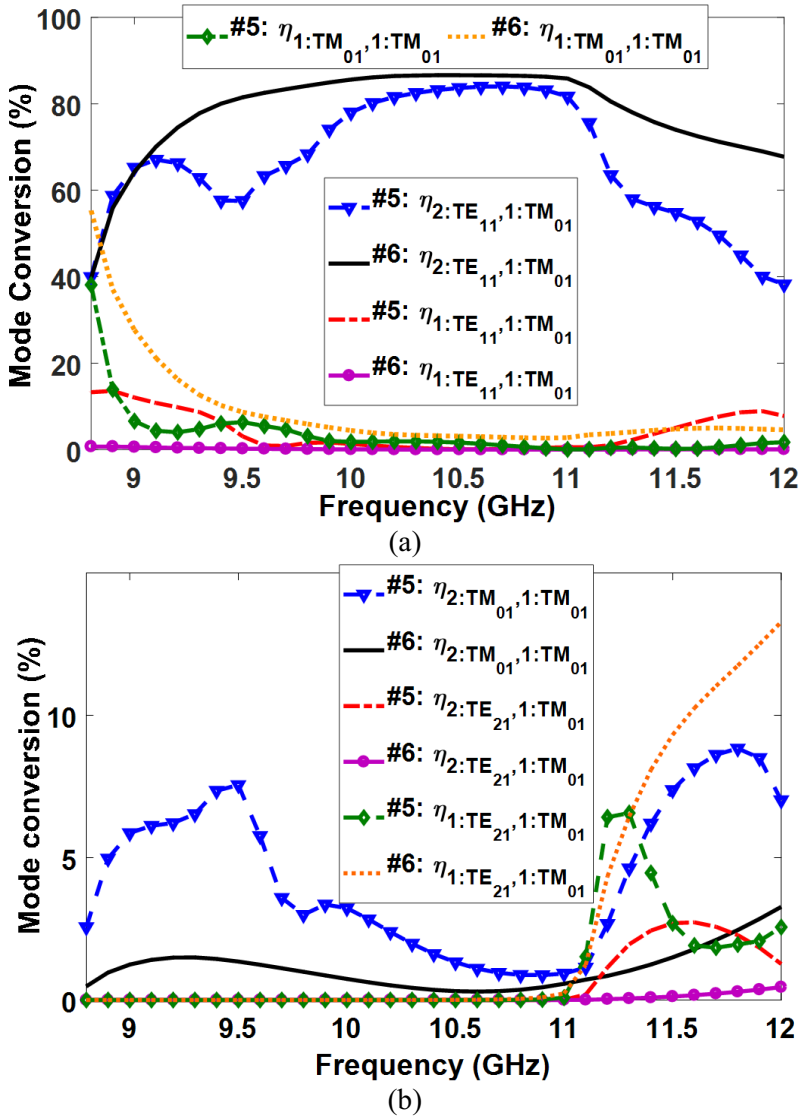

Fig. 3.5. Performance of the conventional (case #5) and HCDL (case #6) mode converters, (a) $\eta_{2:TE_{11},1:TM_{01}}$, $\eta_{1:TE_{11},1:TM_{01}}$, and $\eta_{1:TM_{01},1:TM_{01}}$ and (b) $\eta_{2:TM_{01},1:TM_{01}}$, $\eta_{2:TE_{21},1:TM_{01}}$, and $\eta_{1:TE_{21},1:TM_{01}}$.

Fig. 3.5 shows the performance of the conventional and HCDL mode converters. As shown, the bandwidth of the conventional structure is 11.6% from 9.9 GHz to 11.12 GHz. Although the HCDL structure is lengthy compared to the conventioal one, it increases the bandwith by 20.4% that is from 9.25 GHz to 11.35 GHz. The maximum efficiency of the conventional and HCDL mode converters are 0.84% and 87% respectively. Fig. 3.5(b) demonstrates that the

conversion of TM_{01} to TE_{11} modes in the conventional structure is not appropriate at frequencies away from the center frequency due to high transmission of TM_{01} mode at the output. However, the conversion of the modes happens efficiently in the proposed HCDL mode converter.

3.2.2 Metallic-Septum Based Mode Converters

A metallic full thin septum placed in the center of a circular waveguide can convert TM_{01} mode to TE_{11} mode [82]. The upper edge of the septum is linearly tapered downward as shown in Fig. 3.6(a). The parameters T, L_1, and L_2 can be selected in a way to maximize the conversion efficiency. Since it is a full septum with a height equal to the diameter of the circular waveguide, it will be stable when it is assembled into the circular waveguide. The existence of a full septum increases the reflection because it distorts the field distribution a lot. Additionally, a relatively high portion of TM_{01} is transmitted to the output due to the large height of the septum.

Fig. 3.6(b) proposes a metallic triangular half septum (THS) mode converter which can improve the conversion efficiency [93]. The proposed septum is tapered upward toward the center of the circular waveguide and then downward toward the lower wall of the waveguide with the length of L_1 and L_2, respectively, in the direction of the propagation.

Each mode converters were optimized to obtain the maximum conversion efficieny. The optimum values for the metallic full septum and the proposed THS mode converters are T= 2 mm, L_1= 1.25 mm, L_2=43.9 mm, and T= 1 mm, L_1= 3.8 mm, L_2=45.6 mm, respectively. Fig. 3.7 demonstrates the performance of both mode converters. It is obvious that the proposed THS mode converter has a better performance than the full septum mode converter.

As the wave propagates through the THS mode converter, the lower edge of centrally placed triangular half septum makes the electric field terminated to the ground, and continuously tapered half septum converts the TM_{01} mode to TE_{11X} mode smoothly. Fig. 3.8 shows this conversion for apertures AA', BB', CC', and DD' depicted in Fig. 3.6(b). The field distributions on the apertures defmonstrate how the TM_{01} mode in the aperture AA' is converted to the TE_{11X} mode in the aperture DD'.

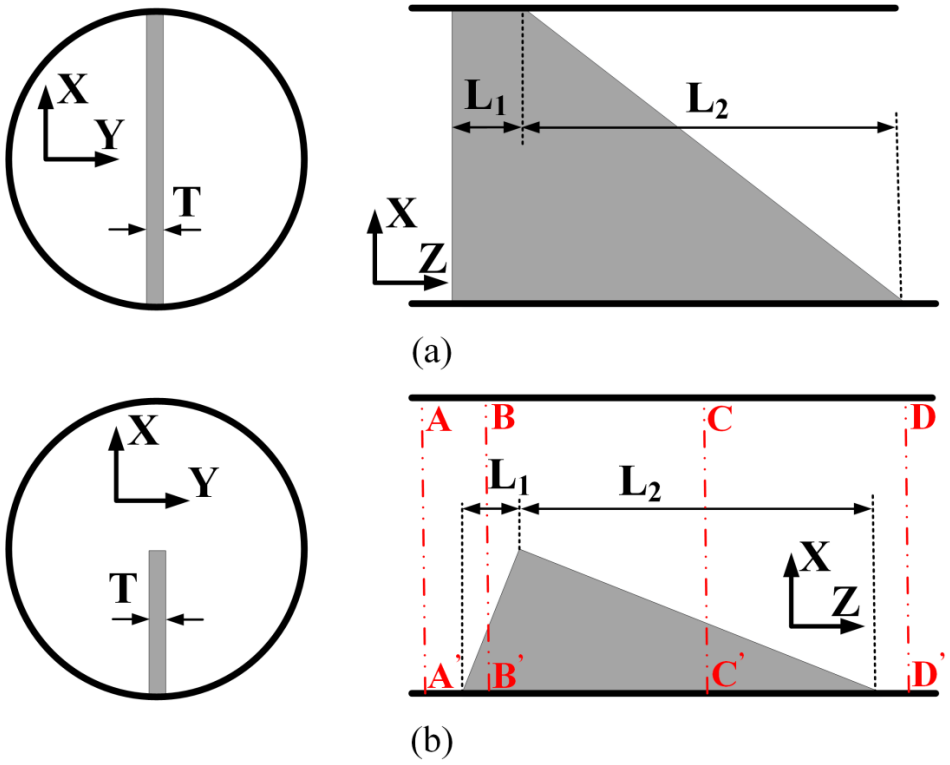

Fig. 3.6. Configuration of (a) the metallic full septum and (b) proposed metallic triangular half septum (THS) mode converters.

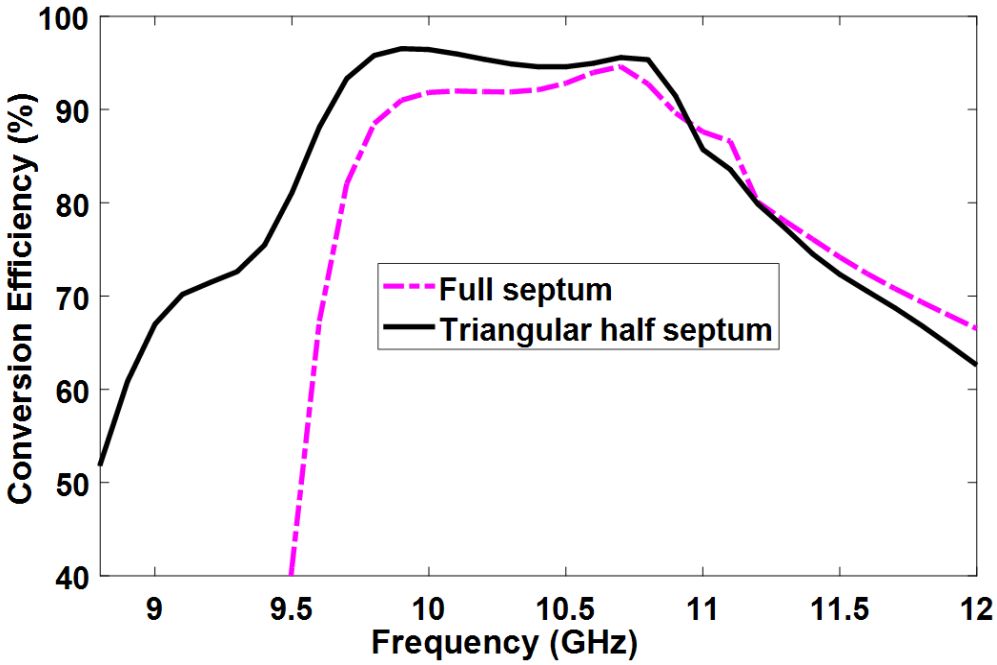

Fig. 3.7. Conversion efficiency of the metallic full septum and proposed THS mode converters.

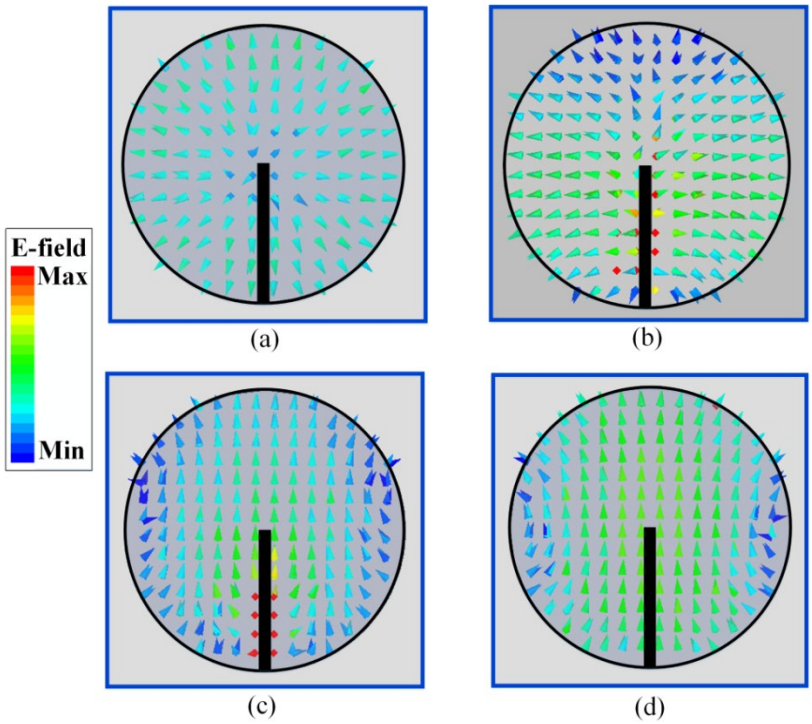

Fig. 3.8. Electric field distribution on the aperture (a) AA', (b) BB', (c) CC', and (d) DD' for input TM_{01} mode at the center frequency.

One of the advantages of metallic septum based mode converters is that the TE_{11Y} mode passes through the septum without conversion to other modes due to its perpendicular electric field to the septum. Fig. 3.9 shows the transmission efficiency of getting an output TE_{11Y} mode when the TE_{11Y} mode is excited for designed full septum and THS mode converters with the parameter values above. As shown, the proposed THS mode converter gives a better performance in this regard.

The proposed THS mode converter can be modified to provide higher conversion efficiency or higher bandwidth. Fig. 3.10 proposes two modified THS mode converters for the peak conversion efficiency and bandwidth improvement [93]. Inserting two rectangular ridges at both sides of the THS mode converter along the septum as shown in Fig. 3.10(a) results in a higher conversion efficiency due to helping with field distribution. Furthermore, optimum radially stubs at the upper wall of the waveguide in THS mode converter as depicted in Fig. 3.10(b) improve the operational bandwidth significantly.

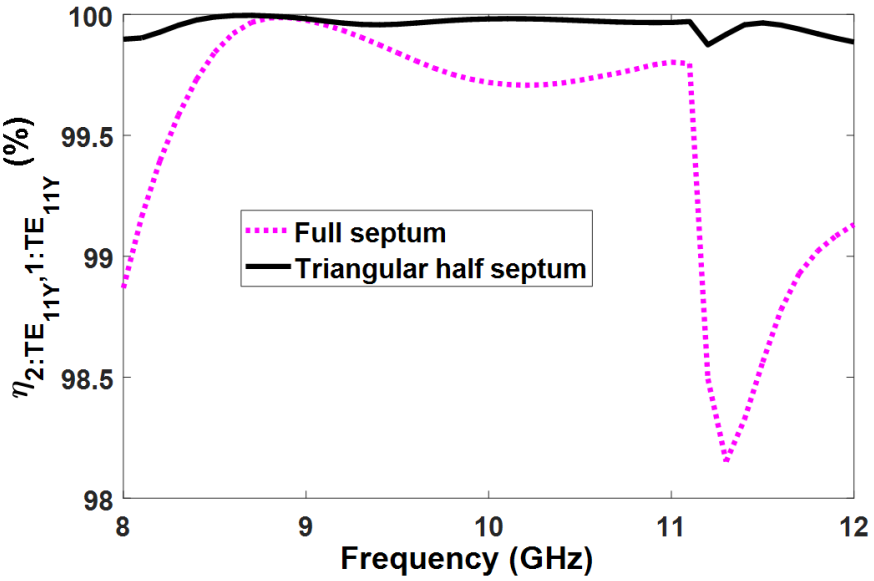

Fig. 3.9. Transmission efficiency of the output TE_{11Y} mode with the input TE_{11Y} mode.

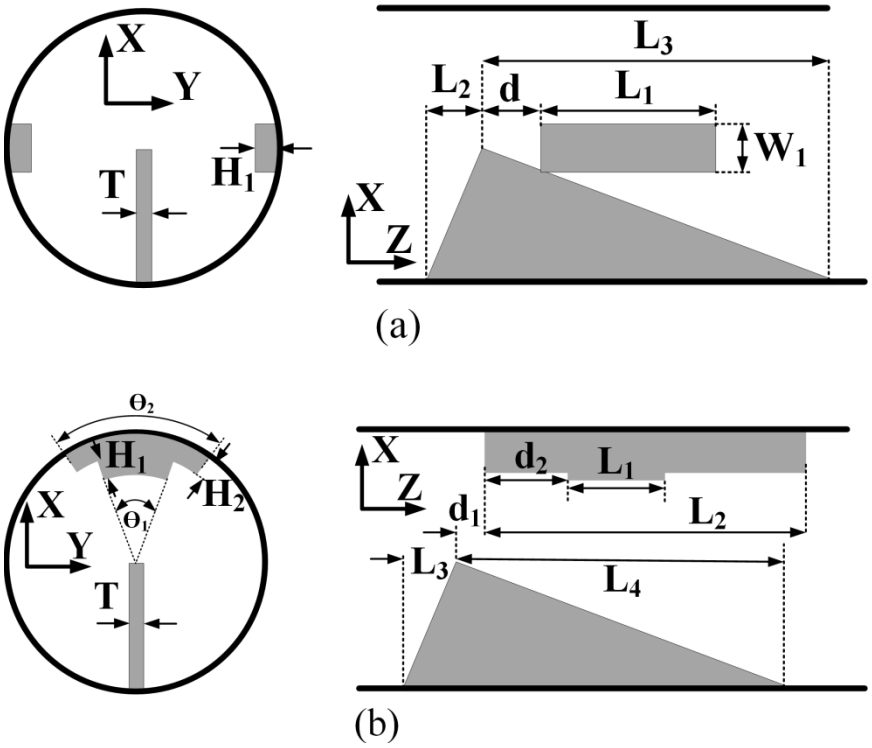

Fig. 3.10. Modified THS mode converters for (a) peak conversion efficiency and (b) bandwidth improvement.

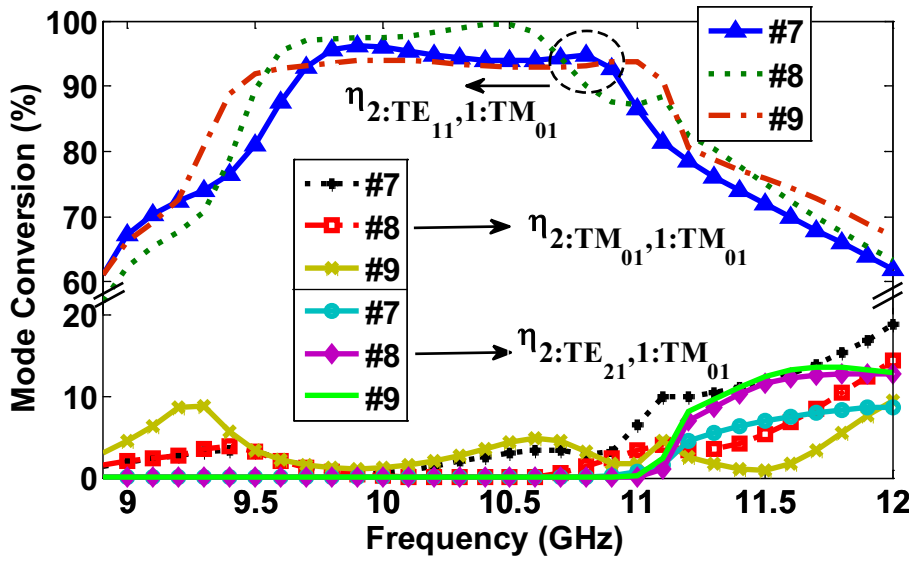

(a)

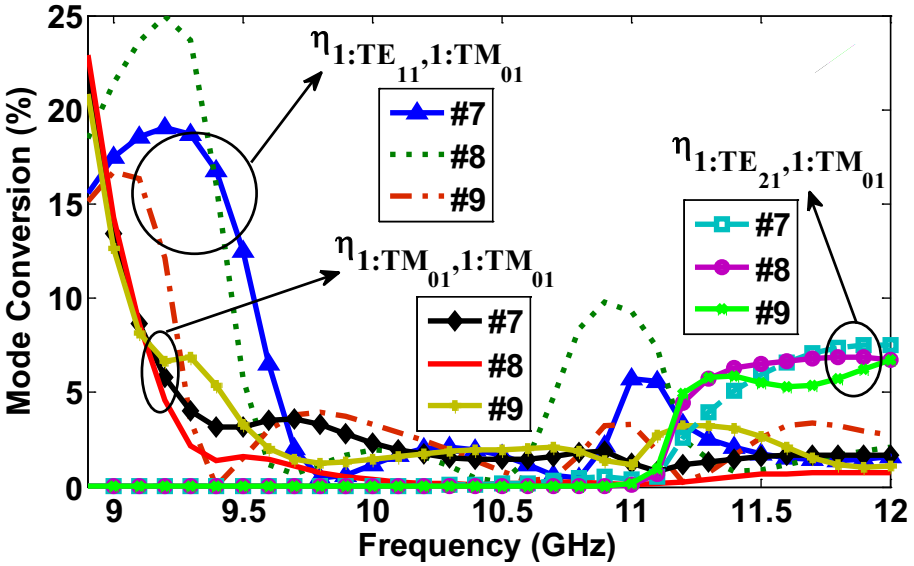

(b)

Fig. 3.11. Different mode conversions for cases #7, #8, and #9, (a) $\eta_{2:TE_{11},1:TM_{01}}$, $\eta_{2:TM_{01},1:TM_{01}}$, and $\eta_{2:TE_{21},1:TM_{01}}$, (b) $\eta_{1:TE_{11},1:TM_{01}}$, $\eta_{1:TM_{01},1:TM_{01}}$, and $\eta_{1:TE_{21},1:TM_{01}}$.

The parameters of the proposed mode converters are optimized, and the optimum parameters are listed in TABLE 3.3 for THS (case #7) and modified THS (cases #8 and #9) mode converters. Fig. 3.11 shows different mode conversions for the mode converters listed in TABLE 3.3. As shown, the modified THS mode converters presented as cases #8 and #9 improve

TABLE 3.3
Parameters of the THS and Modified THS Mode Converters

Case no.	Type	Parameters					
#7	THS	T=1 mm	L_1=3.8 mm	L_2=45.6 mm			
#8	Modified THS(Fig. 10(a))	T=1 mm	W_1=4 mm	H_1=2 mm	d=6 mm	L_1=25 mm	L_2=3.8 mm
		L_3=47.5 mm					
#9	Modified THS(Fig. 10(b))	T=1.5 mm	H_1=1.5 mm	H_2=1.5 mm	d_1=5 mm	d_2=10 mm	Θ_1= 30°
		Θ_2= 50°	L_1=10 mm	L_2=45 mm	L_3=4.75 mm	L_4=47.4 mm	

the peak conversion efficiency and the operational bandwidth, respectively. The peak conversion efficiency of the case #8 is 99.8% at 10.45 GHz. This high conversion efficiency is due to adding two ridges on both sides of the THS mode converters which could suppress the reflection/transmission TM_{01} mode at input/output as demonstrated in Fig. 3.11. For the modified THS mode converter (case #9), although compared to the THS mode converter (case #7), its peak conversion efficiency decreases from 96.6% to 94%, its bandwidth increases from 11.7% to 17% (9.4 GHz to 11.15 GHz). The enhanced bandwidth is mainly due to lower reflection TE_{11} and transmission TM_{01} modes at the edges of the frequency bandwidth as displayed in Fig. 3.11.

3.2.3 Metallic-Septum Based Mode Converters

Many mode converters utilize intermediate modes such as the TEM mode for the TM_{01}-TE_{11} mode conversion to improve the peak conversion efficiency or the operational bandwidth. Working with the TEM mode is simple and one can easily analyze it. In [94, 95], TEM-TE_{11} mode converters were presented. By using a transition , they can be designed as TM_{01}-TE_{11} mode converters.

Fig. 3.12 shows the configuration of the proposed TM_{01}-TE_{11} mode converter (case #10). It consists of two metallic cones at both sides, a cylindrical center conductor, and four metallic plates. The cylindrical conductor section provides TEM mode in the waveguide. This section is called coaxial waveguide. Two metallic cones at the input and output sections are important since the cone at the input, convert the TM_{01} mode to TEM mode and the cone at the output convert TEM mode to TE_{11} mode (by making 180° phase difference in the electric field between the top and bottom of the cylinder) efficiently.

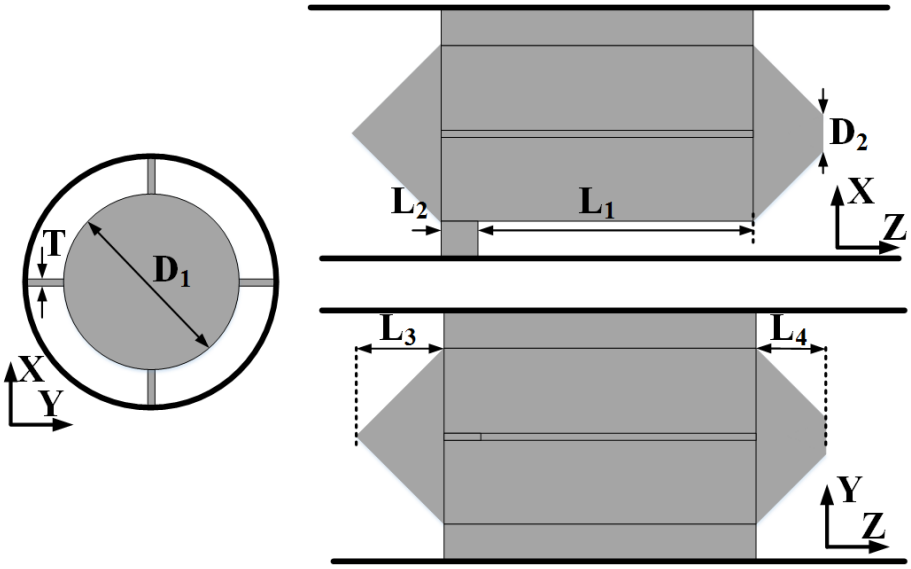

Fig. 3.12. Configuration of the proposed TM_{01}-TE_{11} mode converter (case #10).

TABLE 3.4
Parameters of the Design TM_{01}-TE_{11} Mode Converter.

Case no.	**Type**	**Parameters (mm)**			
#10	converter with TEM intermediate mode	D_1= 20	D_2= 4	L_1= 43	L_2= 7
		L_3= 9	L_4= 15	T= 0.2	

During the length of L_1, the coaxial waveguide is divided into three sections by three metallic plates; two 90° sector waveguides at the top (positive X-direction), and one 180° sector waveguide at the bottom (negative X-direction). An optimum length of L_1 that could create a phase difference of 180° between the 90° and 180° sector waveguides is the main parameter of the design since it helps to convert the quasi TEM mode of the coaxial waveguide to a TE_{11} mode by the help of the metallic cone at the output. The small metal plate with the length of L_2 as shown in Fig. 3.12 is a matching plate and increases the efficiency. The optimum design parameter of the mode converter for the center frequency of 10 GHz is given in TABLE 3.4.

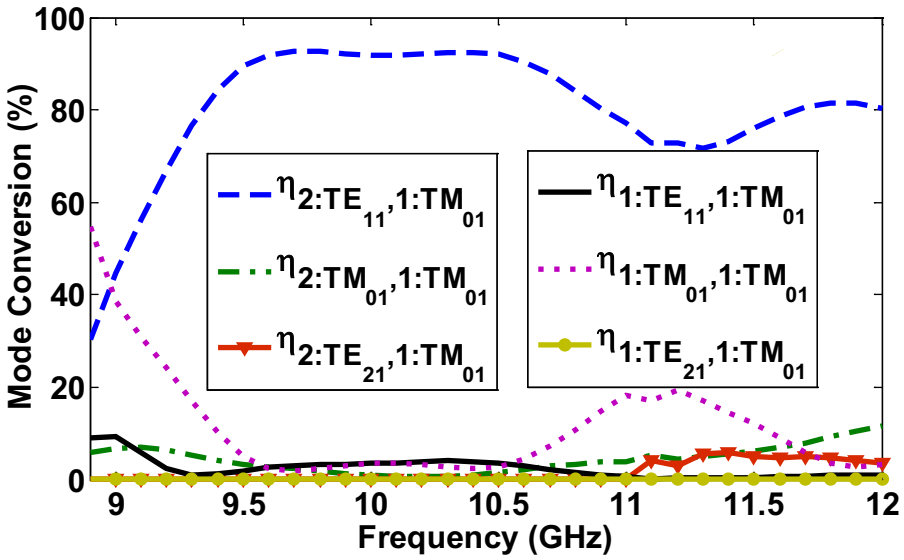

Fig. 3.13. Different mode conversions for the designed mode converter with TEM intermediate mode for the parameters listed in TABLE 3.4 (case #10).

Fig. 3.13 shows different mode conversions of the mode converter designed with the parameter listed in TABLE 3.4. A maximum conversion efficiency of 93.3% and a bandwidth of 12.4% over 9.45-10.7 GHz have been achieved. Although fabricating such mode converters using conventional methods is very difficult and expensive, realizing them with 3D printer makes it easy, light weight and cost-effective as will be discussed in the next section.

3.3 3D Printing Process

In our work, for the printing process, a Mark Two® 3D printer from Markforged® was used which works based on the fused deposition modeling technique. The resolution capability of 3D printer is 100 micrometer. Beside the material, there are factors such as the type of the filling and the nozzle temperature that affect the electrical characteristic of the printed material. Therefore, the characterization methods are required to measure the permittivity and loss tangent of the printed material. A Nylon filament was used to print the circular waveguide and all mode converters. The Nylon was printed with the rectangular filling of 100% density, and the layer height of 0.1 mm. Although increasing the temperature of the nozzle increases layer-to-layer

adhesion, it eventually comes at the cost of lower print quality. Therefore, an optimum nozzle temperature is need. The nozzle temperature in this work for printing the Nylon is 275°C.

The accurate dielectric characterization of 3D-printed materials is necessary to simulate, design, and fabricate the devices accurately. In our work, the permittivity and loss tangent of the printed Nylon were extracted using two WR90 waveguides. The 3D printed Nylon was put in the middle of two back-to-back WR90 waveguides. Comparing the measured S-parameters and phase responses of the setup with/without the 3D printed Nylon with simulation ones, we extracted the permittivity and loss tangent of the 3D printed Nylon which are 2.8 and 0.03 respectively. Obviously low loss materials and advanced 3D printing technologies can be implemented in the industrial scale production.

The fabrication processes are done in two steps for implementing the proposed mode converters and waveguides. First, we print them all with Nylon. Second, we coat the conductor sections with conductive ink and silver epoxy. The non-ideal conductor coating adds some degree of loss to the mode converters. To avoid this conductor loss in production, one may use industrial metallization process. Fig. 3.14 shows all circular waveguide and mode converters 3D printed with Nylon by Mark Two® 3D printer.

3.4 Measurement Results

To measure the mode converters in the lack of HPM sources which make a radially TM_{01} mode, we need to design a feed that could generate this mode. The output mode of the feed, which feeds the mode converters, should be a pure TM_{01} mode in order for the mode converters to work appropriately. The monocone structures offer a wideband response for this transduction [96]. The feed, in this case, converts the TEM mode of the coaxial cable to the TM_{01} mode over a wide bandwidth. Fig. 3.15(a) shows the designed TM_{01} feed which is fed by a coaxial cable. The dimensions of the feed are optimized to provide a wide bandwidth over the band of interest. The inner and outer radii of the coaxial cable are respectively 0.55 mm and 1.2 mm in the design. The designed feed depicted in Fig. 3.15(a) was 3D printed and coated by conductive ink. Fig. 3.15(b) shows the simulated and measured results of the designed TEM-TM_{01} feed. As demonstrated, the

Fig. 3.14. Fabricated mode converters by 3D printing technology.

simulated responses for two-port excitation ($S_{1:TEM,1:TEM}$ and $S_{2:TM_{01},1:TEM}$) show an excellent conversion from the coaxial TEM mode to the TM_{01} mode over 9-12 GHz. But, to be able to measure the performance, a small flare-angle conical horn was joined at the output port of the feed as a matching from the feed to free space. Then, the reflection coefficient of the feed is measured. The corresponding simulated and measured s-parameters for this case, which are in agreement, are also presented in Fig. 3.15(b).

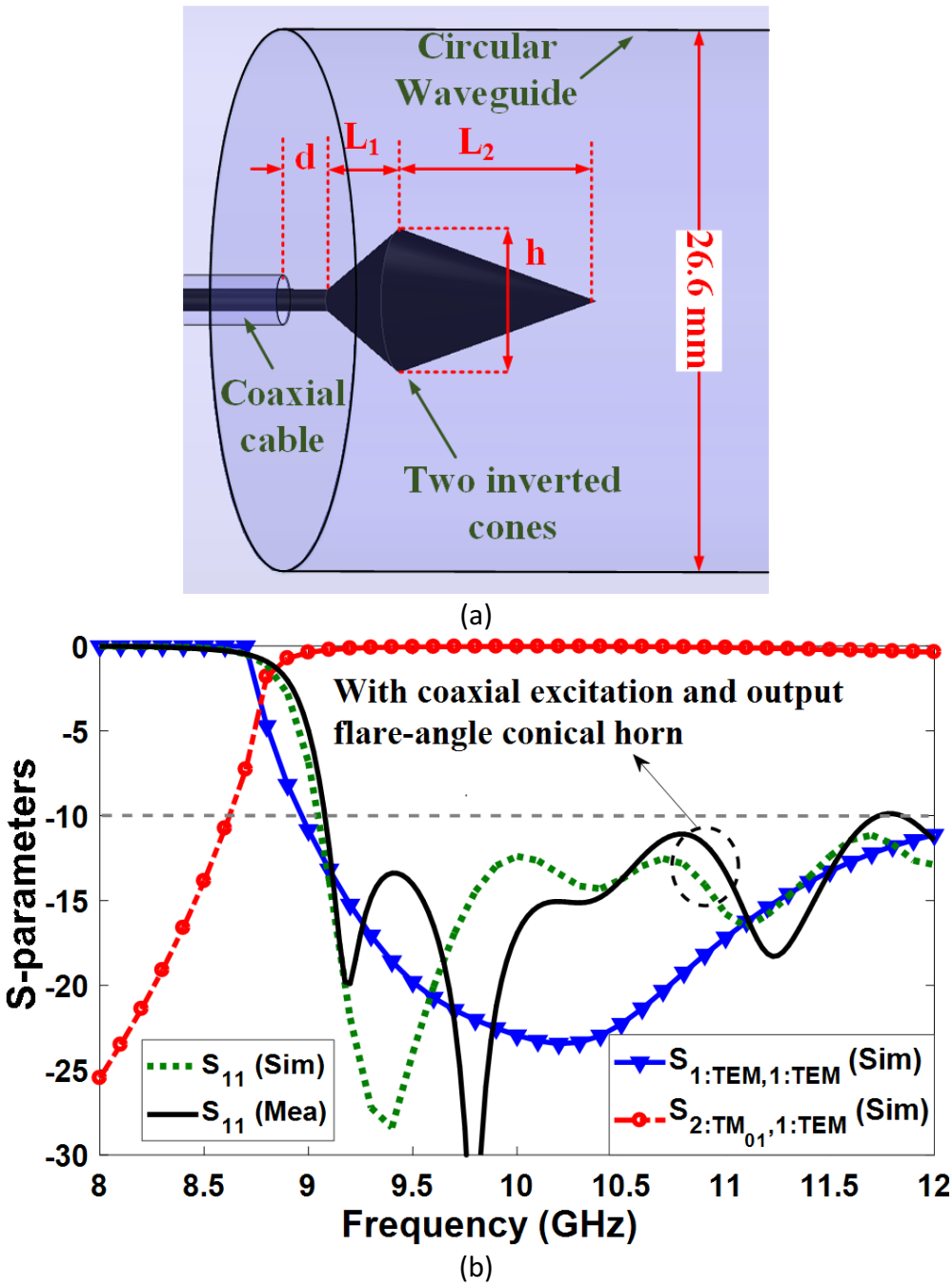

Fig. 3.15. (a) Designed feed for TM_{01} mode excitation with the dimensions d=2.35mm, h= 7mm, L1= 3.65 mm, and L2= 10mm, and (b) corresponding simulated and measured s-parameters.

Measuring the mode conversion of the mode converters is very difficult. Usually it is verified by measuring the far-field radiation patterns [95]. We used the designed TM_{01} mode feed at the input port of the 3D printed mode converters of cases #3, #6, #7, and #10, and measured their corresponding radiation patterns in an anechoic chamber.

As shown in Fig. 3.16(a), the TM_{01} mode feed has a null at the broadside with an amplitude around -20 dB. Also, for dielectric-loaded mode converters of cases #3 and #6, a maximum at the center frequency of 10 GHz is acheived at the broadside, as presented in Fig. 3.16 (a), indicating that the input TM_{01} mode is successfully converted to the TE_{11} mode at the output with a high conversion efficiency. Fig. 3.16(b) also shows that a constructive radiation pattern is obtained for THS mode converter of case #7 and mode converter with intermediate mode (case #10).

In design of mode converters, there is a trade-off between the length and bandwidth. As reported in [97], authors achieved a miniaturized TM_{01}-TE_{11} mode converter using photonic crystal. But, the fractional bandwidth of their design is narrow. A comparison between some works in literature and the proposed TM_{01}-TE_{11} mode converters is performed and summarized in TABLE 3.5.

As shown, compared to the reported TM_{01}-TE_{11} mode converters listed, the proposed mode converters have wider bandwidth with reasonable length. In [78], a TM_{01}-TE_{11} mode converter with wide bandwidth is designed which is comparable to this work. However, added arms to the circular waveguide increases the dimensions of the structure significantly.

For high-power applications, the designed mode converters can be used between HPM sources and corrugated antennas, which will be addressed in next chapters, to produce a broadside far-field radiation pattern. There are, of course, many challenges such as strategies for cooling down the system, and thermal issues due to the loss in the structure, especially for high power applications. The study of the thermal behaviour of the structure is probably needed in industrial applications.

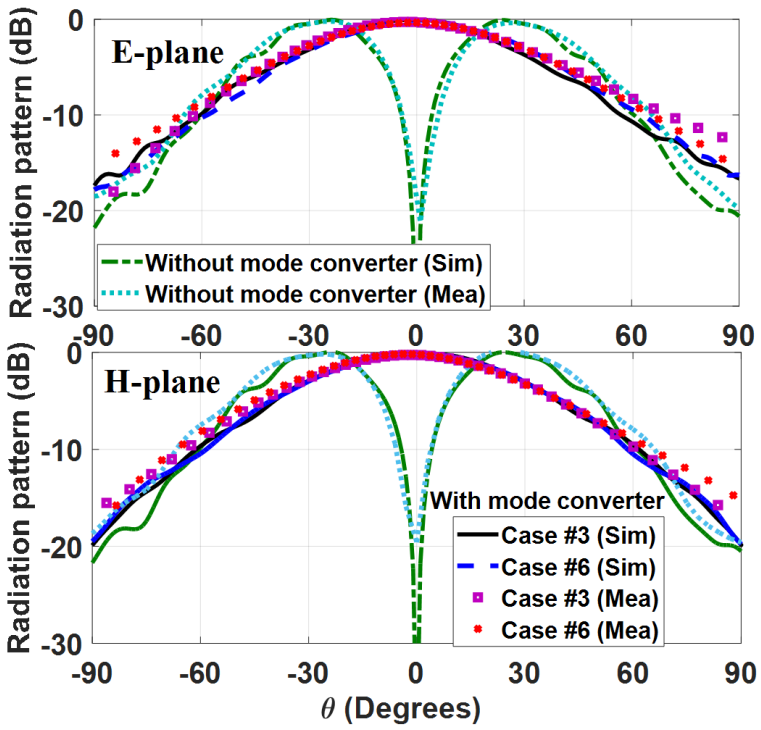

(a)

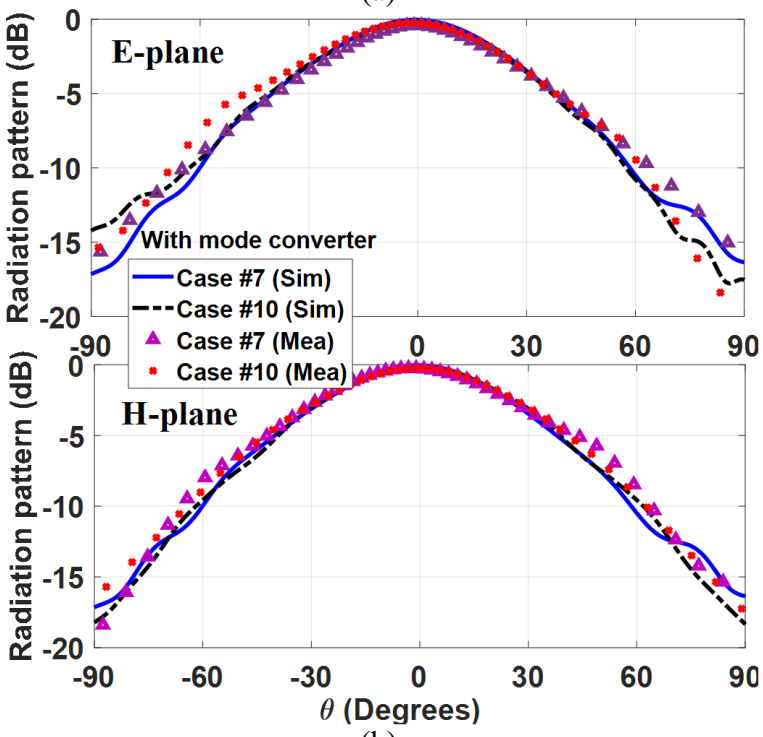

(b)

Fig. 3.16. (a) Radiation patterns of the feed without/with proposed mode converters of (a) cases #3 and #6, and (b) cases # 7 and #10 at the center frequency of 10 GHz.

TABLE 3.5
Comparison of TM_{01}-TE_{11} Mode Converters

TM_{01}_TE_{11} mode converters	**Center frequency**	**Length/λ**	**Radius/λ**	**Bandwidth**
[2]	3.55 GHz	2.95	0.53	11.7%
[78]	1.75 GHz	____	____	18.3%
[80]	4.03 GHz	4.65	0.85	12.2%
[82]	3.1 GHz	2.32	0.48	9.1%
[83]	1.9 GHz	2.53	0.57	10%
[97]	1.6 GHz	1.2	0.58	4.1%
This work: case #3	10.35 GHz	2.1	0.46	20.8%
This work: case #6	10.3 GHz	4.63	0.46	20.4%
This work: case #9	10.3	1.88	0.46	17%
This work: case #10	10.1	2.49	0.46	12.4%

Chapter 4

Planar Corrugated Antennas: Design and Analysis

In advanced multi-antenna wireless systems, it is necessary for antennas to be integrated with the rest of the system. This requirement favors planar antennas manufactured using commodity PCB or IC processes. However, conventional medium- and high-gain antennas such as horn and reflector antennas have non-planar bulky structures with heavy weight and expensive manufacture process. In this chapter, planar corrugated antennas are discussed as candidates to be used in many applications such as space and satellite communications and to be easily integrated with other circuits in a low-cost manner. Here, we first present a simple technique to design corrugated antennas, which are not conventionally planar and are fabricated on metallic sheets, on PCBs using SIW technology. Then, we propose a novel design and analysis of corrugated antennas based on its corresponding unit-cell. In fact, by analyzing a unit-cell of corrugated structure, a general radiation performance of antenna such as resonant frequency, spectral bandwidth, and directivity can be estimated which avoids the time-consuming optimization process for designing such large antennas.

4.1 Corrugated Antennas Designed on Laminate Boards Using SIW Technology

Instead of a perforated metallic layer as used in conventional corrugated antennas, we propose a simple approach to design them on PCBs using SIW technology. Two 1D corrugated antennas with two and four grooves are proposed in this section [98]. The geometries of the

proposed antenna are shown in Fig. 4.1 and Fig. 4.2. To make the structure compact, the microstrip feed structure is designed on the bottom of the antenna. In addition, contrary to the conventional corrugated antennas which use a longitudinal resonance, the proposed antenna uses the coupled resonance between the transmission line on the bottom layer and patch through the cavity. This shrinks the antenna thickness substantially. The grooves have been realized using SIW technology. As shown, the structure consists of three dielectric layers. The first layer (feed substrate) and third layer (patch substrate) are Rogers 4003 with relative permittivity of 3.38, thickness of 0.508 mm, and loss tangent of 0.0027. The second layer is Rogers TMM4 with relative permittivity of 4.5, thickness of 3.175 mm, and loss tangent of 0.002. A 50-Ω transmission line feeds the antenna from the bottom layer. The dimensions of the rectangular shape at the end of the feed line are optimized in order to provide broadband matching.

The mechanism of operation of the proposed structure is as follows. Power is coupled to the rectangular patch through the cavity and from there propagates into the free space like aperture coupled antennas [99-101]. However, by using two SIW grooves shown in Fig. 4.1, the gain of the antenna can be enhanced due to constructive superposition of electric field.

The construction of cavity wall using vias in an SIW structure has a considerable impact on the cavity performance and makes it difficult to adjust its resonant frequency. Therefore, the rectangular cavity is created within the middle substrate by drilling out two L-shapes to form the rectangular cavity's edges, leaving two of the corners of the cavity connected to the main body of the substrate to keep the substrate inside the cavity in place. The cavity's walls are then metalized. Both drilling and metallization are standard PCB manufacturing processes. The dimensions of the cavity, patch and feed line in the single pair of grooves (Fig. 4.1) and the double pair of grooves (Fig. 4.2) are the same and the only difference is the number and dimension of the grooves.

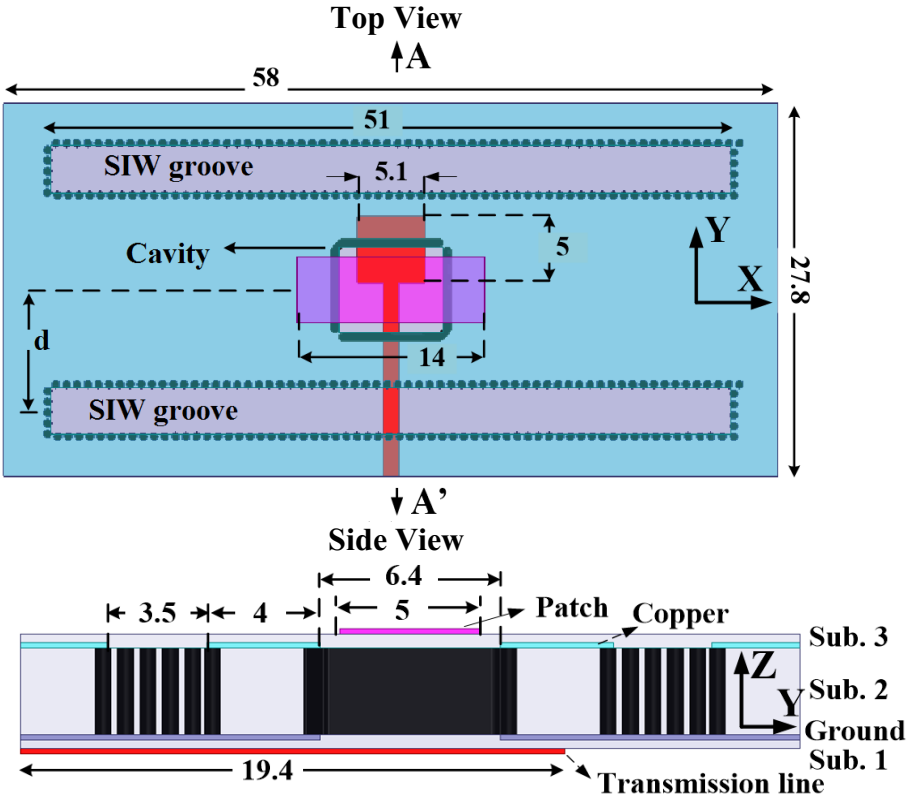

(a)

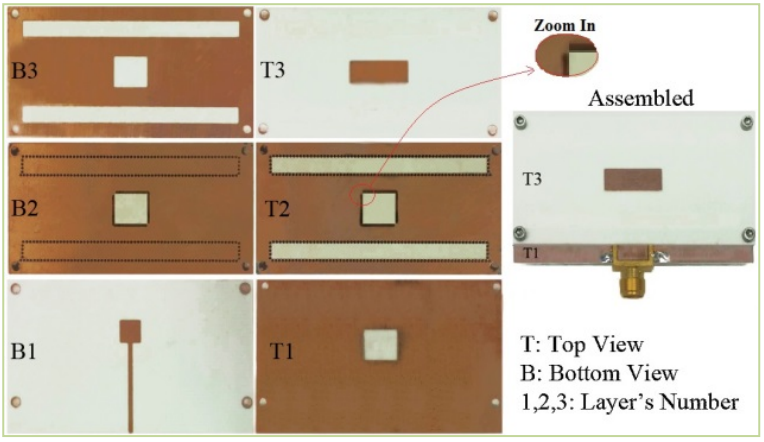

(b)

Fig. 4.1. (a) Configuration of proposed corrugated antenna with two grooves (All dimensions are in mm), and (b) its fabricated prototype.

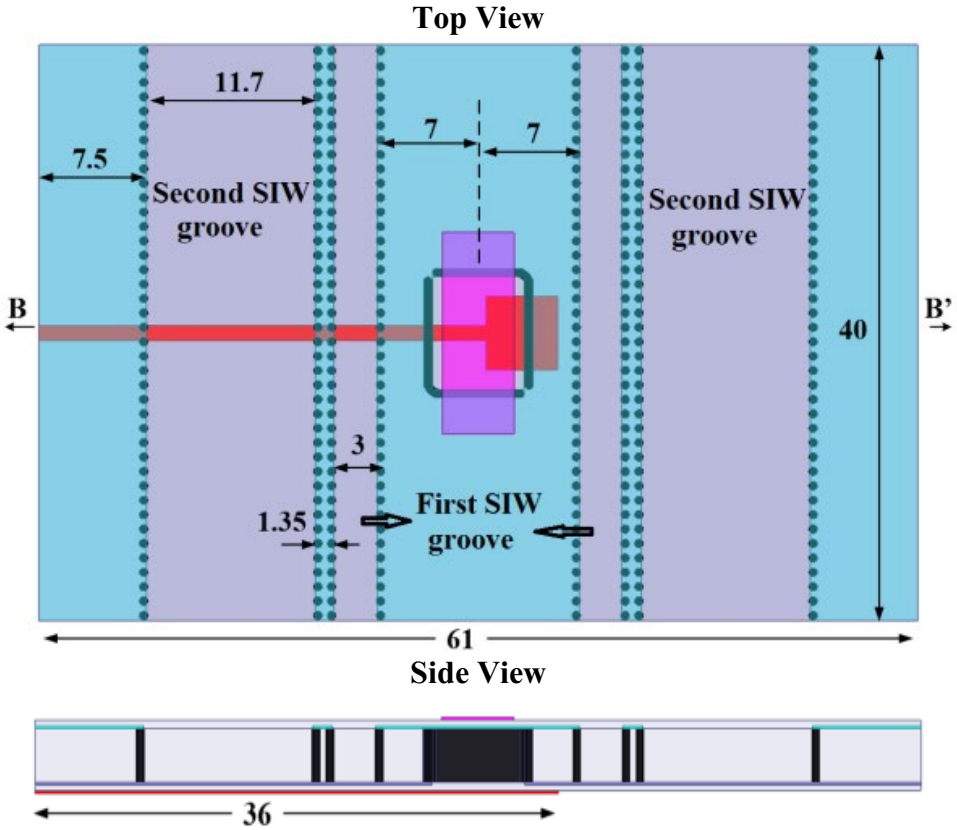

(a)

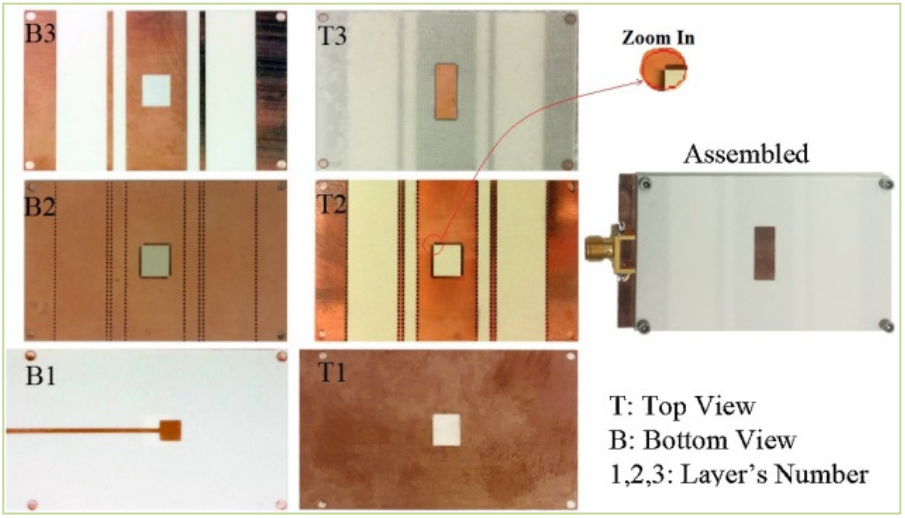

(b)

Fig. 4.2. (a) Configuration of proposed corrugated antenna with four grooves (All dimensions are in mm), and (b) its fabricated prototype.

Fig. 4.3 shows the reflection coefficient of the antenna without grooves, with two grooves, and with four grooves. As adding the grooves has only a minor effect on reflection coefficient if they are not very close to the patch, the first step in the design of this type of antenna is to design a patch with the desired bandwidth and center frequency, neglecting the effect of the grooves. The next step is to design the grooves, finding location and dimensions which provide the desired gain. We have designed the antenna with two grooves and four grooves to have the superposition of electric field in just X-direction and both X- and Y-directions, respectively, as shown in Fig. 4.4. This results in having a directional beam in H-plane for the antenna with two grooves, and in E- and H-planes for the antenna with four grooves as shown in Fig. 4.5.

The simulated and measured reflection coefficients are depicted in Fig. 4.6. The measurement result shows an impedance bandwidth of nearly 10.02 -10.65 GHz (6.1%) and 10.09-10.7 GHz (5.9%) for $|S_{11}|$ <-10 dB for the antennas with two and four grooves, respectively.

The measured radiation patterns of the antennas at 10.25 GHz are depicted in Fig. 4.7. The measured half-power beamwidths of E- and H-planes for the antenna with two grooves as shown in Fig. 4.7(a) are almost 60^o and 37^o, respectively. For the antenna with four grooves as shown in Fig. 4.7(b), the measured half-power beamwidth is 30^o for E-plane and 40^o for H-plane. Also, all cross-polarizations of both antennas are at least 13 dB below co-polarizations in 3-dB beamwidth. Fig. 4.8 illustrates the radiation gain of both antennas. Although the measured peak gains have a small shift to higher frequencies for both antennas, it is still in agreement with simulation. The peak gain measured for antennas with two and four grooves are nearly 11.3 dBi and 12.8 dBi, respectively. It should be mentioned that the standard horn antenna used in gain measurement was not calibrated which may create a measurement error of around 1 dB.

Design and full-wave simulation of corrugated antennas with more grooves are very time-consuming due to large antenna structure. Therefore, a simple/fast approach is required to design and analyze corrugated antennas and estimate their general radiation performance.

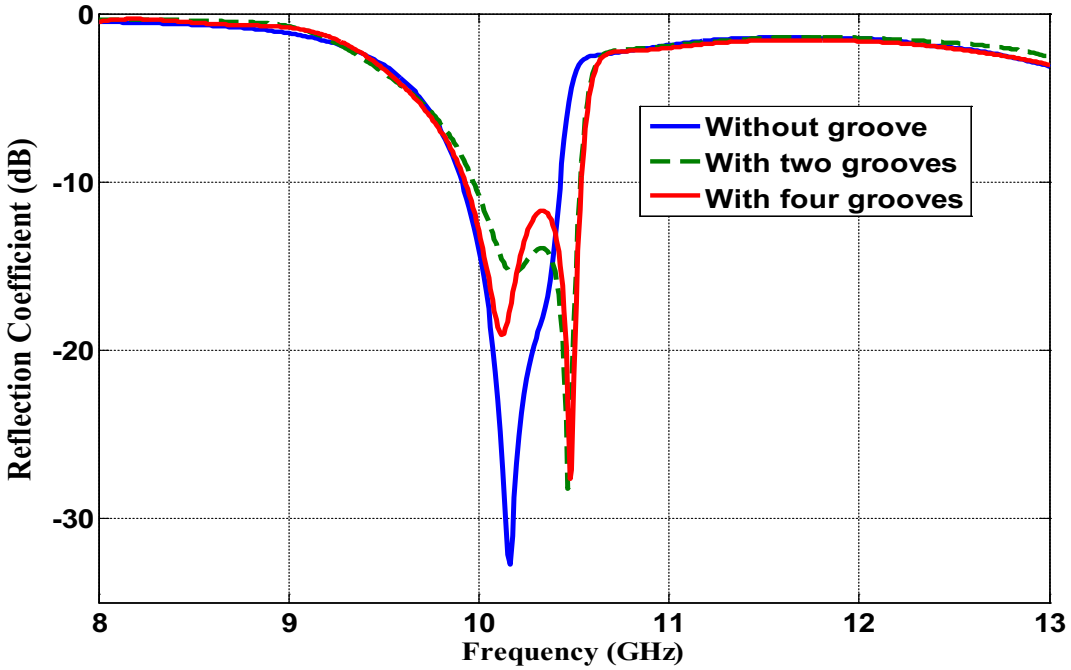

Fig. 4.3. Reflection coefficient of the proposed antenna without/with grooves.

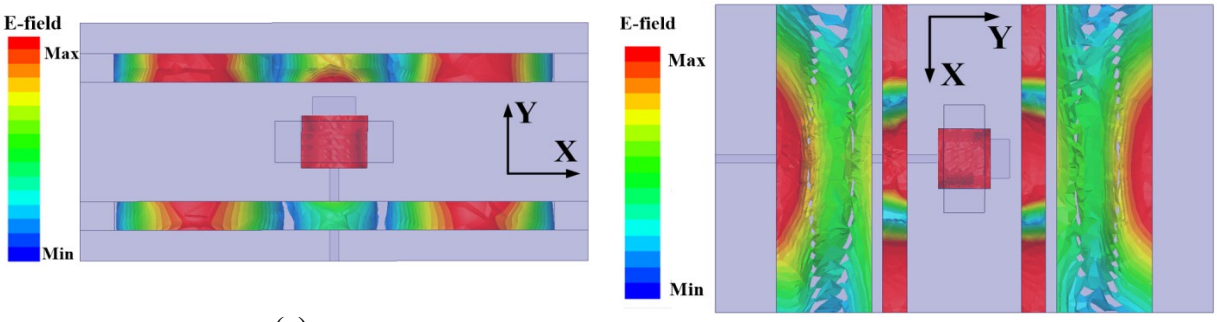

(a) (b)

Fig. 4.4. Electric field distribution inside the cavity and grooves in proposed antennas with (a) two grooves, (b) four grooves.

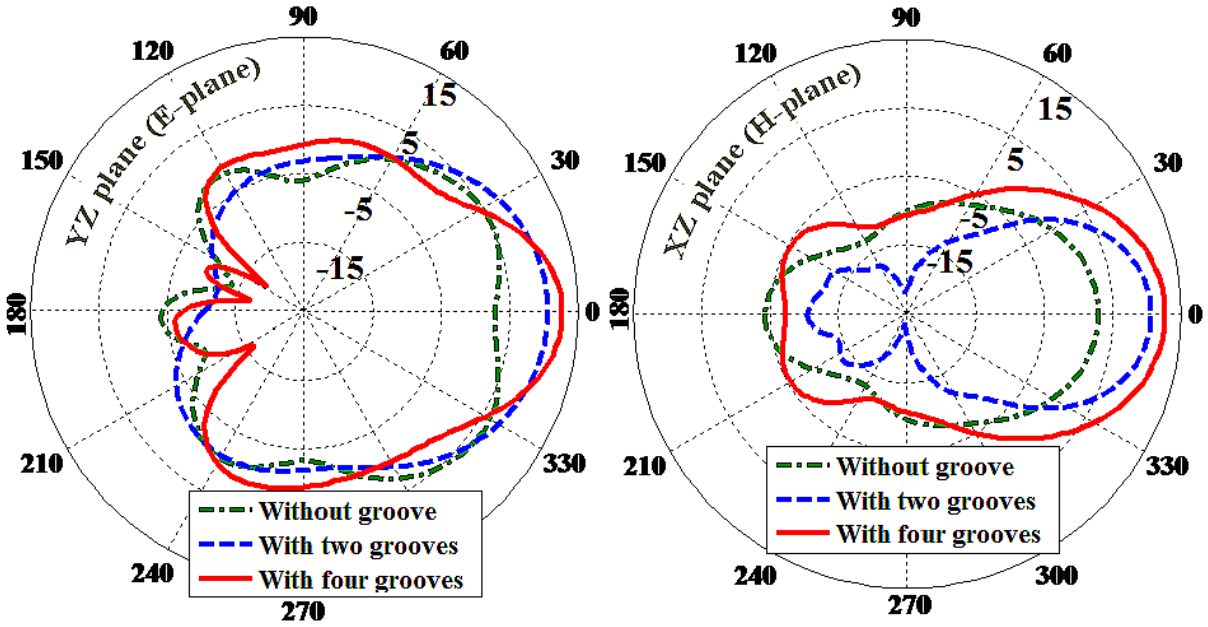

Fig. 4.5. Radiation pattern of the proposed antenna with/without grooves at the center frequency.

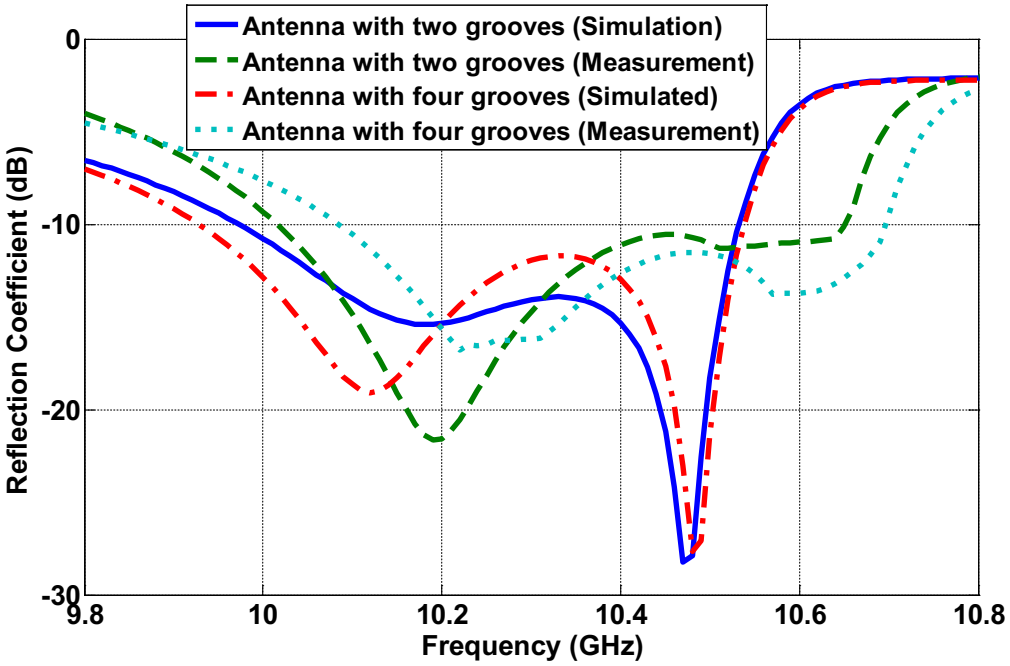

Fig. 4.6. Reflection coefficient of antennas with two and four grooves.

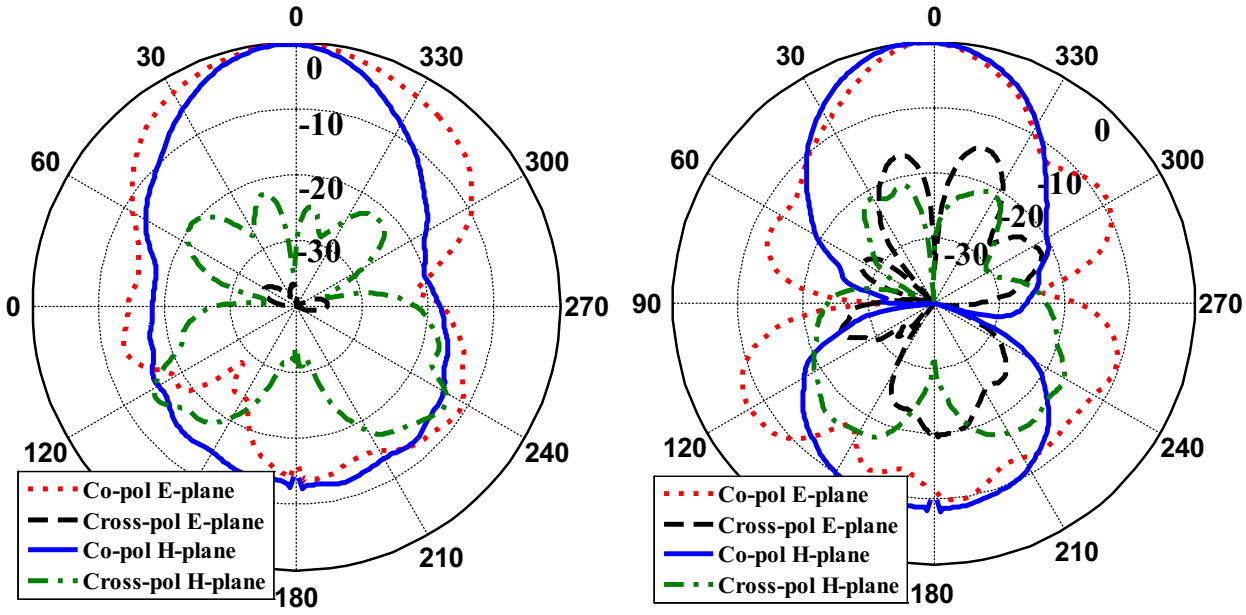

(a) (b)

Fig. 4.7. Radiation pattern of the proposed antenna at the center frequency with, (a) two and (b) four grooves.

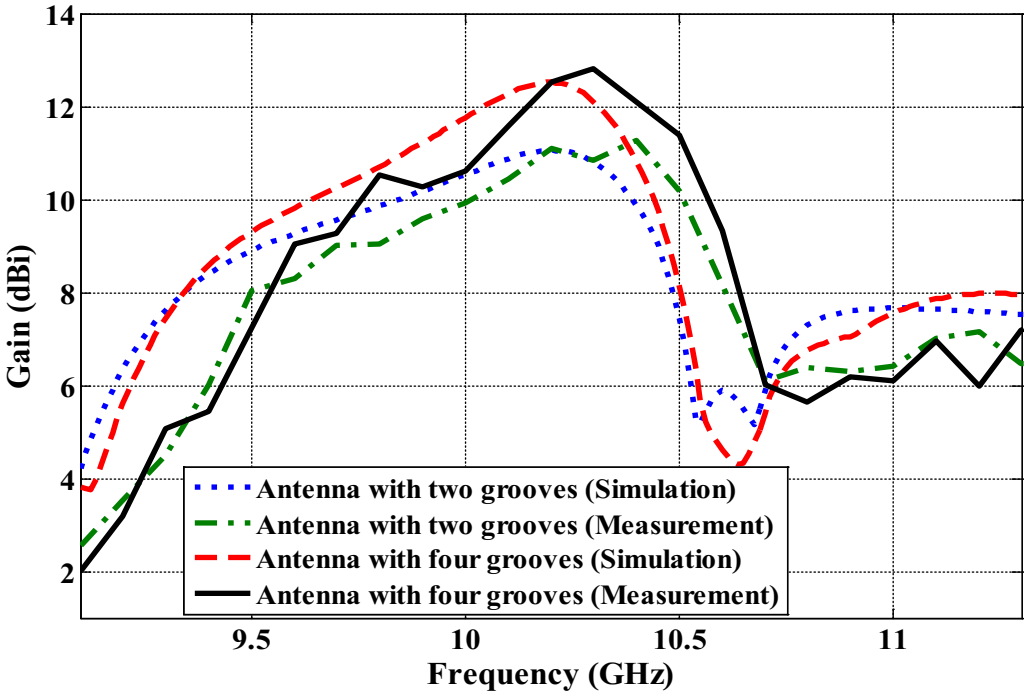

Fig. 4.8. Gain of the antenna with two and four grooves.

4.2 Design and Analysis of Corrugated Antennas Based on Surface Susceptance of Structures' Unit-Cell

There are several works in literature related to the analysis of corrugated antennas. For example, 1D corrugated antennas were investigated using Eigenfunction expansion, Fourier transform and mode matching method [3]. Furthermore, in [4], authors studied corrugated antennas utilizing the singular integral equation approach in a rigorous manner. Although, these methods give a full perspective view of the problem, it is hard to do a rough estimation of a general radiation performance of the antenna. In many papers, different types of corrugations along with their dimensions were optimized to get the best antenna performance. However, due to a large antenna size, this process is very time consuming. Here, the performance of corrugated antennas is estimated based on its surface susceptance of the antennas' unit-cell and the design of corrugated antennas is reduced to the design of a corrugated unit-cell, which reduces simulation time and eliminates the optimization process.

4.2.1 Transverse-Equivalent Network (TEN) Model of Corrugated Structures

In this section, corrugated structures filled by a material with permittivity of ε_r are studied. The structure along the XZ plane is depicted in Fig. 4.9(a). It is assumed that the structure is infinite in Y-direction. The structure can be excited by electric or magnetic current sources on the structures' surface. The magnetic current can be realized by a waveguide cavity or a coupled slot on the metallic surface, while an electric current can be realized by an electric dipole at a distance h_1 from the surface.

It is assumed that the period of the structure is larger than a half-wavelength, which is necessary for leaky wave excitation. Under this assumption, the attenuation constant, and propagation constant vectors, $\overline{\alpha} = \alpha_x \overline{a}_x + \alpha_z \overline{a}_z$ and $\overline{\beta} = \beta_x \overline{a}_x + \beta_z \overline{a}_z$, are shown in Fig. 4.9 (a).

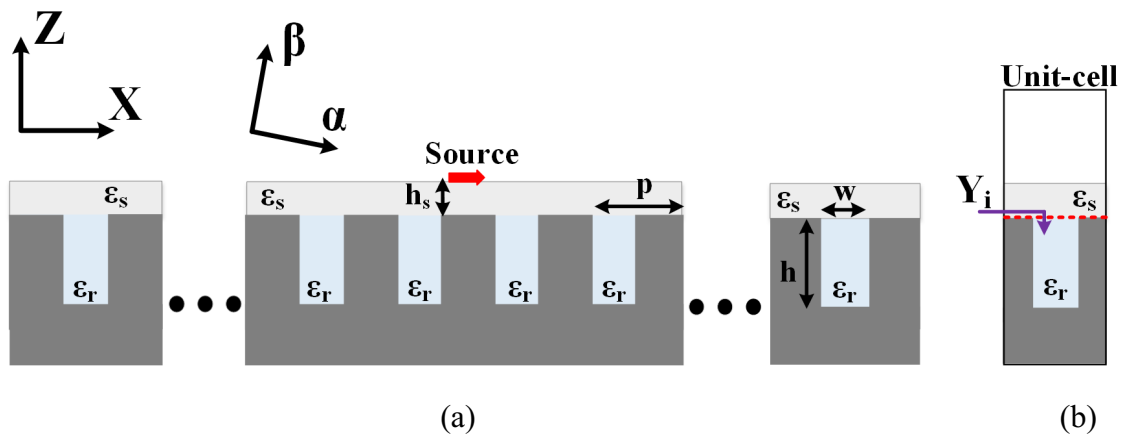

Fig. 4.9. Corrugated structure filled by a material with permittivity of ε_r, (a) side view of corrugated structure, and (b) the corresponding unit-cell.

If the structure is large in extent, one can use periodic analysis to estimate its performance, and simply consider a single unit-cell, as shown in Fig. 4.9 (b). Based on the reciprocity theorem, the transverse-equivalent network (TEN) of a leaky wave antenna can be used for far-field estimation [102]. Fig. 4.10 shows the TEN model of the corrugated structure with a shorted two-port network as representation of corrugations excited by electric or magnetic sources. In TEN model, the corrugated structure is assumed to be infinite (or large) along the reference plane (along X-axis shown in Fig. 4.9). The free-space is represented by a transmission line of an infinite length and free-space characteristic impedance. In the model, the electric or magnetic sources are modeled by the current and voltage sources, respectively. In the case of electric current source, on top of the corrugated structure, there can be another substrate with a thickness of h_s as a support layer of the source. In Fig. 4.10, this is shown as a transmission line with characteristic impedance and length of $Z_s = Z_0/\sqrt{\varepsilon_s}$ and h_s, respectively, where Z_0 is the free-space characteristic impedance $Z_0 = \sqrt{\mu_0/\varepsilon_0}$. The corrugated structures with both electric and magnetic sources are similar in their radiation performance. For magnetic sources such as cavity or slot which are exactly on top of structure, h_s is zero ($Y_{down} = Y_i$).

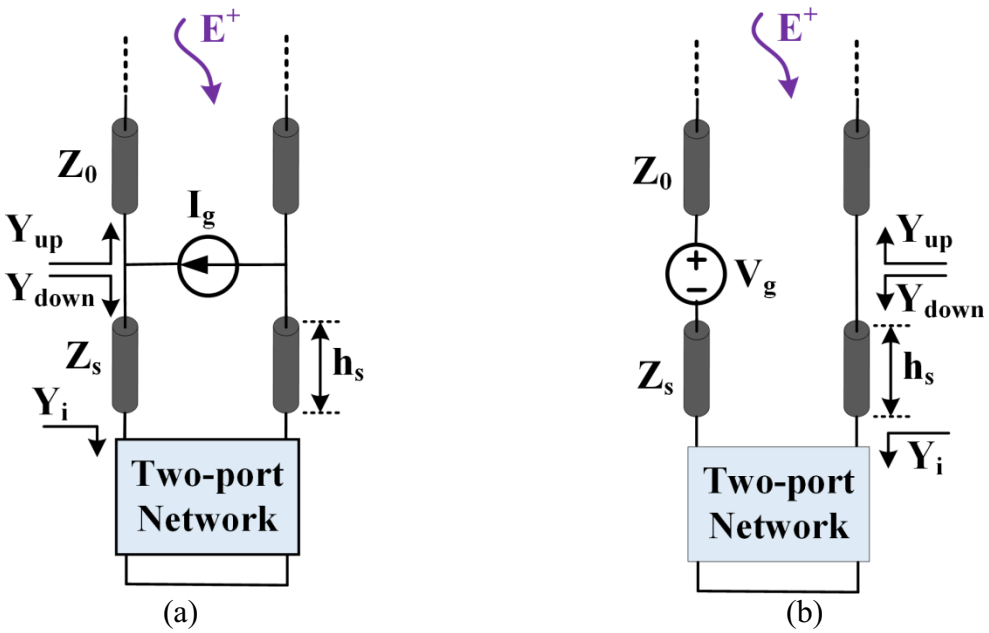

Fig. 4.10. Transverse-equivalent network of the corrugated structure, excited by (a) electric source, and (b) magnetic source.

For simplicity, the structures with magnetic sources are considered with the assumption $h_s=0$. In this case, the dispersion equation of corrugated structure with TM excitation is given by:

$$Y_i\left(k_x, k_0\right)+\frac{\omega\varepsilon_0}{k_z}=0 \tag{4.1}$$

where $Y_i(k_x, k_0)$ is the surface admittance, k_x, k_0 are the transverse and free-space propagation constants respectively, ω is the angular frequency, ε_0 is the free-space permittivity, and $k_z = \sqrt{k_0^2 - k_x^2}$ is the normal propagation constant. Using Eigenmode analysis, the dispersion diagram of the structure can be obtained. It is worth mentioning that the n=-1 space harmonic is the propagating harmonic in corrugated antennas. Although dispersion diagram of corrugated structures provides useful information about the far-field radiations versus frequency, they are not related to the physical parameters of the corrugations. In what follows, simple formulas based on the surface admittance of corrugations are obtained to assess the broadside radiation characteristics of corrugated antennas.

4.2.2 Resonance Condition for Corrugated Antennas

In this section, the excitation may be created by using an opening slot or cavity on top of the antenna. The corrugated antennas studied are assumed to provide high gain at broadside. Therefore, at the desired frequency where the maximum gain happens, the direction of propagation constant vector is very close to the broadside (i.e. $\beta_z >> \beta_x$ and $\alpha_z << \alpha_x$) [103]. The antenna configuration in this case is shown in Fig. 4.11(a) with its corresponding TEN model where the corrugations are represented by a shorted two-port network. The arrow in the figure displays the polarization of the magnetic source. Based on the reciprocity theorem, the far-field radiation of the antenna excited by an electric current is equivalent to finding the electric field induced at the excitation point when the antenna works in receiving mode and is impinged by a plane wave. In this case, we neglect the dependency of the free-space impedance characteristic and admittance of the corrugations (Y_{down} in Fig. 4.11(b)) on the angle of incidence in the TEN model for angles close to broadside. For the aforementioned case, the far-field characteristics can be calculated from the transfer function of the TEN model at the antennas' excitation point with the plane wave input. The voltage induced on the antenna located over the corrugated structure can be given by:

$$V^+ = \frac{Y_0}{Y_0 + Y_{down}} E^+ \tag{4.2}$$

where $Y_0=1/Z_0$ is the free-space characteristic admittance, and E^+ is the incident wave illuminated. The surface admittance Y_{down}, which is pure imaginary, is a function of dimensions of the corrugation, structures' periodicity, ε_r, and frequency and can be defined as:

$$Y_{down} = jY_0 \bar{Y}(w, h, p, \varepsilon_r, k_z) \tag{4.3}$$

where $\bar{Y}(w, h, p, \varepsilon_r, k_z)$ is the surface susceptance normalized to Y_0, and w, h, and p are respectively, the corrugations' width, corrugations' height, and the structure periodicity, ε_r is the material permittivity inside the corrugations, and k_z is the structures' wavenumber.

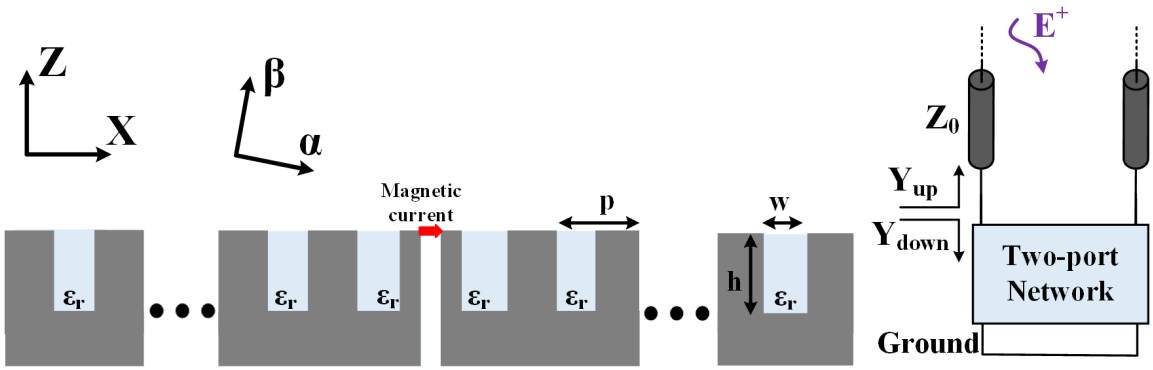

Fig. 4.11. (a) 1D Corrugated antenna structure excited by slot/cavity and (b) its corresponding TEN model.

Using (4.2) and (4.3), the radiated power density around broadside is written as:

$$P = \frac{P^{+}}{1+\overline{Y}^{2}(w,h,p,\varepsilon_r,k_z)} \tag{4.4}$$

where P^{+} is the power density of the incident wave which is constant. It should be mentioned that the radiated power density in (4.4) is valid for highly directive corrugated antenna with a small radiation angle of θ respect to broadside where TM characteristic impedance/admittance converges to TEM form. Furthermore, the loss contributed in the structure has been neglected in the derivation of (4.4). The resonance condition of the structure, corresponding to the maximum broadside antenna directivity, occurs where the imaginary part of the total admittance of the antenna is zero [104, 105] (i.e. $Im\,(Y_{up}+Y_{down})=0$, where Y_{up} and Y_{down} are shown in Fig. 4.11(b)). Since $Im(Y_{up})=0$, the resonance condition of the structure is simplified to

$$\overline{Y}(w,h,p,\varepsilon_r,k_{0,r}) = 0 \tag{4.5}$$

where $k_{0,r}$ is the resonant free-space wavenumber in which the resonance happens. Since, the radiation characteristic at broadside is considered, the normalized surface susceptance is not a function of k_z, ($k_z=k_0$).Considering (4.4) and (4.5), the maximum radiated power density at broadside is expressed as

$$P_{\max} = P_{res} = P^{+} \tag{4.6}$$

4.2.3 Spectral Bandwidth, and Maximum Directivity of Corrugated Antennas

The radiation performance of the corrugated antennas can be studied and assessed based on the corrugation impedance/admittance of a unit-cell of the antenna around broadside. The spectral bandwidth (SBW) of the antenna, which is helpful to evaluate the normalized 3dB gain bandwidth, is defined as $SBW=(f^{+}_{3dB}-f^{-}_{3dB})/f_{res}$ in which f^{+}_{3dB}, and f^{-}_{3dB} are the upper- and lower-band frequencies, respectively, with their radiated power density -3 dB lower than the maximum power density at resonant frequency f_{res}. By the definition, $f^{\pm}_{3dB}$ is found by

$$P(f^{\pm}_{3dB}) = \frac{P_{\max}}{2} = \frac{P^{+}}{2} \tag{4.7}$$

where $P(f^{\pm}_{3dB})$ is radiated broadside power density at the upper-/lower-band frequencies. Considering (4.4), and (4.7), these frequencies are where $\bar{Y}=\pm 1$. Therefore, the SBW can be expressed as

$$SBW = \left| \frac{f\big|_{\bar{Y}=1} - f\big|_{\bar{Y}=-1}}{f\big|_{\bar{Y}=0}} \right| \tag{4.8}$$

As previously mentioned, these calculations are valid for the periodicity of the structure larger than a half-wavelength, and hence antenna works in leaky mode. Similarly, the half-power beamwidth (HPBW) of the antenna at resonant frequency is defined as the angular span in which the magnitude of radiated power density decreases 3 dB from its maximum amplitude and can be estimated by the following relation:

$$P(f_{res}\big|_{\theta=\theta_{3dB}}) = \frac{P(f_{res}\big|_{\theta=0})}{2} = \frac{P_{\max}}{2} = \frac{P^{+}}{2} \tag{4.9}$$

where the radiated power density at resonant frequency and at the angle of $\theta=\theta_{3dB}$ can be estimated by (4.4), where $k_z = k_0\sqrt{1-sin^2\theta_{3dB}}$. Having (4.9) solved using (4.4) with the assumption of $sin\,\theta_{3dB} \cong \theta_{3dB}$ for a high directive antenna yields to

$$\bar{Y}(w,h,p,\varepsilon_r,k_{0,r}\sqrt{1-\theta^2_{3dB}}) = \pm 1 \tag{4.10}$$

Utilizing the approximation $\sqrt{1-\theta^2_{3dB}} \cong 1-\theta^2_{3dB}/2$ for an antenna with a narrow

beamwidth (very small θ_{3dB}) and expanding (4.10) with the Tylor series around $k_{0,r}$, result in:

$$\bar{Y}(w,h,p,\varepsilon_r,k_{0,r}) - k_{0,r}\frac{\theta_{3dB}^2}{2}\bar{Y}'(w,h,p,\varepsilon_r,k_{0,r}) + R(2) = \pm 1 \tag{4.11}$$

where $\bar{Y}'(w,h,p,\varepsilon_r,k_{0,r})$ is the first derivative of the characteristic admittance at the resonant frequency and *R(2)* shows the residual of the Tylor series including the second order derivative and above. According to (4.5), the normalized surface susceptance at the resonant frequency is zero. To further simplify (4.11), the residual *R(2)* can be neglected, and the first order estimation of HPBW is obtained as:

$$\theta_{3dB} = \frac{HPBW_E}{2} \cong \sqrt{\frac{c}{\pi f_r \bar{Y}'(w,h,p,\varepsilon_r,k_{0,r})}} \tag{4.12}$$

where c is the speed of light in free-space, f_r is the resonant frequency at which the maximum gain happens, and $HPBW_E$ is the half-power beamwidth in E-plane. Since, the corrugated antenna studied in this work is polarized in *1D* as shown in Fig. 4.11, the corrugations do not affect the HPBW in H-plane much. As (4.12) shows, a normalized surface susceptance with higher slope at the resonance and also a higher resonant frequency provides a lower $HPBW_E$. Using (4.12), the maximum directivity of the corrugated antennas can be approximately expressed as [106]:

$$D \cong \frac{\pi^2}{HPBW_E.HPBW_H} \propto \sqrt{f_r \bar{Y}'(w,h,p,\varepsilon_r,k_{0,r})} \tag{4.13}$$

4.2.4 Attenuation and Propagation Constant at Resonance Condition

The corrugated antennas can be analyzed based on the dominant TM leaky modes excited on top of the structure. The attenuation and propagation constant in the leaky wave complex wavenumber $k_x=\beta_x-j\alpha_x$ can be calculated using (4.1) which can be written in terms of the normalized surface susceptance as follows:

$$j\bar{Y}(w,h,p,\varepsilon_r,k_z) + 1 = 0 \tag{4.14}$$

As extensively discussed in [50] as an excellent reference on leaky-wave antennas, the optimum condition for a leaky-wave antenna radiation at broadside happens where $\beta_x \cong \alpha_x = \mathrm{k}_{0,r}\delta,\ \delta \ll 1$. Therefore, the dispersion equation of (4.14) at resonant frequency can be rewritten as:

$$j\bar{Y}(w,h,p,\varepsilon_r,k_{0,r}\sqrt{1+j2\delta^2})+1=0 \tag{4.15}$$

Using the approximation $\sqrt{1+j2\delta^2} \cong 1+j\delta^2$ for $\delta \ll 1$, and expanding (4.15) with the Tylor series around $k_{0,r}$, (4.15) is estimated with:

$$\bar{Y}(w,h,p,\varepsilon_r,k_{0,r})+jk_{0,r}\delta^2\,\bar{Y}'(w,h,p,\varepsilon_r,k_{0,r})+R(2)=j \tag{4.16}$$

Considering the first order approximation ($R(2) \cong 0$) and normalized surface susceptance of zero at resonant frequency according to (4.5), the attenuation and propagation constant of the structure at the resonant frequency are given by

$$\beta_x \cong \alpha_x = k_{0,r}\delta \cong \sqrt{\frac{c}{2\pi f_r\,\bar{Y}'(w,h,p,\varepsilon_r,k_{0,r})}} \tag{4.17}$$

As shown in (4.17), the attenuation and propagation constant at resonant frequency in the optimum condition for the leaky structure studied here, are in line with (4.13) for the antenna maximum directivity. The higher resonant frequency and the higher slope of the normalized surface susceptance at resonance result in lower attenuation constant which in turn make the antenna directivity improved.

The calculated formulas of (4.5), (4.8), (4.12), and (4.13) for radiation performance estimation of the corrugated structures are valid when the number of corrugations is large enough. There are several assumptions in obtaining these formulas that creates some errors. One of the main assumptions was that of having a high directive antenna. Also, in calculating the $HPBW_E$ and directivity, the first order approximation was taken into account which is valid where at resonant frequency, the normalized surface susceptance $\bar{Y}(w,h,p,\varepsilon_r,k_{0,r})$ versus frequency is close-to-linear that causes its second derivative to be close-to-zero. Otherwise, depending on the sign of the

second derivative of the normalized surface susceptance curve versus frequency, $HPWW_E$ and directivity can be higher/lower than (4.12), and (4.13).

Fig. 4.12 shows 1D and 2D corrugated antennas that can be designed using a corrugated unit-cell. The array factor of these antennas with infinite number of corrugations can be given as:

$$AF = A_0 + \sum_{i=1}^{\infty} e^{j(k_0 \sin\theta - k_x)ip} + \sum_{i=-1}^{-\infty} e^{j(k_0 \sin\theta + k_x)ip} \tag{4.18}$$

where A_0 contributes to the direct propagation of the magnetic/electric source into free-space, θ is the angle from of propagation from broadside, and $k_x=\beta_x-j\alpha_x$. In the analysis above, we neglected the effect of direct propagation (A_0). This increases the errors of the analysis, especially when there are few corrugations.

4.2.5 Parametric Study

In previous section, the corrugated antenna was analyzed based on the surface admittance/normalized surface susceptance of a unit-cell of the corrugated structure. Then, the antenna radiation performance could be estimated by analytic formulas provided. In this section, the normalized surface susceptance is investigated based on corrugation dimensions, permittivity inside corrugations and the periodicity.

For a corrugated structures with physical dimensions $p<<\lambda$, $w<<h$, and $(p-w)<<w$, the corrugated surface admittance may be considered as a homogenized surface with an admittance [107]:

$$Y_{down} = Y_s = -j(\frac{p}{w})\sqrt{\varepsilon_r}Y_0 \cot(\sqrt{\varepsilon_r}k_0 h) \tag{4.19}$$

where ε_r is the material permittivity inside the corrugations and (p/w) is the filling coefficient accounting for the filling ratio. Obviously, since $p>\lambda/2$, in a corrugated leaky wave antenna, (4.19) cannot be used as corrugated admittance for precise calculation. In this case, the corrugated admittance equation will be more complicated and can be calculated by analyzing a unit-cell of the structure using full-wave electromagnetic software.

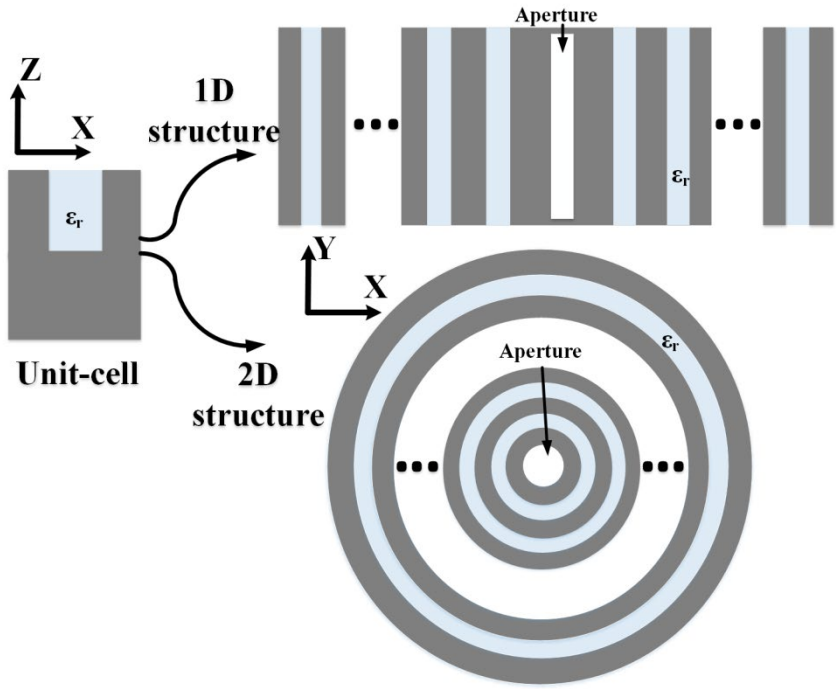

Fig. 4.12. 1D and 2D corrugated structures using a corrugated unit-cell.

Here, it is demonstrated that by designing and analyzing a unit-cell of a corrugated structure, a corrugated high-gain antenna can be designed. Then, unit-cell can be used in rectangular 1D corrugated structure or 2D bull's-eye configuration as shown in Fig. 4.12 with several corrugations. Although, the formulas (4.8), (4.12), and (4.13) are calculated for 1D structure, they can still provide a rough estimation for 2D structures.

As a case study, a corrugated antenna consisting of six corrugations each side of a rectangular aperture is investigated as shown in Fig. 4.13, and the effect of the width, and height of corrugations and the materials' permittivity inside corrugations are studied. The periodicity of the antenna is assumed to be p= 22 mm. However, all results can be scaled for different values of periodicity. Fig. 4.14 shows the effect of corrugations' width on the unit-cell suscptance $(\overline{Y})$ and the directivity of the corrugated antenna assuming p= 22 mm, ε_r=3, h= 3 mm. As shown, the maximum directivity happens around the resonance condition where $\overline{Y} = 0$.

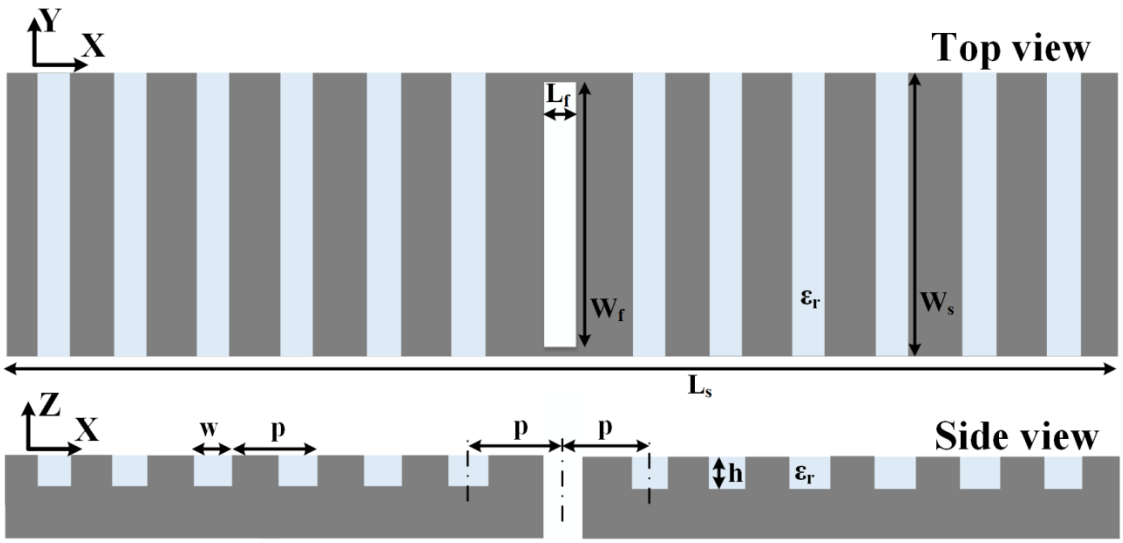

Fig. 4.13. Top and side views of the corrugated antenna under study. The antenna parameters are: W_f= 48 mm, L_f= 4 mm, W_s= 50 mm, and L_s= 13×p= 286 mm.

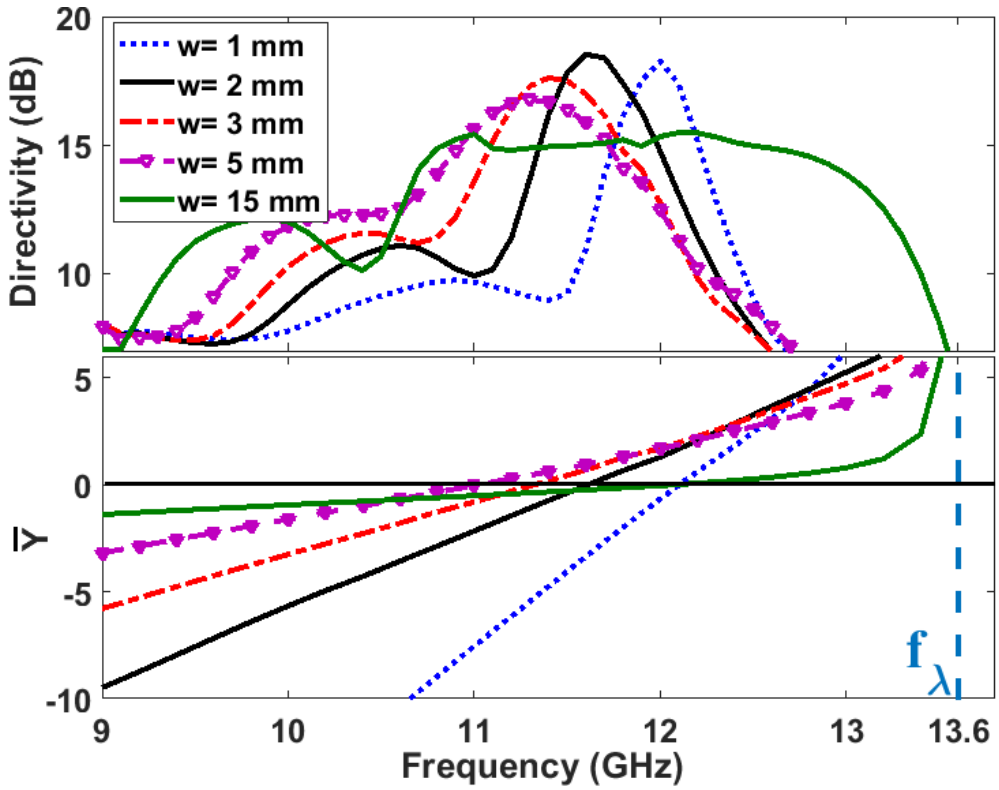

Fig. 4.14. Directivity and normalized surface susceptance of the corrugated antenna versus frequency for different corrugations' width and p= 22 mm, ε_r=3, h= 3 mm.

It is demonstrated that the different values of corrugations' width (w) result in different slope of $\overline{Y}$ which in turn provide different gain bandwidth and directivity. As the corrugations' width increases, the slope of $\overline{Y}$ decreases. Therefore, over a wider frequency range, we have $|\overline{Y}| \leq 1$ and according to (4.8), the gain bandwidth increases. On the other hand, according to (4.13), a lower slope results in a lower directivity as shown in Fig. 4.14 for w= 15 mm. Therefore, there is a trade-off between the maximum directivity and maximum gain bandwidth as we could predict. When w gets very small values, the second derivative of surface susceptance in the term *R(2)* in (4.11) becomes significant and the directivity decreases. It is worth mentioning that f_λ in Fig. 4.14 shows the frequency in which the structures' periodicity (p= 22 mm) becomes the size of the wavelength. The surface susceptance value at this point goes to high values.

Fig. 4.15 plots the directivity and surface susceptance of the antenna in Fig. 4.13 for different corrugations' heights (h), p= 22 mm, ε_r= 3, and w= 5 mm. Higher h shifts the resonance condition and maximum directivity to lower frequencies. According to (4.13) and assuming a similar slope of the susceptance curve for different h, the resonance condition happens in lower frequencies for higher h, and the maximum directivity drops. On the other hand, for very small heights (h= 1.5 mm), the second derivative in the term *R(2)* in (4.11) becomes large and the directivity decreases. As shown, a size reduction can be achieved with higher h; however, the directivity needs to be sacrificed. Similarly, as shown in Fig. 4.16, increasing the permittivity inside corrugations shifts the resonance to lower frequencies which can be used for the antenna miniaturization. In this case, however, the antenna directivity drops. This is consistent with (4.13) implying that a higher resonant frequency (f_r closer to f_λ) corresponds to a higher directivity.

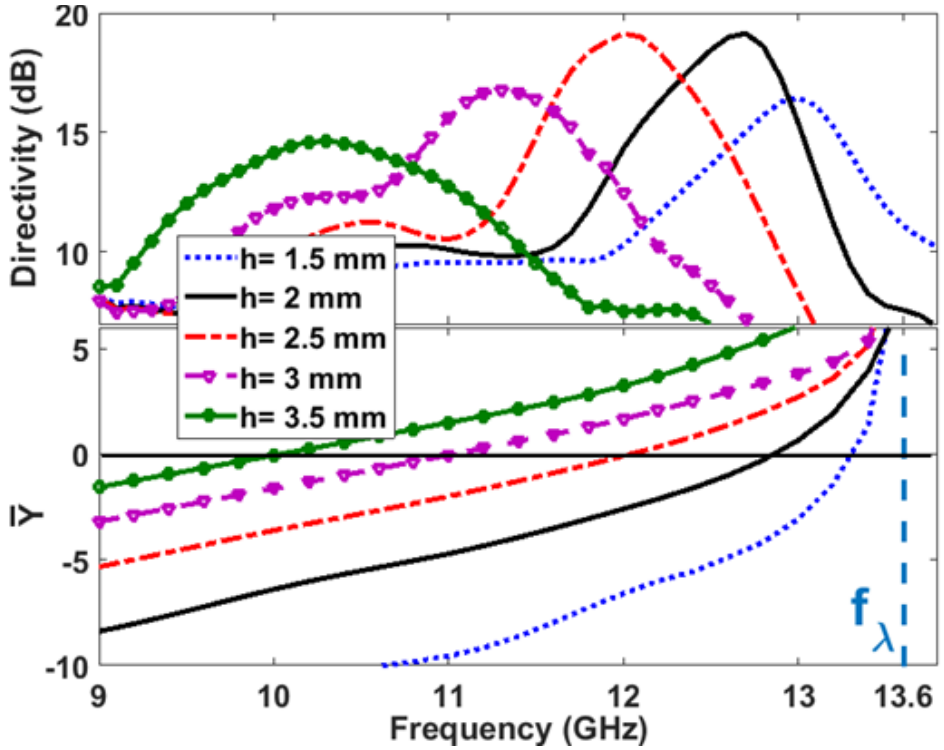

Fig. 4.15. Directivity and normalized surface susceptance of the corrugated antenna versus frequency for different corrugations' height and p= 22 mm, ε_r= 3, w= 5 mm.

In general, from the parametric study and many simulations, as the resonance takes distance from f_λ, the directivity drops in accordance with (4.13). Furthermore, if the resonance gets very close to f_λ, the term *R(2)* in (4.11) becomes larger and the directivity declines. Therefore, the optimum condition for maximum directivity is when f_r (resonant frequency) is large and $\bar{Y}$ at the resonance is almost linear (for negligible *R(2)*).

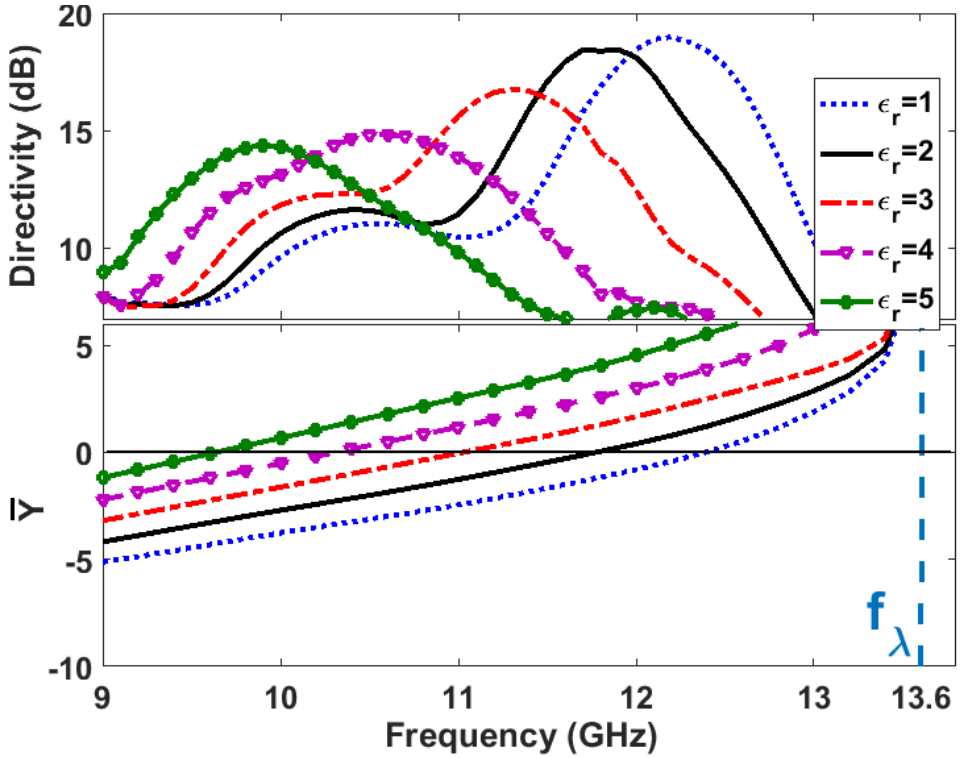

Fig. 4.16. Directivity and normalized surface susceptance of the corrugated antenna versus frequency for different materials' permittivity and p= 22 mm, h= 3 mm, w= 5 mm.

As described previously, conventional corrugated antennas used to be fabricated on metallic films. This increases the fabrication cost of the antenna and its weight especially when the structure is large. Besides, the integration of the antenna with other planar systems becomes difficult. To address these issues, it was proposed that the antennas be fabricated on laminates which provide more degrees of freedom for the design. In low frequencies, the height of the corrugations becomes large which needs a very thick substrate for fabrication. In addition to the board availability issues, this increases the antenna weight. To solve this issue, a substrate with a high permittivity can be used.

In a parametric study, Fig. 4.17 shows how an antenna presented in Fig. 4.13 with lower height (substrate thickness) can be designed with a substrate of high permittivity without any degradation in the performance.

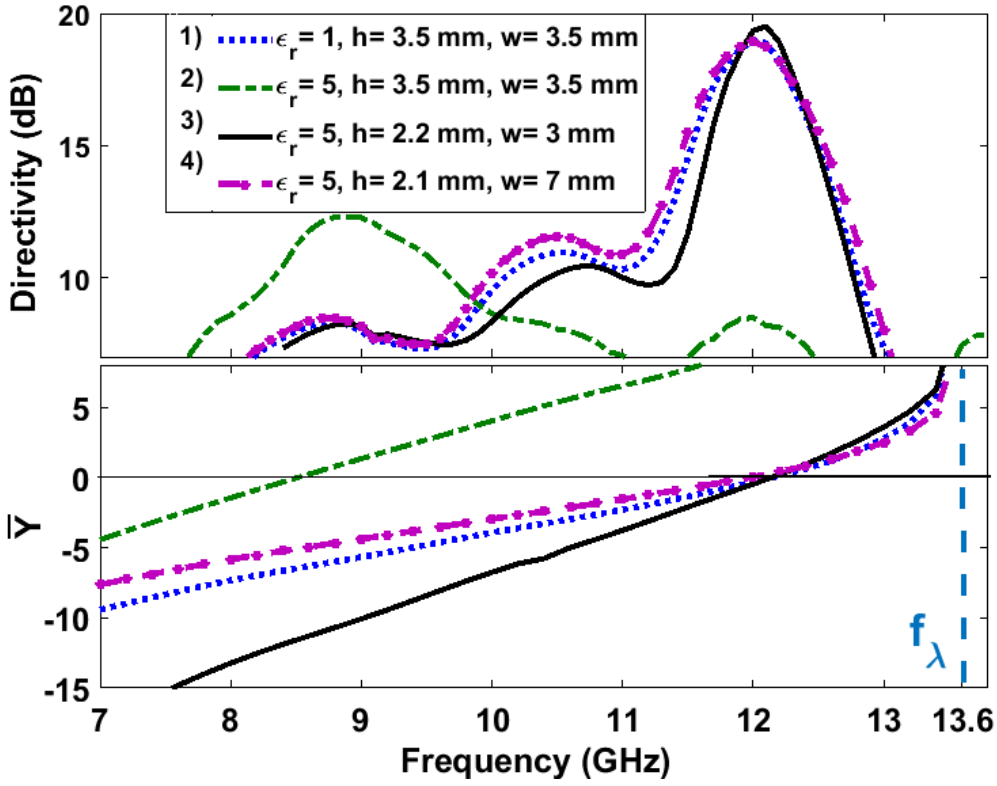

Fig. 4.17. Directivity and normalized surface susceptance for four design cases.

As shown, four cases have been designed and simulated. In case 1, a conventional antenna with the permittivity of 1 is designed for the maximum directivity at 12 GHz. The maximum antenna directivity for this case is 19 dB. Then, the permittivity of antenna is increased to 5 and *w* and *h* are kept fixed in case 2. As expected, the resonant frequency shifts to lower frequencies where the antenna has a lower directivity. As demonstrated earlier in Fig. 4.15, decreasing the corrugations' height shifts the resonance to higher frequencies. Therefore, reducing the corrugations' height can compensate for the frequency shift resulted from a dielectric with higher permittivity. Case 3 shows an antenna with same resonant frequency of case 1, but with lower corrugations' height. In other words, using a higher permittivity inside corrugations can lead to miniaturizing the antenna thickness. It is worth mentioning that as reported in [60], this may also enhance the antenna directivity as case 3 shows a directivity of 19.55 dB which indicates a directivity improvement of 0.55 dB with respect to the conventional structure. As discussed earlier,

to have a wide gain bandwidth, the corrugations' width needs to increase. This is demonstrated in case 4 where we could get the same performance of conventional structure (case 1) with a lower substrate thickness. The corresponding normalized surface susceptances of all cases in Fig. 4.17 are in line with the directivity and gain bandwidth achieved. For instance, since cases 1 and 4 have almost the same $\bar{Y}$, it could be predicted that they would have similar directivity and gain bandwidth. Also, according to (4.13), with fixed f_r, since case 3 has a higher first derivative of $\bar{Y}$ compared to cases 1 and 4, we could expect it to have a higher directivity. This presents how a corrugated antenna can be designed by analyzing a corrugated unit-cell.

4.3 Aperture Efficiency of Corrugated Antennas

The aperture efficiency of corrugated antennas is very low [63]. In addition to the nature of the antenna, another issue that would not allow having higher aperture efficiency is the direct wave propagation/transmission of the aperture in the transmitting/receiving mode. Fig. 4.18 shows the directivity and aperture efficiency of the design case 3 in previous section versus the number of corrugations in each side of the central aperture. The maximum gain and efficiency of 19.98 dB and 33.1% are achieved for nine, and four corrugations, respectively. As demonstrated, although increasing the number of corrugations enhances the antenna directivity, the rate of this directivity enhancement reduces as the number of corrugation increases. The main reason is that the wave leaks to the free space as it gets far from the aperture in the transmitting mode and after certain number of corrugations, most of the power has propagated, hence the contribution of the corrugations far from aperture to propagation is lower. As shown in Fig. 4.18, by increasing the number of corrugation from 1 to 4 in each side of aperture, the aperture efficiency improves from 28% to 33.1%, but it drops afterward as the number of corrugation increases and it gets to 23.7% for nine corrugations. The reason for this decline is that the rate of gain enhancement is less that the rate of increase in antenna size.

Fig. 4.19 shows the electric field distribution of the corrugated antenna with nine corrugations at its resonant frequency. As clearly demonstrated, the corrugations far from the

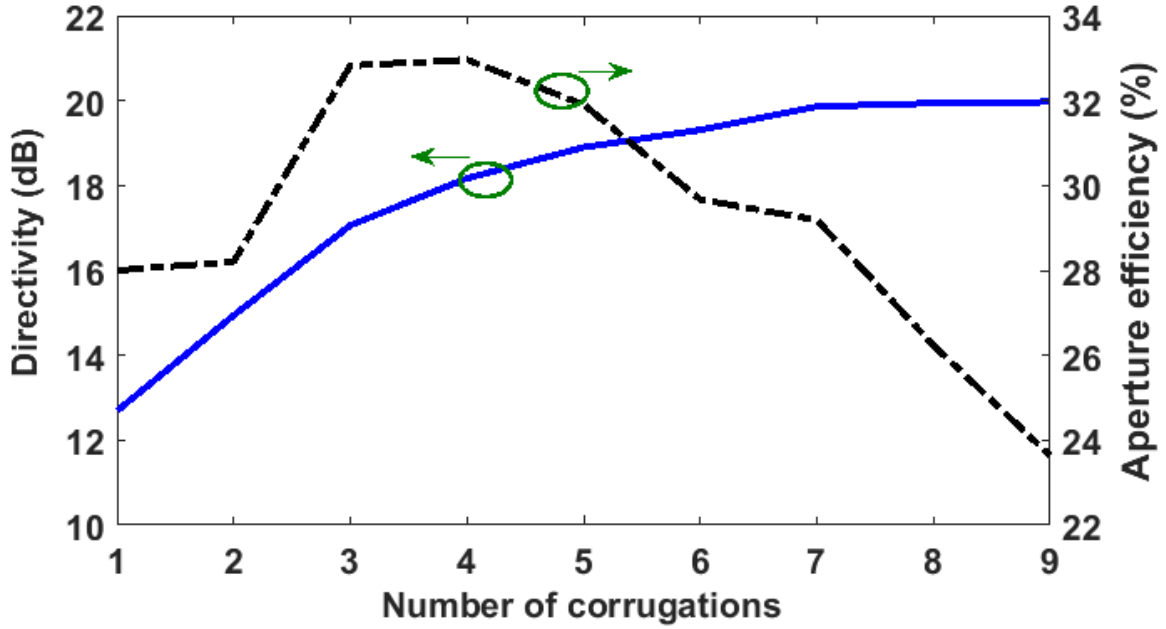

Fig. 4.18. Directivity and aperture efficiency versus the number of corrugations in each side of the central aperture (the design frequency is 12 GHz and the corrugation parameters are p= 22 mm, ε_r=5, h= 2.2 mm, and w= 3 mm).

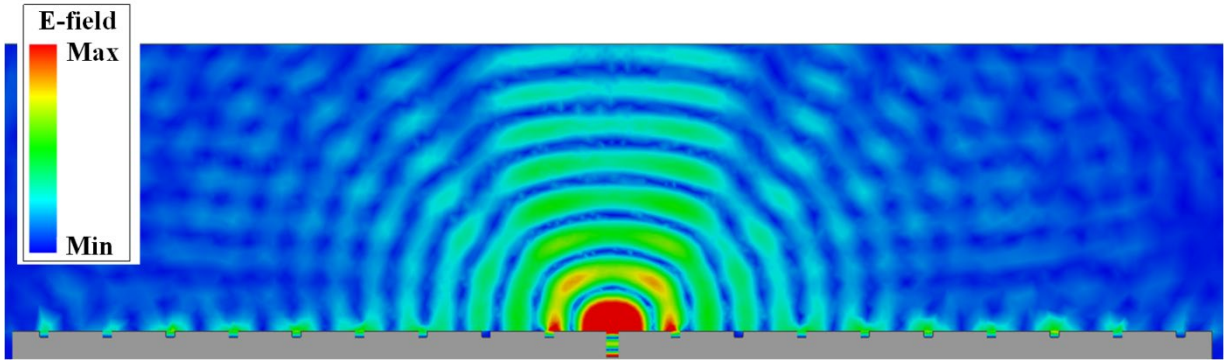

Fig. 4.19. Electric field distribution of the antenna with nine corrugations at the resonant frequency (p= 22 mm, ε_r=5, h= 2.2 mm, and w= 3 mm).

aperture contribute less to directivity enhancement. This explains the decline in directivity enhancement by increasing the number of corrugations.

4.4 2D Corrugated (Bulls'-Eye) Antennas: Fabrication and Measurement

In this section, a 2D corrugated structure is designed on laminate substrates at the center frequency of 10 GHz based on the unit-cells' analysis and then the whole antenna is designed, fabricated, and measured [108]. Since commercial substrates have standard thickness and permittivity, we need to choose the right board with the appropriate thickness and permittivity to achieve the resonance condition at 10 GHz. By analyzing the unit-cell, the resonant frequency of three commercial substrates (i.e. Rogers 5880, Rogers 4003, and Rogers TMM4, with permittivity of 2.2, 3.38, and 4.5 respectively) are obtained for standard thicknesses of 75, 100, 125, and 150 mils and for various corrugations' widths (w) as shown in Fig. 4.20. According to the curves plotted in Fig. 4.20, to have a resonant frequency at 10 GHz, Rogers TMM4 with the thickness of 125 mil (h= 3.175 mm) and w= 12 mm is selected. Fig. 4.21 shows the unit-cell analysis and full-wave simulation of the 2D corrugated antenna with 3 corrugations for this case. For the full-wave simulation, the diameter of the circular aperture is taken to be 10 mm is considered between the corrugations with p= 22mm and circular aperture.

It is very interesting to look at the dispersion diagram of the unit-cell and find these results in line with each other. The dispersion curve of the unit-cell of the antenna is depicted in Fig. 4.22. According to leaky wave theory, the $n=-1$ space harmonic of leaky modes of the structure can be a radiating mode. Fig. 4.22 shows the fundamental mode and $n=-1$ radiating mode of the proposed structure. The dispersion curve which is the Fourier transform of the wave on the structure can be obtained using Eigenmode analysis of commercial software such as HFSS. From Fig. 4.22, it can be seen that the in-phase superposition (which makes the structure propagate at broadside due to the symmetry) happens around 10 GHz.

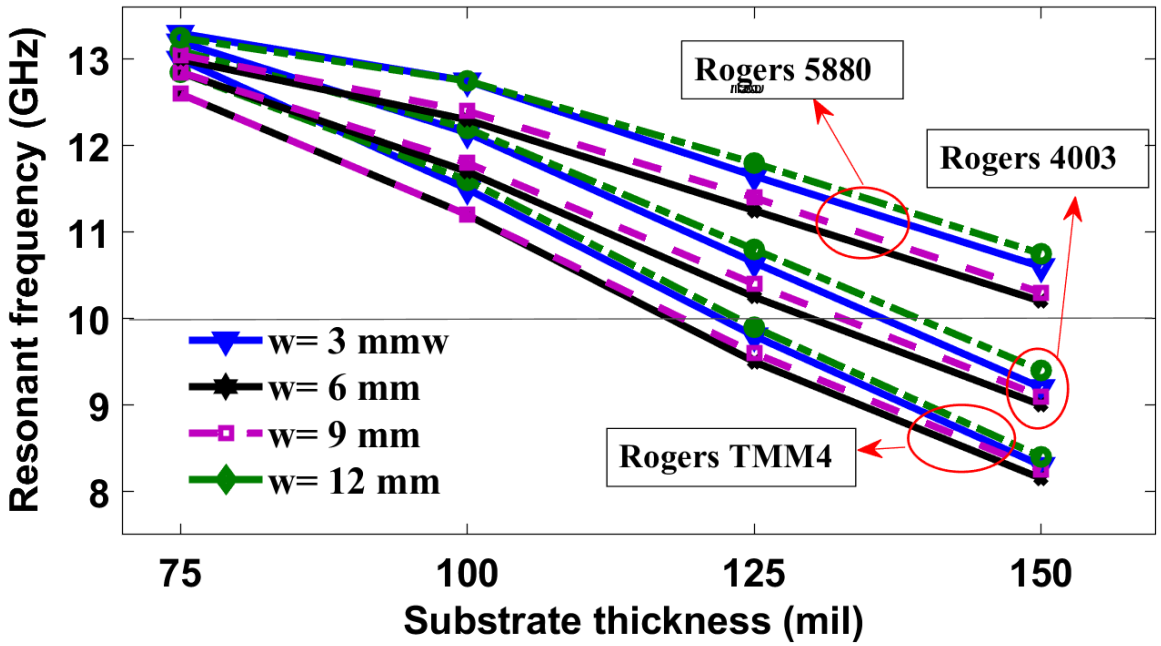

Fig. 4.20. The resonant frequency of corrugated antenna calculated by simulation of a corrugated unit-cell for three commercial substrates with standard thicknesses of 75, 100, 125, and 150 mil and for different corrugations' width and p= 22 mm.

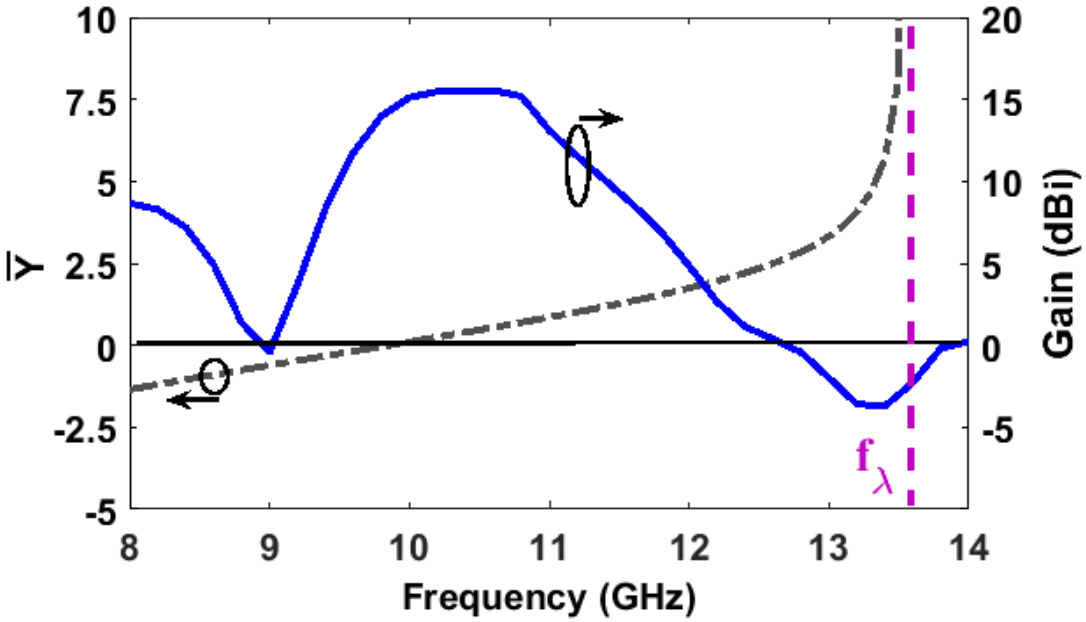

Fig. 4.21. Gain and normalized surface susceptance of the 2D corrugated antenna with 3 corrugations (p=22 mm, ε_r= 4.5, w= 12 mm, h= 3.175 mm).

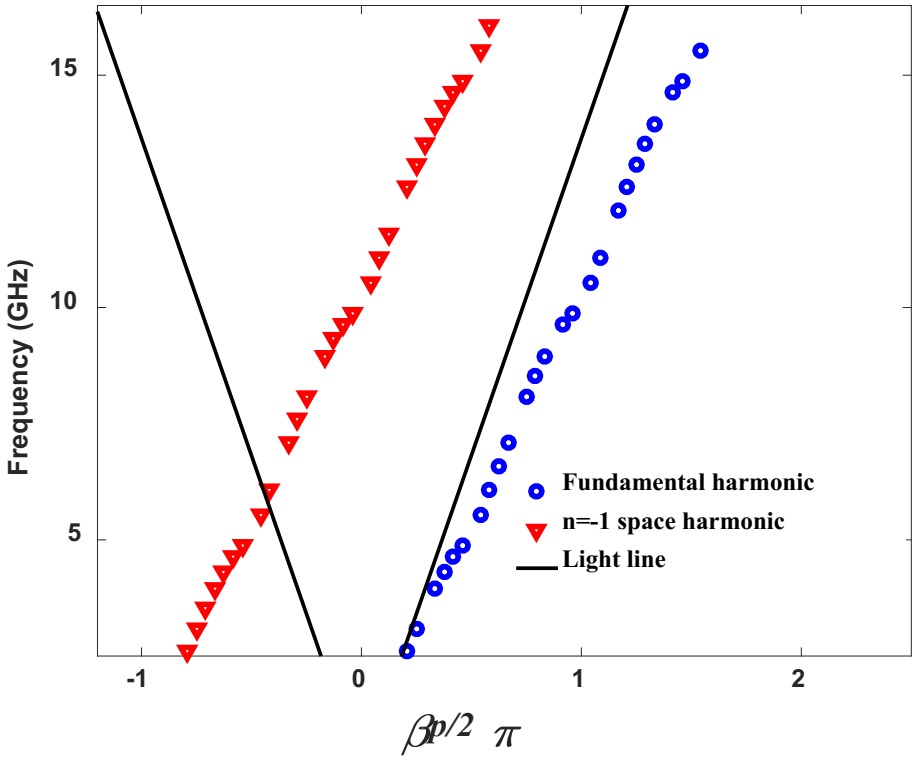

Fig. 4.22. Dispersion curve of the proposed structure for fundamental harmonic and *n=-1* radiating space harmonic.

A 2D corrugated antenna with 3 corrugations is designed as shown in Fig. 4.23. The antenna is made of three substrate layers stacked on top of each other. The first substrate (Sub. 1) is use to design the feed line. This substrate is chosen to be Rogers 4003 with the thickness of 20 mil. A 50-Ω feed line is etched on the bottom layer of Sub. 1 to excite and couple the energy through a cavity fabricated on the second layer (Sub. 2). The second and third substrates (Subs. 2 and 3) are Rogers TMM4 with thickness of 125 and 20 mils, respectively. A ring patch is printed on top layer of Sub. 3 that helps to match the impedance to 50 Ω. To realize the corrugations on the Sub. 2, the SIW technology can be used. The corrugations have a minimal effect on the impedance matching. The cavity in the Sub. 2 is made by overall cutting and removing away the dielectric material inside and then metalizing to shape a cylindrical cavity.

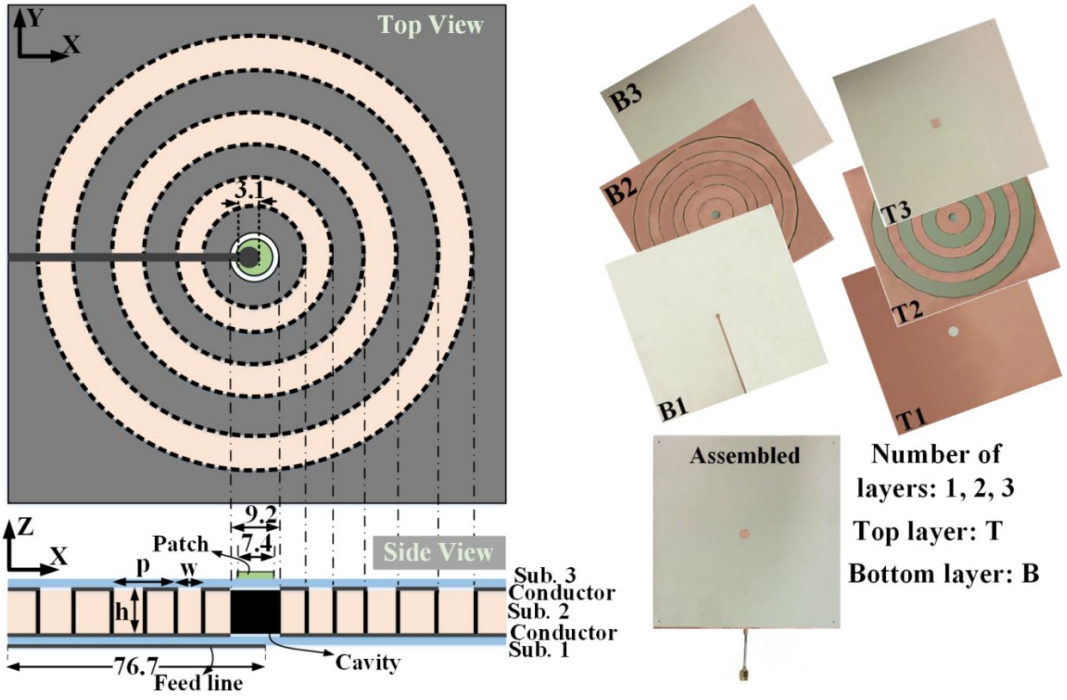

Fig. 4.23. The corrugated antenna designed on substrates at the center frequency of 10 GHz (p= 20 mm, w= 12 mm, and h= 3.175 mm), and the fabricated prototype.

Fig. 4.24 shows the magnitude of the electric current distribution inside Subs. #2 and #3 at the center frequency of 10 GHz. The resonance inside and above the corrugations are clearly depicted in these plots. Since the resonance happens along feed line direction (X direction), it is expected to have a narrow radiation beamwidth in XZ plane (E-plane) at 10 GHz. As it can be seen in Fig. 4.24, the amplitude of electric field over corrugations away from the cavity reduces due to the conversion of a portion of waves into the space radiating modes in the closer corrugations (attenuation constant of leaky nature of the structure). For the same reason, with an increase in the number of grooves, the rate of the increase in the antenna gain decreases.

The reflection coefficient and gain of antenna are plotted in Fig. 4.25 and Fig. 4.26. The measurement result shows an impedance bandwidth of almost 9.5-10.45 GHz for the reflection coefficient better than -10 dB, which corresponds to the bandwidth of 9.52%. Moreover, the result confirms that the maximum antenna gain of 17.4 dBi at broadside is obtained around 10 GHz. It is

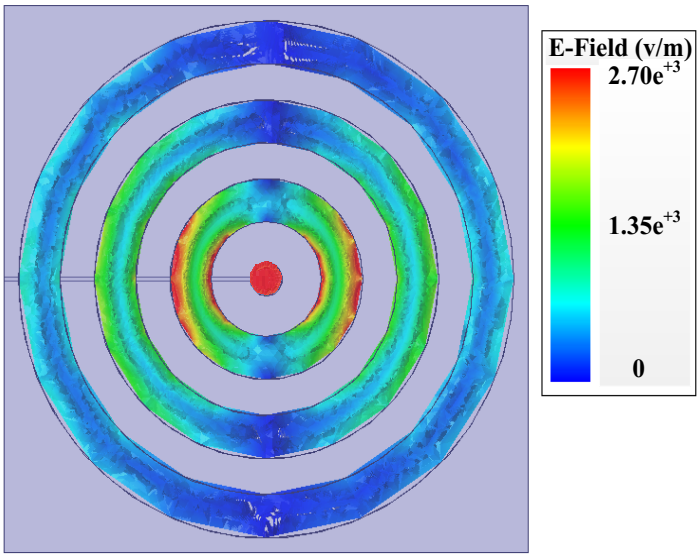

(a)

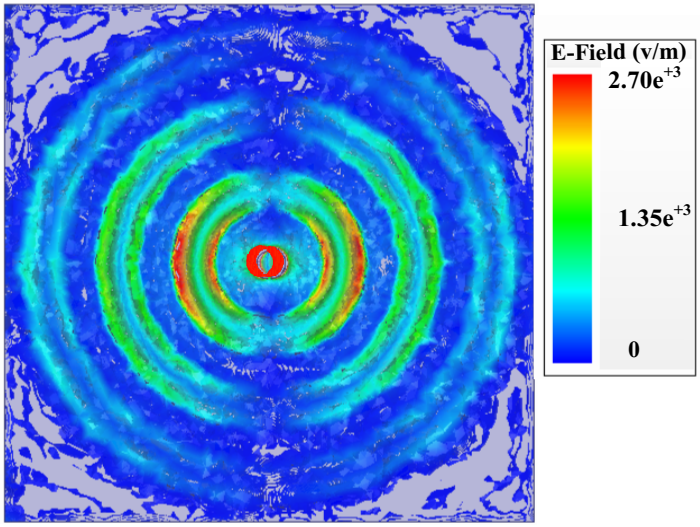

(b)

Fig. 4.24. Magnitude of electric field distribution inside, (a) the cavity and grooves in Sub. #2, and (b) Sub. #3 at 10 GHz.

worth mentioning that the maximum antenna gain for structure without any corrugations (i.e. the depth of the corrugations equals to zero) is about 5 dBi which means a 12.4 dB improvement is achieved. Due to having a patch above the cavity, the gain and spectral bandwidth of the fabricated antenna are, respectively, more and less compared to those plotted in Fig. 4.21 for a corrugated antenna with circular waveguide feed.

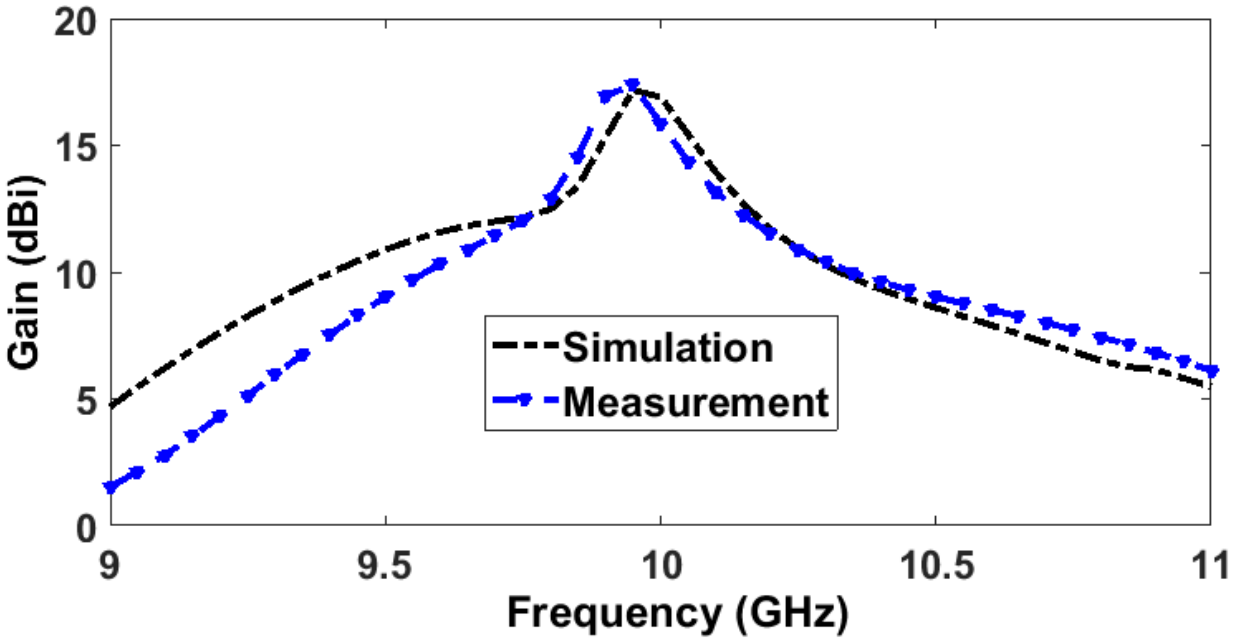

Fig. 4.25. Gain of the proposed antenna.

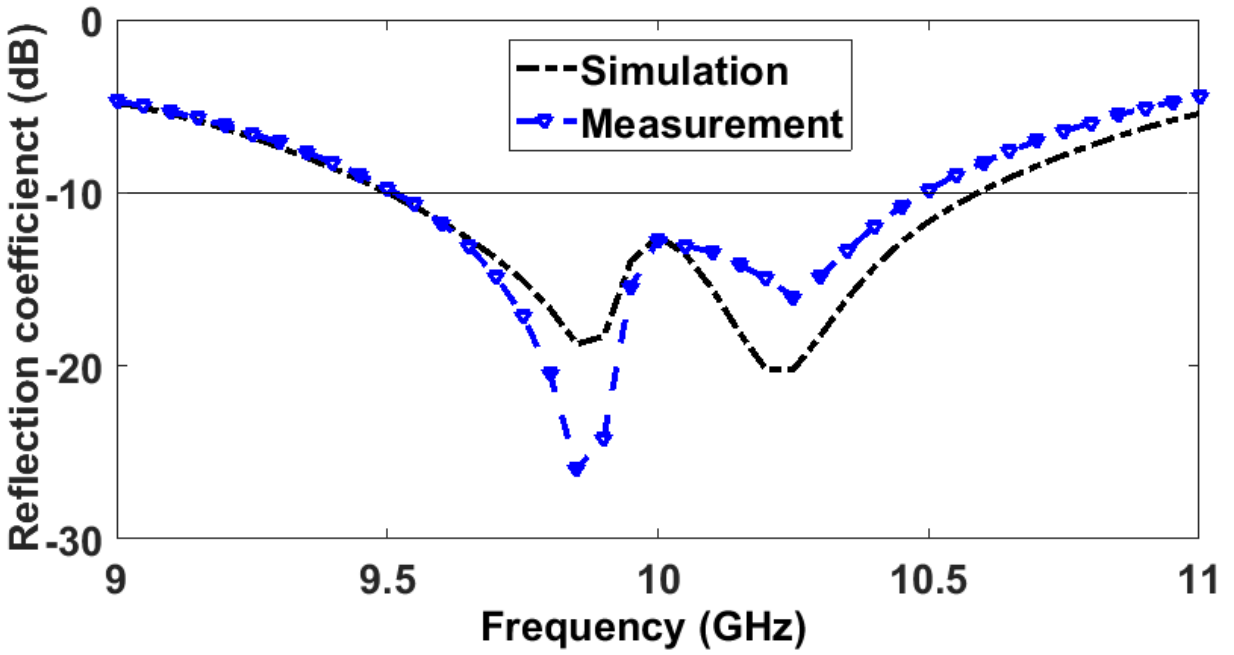

Fig. 4.26. Reflection coefficient of the proposed antenna.

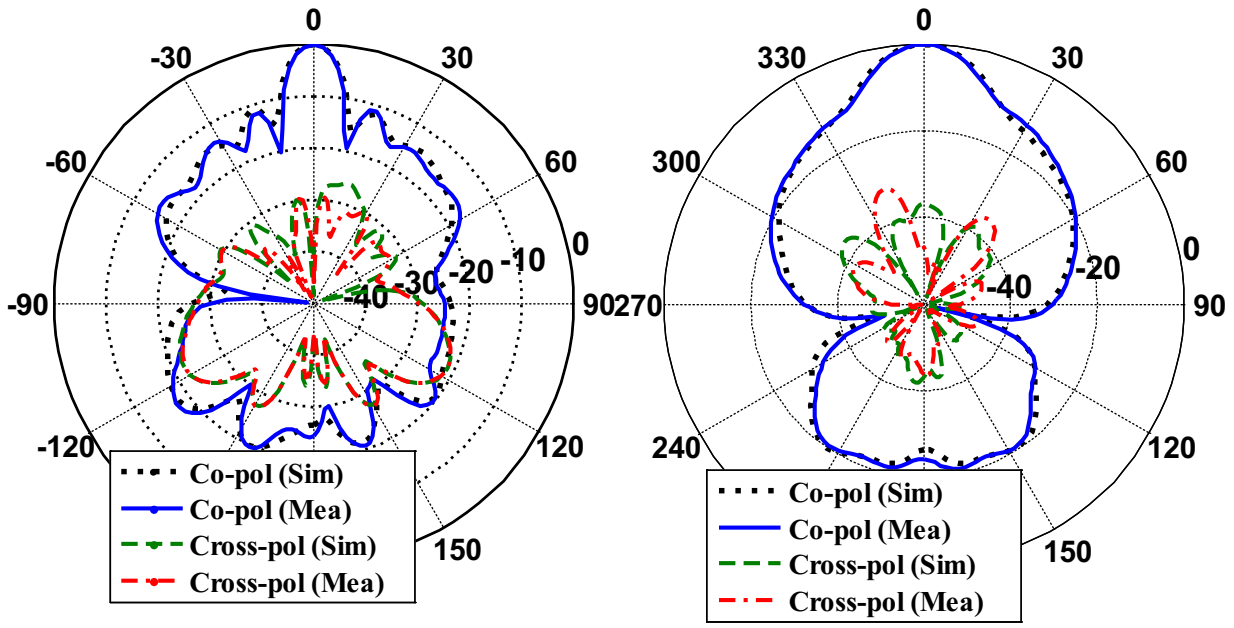

(a) (b)

Fig. 4.27. Radiation patterns of the proposed antenna, (a) E-plane (XoZ plane), and (b) H-plane (YoZ plane) at the center frequency of 10 GHz.

In Fig. 4.27, the simulated and measured radiation patterns of the proposed antenna are plotted at both orthogonal planes at the center frequency of 10 GHz. The cross-polarization levels are lower than Co-polarization levels by at least 28 dB in the 3 dB beamwidth in both E-plane and H-plane. Measurement results show that half-power beamwidths of E-plane and H-plane are 9.9° and 18.4°, respectively. Moreover, a side-lobe-level of 11 dB is measured as shown in Fig. 4.27.

In this chapter, corrugated antennas were discussed. A method of fabrication of these antennas on laminates was presented using SIW technology. Moreover, corrugated antennas were analyzed based on their surface susceptance. It was shown that the unit-cell analysis, performed in this work, could roughly estimate the radiation performance of these antennas very fast. In many applications multi-band high-gain antennas are required. This will be discussed in the next chapter.

Chapter 5

Dual-Band Planar Corrugated Antennas with Integrated Feed Structures

In chapter 4, the single-band corrugated antennas were studied and analyzed. However, the demand for multi-band high gain antenna has increased in recent decades due to their capability to simultaneously communicate with multiple standard systems in a single low-profile package. For instance, if it is required to receive a signal in one frequency band and transmit another signal in a different frequency, a dual-band antenna is needed. Therefore, there is a need to design a single antenna in order to cover the desired bands. With advent of advanced wireless systems, it is more desirable that such antennas can be integrated with the rest of the system. In this chapter, novel dual-band planar corrugated antennas are presented. Dual-band operation can be achieved by designing the grooves with different shapes or dimensions on the flat surface of the corrugated antennas. Two geometries for dual-band corrugated antenna are proposed, fabricated, and measured in this chapter.

5.1 Dual-Band Corrugated Antenna with a Microstip Feed Line

In chapter 4, it was shown that the superposition of electric field (cavity resonance) in the direction of the polarization of the current source may enhance the antenna gain. In this section, it is demonstrated that the dual-band operation can be achieved using two different cavity resonances in two different directions [109]. The proposed antenna configuration is shown in Fig. 5.1. As shown, the structure consists of three dielectric layers. Subs. 1 and 3 are Rogers 5880 with relative permittivity of 2.2, thickness of 0.508 mm, and loss tangent of 0.0009.

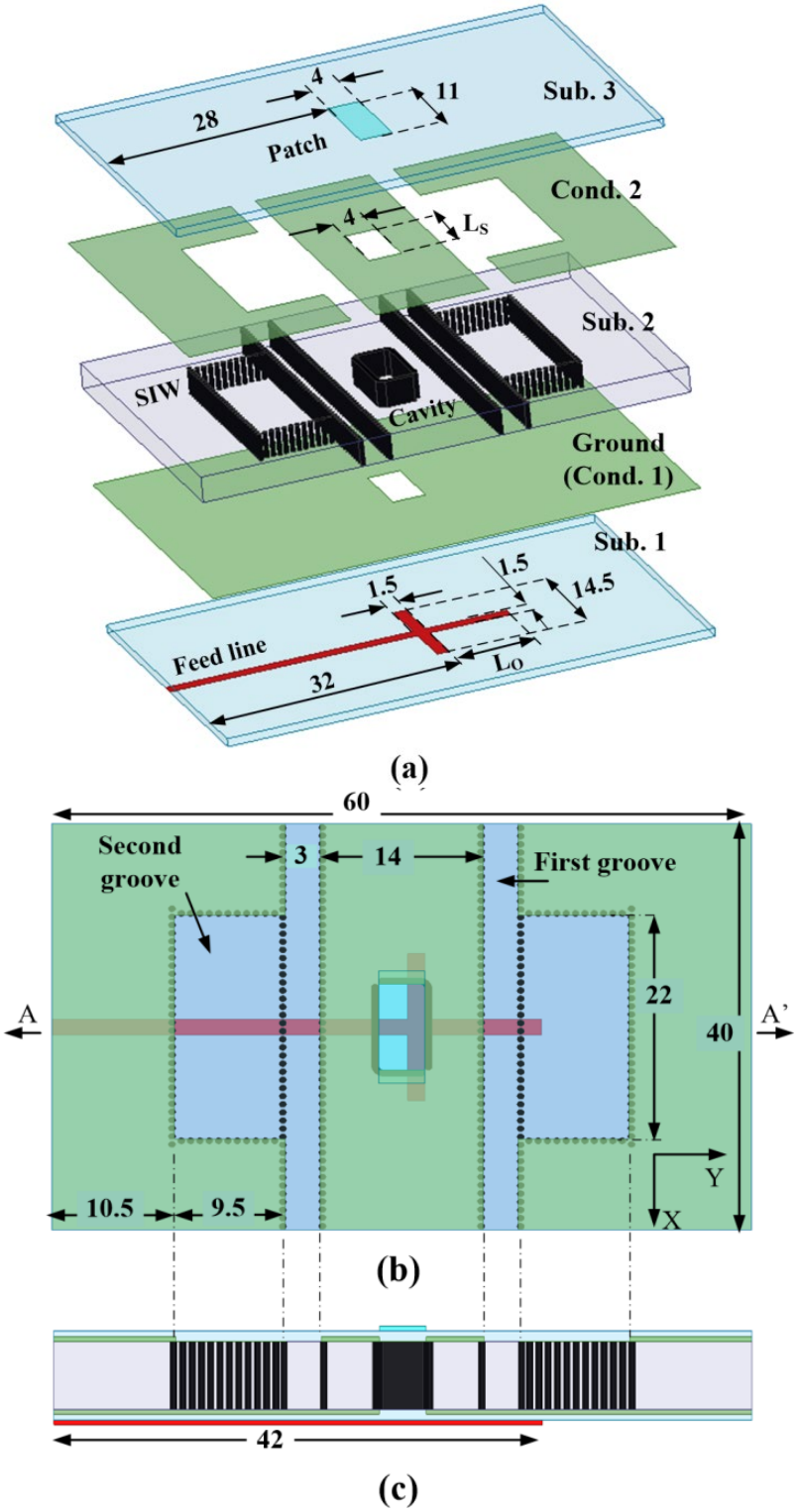

Fig. 5.1. Dual-band antenna configuration, (a) 3D View, (b) Top view, (c) AA' view (All dimensions are in mm).

Second layer (Sub. 2) is Rogers TMM4 with relative permittivity of 4.5, thickness of 3.175 mm, and loss tangent of 0.002. The antenna is excited by a resonant feed line at the bottom layer. The feeder is a 50-Ω line and designed to provide a resonance at the upper band. The lower resonance could be established by the length of the cavity within Sub. 2. The power is coupled from feed line through the cavity to the patch at the top layer. The width of the cavity and the shape of feed line underneath have great effects on the radiation pattern. The construction of cavity wall using vias in an SIW structure has a considerable impact on the cavity performance and makes it difficult to adjust its resonant frequency. Therefore, the rectangular cavity is taken out of Sub. 2 using a drill and then its walls are metalized (drilling and metallization are part of standard PCB manufacturing process). For size reduction, the substrate inside the cavity has been kept with connections to the main body of Sub. 2. The rectangular patch on top of the cavity improves the impedance matching of the corrugated antenna and increases the power coupled from transmission line to the cavity. The patch affects the overall cavity resonant frequency and radiation pattern. Therefore, both patch and cavity have to be designed in conjunction with each other.

The dual-band characteristic of the antenna is illustrated in Fig. 5.2. It can be seen that the lower resonance has a large variation with respect to the length of cavity, but the upper one is not affected so much. This shows the lower resonance is mainly determined by the cavity length. Also, the upper resonance is dominantly determined by L_o. Therefore, the proposed dual-band antenna can easily be designed for any desired operating bands. For the selected values of L_o= 10 mm and L_s= 8.5 mm, the resonant frequency of 10.1 and 12.45 GHz are obtained as the lower and upper bands, respectively.

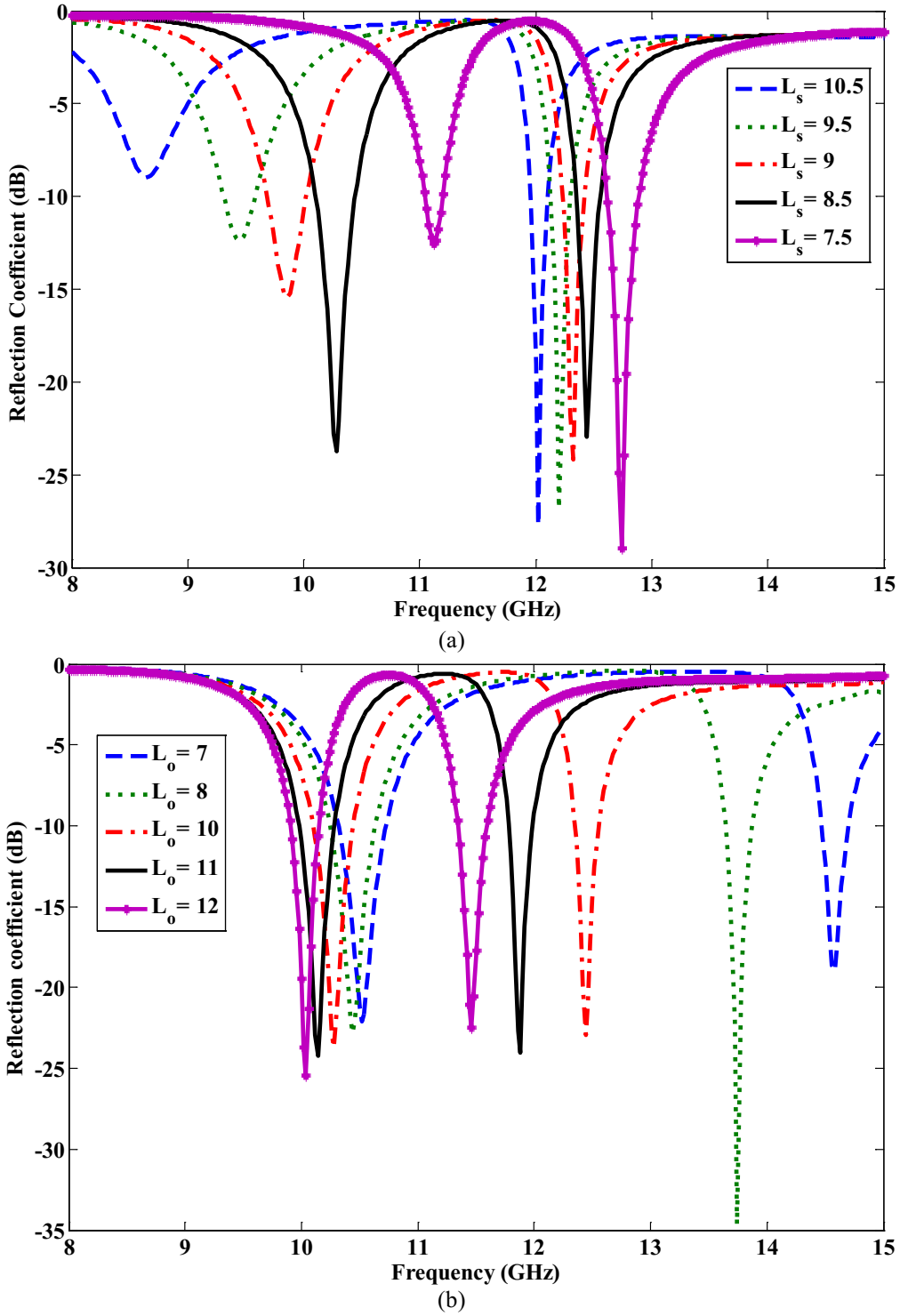

Fig. 5.2. (a) Reflection coefficient versus the cavity length with L_o= 10 mm, (b) Reflection coefficient versus open circuit length of the feed line with L_s= 8.5 mm.

Two different shapes of grooves have been made in order to provide two resonances at the desired bands. To investigate the effects of grooves on enhancing the antenna gain, the first and second pairs of grooves are studied separately. Then, the effect of both pairs of grooves together on antenna gain is considered. Fig. 5.3 shows the electric field distribution inside the cavity and grooves when there is just the first pair of grooves. Here, the distance between patch and grooves (d_1) is 8.5 mm that is near half wavelength. As shown in Fig. 5.3 (a), there is an in-phase superposition of electric field at both sides of the grooves at 10.1 GHz; however, this effect for the frequency of 12.45 GHz is very minimal, as seen in Fig. 5.3 (b). Therefore, it is expected to have a narrow radiation beamwidth in XZ plane (H-plane) at 10.1 GHz with relatively higher directivity. According to the simulation, broadside gains at 10.1 and 12.45 GHz are 10 and 6.95 dBi, respectively, which are in-line with the expectation of Fig. 5.3 for both resonant frequencies. A very interesting point for the grooves is that the locations of in-phase fields inside the grooves are a wavelength away from center of the patch.

To increase the gain of the upper band, a second pair of grooves is employed. The effects of these grooves are investigated separately. Here, the distance between patch and the second pair of grooves (d_2 as shown in Fig. 5.4) is about a wavelength (15 mm) at the frequency of 12.45 GHz (upper band) based on the analysis performed in chapter 4. According to Fig. 5.4, with the optimized dimensions, the in-phase superposition of electric field strongly exists in Y-direction for the upper band. Therefore, it is expected to have a more directional pattern (and in turn narrower beam) in YZ-plane (E-plane) at 12.45 GHz, but less effect on the gain at 10.1 GHz. As demonstrated by simulation for this case, the broadside gain at 10.1 and 12.45 GHz are 8.8 and 10 dBi, respectively, which are in-line with Fig. 5.4, at both resonant frequencies. The whole configuration has the capability to be easily integrated with planar devices unlike conventional corrugated/feeder antennas that are fed by waveguides.

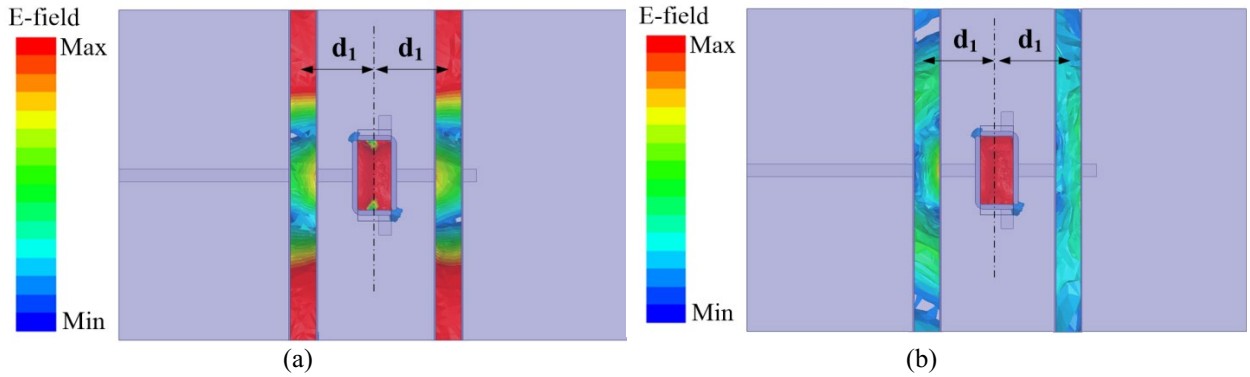

(a) (b)

Fig. 5.3. Electric field distribution inside cavity and first pair of grooves for the proposed antenna at frequency of, (a) 10.1 GHz and (b) 12.45 GHz.

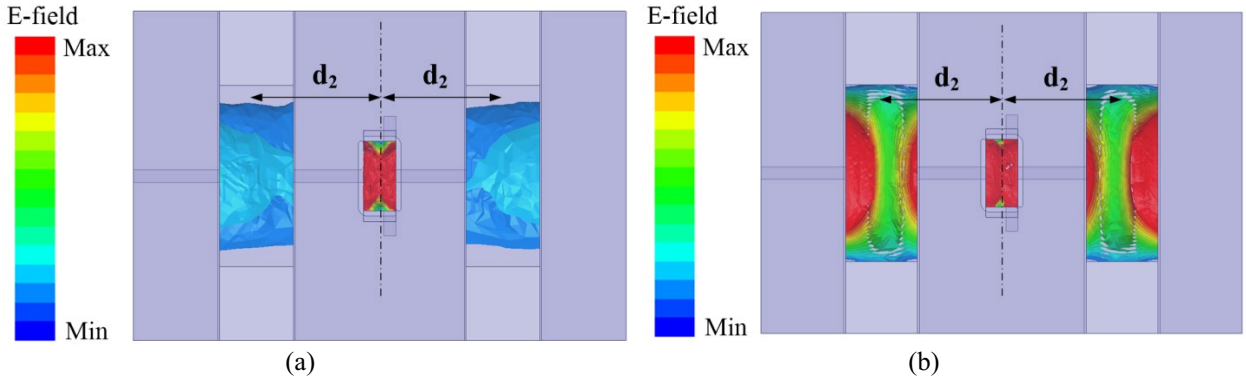

(a) (b)

Fig. 5.4. Electric field distribution inside cavity with second pair of grooves for the proposed antenna at frequency of, (a) 10.1 GHz and (b) 12.45 GHz.

The fabricated antenna along with its corresponding reflection coefficient is shown in Fig. 5.5. All layers are shown separately to illustrate the ease of PCB fabrication process. The measurement result shows a dual impedance bandwidth of nearly 9.89-10.16 GHz and 12.08-12.31 GHz for $|S_{11}| < -10$ dB which corresponds to the bandwidths of 2.7% and 1.9% for the lower and upper bands, respectively. The simulated and measured radiation patterns of the antenna for the measured operating frequencies of 10 and 12.18 GHz are shown in Fig. 5.6 and Fig. 5.7, respectively. As shown in Fig. 5.6Fig. 5.6 for 10 GHz, the antenna is more directional in H-plane than E-plane as explained by field distribution analysis. The measured half-power beamwidth of E- and H-plane are almost 42^{o} and the measured side-lobe-level of H-plane is nearly -14 dB. The measured cross-polarization level in the 3-dB beamwidth is at least 22 dB below the co-polarization

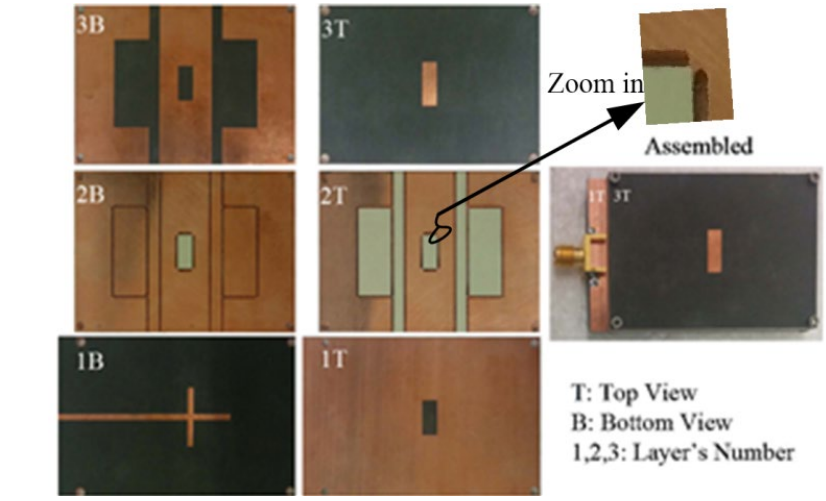

(a)

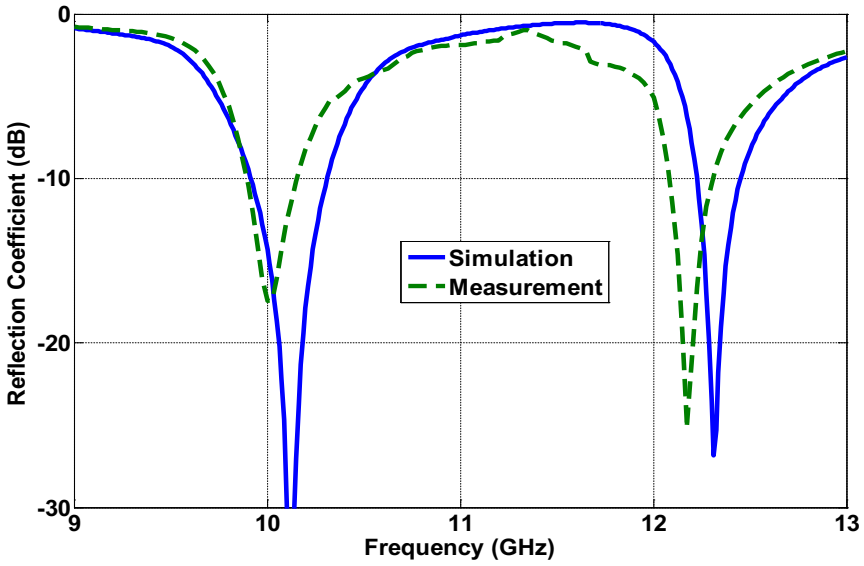

(b)

Fig. 5.5. (a) Fabricated antenna, and (b) its corresponding reflection coefficient [44].

in the E-plane and almost 29 dB below the co-polarization in the H-plane which indicate a perfect linear polarization at 10 GHz.

Fig. 5.7 shows the radiation pattern at second resonance. It shows that E-plane becomes more directional than H-plane as explained in terms of field distribution inside the grooves. The measured half-power beamwidth of E- and H-planes is 31° and 56° respectively. The side-lobe-level of E-plane is about -6 dB which is larger than the lower band. The measured cross-

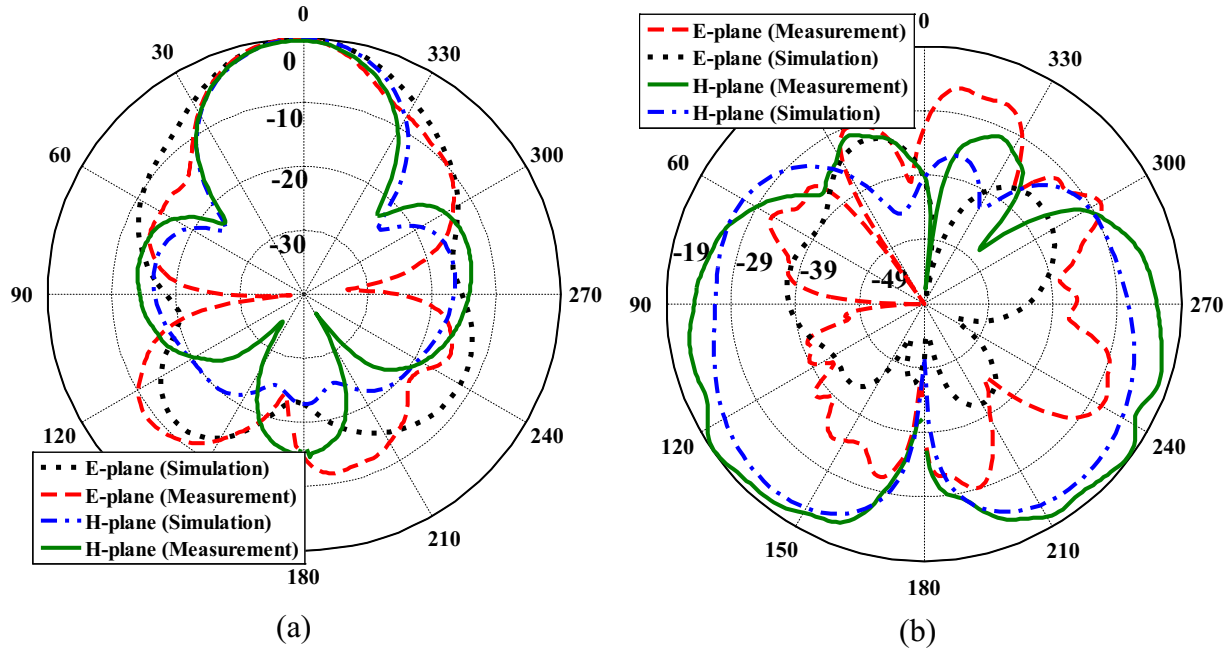

(a) (b)

Fig. 5.6. Radiation patterns of the antenna at 10 GHz, (a) Co-polarization, (b) Cross-polarization.

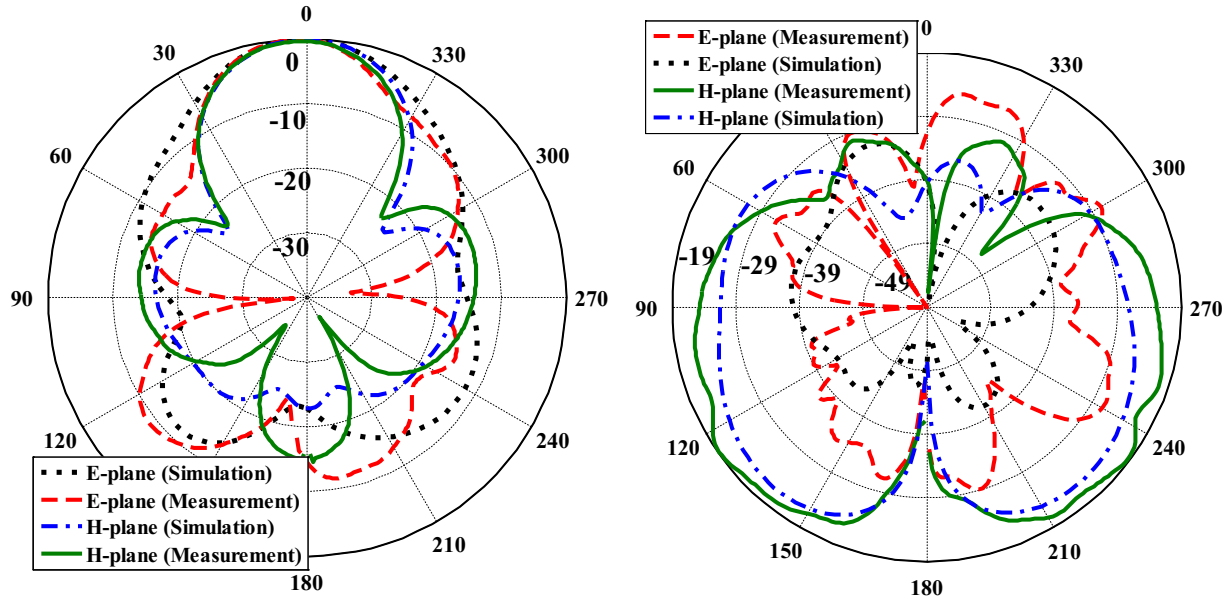

(a) (b)

Fig. 5.7. Radiation patterns of the antenna at 10 GHz, (a) Co-polarization, (b) Cross-polarization.

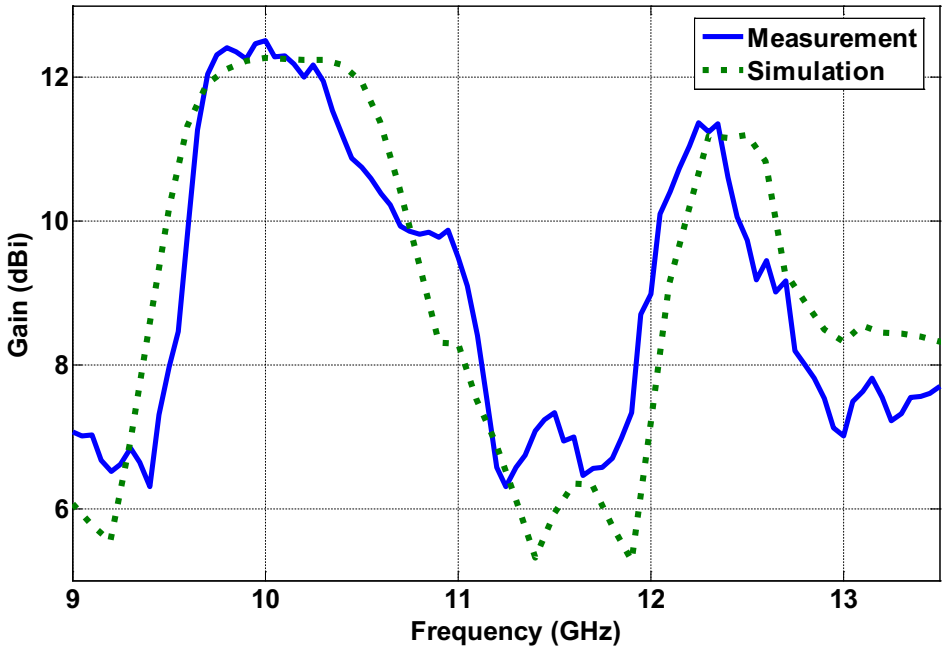

Fig. 5.8. Gain of the proposed antenna versus frequency.

polarizations of E- and H-planes in 3-dB beamwidth are about 32 and 17 dB below co-polarizations of E- and H-planes, respectively, which indicates the polarization is purely linear. As discussed before and confirmed by measurement here, the antenna is directional in H-plane at the lower band (10 GHz) because of high field intensity at the edges of the first pair of grooves (lateral effect of in-phase superposition of electric field); however, it is directional in E- plane at the upper band (12.18 GHz) due to high field intensity at the middle of the second pair of grooves (longitudinal effect of in-phase superposition of electric field). The antenna gain has been calculated and measured as shown in Fig. 5.8. The measured gain of the antenna at 10 and 12.18 GHz are 12.5 and 11.3 dBi, respectively. The proposed dual-band antenna has one effective groove for each band.

Although the proposed antenna provides dual-band feature with a planar corrugated geometry, it suffers from feeds' back radiation. Furthermore, it is very difficult to obtain more gain by adding more grooves to the structure. In what follows, we propose another corrugated antenna which could solve these problems.

5.2 Dual-Band High-Gain Corrugated Antenna with a Cavity-Backed Feed Structure

As previously analyzed in chapter 4, corrugations with different periodicity and height provide different resonant frequencies. Therefore, by proper design of two different periodic corrugations, a dual-band operation over desired frequencies is obtained. In this section, a 2D dual-band antenna is designed on laminate boards for the center frequencies of 9.7 GHz and 13.85 GHz for the application of satellite and space communications. In order to prevent back radiation, a cavity-backed feed structure is integrated with the corrugated structure.

The proposed corrugated antenna structure is shown in Fig. 5.9. The antenna consists of two different ring-shaped (bulls'-eye) corrugations and a cavity, all realized on laminate substrates. Creating two different perodic corrugations (first corrugations, and second corrugations as shown in Fig. 5.9) can provide two different bands. As shown, the larger corrugations which creates the lower band are etched and realized by vias on both substrates 1 and 2. However, the smaller corrugations are made by only substrate 2. The top substrate (Sub. 3) is used for miniaturization purposes and does not play any other roles. For further miniaturization, with the theory discussed earlier, the substrates 1 and 2 are selected to be Rogers TMM4. To obtain the desired resonant frequencies of 9.7 GHz and 13.85 GHz, the thicknesses of substrates 1 and 2 are required to be selected properly. We have used only three corrugations for each frequency band in this work; however, if more gain is required, more corrugations need to be used. The corrugations are realized by creating vias or through-driling walls which are metallized afterward. The antenna is fed from inside the cavity by any feeder antenna which can produce a TE_{11}-shaped field distribution on the opeing slot over the cavity.

5.2.1 Integrated Dual-Band Feeders

To make the overall antenna as compact as possible, a feeder is required to be integrated in center of the corrugated structure. A wideband antenna that covers both bands can be used as feeder antenna. However, to prevent the intermediate frequencies from radiation and suppress

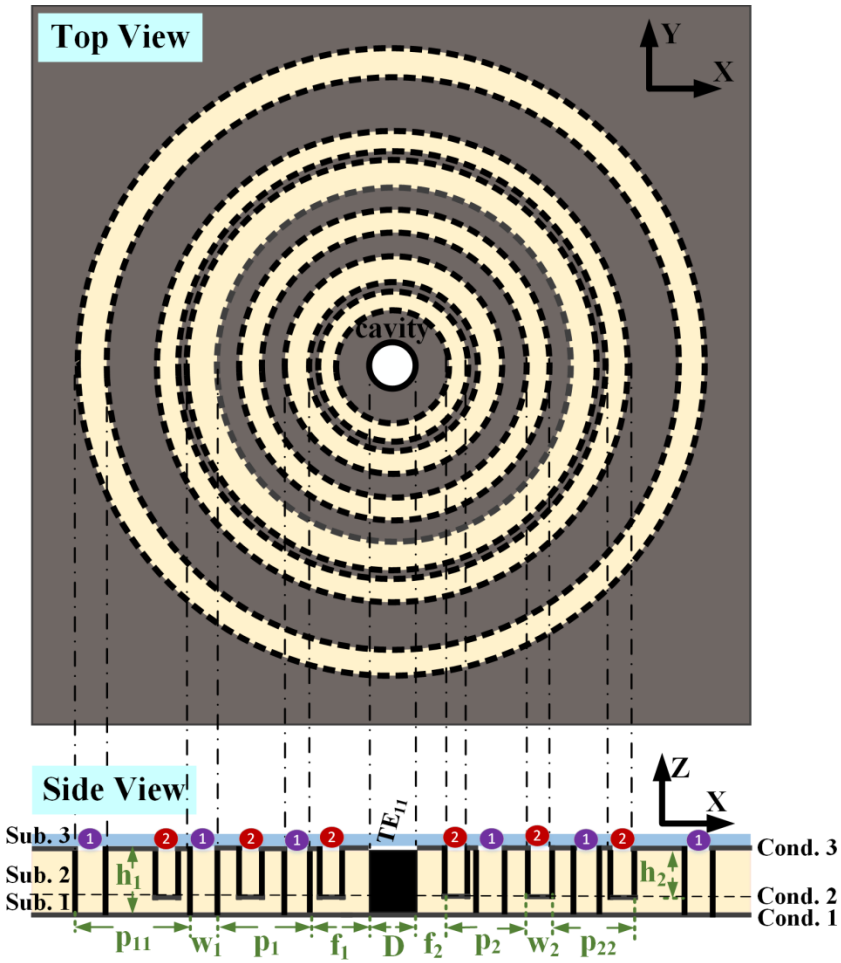

Fig. 5.9. Top and side views of the proposed dual-band corrugated antenna.

them better, a dual-band feeder is a better choice. The feeder needs to be composed of a central aperture that feeds the corrugated structure. In fact, a dual-band open-ended waveguide (OEW) feeder is required. In order to be compatible with the proposed dual-band corrugated structure, as a requirement for compactness, the feeder and corrugated structure in Fig. 5.9 must be designed on the same layers.

Although different configurations of slot and patch antennas along with probe can be found for the design of feeder as in [110], these feed structures provide a null at broadside if they are used as feeder for the proposed dual-band corrugated structure. They produce TM_{01} mode which

is symmetric around the center and since the proposed corrugated structure is symmetric, their integration generates a null at broadside. To overcome this issue, and also miniaturize the antenna and provide high power-handling capability, a collinear end-launcher transition type from coaxial cable to the feeder is chosen [111]. To the best of our knowledge, feeder antennas with these features have not been reported yet.

An exploded view of the proposed antenna configurations is shown in Fig. 5.10 [112]. Both antennas A and B consist of three substrate layers with the details listed in TABLE 5.1. For size reduction, the permittivity of substrates 1 and 2 is selected to be relatively high. For both antennas, the feed structure is designed in substrate 1 and also the OEW is embedded in the substrate 2. The third substrate has been added for size reduction.

The geometry of antenna A consists of two circular-waveguide structures in substrates 1 and 2 with different radii, a resonator structure etched on conductor 2 in Fig. 5.11(a) and a via connecting the inner conductor of coaxial cable to the body of the waveguides. The via with diameter *D* is offset from the center of the waveguide by the distance labeled *off* in Fig. 5.11(a). Also, the output aperture etched on conductor 1 is designed to be 4.4 mm; the same size of the outer diameter of the coaxial cable which feeds the antenna. The structure is inspired by conventional collinear end-launchers; however, the resonator structure and waveguides with different radii make the structure dual-band.

Antenna B is composed of two radial cavities with different radii embedded in substrate 1, a circular waveguide in substrate 2, and a cylindrical post in the center of the cavities as shown in Fig. 5.11(b). The post with a diameter of *D* is at the center of the waveguide. The inner conductor of the input coaxial cable is connected to the cylindrical post. The outer diameter of the coaxial cable and the output aperture etched on conductor 1 are 4.4 mm.

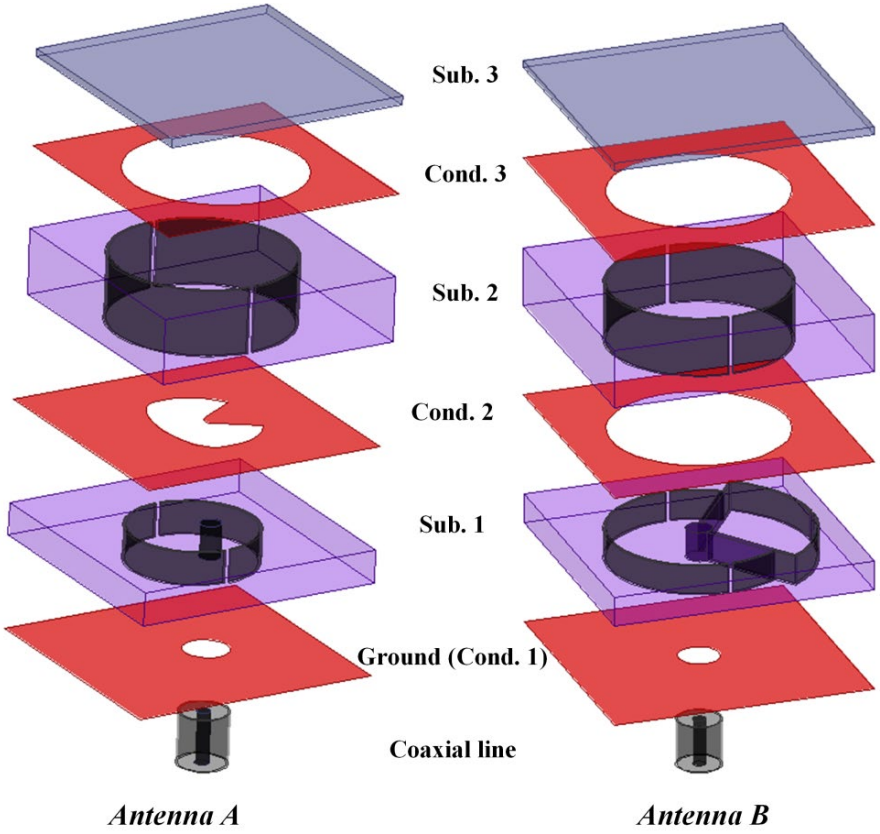

Fig. 5.10. Exploded view of the two proposed feeder antenna configurations with all substrate layers.

TABLE 5.1
Substrate Information of the Proposed Antennas

Antenna #1	**Substrate 1**	**Substrate 2**	**Substrate 3**
Material	Rogers TMM4	Rogers TMM4	Rogers 4003
Thickness	3.175 mm	6.35 mm	0.81 mm
Antenna #2	**Substrate 1**	**Substrate 2**	**Substrate 3**
Material	Rogers TMM4	Rogers TMM4	Rogers TMM4
Thickness	3. 175 mm	6.35 mm	0.51 mm

Material	**Permittivity**	**Loss tangent**
Rogers TMM4	4.5	0.002
Rogers 4003	3.55	0.0027

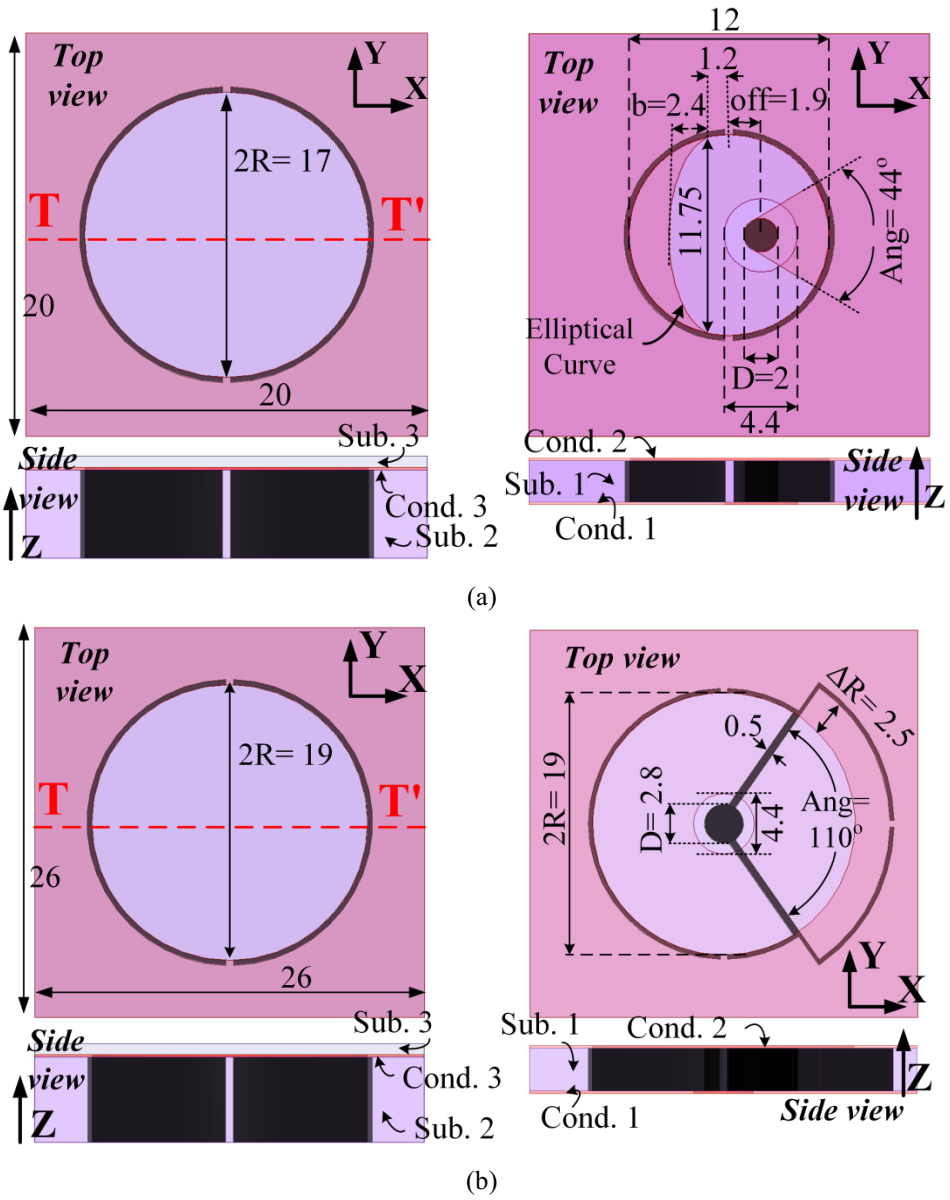

Fig. 5.11. The top and side views of the substrates 1 and 2 along with the dimensions for (a) Antenna A and (b) Antenna B (All dimensions are in mm).

5.2.1.1 Feeding Mechanism

Generally, the collinear end-launcher transitions can be used to provide stable gain and handle higher power due to being connected to ground, making a great heat pathway. However,

they have bulky and lengthy structures, higher reflection and narrower bandwidth. In the proposed antennas, the collinear end-launcher transition type is mainly chosen due to the collinearity enforced by feeder design constraint. The proposed antennas are fed from the bottom (substrate 1) using a coaxial cable similar to collinear end-launchers.

5.2.1.2 Cavity-Backed Dual-Band Resonators

Using a cavity-backed patch antenna as a transition can solve the problem of the lengthy structures of collinear end-launchers and mode converters and convert the TEM mode of coaxial cable to the fundamental mode of the waveguide [113]. In this case, the patch fed by the coaxial cable radiates into the waveguide so as to excite its fundamental mode [114] that provides a stable gain in a single frequency band. Since the substrates' thickness which can be adjusted by proper design of patch antenna determines the length of the structure, this transition can be significantly short. The stacked structure of this patch transition was also reported which increases the operational bandwidth and eases the matching by tuning more resonant elements [115]. However, the stacked patches in cavity-backed configuration cannot provide a tunable dual-band and high power-handling operations. However, resonator structures in cavity-backed configuration as used in the proposed antennas can create two adjustable resonances in both antennas for dual-band operation.

Fig. 5.12 and Fig. 5.13 demonstrate the dual-band operation of the proposed antenna structures. As shown in Fig. 5.12 for antenna A, the current path is on the element containing the elliptical curve at the first resonant frequency and on the loop with the radial arm at the second resonant frequency. Therefore, it is expected that these curve and loop features have the greatest effects on the first and second resonant frequencies, respectively. Similarly, as shown in Fig. 5.13 for antenna B, the current path for the first and second resonant frequencies is inside the cylindrical cavities with larger and smaller radii, respectively. Hence, the radii of two cylindrical cavities are expected to determine the first and second resonant frequencies.

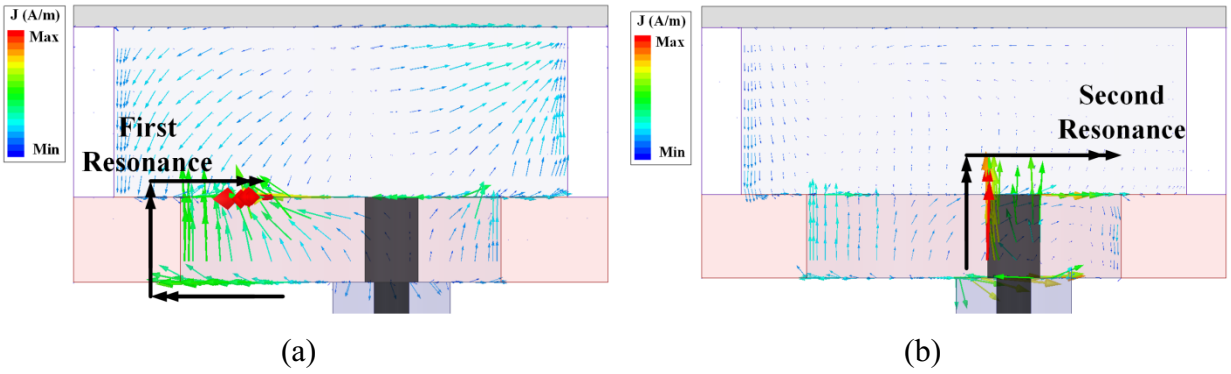

Fig. 5.12. The electric-current distribution of the antennas A at the sectional cut AA' for (a) the first and (b) the second resonant frequencies.

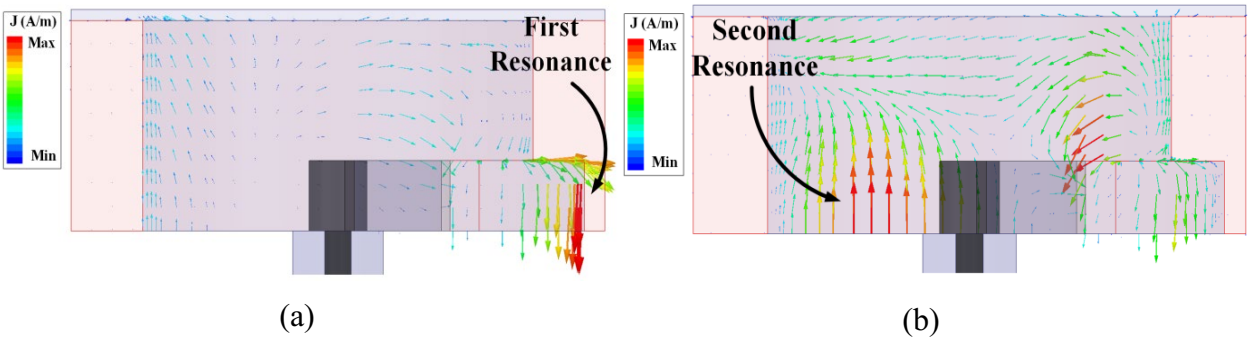

Fig. 5.13. The electric-current distribution of the antennas B at the sectional cut AA' for (a) the first and (b) the second resonant frequencies.

5.2.1.3 Broadside Radiation Patterns

To have a stable broadside gain in both bands, the modes produced inside the structure and produced on its output aperture of the waveguide (conductor 3) must radiate constructively at broadside. This can be done by looking at the field distribution of the proposed antennas. The field distribution on the output aperture of the circular waveguide is expected to include many modes such as TE_{11}, TM_{01}, and TE_{21}. Among those modes, only the TE_{11} mode creates a broadside pattern. Therefore, for a fairly stable radiation pattern, the overall field distribution pattern should be as close to the TE_{11}-mode field distribution as possible. The proposed antennas can provide such a field distribution in both bands, as shown in Fig. 5.14. It is evident that the field distribution over the output aperture for the first and second bands in both antennas A and B is constructive

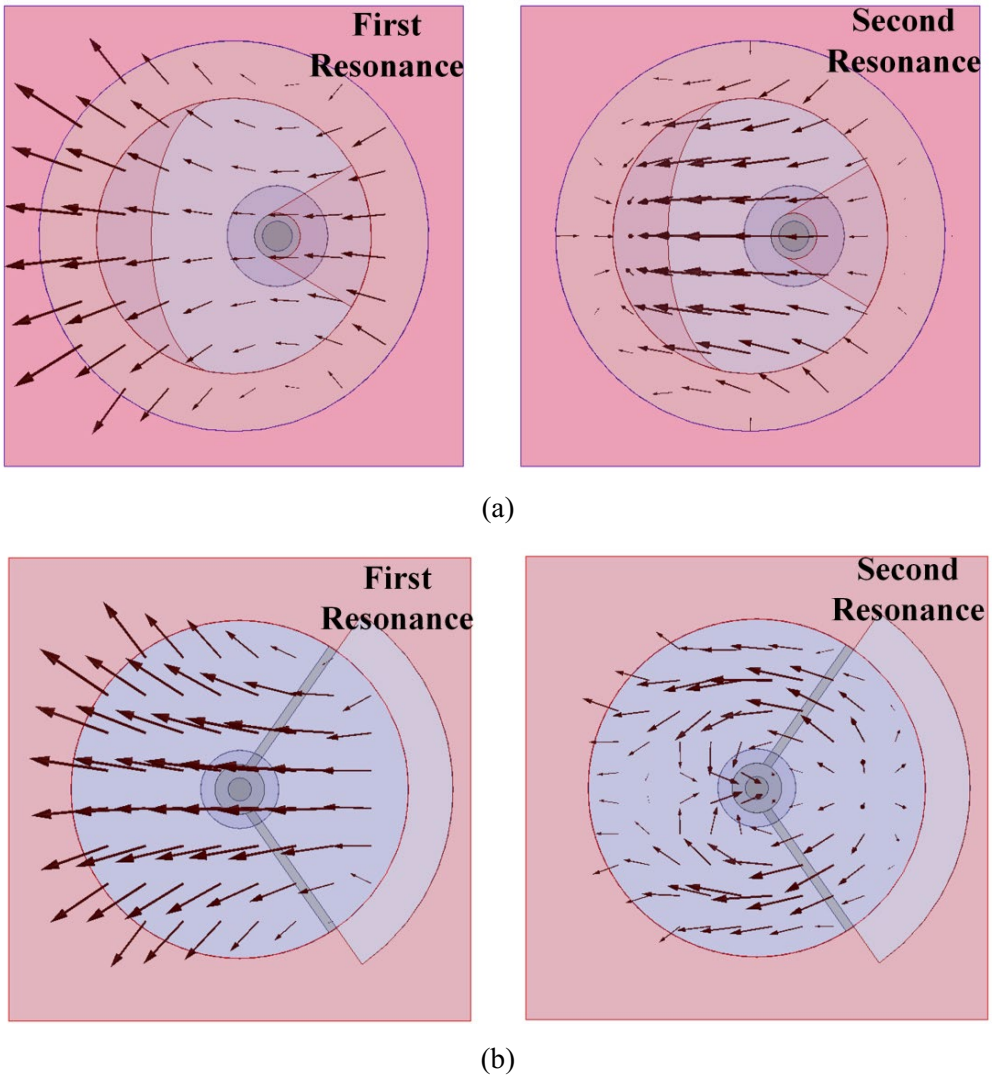

Fig. 5.14. Field distribution on the output aperture of the antennas for the first and second bands, (a) Antenna A, and (b) Antenna B.

and close to the TE_{11} mode which implies that the proposed structures are capable of providing a broadside pattern in the bands of interest. It is worth mentioning that for the upper band, the number of excited modes is more, and hence achieving a stable gain over the upper band is more difficult.

5.2.1.4 Parametric Study

There are some important parameters in designing the proposed dual-band feeder antennas. We briefly discuss those parameters here. For antenna A, by selecting the radii of the waveguides and the shape of conductor 2 appropriately, two resonances can be found and adjusted to desired frequencies. Parameter *b,* as shown in Fig. 5.15, can adjust the first band relative to the second band. By changing *b* from 1.55 mm to 2.7 mm, the first resonance shifts around 1.3 GHz from 8.9 GHz to 10.2 GHz. With a shift in resonant frequency of the first band, the associated antenna gain will not degrade. As shown in Fig. 5.15, the $|S_{11}|$ and antenna gain for the second band shifts slightly. As a result, we can adjust both bands with respect to each other. On the other hand, the second band can be adjusted by the via offset (the parameter *off*) from the center of the circular waveguide, since as demonstrated in Fig. 5.12(b), it affects the path of the electric current at the second resonant frequency. Also, the $|S_{11}|$ and gain at both bands can be adjusted by the parameters *D* and *Ang*, respectively.

For antenna B, the most important parameters which have detrimental effects on the resonant frequencies are the radii of two cavities (i.e. *R* and $R+\Delta R$). The effect of parameter *R* on the $|S_{11}|$ and antenna gain is shown in Fig. 5.16. With an increase in *R* from 8.5 mm to 10 mm, the first and second resonant frequencies shift from 9.9 GHz to 9.4 GHz and 16 GHz to 14.25 GHz, respectively, which shows that the second resonance is affected more. It is worth noting that with a shift in resonant frequencies, the antenna gain shifts accordingly so that we have a gain of more than 5 dBi over the bands of interest. On the other hand, the parameter ΔR adjusts the first resonant frequency as demonstrated in Fig. 5.13(a) by electric-current distribution. Therefore, the desired bands can be tuned by adjusting *R* and ΔR. Also, the antenna matching can be adjusted by two parameters of *Ang* and *D.*

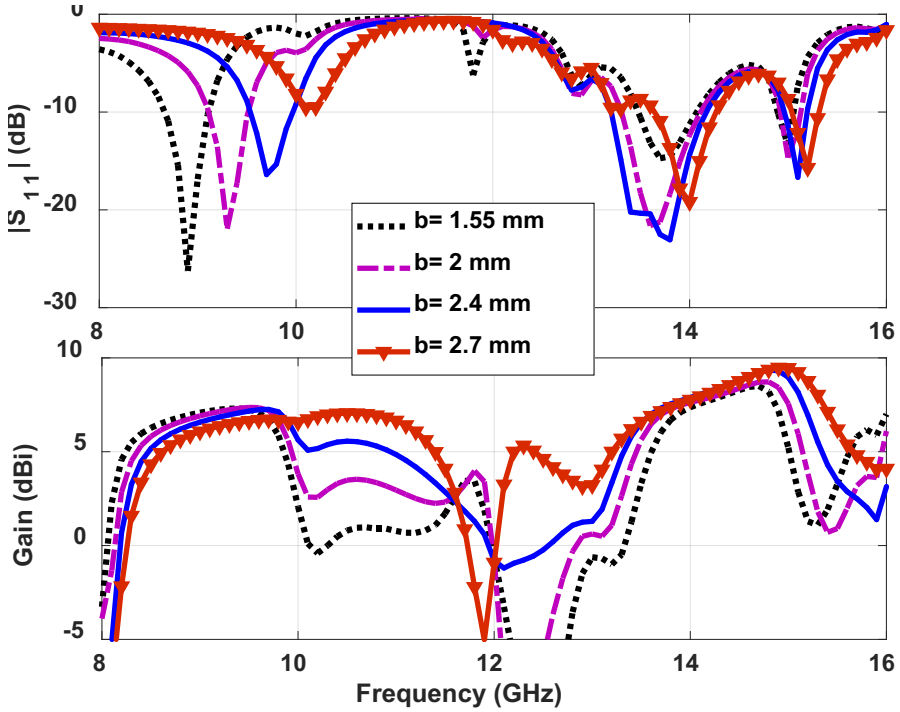

Fig. 5.15. Antenna matching and gain versus frequency for different values of parameter *b* of antenna A.

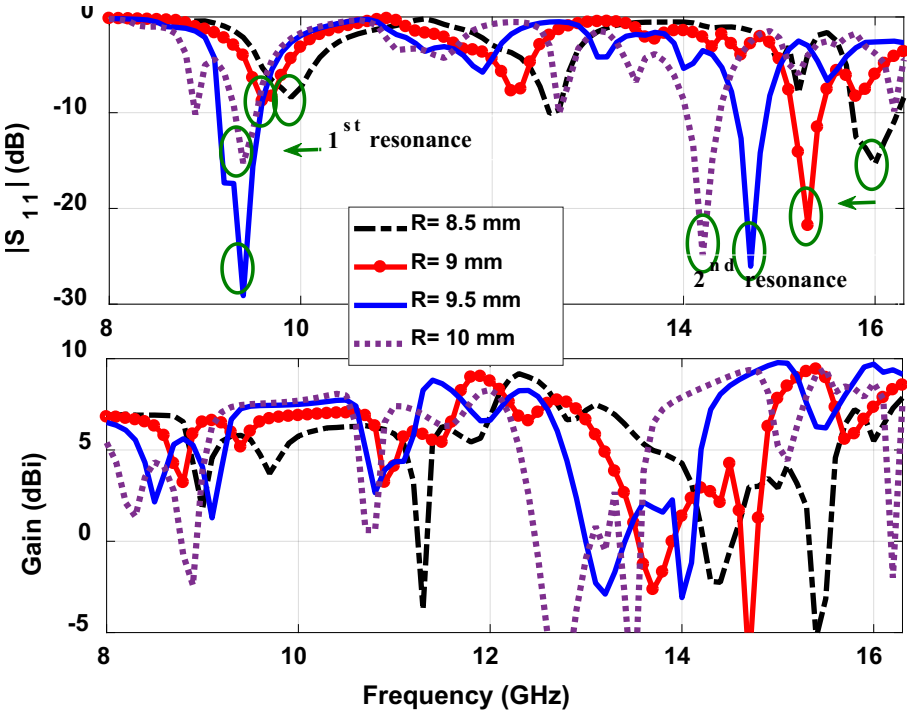

Fig. 5.16. Antenna matching and gain versus frequency for different values of parameter *R* of antenna B.

5.2.1.5 Measurement Results and Discussion

Depending on the kind of feeder or the selected application of the proposed antennas, the thickness of substrate 2 (and therefore, the length of the corresponding open-ended waveguide) may vary. However, by optimizing the important parameters previously introduced, the antennas can be redesigned for the desired bands. In our work, the thickness of substrate 2 of both antennas is chosen to be 6.35 mm and based on that, the antennas are designed and optimized by Ansys HFSS and fabricated using through-drilling inside the substrates. The through-drilling walls, vias and cavities are metallized and then filled out by copper tape and conductive paste. It should be noted that the vias are filled out with conductive paste when the SMA connectors are attached. This adds a small amount of loss to the antennas and may modestly decrease the antenna radiation efficiency. Finally, all substrates are glued together and assembled to create the proposed antenna structures. The 3D views of fabricated antennas are indicated in Fig. 5.17. The simulated and measured $|S_{11}|$ of antennas A and B are depicted in Fig. 5.18, which shows the anticipated dual-band operation. The measurement result indicates impedance bandwidths of 9.43-9.85 GHz and 13.17-14.45 GHz for $|S_{11}| < -10$ dB for antenna A, which corresponds to a percentage bandwidth of 4.36% and 9.27% for the first and second bands, respectively. For antenna B, as depicted in Fig. 5.18(b), measured impedance bandwidths of 5.41% and 2.1% are achieved from 9.17 to 9.68 GHz for the lower band and from 14.64 to 14.95 GHz for the upper band, respectively. The measured $|S_{11}|$ in the first band achieves values up to 9.8 dB at 9.33 GHz due to the fabrication errors. For applications that need more bandwidth, antenna A is a better choice since it provides more bandwidth because of its resonator structure.

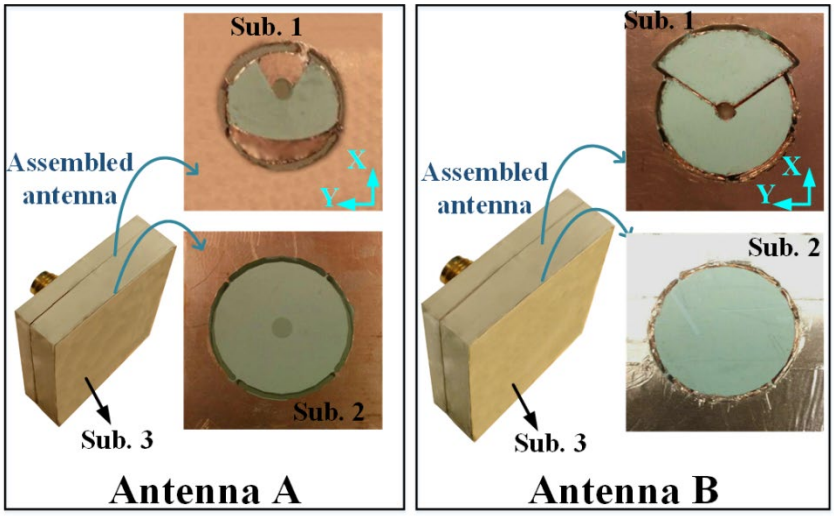

Fig. 5.17. The 3D view of the fabricated antennas.

The gains of the proposed antennas have been measured over the bands of interest, and are depicted with their corresponding simulation data in Fig. 5.18. The antennas under test are replaced by standard gain horn antennas for both bands to measure the antenna gain. In Fig. 5.18, the measured antenna gain at boresight versus frequency is discretely plotted at 0.2 GHz intervals over the bands of interest for both fabricated antennas. It should be noted that to plot the measured antenna gain, the measured $|S_{11}|$ is de-embedded from the antenna realized gain data. For antenna A, the measured minimum and maximum antenna gains are 6.6 and 8 dBi over the first band and 3 and 9.2 dBi over the second band, respectively. These values for antenna B are 3.3 and 7.8 dBi over the first band and 7.5 and 9.2 dBi over the second band, respectively. Although the trends of the measured antenna gain closely follow the simulated gain data, discrepancies may be attributed to tolerances in the complex fabrication process. It is worth mentioning that the simulated efficiencies for antenna A are more than 86% and 85%, and for antenna B more than 87% and 85% over the first and second bands, respectively.

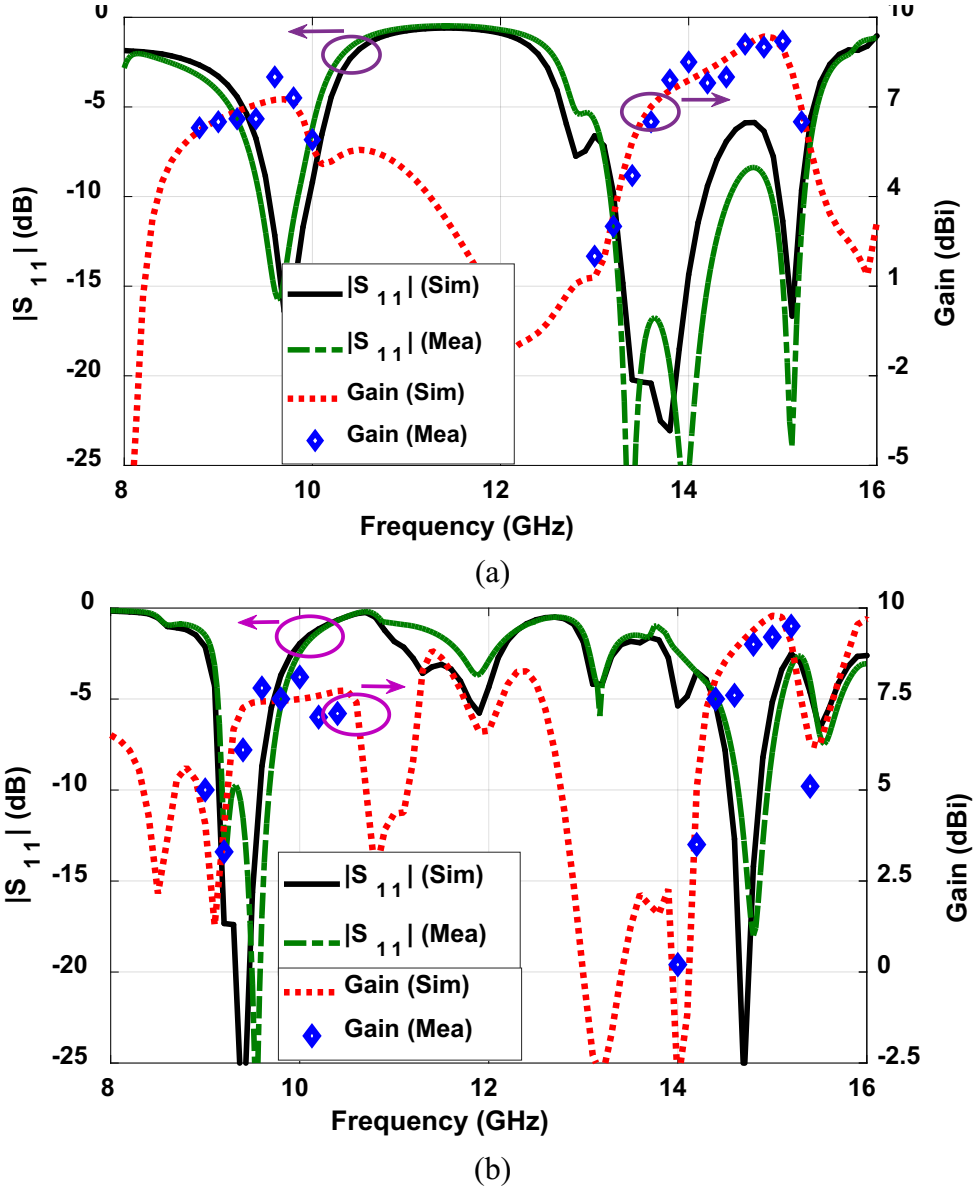

Fig. 5.18. Simulation and measurement results of $|S_{11}|$ and gain for, (a) antenna A, and (b) antenna B.

Fig. 5.19 shows the simulated and measured radiation patterns of antenna A at both orthogonal planes (i. e. YoZ or E-plane and XoZ or H-plane) for the center frequencies of 9.6 and 13.8 GHz within the bands of interest. The measured half-power beamwidths are 71° and 70° at 9.6 GHz and 66° and 72° at 13.8 GHz for E- and H-planes, respectively. As shown in Fig. 5.19(a), the measured cross-polarization levels of E- and H-planes (within the 3-dB beamwidth) are at least

16.5 dB below the co-polarizations at 9.6 GHz which states the extreme linearity of polarization of the antenna at this frequency. However, at a frequency of 13.8 GHz, cross-polarization in E-plane increases when we exceed θ=25^o. Therefore, for angles greater than 25^o, the polarization purity is worsened.

Fig. 5.20 demonstrates the radiation pattern of antenna B at the E- and H-planes for the center frequencies of both bands. The measured half-power beamwidths for the E- and H-planes at 9.4 GHz are 70^o and 68^o, respectively; however, these values for E- and H-planes at 14.8 GHz are 58^o and 63^o respectively. As shown, for antenna B at 9.4 GHz, the measured cross-polarizations of the E- and H-planes (within 3-dB beamwidth) are about 10 and 34 dB below the co-polarizations of the E- and H-planes, respectively. Also, at 14.8 GHz, the cross-polarizations of the E- and H-planes (within the 3dB beamwidth) are at least 14 dB smaller than the corresponding co-polarization. Therefore, the antenna polarizations in both bands are strongly linear. As a result, although antenna B has a narrower bandwidth at the second band compared to antenna A, its polarization is more linear for higher θ. Both antennas are good candidates to be used in high-gain dual-band and high-power applications.

The amount of power the proposed antennas can handle depends on the electrical strength of the design medium. The medium in the proposed antennas is TMM4 Rogers substrate which has an electrical strength of 2.56×10^7 V/m [21]. For a 1 MW input power, the maximum electric field inside the structure of antenna A is 2.73×10^7 V/m and 1.68×10^7 V/m at the first and second resonant frequencies and this amount for antenna B is 1.24×10^7 V/m, and 1.2×10^7 V/m, respectively. Therefore, the proposed antennas can handle on the order of 1 MW input power. This shows that these antennas can be used in high-power applications.

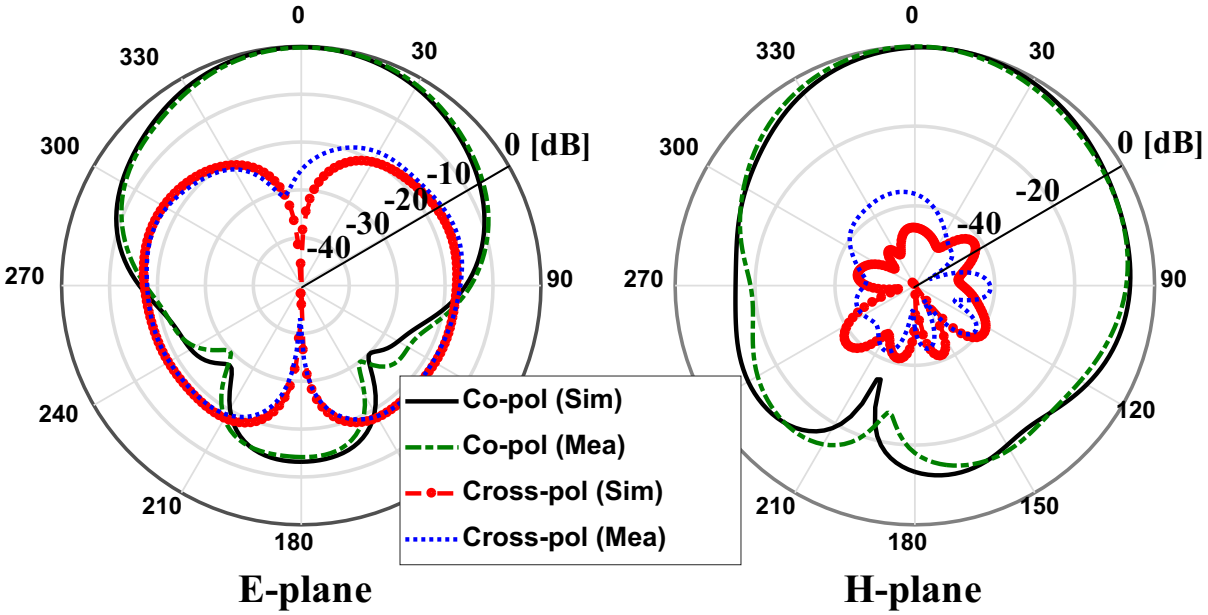

(a)

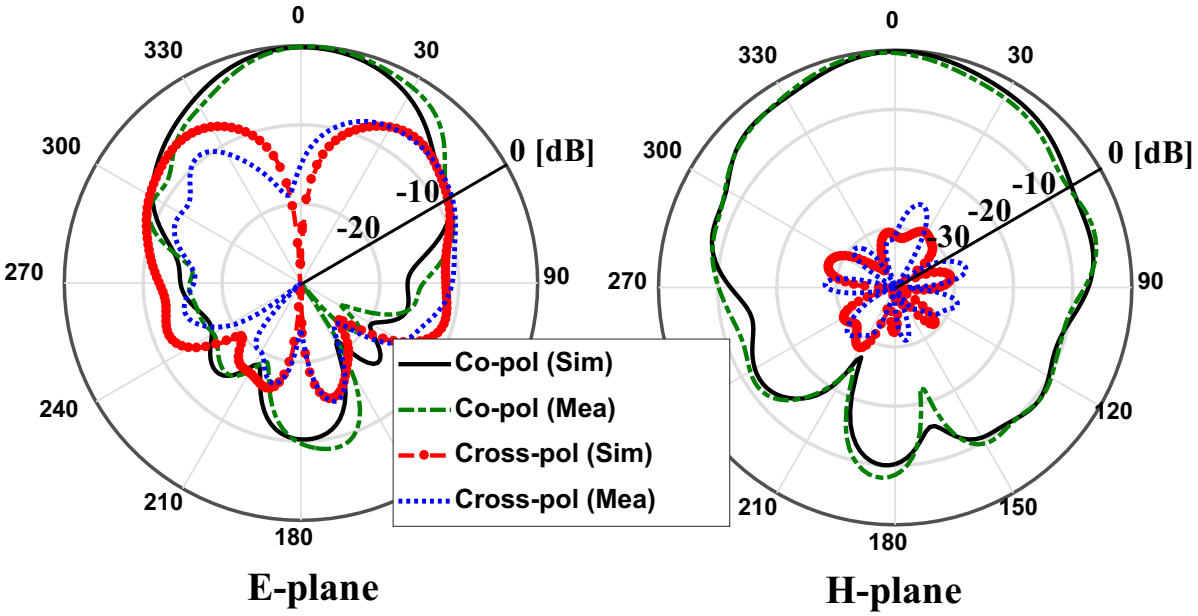

(b)

Fig. 5.19. Radiation pattern of antenna A in E- and H-planes at (a) 9.6 GHz, and (b) 13.8 GHz.

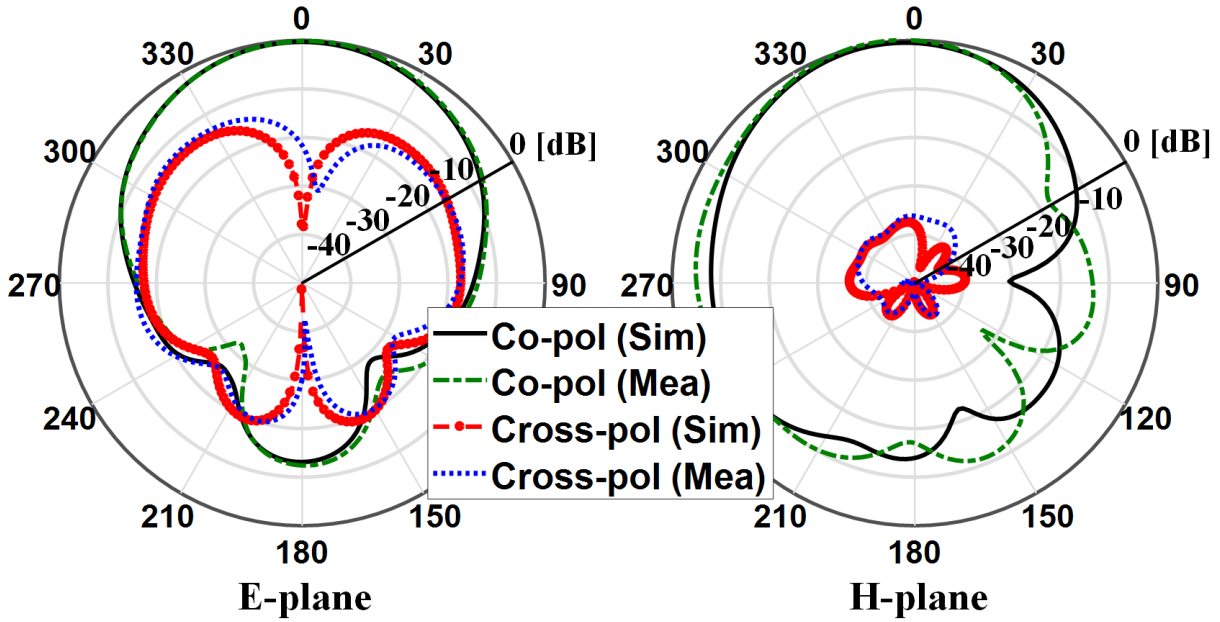

(a)

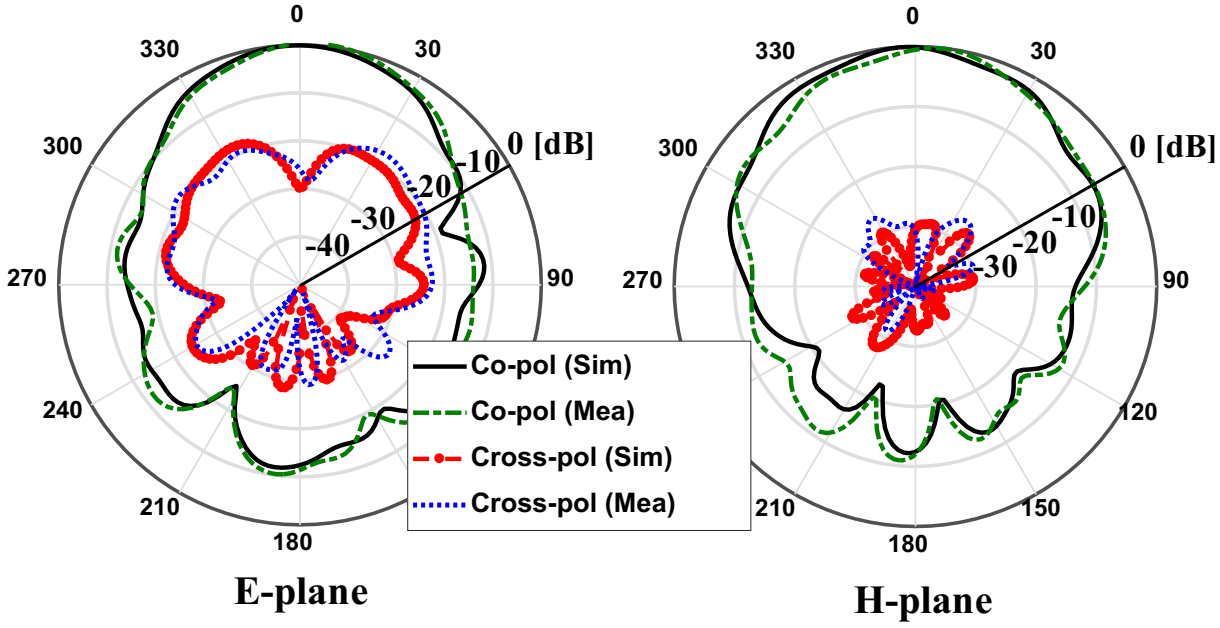

(b)

Fig. 5.20. Radiation pattern of antenna B in E- and H-planes at (a) 9.4 GHz, and (b) 14.8 GHz.

5.2.2 Study of the Resonance Condition for Corrugated Structures with Anti-Resonance

For ease of fabrication, structures' planarity, and integration, it is desired that both corrugated structure and feeder antennas (designed in the previous section) are designed and fabricated on the same substrates. As demonstrated in chapter 4, the resonance condition of corrugated structure happens when the corrugation susceptance becomes zero (i.e. $\overline{Y}(w,h,p,\varepsilon_r,k_{0,r})=0$). In all case studies in chapter 4, in the resonance condition, the height of corrugations is less than a quarter of effective wavelength of material inside corrugations. However, the height of the dual-band feeder antennas A and B is higher than a half of effective wavelength of substrates. In this section, it is shown that the resonance condition of corrugated structures happens around both the height of a quarter wavelength and three-quarter wavelength.

Fig. 5.21 demonstrates the normalized corrugation susceptance of a unit-cell of the corrugated structure with parameters p= 22 mm, w= 5 mm, ε_r= 4.5. For a corrugations' height of h= 2.2 mm, the resonance happens at 12 GHz which corresponds to the effective wavelength of 11.8 mm. Therefore, the corrugations' height is $0.18\lambda_g$ where $\lambda_g = \lambda_0/(\varepsilon_r)^{0.5}$ is the effective wavelength inside corrugations. Note that f_λ is the frequency in which the structures' periodicity (p=22 mm) becomes the size of the free-space wavelength. Fig. 5.21 shows that increasing the corrugations' height from 2.2 mm to 5 mm shifts the resonance to lower frequencies. However, for the corrugations height more than $0.5\lambda_g$, an anti-resonance appears as labeled in Fig. 5.21 with $f_{\lambda_{g1}/2}$ and $f_{\lambda_{g2}/2}$ for the corrugations' height of 7 mm, and 9 mm, respectively. These anti-resonances happen exactly at the frequency in which $h= 0.5\lambda_g$. In these cases, the resonance happens for frequencies around three-quarter of effective wavelength. For instance, as shown in Fig. 5.21, the resonance for h= 9 mm occurs at 10.9 GHz. Now, the corrugated structure can be designed based on the resonance in structures with anti-resonance condition which allows integrating the feeder antennas in corrugated structure.

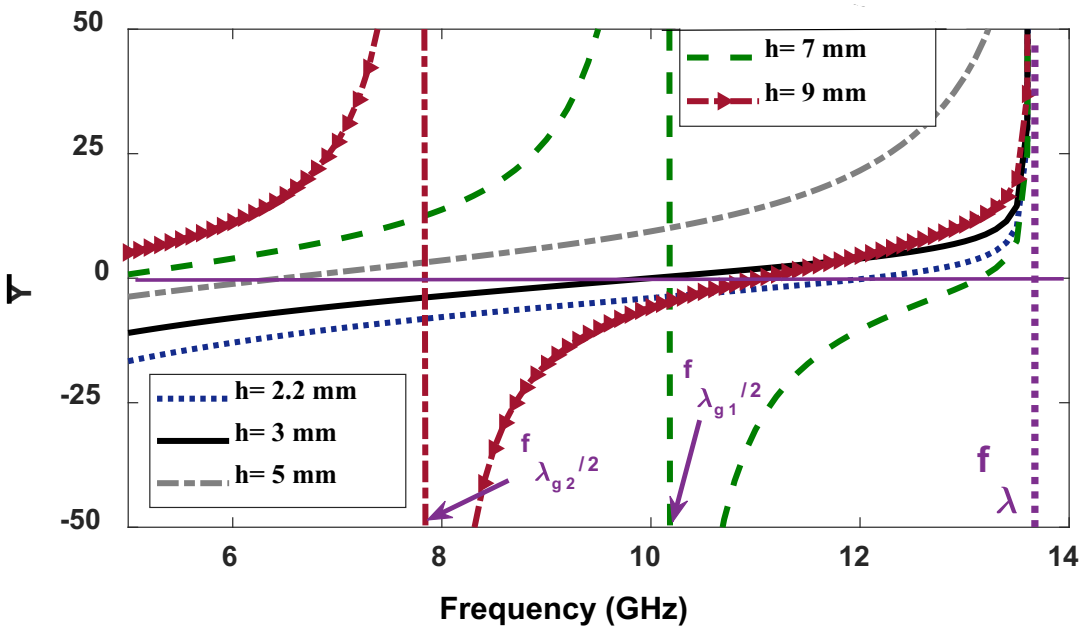

Fig. 5.21. Normalized corrugation susceptance of a unit-cell of the corrugated structure for different corrugations' height and p= 22 mm, ε_r= 4.5, w= 5 mm

To investigate the structures with anti-resonances, the resonance condition of corrugated antenna of Fig. 5.22 is parametrically studied when there is anti-resonance condition (i.e. the height of corrugations is bigger than a half wavelength). Similar to chapter 4, the effect of materials' permittivity, periodicity and the corrugations' height on normalized corrugation susceptance of the structure is explored. In Fig. 5.22, a circular cavity with a diameter of D is surrounded by 5 corrugations. The period of the corrugations is p and their width and height are labeled with w and h, respectively. The material inside the corrugations and cavity has a permittivity of ε_r. The distance between circular cavity and first corrugations is f which is needed to be adjusted for in-phase radiation of circular cavity and corrugations. In this parametric study, we take f= p+ 3mm, D= 12 mm, and w= 5 mm and we investigate the effect of p, h and ε_r on the antenna gain and normalized corrugation susceptance of a unit-cell of the structure.

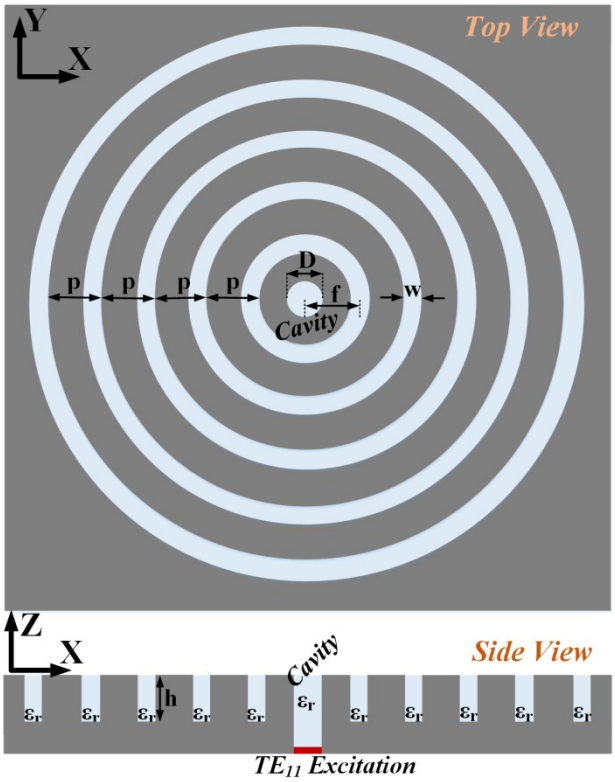

Fig. 5.22. Top and side views of the corrugated antenna under study.

Fig. 5.23 shows the antenna gain and normalized corrugation susceptance of a unit-cell of the antenna for different values of corrugation periodicity. As shown, the maximum antenna gain happens at resonance condition as predicted by (4.5). It should be mentioned that $f_{\lambda 1}$= 12 GHz and $f_{\lambda 2}$= 13.6 GHz in Fig. 5.23 show the frequency in which the structures' periodicity becomes the size of the free-space wavelength. The corrugated surface susceptance value is infinite at these points.

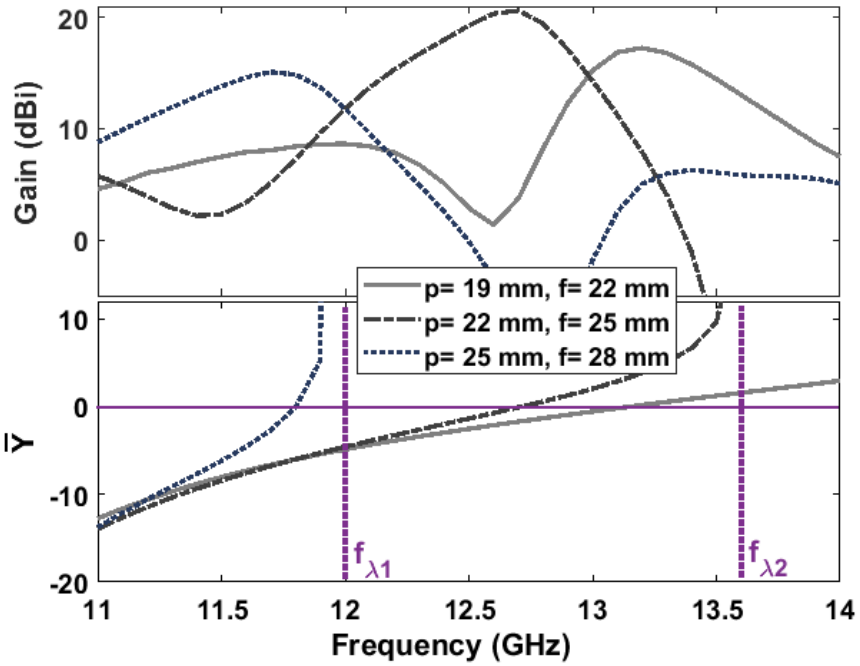

Fig. 5.23. Antenna gain and normalized corrugation susceptance of a unit-cell of the antenna versus frequency for different corrugation periodicity and ε_r= 4.5, h= 7.5 mm, w= 5 mm, D= 12 mm.

Fig. 5.24 shows the effect of different corrugations' height on the antenna gain and normalized corrugation susceptance of a unit-cell of the antenna. Similar to structures with $h< 0.5\lambda_g$ studied in chapter 4, increasing the height shifts the maximum antenna gain to lower frequencies. Fig. 5.25 demonstrates that using materials with higher permittivity inside corrugation shifts the resonant frequency toward lower frequencies. From Fig. 5.24 and Fig. 5.25, it can be inferred that to have a fixed resonant frequency and by selecting a martial with higher permittivity inside the corrugations, the corrugations' height needs to be reduced. After finding a desired resonant frequency, the corrugations' width must be optimized to achieve an optimum antenna gain.

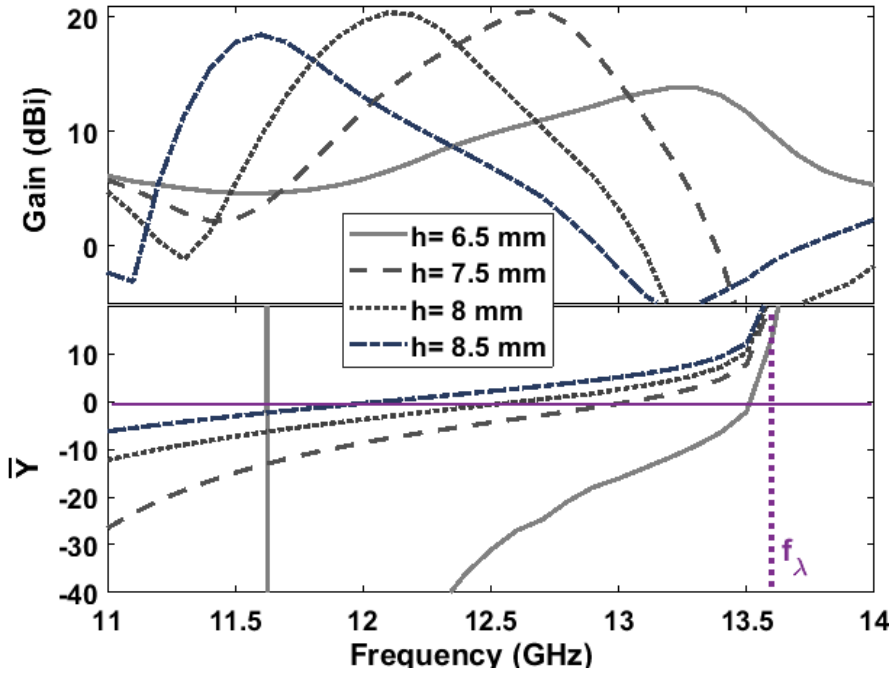

Fig. 5.24. Antenna gain and normalized corrugation susceptance of a unit-cell of the antenna versus frequency for different corrugations' height and p= 22 mm, ε_r= 4.5, w= 5 mm, D= 12 mm, f= 25 mm.

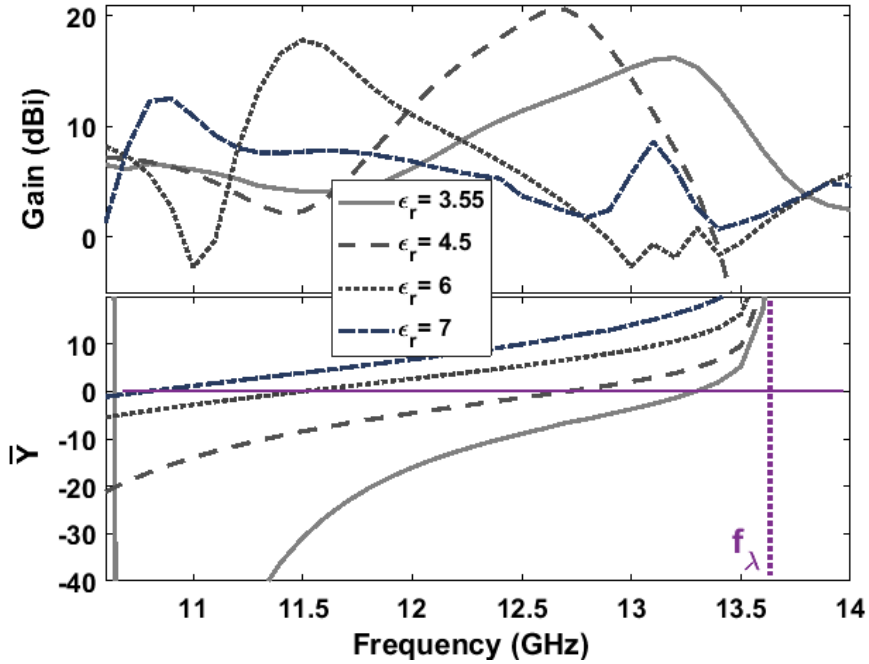

Fig. 5.25. Antenna gain and normalized corrugation susceptance of a unit-cell of the antenna versus frequency for different materials' permittivity and p= 22 mm, h= 7.5 mm, w= 5 mm, D= 12 mm, f= 25 mm.

5.2.3 Proposed Dual-Band corrugated Antenna

By integrating the designed feeder antenna A into the corrugated antenna structure in Fig. 5.9, the proposed compact dual-band corrugated antenna is finalized. Based on the unit-cell analysis, for the selected substrates with given thicknesses in TABLE 5.1, to have resonant frequencies of 9.7 GHz and 13.85 GHz (for satellite applications), the periodicity should be close to 25 mm and 20 mm, respectively. These values are the initial values for optimization. The dimensions of the antenna are optimized for having the maximum gain in both bands. TABLE 5.2 shows the optimum parameters of the proposed dual-band corrugated antenna.

Although the corrugations are responsible for the antenna radiation performance, they do not affect the reflection coefficient of the whole antenna much. This is shown in Fig. 5.26 where the effect of first corrugations and second corrugations alone and also all together is investigated on the reflection coefficient of the antenna. Due to minor effect of corrugation on the reflection coefficient, the feeder can be designed separately without considering the corrugations.

Fig. 5.27 depicts the effect of first and second corrugations alone and all together on the radiation gain of the antenna. As shown, the first and second corrugations alone (assuming $h_2 = 0$, and $h_1 = 0$ in Fig. 5.9) make the first and second resonant frequencies at 9.7 and 13.85 GHz, respectively. It is interesting that incorporating both corrugations will add up both resonances creating a dual-band corrugated antenna without any tangible shift in resonant frequencies.

As mentioned previously, the features of corrugations determine the resonant frequency and the width of corrugations changes the antenna gain and does not contribute to a change in resonant frequency. This can be seen in Fig. 5.28, where the antenna gain versus frequency has been plotted for different corrugations' widths. As shown, if the width of the corrugations is decreased to 3 mm for both first and second corrugations from their optimum values, a small shift in the first resonant frequency happens while the second resonant frequency stays unchanged. Also, the antenna gain drops to less than 1.5 dBi at both resonant frequencies. Using corrugations with smaller widths is necessary to avoid collision of first and second corrugations while more corrugations are required for having a better antenna gain.

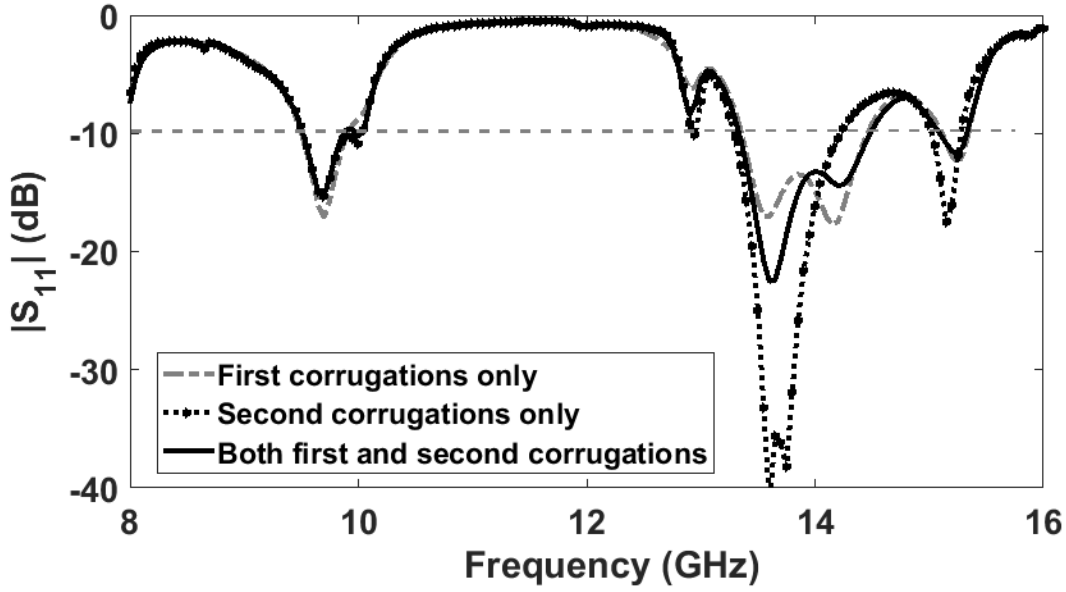

Fig. 5.26. Effect of first and second corrugations on the reflection coefficient of the proposed corrugated antenna.

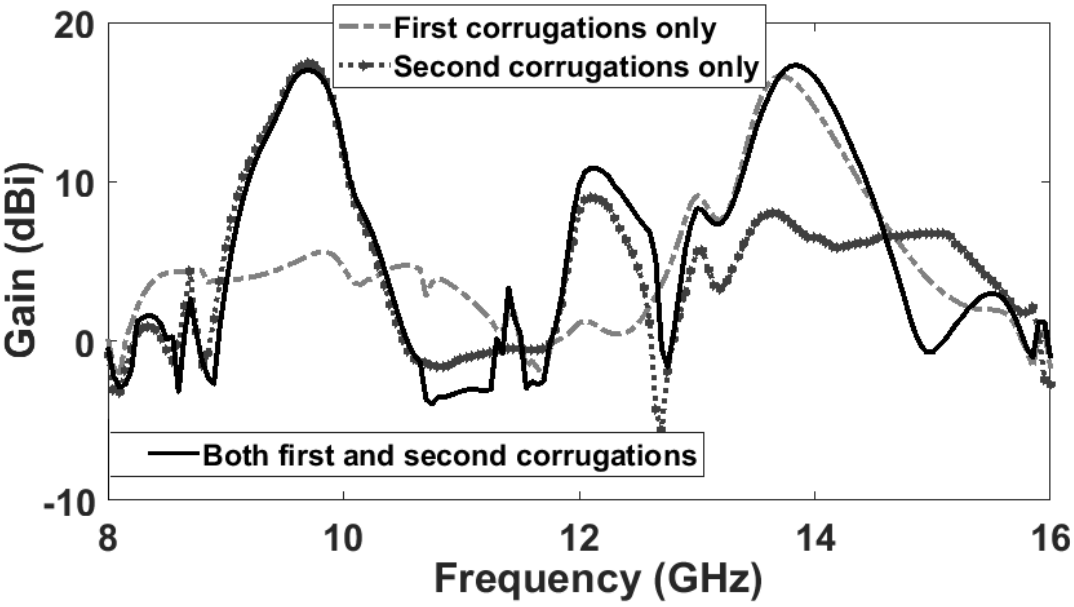

Fig. 5.27. Effect of first and second corrugateions on the radiation gain of the proposed corrugated antenna.

TABLE 5.2
Parameters of the Dual-Band Corrugated Antenna

w_1	h_1	p_1	p_{11}	w_2	h_2
9 mm	9.525 mm	23.5 mm	28 mm	7 mm	6.35 mm
p_2	p_{22}	f_1	f_2	D	
19	21.25 mm	17.5 mm	10 mm	17 mm	

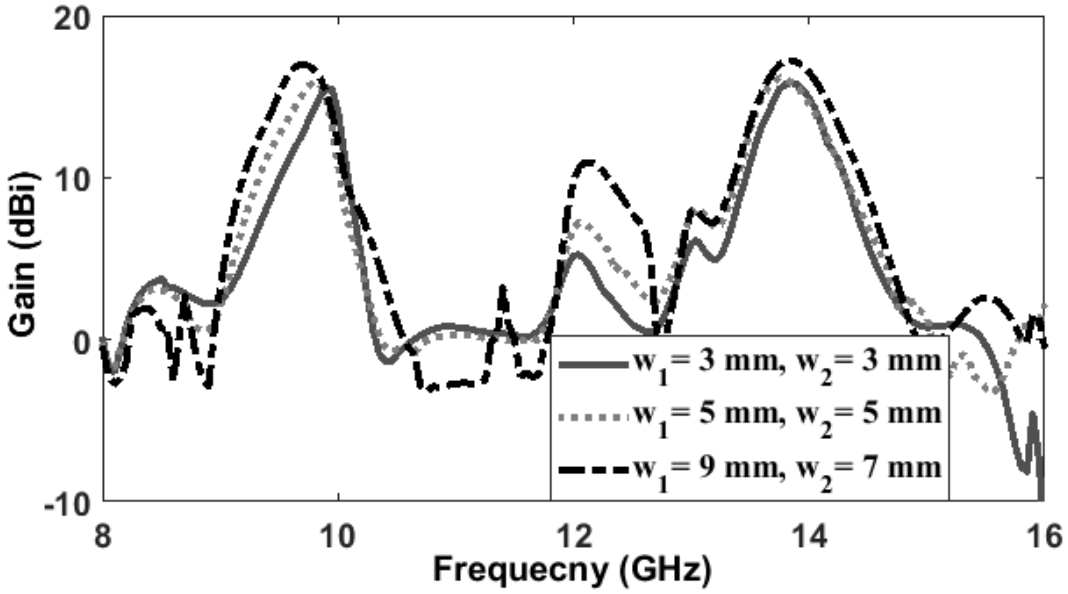

Fig. 5.28. Effect of width of the corrugations on the antenna gain.

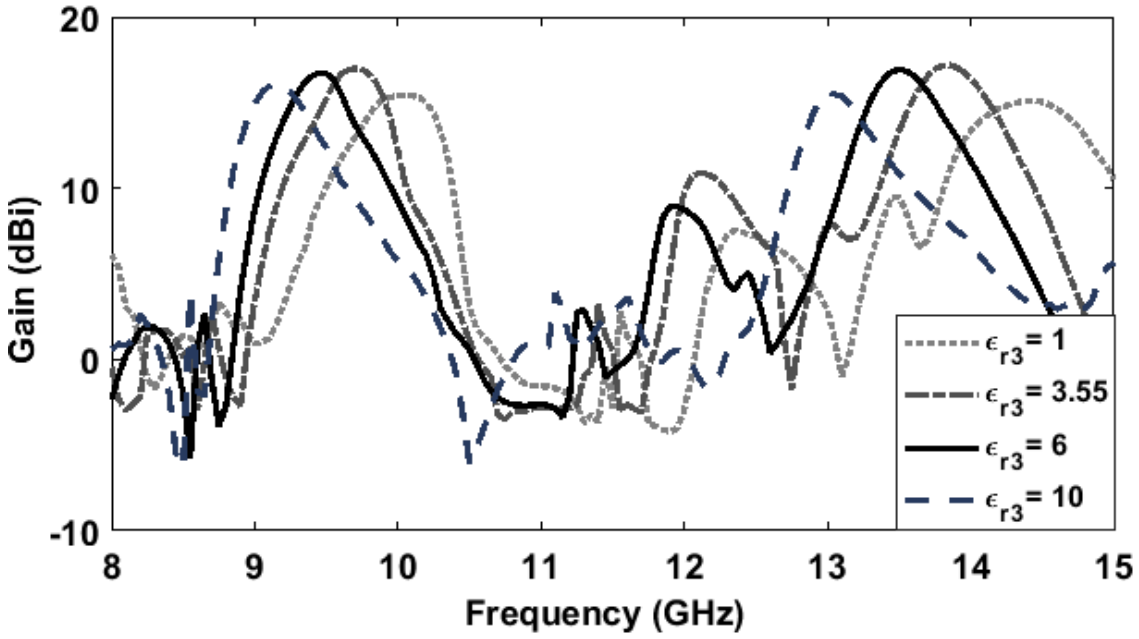

Fig. 5.29. Effect of permittivity of the top layer (Sub. 3) on the antenna gain.

As studied in [108], the top substrate can help to miniaturize the antenna. Fig. 5.29 shows the effect of permittivity of the top substrate (Sub. 3) on the antenna gain. It is demonstrated that

by increasing the permittivity of the top substrate of the antenna, the resonant frequency shifts toward lower frequencies resulting in a more compact antenna. This can also be used to adjust the first and second resonant frequencies.

Fig. 5.30 shows the magnitude of the electric field distribution inside the substrate 3 at both resonant frequencies of 9.7 and 13.85 GHz. The resonances above the corrugations, which happen in the direction of the feed polarization (X-direction), are obviously seen in these graphs. As shown, the magnitude of electric field distribution intensifies over the first corrugations at 9.7 GHz and over the second corrugations at 13.85 GHz. This clearly shows that the first corrugations and second corrugations independently make the first and second resonant frequencies, respectively. These resonances create in-phase superposition of electric fields leading to the antenna gain enhancement. Since the superposition of electric field is along X-direction, it is predictable to have a narrower radiation beamwidth in XZ plane at both resonant frequencies. Moreover, since the mechanism of operation is leaky-wave, the intensity of electric field decays when the wave travels away from the cavity. This is the reason that the intensity of electric field over grooves far away from the cavity is lower than the grooves close to the cavity.

5.2.4 Fabrications and Measurement Results

A prototype of the proposed dual-band corrugated antenna is fabricated as shown in Fig. 5.31. Note that Sub. 2 has six rings, three of that coincide with those of Sub. 1 and three other rings with shallower corrugations are for upper band. The antennas are fabricated using through-drilling walls inside substrates. Then, the through-drilling walls, and vias are metalized and after that filled out by conductive paste. Finally, all substrates are assembled on top of each other by glue.

Fig. 5.32 shows the reflection coefficient and gain of the proposed dual-band corrugated antenna shown in Fig. 5.31. As indicated, the simulation and measurement results are in good agreement. The measurement results demonstrate that impedance bandwidths of 9.45-9.9 and13.25-14.2 GHz are achieved for $|S_{11}| < -10$ dB corresponding to a fractional bandwidth of 4.7% and 6.9% for the first and second frequency bands, respectively. As shown in Fig. 5.32, the

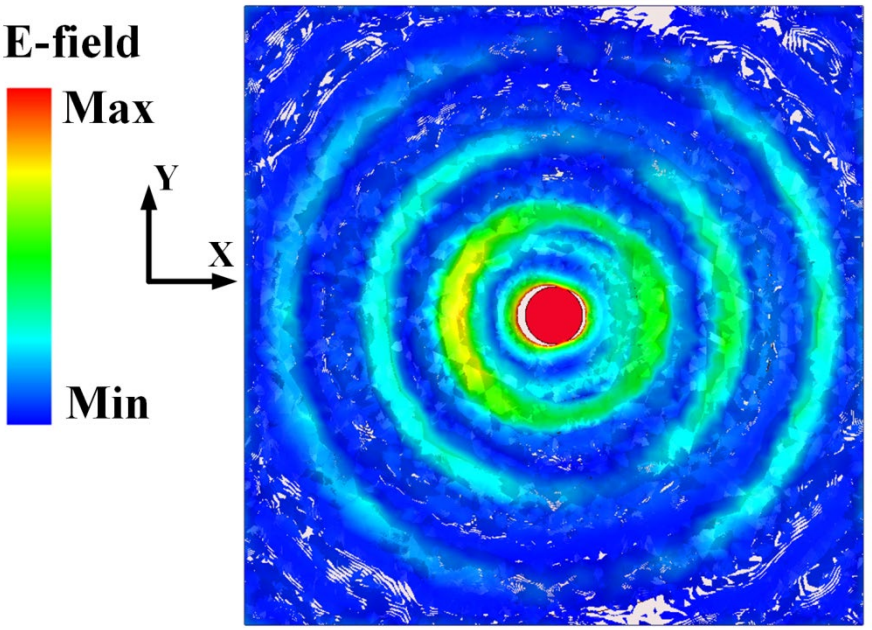

(a)

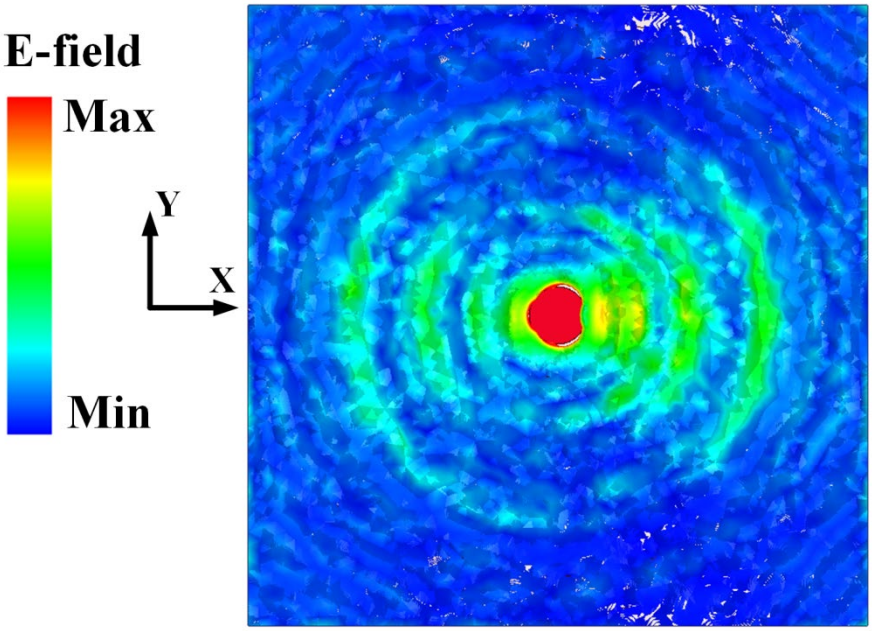

(b)

Fig. 5.30. Magnitude of electric field distribution inside the top substrate (Sub. 3), at (a) 9.7 GHz, and (b) 13.85 GHz.

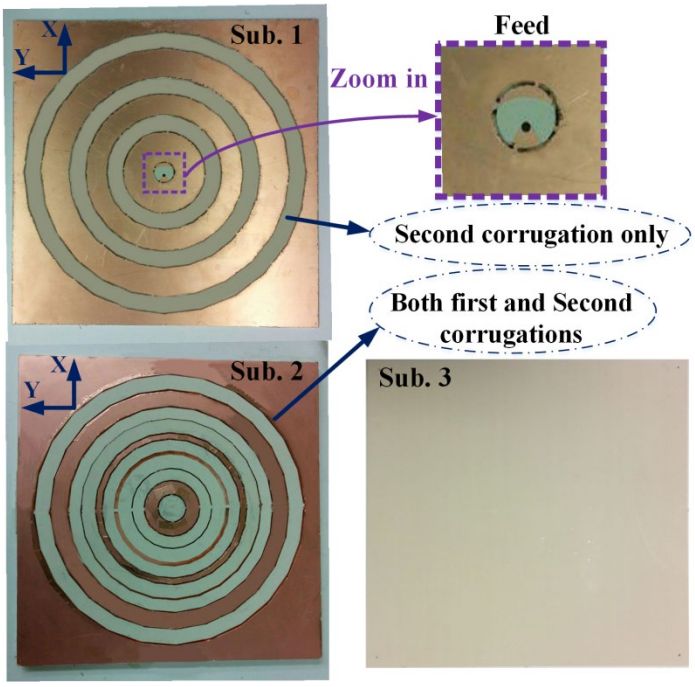

Fig. 5.31. Fabricated dual-band corrugated antenna (dual-band corrugated structure integrated with dual-band feeder antenna A).

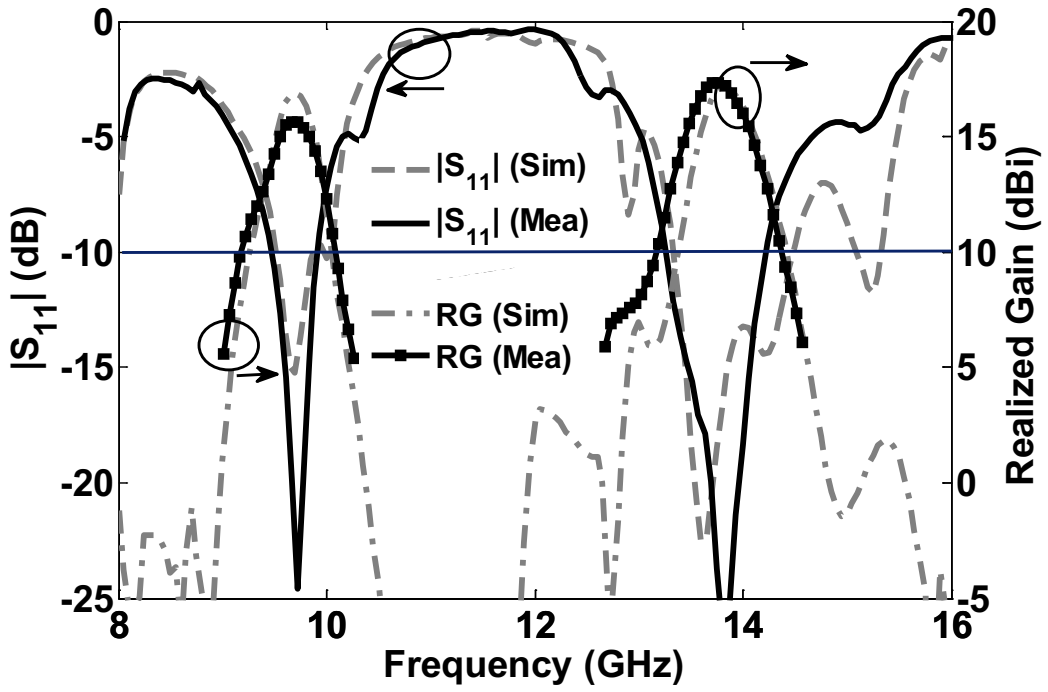

Fig. 5.32. Reflection coefficient and gain of the dual-band corrugated antenna.

measured maximum realized gain over the first and second bands are 15.8 and 17.5 dBi, respectively. For the proposed antenna with dimensions of 180 mm× 180 mm, these measured gains correspond to the aperture efficiencies of 9% and 6.5% for the first and second bands, respectively. Although the measured realized gain over frequency follows the simulated one, the discrepancies may be due to the fabrication tolerances. If a dual-band wideband corrugated antenna is required, in addition to the need for a wideband feeder, the 3-dB gain bandwidth of the antenna also needs to be designed wideband. This, however, needs a more sophisticated corrugated structure which is able to provide proper radiation characteristics.

Fig. 5.33 demonstrates the simulated and measured radiation patterns of the proposed dual-band antenna at the orthogonal planes of *XoZ* (E-plane) and *YoZ* (H-plane) at 9.7 GHz. The measured half-power beamwidths for E-plane and H-plane are 12^{o} and 19^{o}, respectively. Also, a measured side-lobe-level of almost 11 dB is achieved. As shown, the measured cross-polarizations are at least 12 dB below co-polarizations in both E-plane and H-plane within 3 dB beamwidth. Similarly, the radiation pattern of the proposed bull's-eye antenna is plotted in Fig. 5.34 at 13.85 GHz. As shown, the measured half-power beamwidths of 9^{o} and 18^{o} are achieved for E-plane and H-plane, respectively. A measured side-lobe level better than 10 dB is obtained. Similar to the first frequency band, the cross-polarization of the E-plane is negligible at the second frequency band. Also, the cross-polarization of H-plane is at least 9.5 dB below the co-polarization of E-plane within 3 dB beamwidth.

Corrugated structures were investigated as a technique that can be used in many applications such as space and satellite communications to increase the antenna gain with planar structures. However, in some especial applications, it is required to design a separate structure and add it to a main radiator to improve the gain of the system. This technique of gain enhancement will be discussed in chapter 6.

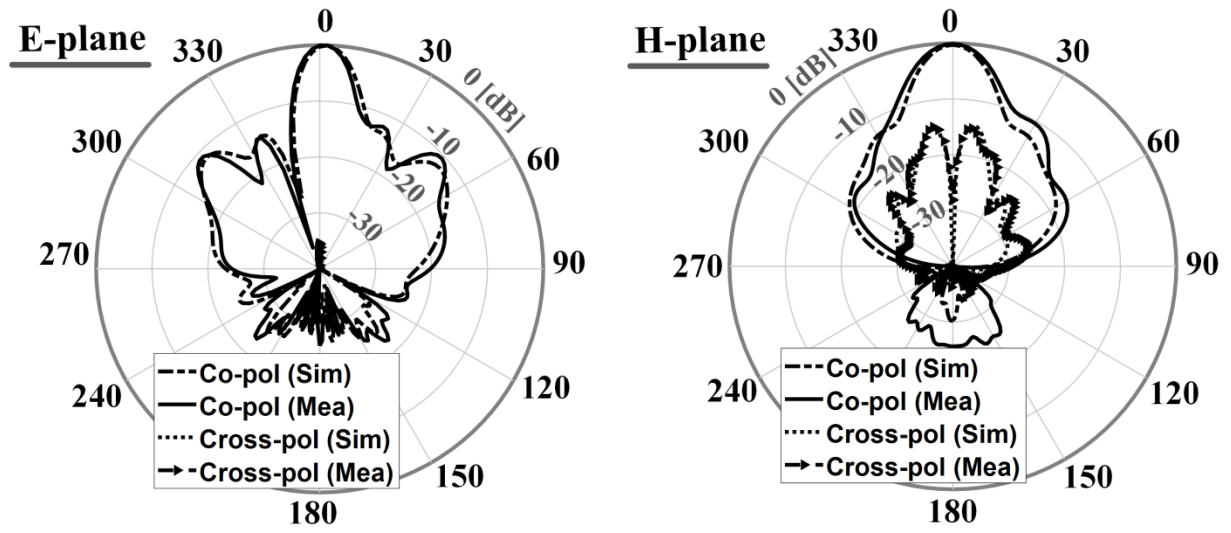

(a) (b)

Fig. 5.33. Radiation patterns of the dual-band corrugated antenna at 9.7 GHz, (a) E-plane, and (b) H-plane.

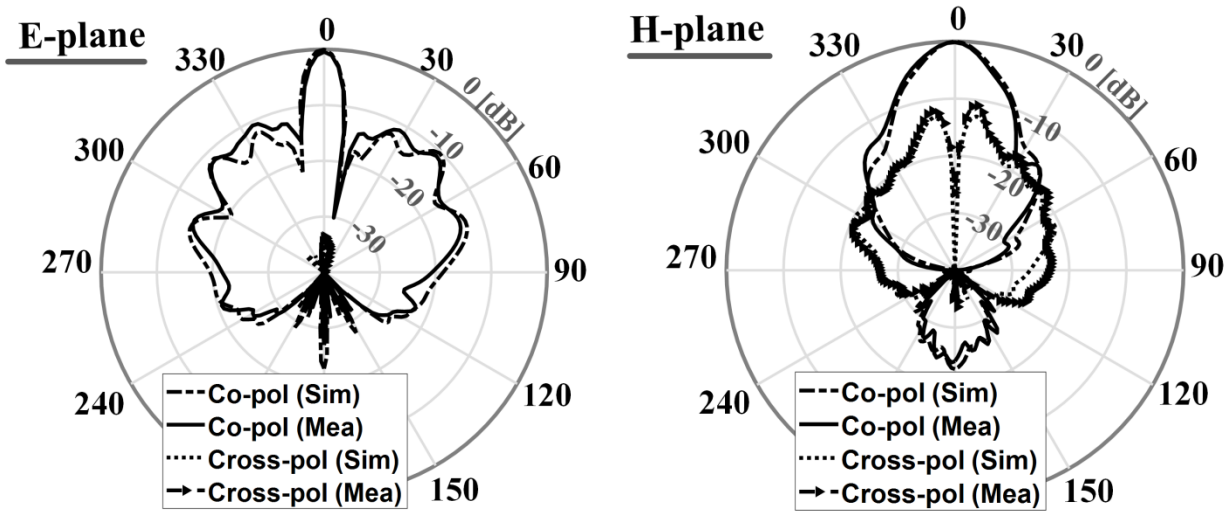

(a) (b)

Fig. 5.34. Radiation patterns of the dual-band corrugated antenna at 13.85 GHz, (a) E-plane, and (b) H-plane.

Chapter 6
Enhancement of Radiation Gain Off of On-Chip Antennas Using Miniaturized-Element Frequency Selective Surfaces (MEFSSs)

Although chapters 4 and 5 investigated the corrugated structures for enhancing the antenna gain, the miniaturized-element frequency selective surfaces (MEFSSs) can also improve the radiation performance of a FPC antenna in many applications. For instance, MEFSS structures can be used in radar instruments and satellite communications and can perform spatial filtering, polarization converting, and antenna gain enhancement. Furthermore, using MEFSS structure on top of on-chip antennas for improving the antenna gain provides a lot of advantages. Throughout the chapter, we study the advantages and challenges of using the MEFSS structure on top of on-chip antennas to increase the antenna gain.

The work presented in this chapter is motivated by the need for the radiation improvement of an active CMOS circuit for on-chip communication and radar applications. To the best of our knowledge, MEFSS structures as a cover for active CMOS circuit to improve the radiation characteristics have not yet been reported. Hence, we propose a technique to improve the radiation characteristics of an on-chip antenna of an active CMOS circuit using MEFSS covers. Two on-chip propagation mechanisms with narrowband and wideband high-gain responses are designed in this work. Miniaturized-element frequency selective surface (MEFSS) covers are utilized on top of on-chip antennas to provide gain enhancement. This is important due to restrictions on thickness of metallic layers, losses in substrate, and limitations in a real estate. The MEFSS covers consist of partially reflecting surface (PRS) and high impedance surface (HIS)/ground plane creating a Fabry-Pérot-type cavity (FPC). Because of using MEFSS structures, the height of FPCs can be

reduced without any deterioration on the antenna radiation. The antennas are embedded in the MEFSS layers and are fed by a small metallic trace on the last layer of chip using coupling mechanism. By utilizing the transverse-equivalent network of the structure and imposing the resonance condition, the geometrical parameters of the MEFSS unit-cell are calculated. For demonstration purposes, two scaled MEFSS covers with narrow and wideband responses for gain enhancement at the center frequency of 10 GHz are designed.

6.1 Geometry of Proposed FPC Antenna

Fig. 6.1 illustrates the configuration of the proposed idea of this chapter. A ground plane has shielded the silicon layer underneath the antenna structure to avoid ohmic and the surface wave losses. The MEFSS layer stacks on top of the passivation/package layer is provided to improve the antenna radiation characteristic. The top metal layer of the chip is employed to design the primary radiator (antenna) or feed structure over. If an antenna is designed over this layer, MEFSS cover plays the role of a superstrate to enhance the radiation. It is also possible to embed a second radiator inside the MEFSS layer that is coupled to the primary radiator designed in the top metal layer to increase the radiation properties or radiation efficiency. One of the main issues related to designing an antenna over the top metal layer is the low efficiency it provides due to its close proximity to the ground plane underneath. However, if this layer is used to design a structure to feed an antenna embedded in the MEFSS layer, the efficiency can be enhanced significantly. In fact, the feed structure couples the waves to the antenna designed in the MEFSS layer. The electromagnetic coupling mechanisms also circumvent the need for interconnections (e.g., wirebond or metalized via holes) that increase the complexity, insertion loss, undesirable radiation, and fabrication cost. An L-shaped feed structure is considered in this work as the feed for the primary antenna in the MEFSS structure (see Fig. 6.2(a)). The material over the ground plane is silicon dioxide with the relative permittivity of about 3.9. For generalization purposes, we consider the permeability and, permittivity of this layer to be μ_a, and ϵ_a, respectively. The passivation/package substrate is also assumed to have a permeability and permittivity of μ_p, and ϵ_p, respectively.

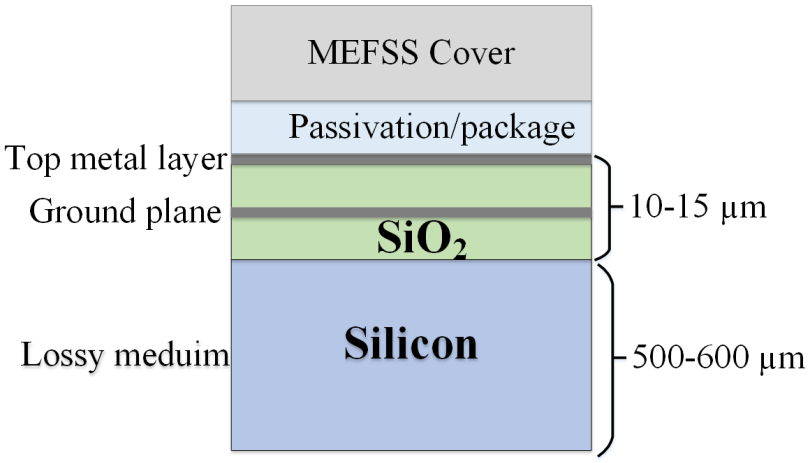

Fig. 6.1. Side view of the proposed On-chip MEFSS cover stacked on an active CMOS circuit.

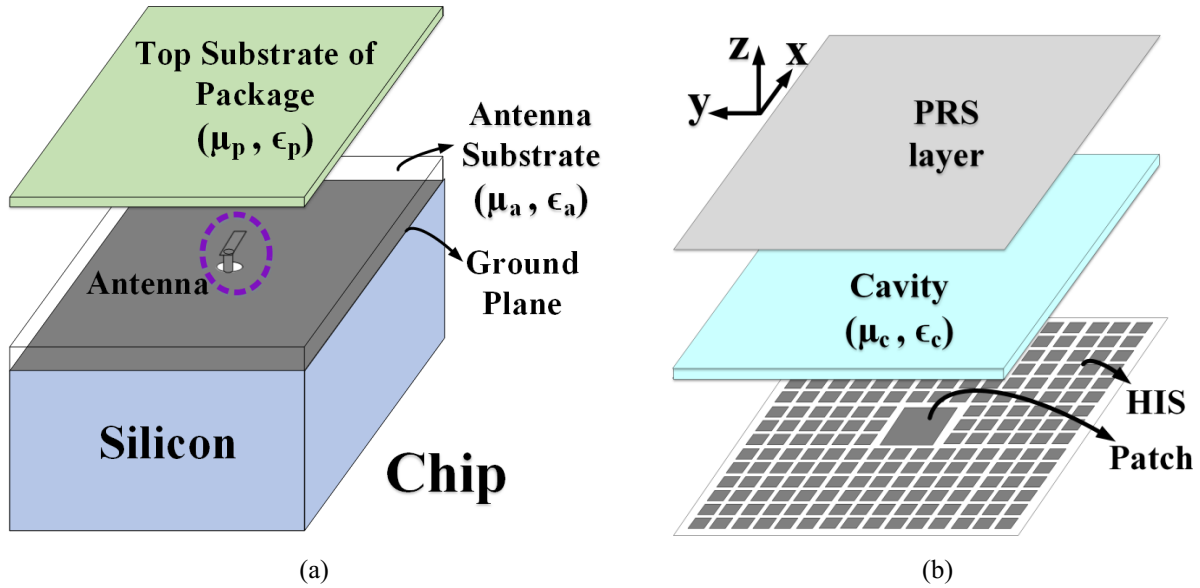

(a) (b)

Fig. 6.2. Side view Stacked view of (a) chip with the L-shaped feed structure, and (b) MEFSS layer with an embedded patch antenna that is placed on top of the package layer.

A MEFSS structure composed of a HIS surface, and a PRS layer as shown in Fig. 6.2(b) can be placed on top of the chip to improve the radiation characteristics. The patch antenna as single radiator that is fed from the feed line inside the chip is in the middle of the HIS layer. Since the PRS layer partially reflects the wave emanated by the antenna back to the structure, a pseudo Fabry-Pérot cavity is stablished. The HIS and PRS layers include MEFSS unit-cells with the

dimensions much smaller than a wavelength. The permeability and permittivity of the substrate layer inside the cavity are μ_c, and ϵ_c, respectively. For an ideal periodic geometry, the size of the structure is infinite; however, the dimensions of the MEFSS cover in this work cannot be large due to practical reasons. The provision of multiple reflections inside the cavity improves the antenna gain significantly while maintaining a very low profile. This is accomplished using a very thin MEFSS cover. For proper operation, the size of MEFSS elements should be very small compared to the wavelength to create a uniform surface for the close-to-normal waves that make the radiations at broadside. It should be noted that the thickness of the PRS layer created by MEFSS unit-cells must be much smaller than a wavelength; otherwise, it affects the performance.

6.2 Principle of Operation

Although, MEFSS structures can be designed to play different roles such as filtering, polarization converting, and side-lobe-level reduction, in what follows, we discuss the theory and analysis of the structure only for gain enhancement.

6.2.1 MEFSS Topology and Equivalent Circuit Model

The exploded view of the PRS layer is shown in Fig. 6.3(a). The PRS, which is symmetric in both x and y directions, is composed of two metallic layers which are separated by a dielectric material with permeability, permittivity, and thickness of μ_s, ϵ_s, and h_s, respectively. Both metallic layers and the intermediate substrate constitute a transmission-line resonator. Since the PRS structure is symmetric, its response is insensitive to the polarization of the normal incident wave. Bottom layer of the PRS is a 2D periodic arrangement of subwavelength patches, whereas the top layer is a 2D wire grid with subwavelength periodicity. The dimension of all unit-cells is *P*, where $P<<\lambda$ and λ is the wavelength at the operating frequency. Several metallic strips in x and y directions form the grids that are inductive, while square patches with a gap in between are characterized to be capacitive. Fig. 6.3(b) depicts the equivalent circuit model of the PRS layer for the inductive and capacitive unit-cell elements shown in Fig. 6.3(c) and (d).

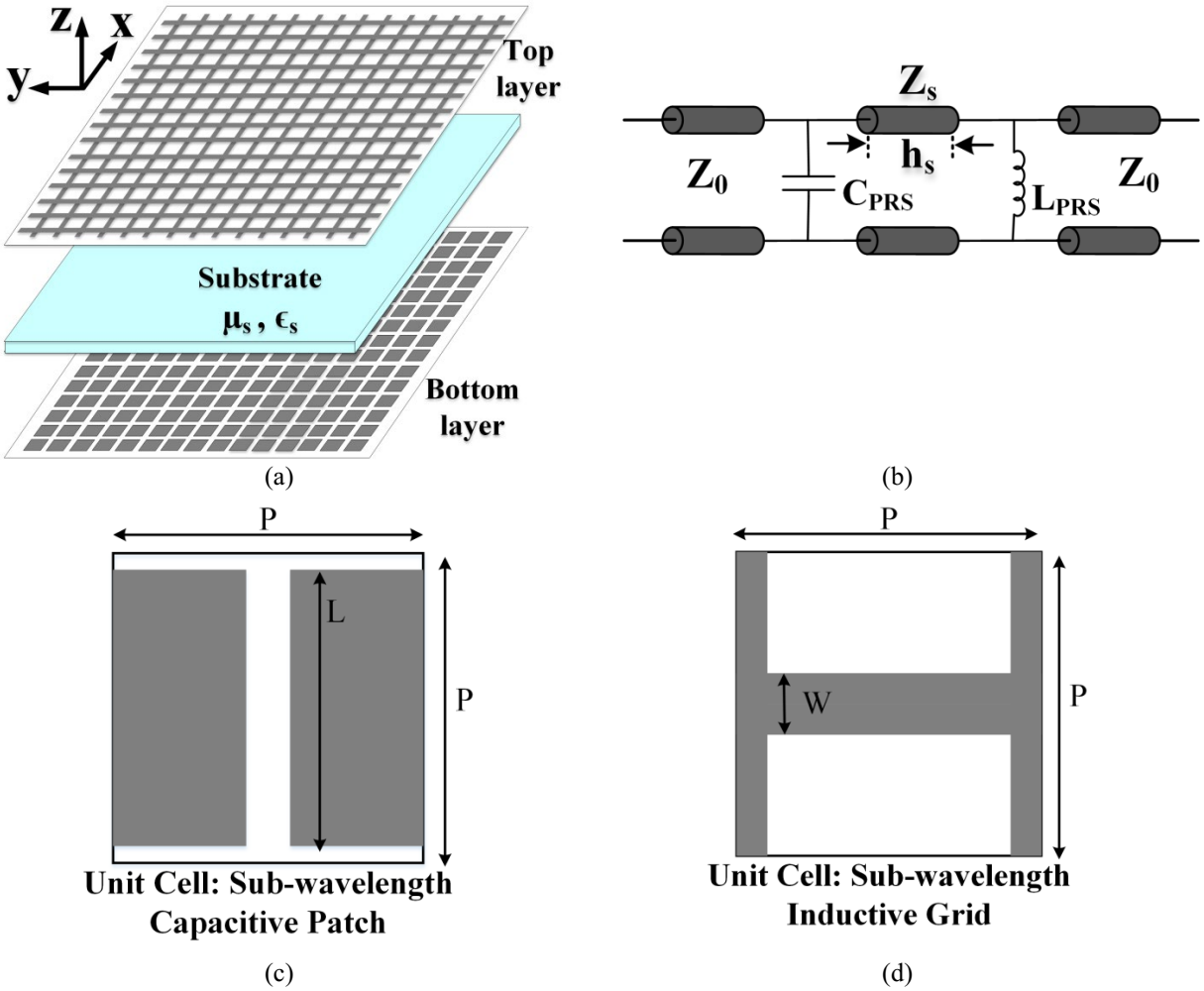

Fig. 6.3. (a) Confutation of the PRS layer, (b) its equivalent circuit model, (c) a unit-cell of capacitive patches, (d) a unit-cell of inductive grids.

In this circuit, the shunt inductor L_{PRS} models the inductive grids, and the shunt capacitor C_{PRS} represents the capacitive patches. Also, the substrate material is demonstrated by a transmission line with a characteristic impedance, and a length of $Zs = Z_0/\sqrt{\epsilon_s}$ ($\mu_s = 1$) and h_s, respectively, where $Z_0 \approx 377\ \Omega$ is the free-space impedance. Since the structure is suspended in the open space, both sides of the PRS are loaded by the characteristic impedance of the free space. Although, one layer of MEFSS unit-cells is used in this work, multilayer structure can be employed for different purposes such as making wideband, controlling polarization, etc.

The structure shown in Fig. 6.3 behaves as a bandpass circuit whose resonance depends on the parallel *LC* circuit. Although the MEFSS structures are commonly used as bandpass filter [116], for antenna gain enhancement, the structure is tuned to present a reactive load. In order to realize the unit-cell dimensions of the PRS structure when the equivalent circuit is designed, we need to map the values of the equivalent circuit model to those of the geometrical parameters of the PRS. The values of L_{PRS}, and C_{PRS} can be related to physical parameters of the inductive grids and capacitive patches with the following equations:

$$L_{PRS} = \frac{\mu_0 \mu_{reff} P}{2\pi} ln\left(\csc\left(\frac{\pi W}{2P}\right)\right) \tag{6.1}$$

$$C_{PRS} = \frac{2\epsilon_0 \epsilon_{reff} P}{\pi} ln\left(\csc\left(\frac{\pi (P-L)}{2P}\right)\right) \tag{6.2}$$

where P is the period of the PRS structure, and $\mu_0, \mu_{reff}, \epsilon_0$, and ϵ_{reff} are the freespace permeability, effective permeability, free space permittivity, and effective permittivity, respectively.

For the HIS structure of the MEFSS cover, capacitive patches with the same period are selected. Fig. 6.4 shows a unit-cell of the HIS structure with its corresponding equivalent circuit. Again, the value of the realized capacitor can be related to the geometrical parameters with the following equation:

$$C_{HIS} = \frac{2\epsilon_0 \epsilon_{reff} P}{\pi} ln\left(\csc(\frac{\pi S}{2P})\right) \tag{6.3}$$

Now, we can design the structure based on the circuit models provided above for the designed wave behavior and then, map the circuit into the geometrical parameters.

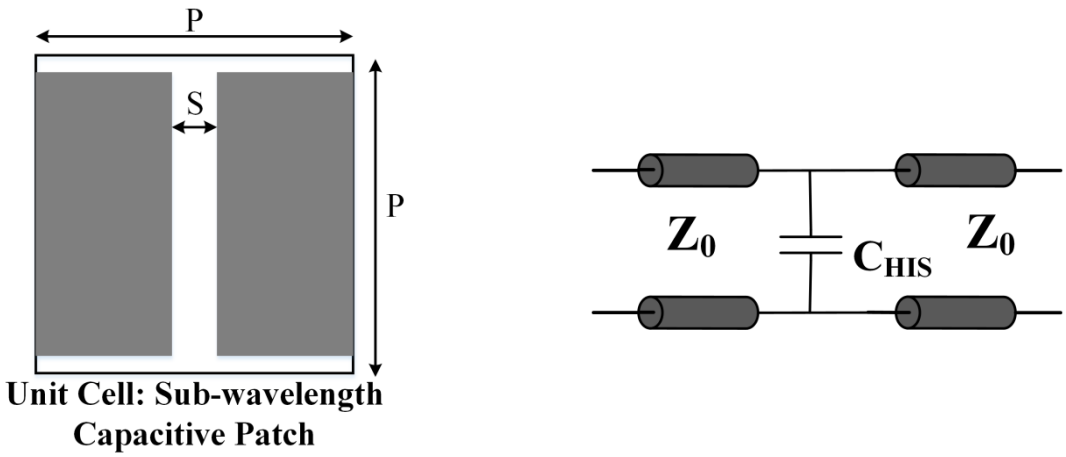

(a) (b)

Fig. 6.4. (a) The unit-cell of capacitive patches in the HIS layer, and (b) its equivalent circuit model.

6.2.2 Resonance Condition for Antenna Gain Improvement

For the application at hand, which is designing a thin cover for a chip to enhance the radiation characteristics, the FPC approach is the best option since it provides a high level of freedom for the design. Furthermore, it is an additive package integrated on top of a main antenna with low-profile, low loss, and cost-effective features. The cavity is formed by a PRS and a fully reflective ground plane. Multiple reflections of waves radiated from the antenna inside the cavity are emitted in-phase at the PRS-air interface and enhance the antenna gain.

For a thin PRS structure, the condition of maximum gain at boresight direction can be obtained from the ray optics model as follows:

$$\varphi_{prs} + \varphi_{ref} - 4\pi h/\lambda_0 = 2\pi N \qquad N=0, \pm1, \pm2, \qquad (6.4)$$

where φ_{prs} and φ_{ref} are the reflection phase of PRS structure and the fully reflective ground plane, respectively, h is the height of the cavity, and λ_0 is the operating wavelength. Although (6.4) is accurate when the PRS is thin compared to wavelength, it fails in the case of a thick PRS (or sometimes two-sided PRS) [102]. The cavity height in conventional FPC structures is

approximately a half wavelength. However, using AMC structures, it can be reduced to a quarter wavelength since a PMC surface and a highly reflective PRS provide a reflection phase close to zero and π, respectively. To further reduce the height of a FPC, $\varphi_{prs} + \varphi_{ref}$ needs to be as small as possible, according to (6.4).

The transverse-equivalent network (TEN) is a more general approach to analyzing a structure [50] based on transmission line model. This model is usually utilized for determination of the radiation characteristics through an application of reciprocity theorem. Since the FPC structures are proved to have a peak radiation gain at broadside, the TEN model is simplified for transverse electromagnetic (TEM) propagations alongside the normal direction to the structure. A TEN, shown in Fig. 6.5, is used to model the MEFSS cover placed on top of a chip. Current and voltage sources are used for a magnetic source (such as slot) and an electric source (such as electric dipole) as a main radiator respectively. These sources are placed inside the cavity with a distance h_{c1}, and h_{c2} from HIS and PRS respectively ($h_c = h_{c1} + h_{c2}$ is the height of the cavity). In the TEN model of the antenna, the PRS, HIS, and cavity are assumed to be infinite. The PRS and HIS structures, composed of MEFSS unit-cells, are shown with two-port networks for generalization. The infinite transmission line with the impedance characteristic Z_0 models the free-space area above the structure. Fig. 6.6 shows the MEFSS cover in this work and its equivalent transmission line model which is obtained by using the MEFSS transmission line models in the TEN model. In Fig. 6.6(b), $Zc = Z_0/\sqrt{\epsilon_c}$ $(\mu_c = 1)$ and h_c are the cavity characteristic impedance and cavity height, respectively.

The resonance condition of the structure for achieving maximum gain at broadside for a desired frequency happens when the imaginary part of the total admittance of the structure is equal to zero; i.e. $Im\ (Y_{up} + Y_{down}) = 0$. The upward and downward admittances Y_{up} and Y_{down} are shown in Fig. 6.6 for the equivalent transmission line model of a unit-cell of the MEFSS cover.

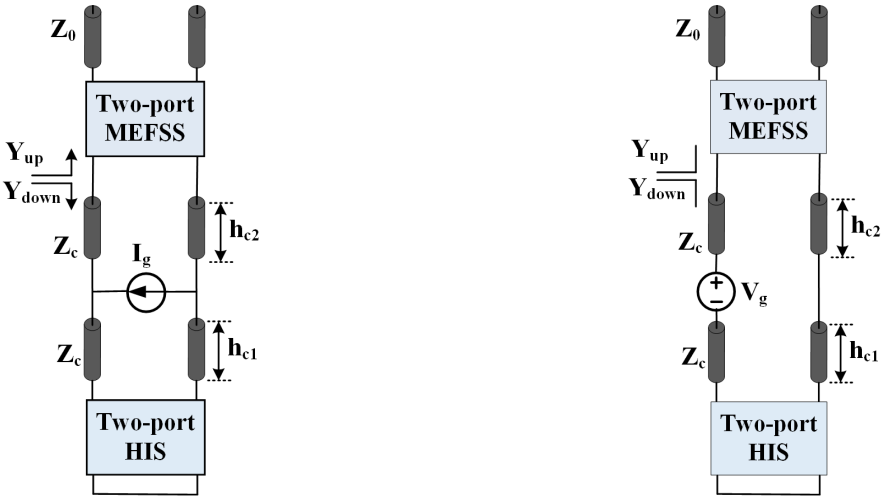

(a) (b)

Fig. 6.5. A general TEN for a MEFSS cover designed to be placed on top of a chip with (a) magnetic source, and (b) electric source as main radiator.

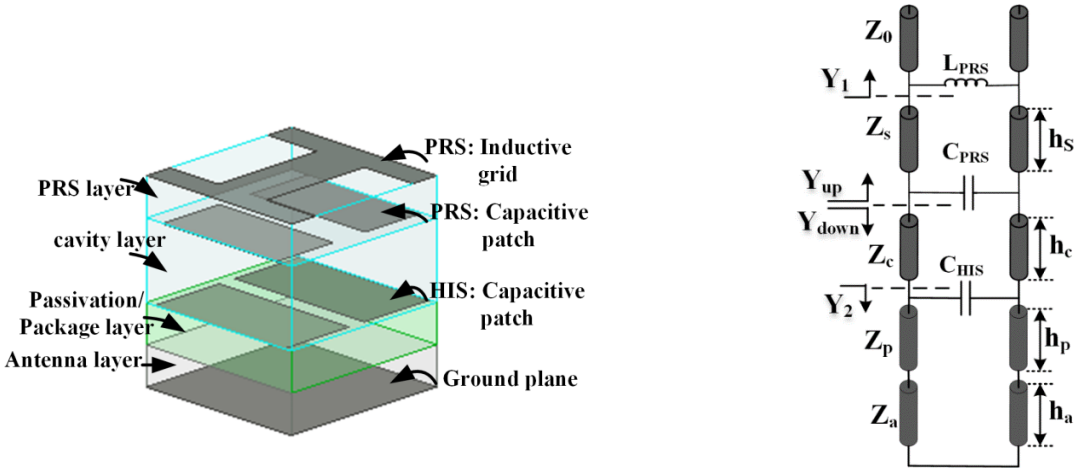

(a) (b)

Fig. 6.6. (a) Unit-cell of MEFSS cover in this work, and (b) its equivalent transmission line model.

The upward admittance Y_{up} is calculated at the bottom surface of the PRS based on the circuit parameters as follows:

$$Y_{up} = jC_{PRS}\omega \quad + \frac{1 - \frac{L_{PRS}\omega}{Z_s}\tan(k_s h_s) + j\frac{L_{PRS}\omega}{Z_0}}{-L_{PRS}\omega\,(\frac{Z_s}{Z_0})\tan(k_s h_s) + j(L_{PRS}\omega + Z_s\tan(k_s h_s))} \tag{6.5}$$

where ω is the angular frequency, and $Zs = Z_0/\sqrt{\epsilon_s}$ and $k_s = k_0\sqrt{\epsilon_s}$. Similarly, the downward admittance is calculated as:

$$Y_{down} = Z_c\left(\frac{1 + jY_2Z_c\tan(k_ch_c)}{Y_2Z_c + j\tan(k_ch_c)}\right) \tag{6.6}$$

Where

$$Y_2 = jC_{HIS}\omega + j\left(\frac{1 - (\frac{Z_a}{Z_p})\,tan(k_ah_a)\,tan(k_ph_p)}{Z_a\,tan(k_ah_a) + Z_p\,tan(k_ph_p)}\right) \tag{6.7}$$

In (6.6) and (6.7), $Z_i = Z_0/\sqrt{\epsilon_i}$ and $k_i = k_0\sqrt{\epsilon_i}$ where *i= a, c, p* represents different layers. Now, by selecting different materials and thicknesses for the layers, and a desired resonant frequency $f = \frac{\omega}{2\pi}$, and imposing resonance condition *Im* (Y_{up}+Y_{down})= *0*, the values for C_{HIS}, C_{PRS}, and L_{PRS} are obtained. Then, using (6.1)-(6.3), the inductors' and capacitors' values are converted to the geometrical parameters of the structure. It should be noted that there might be several inductors' and capacitors' values that satisfy the resonance condition. However, the values corresponding to realizable geometrical parameters are chosen. The obtained geometrical values are used as a great initial values for optimization in HFSS simulator.

6.3 Design of MEFSS Cover: Simulation, and Measurement Results

For the fabrication of the gain-enhancer cover in high frequencies, the MEFSS structures can be fabricated on thin layers of Parylene membranes [116]. Excellent physical and electrical properties such as low intrinsic stress, durability, hermetic sealing capability, ease of fabrication, and low dielectric constant and low loss (ε_r =2.9, tanδ=0.004 @60 GHz [117]), make Parylene suitable for the application at hand. Parylene can be directly deposited over the circuit in a conformal manner. As deposition of Parylene polymer is a low temperature process (25^0C at 0.1 torr), it is compatible with CMOS circuits. Also since Parylene is applied as a gas, using shadow masks, one can cover only a portion of the circuit if needed. For placing MEFSS cover at a distance from the circuit, it is important to emphasize that large areas of a thin layer of Parylene can be

released and handled which makes it ideal for freestanding structures.

In this work, for demonstration purposes, a MEFSS cover is designed and fabricated at the center frequency of 10 GHz. This low frequency is selected due to ease of fabrication and measurement with the available equipment in the Lab.

6.3.1 MEFSS Cover Design

The Silicon di-oxide (SiO_2) in CMOS layers has a permittivity of 4, therefore, to have a similar condition for our prototype, a TMM4 substrate is chosen for the antenna substrate with the permittivity and loss tangent of 4.5 and 0.002 respectively (i.e. $\epsilon_a = 4.5$). For similar reason, the material of the passivation and PRS layers is selected to be TMM4 laminate (i.e. $\epsilon_p = \epsilon_s = 4.5$). TABLE 6.1 shows the detailed material parameters and substrate thickness values for different layers.

Although in conventional FPC designs, the cavity height is around half wavelength, in this design, the cavity height is reduced to a value as small as $\lambda/30$ to make the structure compact. An initial unit-cell design is carried out at the resonant frequency of 10 GHz using the aforementioned approach. The calculated values for unit-cell dimensions *P*, *W*, *L*, and *S* are 4 mm, 1.2 mm, 3.6 mm, and 0.5 mm, respectively. Fig. 6.7 shows the imaginary part of admittances Y_{up} and Y_{down}. The transverse resonance happens at the frequency of 10 GHz, thus we expected a gain improvement at this frequency.

A parametric study is carried out on geometrical parameters of the MEFSS cover to show the effect of each parameter on the upward and downward admittances. This also provides the physical tuning range for each parameter. An increase in the size of inductive grids of PRS layer (*W*), decreases the inductor values and in turn reduces the upward susceptance ($Im\ (Y_{up})$) at a given frequency as shown in Fig. 6.8(a). Similarly, as the size of capacitive patches of PRS layer (*L*) is increased, its capacitor value increases which results in a higher upward susceptance as depicted in Fig. 6.8(b). The downward susceptance decreases as the gap (*S*) size of the capacitive patches in HIS reduces (see Fig. 6.8(c)). It should be noted that, generally, when the resonance condition $Im\ (Y_{up}+Y_{down})= 0$ cannot be realized using practical geometrical parameters, we have to modify

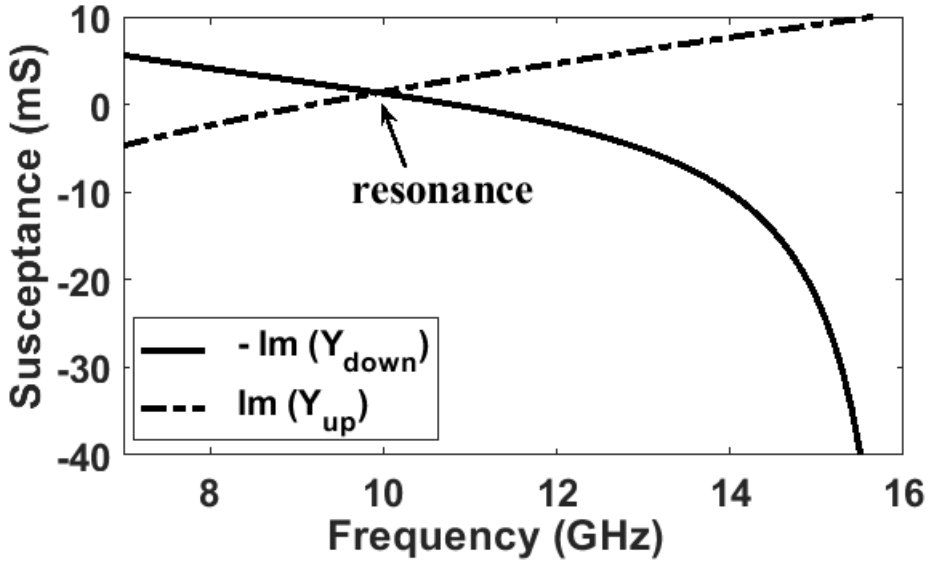

Fig. 6.7. Upward and downward susceptance values of the unit-cell designed for the resonant frequency of 10 GHz (unit-cell dimensions are *P*= 4mm, *W*= 1.2 mm, *L*= 3.6 mm, and *S*= 0.5 mm and the cavity height is 1 mm).

TABLE 6.1
Design Material Selection

Layers / Spec	Antenna layer	Passivation/Package layer	Cavity layer	PRS layer
Material	$\epsilon_a = 4.5$	$\epsilon_p = 4.5$	$\epsilon_c = 1$	$\epsilon_s = 4.5$
Height (mm)	$h_a = 0.51$	$h_p = 0.76$	$h_c = 1$	$h_s = 1.27$

the cavity/substrate thicknesses and their permittivity and again solve the equation for realizable geometrical parameters (*W*, *L*, *S*).

6.3.2 Feed Antenna Design

To excite the MEFSS layer, a patch antenna surrounded by HIS is integrated with the structure. The antenna is fed by a proximity coupling mechanism between a trace in the output layer of the chip and the patch antenna as a non-contact feeding method. This allows the antenna to be designed outside the chip and releases the limitations of designing it inside the chip.

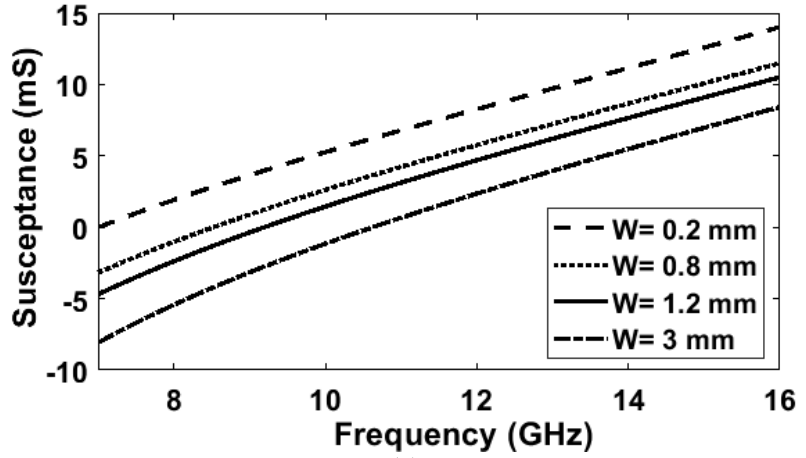

(a)

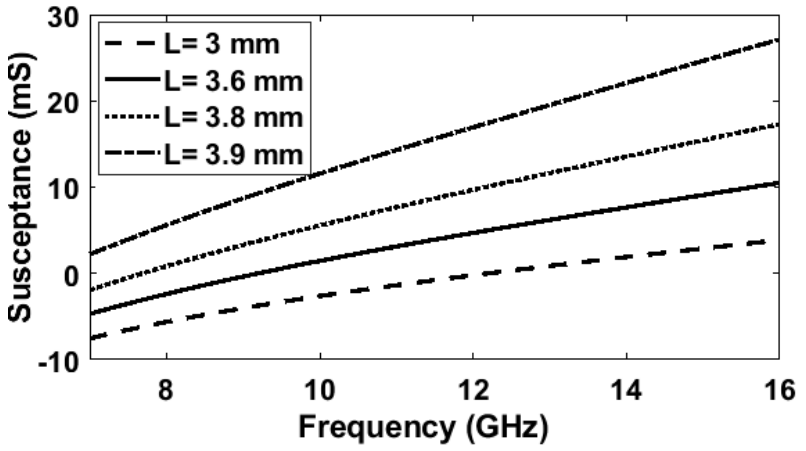

(b)

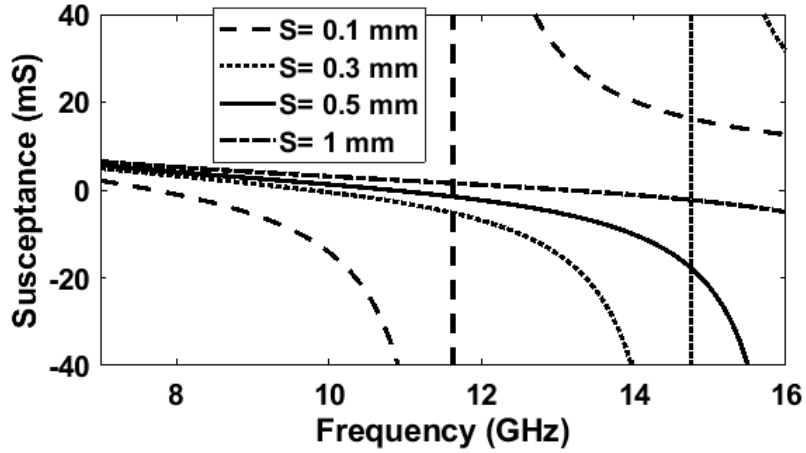

(c)

Fig. 6.8. Parametric study of different geometrical parameters on upward and downward admittances, (a) *Im* (Y_{up}) for different inductive grid sizes of PRS, (b) *Im* (Y_{up}) for different capacitive patch sizes of PRS, and (c) *Im* (Y_{down}) for different inductive grid sizes of HIS.

As mentioned previously, we chose a very small cavity height (~λ/30) in order to have a compact structure. This can create a strong coupling between different parts of the structure (i.e. feed line, patch, HIS, and PRS). Although the gain enhancement is ensured by MEFSS cover design in the previous subsection, the parasitic elements, due to these coupling mechanisms, deteriorate the antenna matching or shift the impedance response of the single patch antenna. Fig. 6.9 shows the configuration of the proximity-fed patch antenna integrated in the MEFSS layer and its equivalent impedance circuit model. It is worth mentioning that for patch antenna itself, the equivalent circuit includes L_p, C_p, R_p, C_u, and the transmission line (TL) with the impedance characteristic and length of Z_0 and θ, respectively. The HIS adds capacitive coupling to the patch and also contributes to the propagation. In the equivalent circuit of Fig. 6.9, the HIS is modeled by C_H, and R_H, where R_H represents the ohmic losses in the substrate. Also, the PRS layer has a huge impact on the impedance matching, since it is above the patch antenna with a short separation distance of cavity height (1 mm in this design). The PRS effect on the impedance matching is modeled by an 1:N transformator, C_R, and L_R. The electromagnetic fields around the offset distance between the feed line and the patch (labeled as S_f in Fig. 6.9(a)) are affected by the HIS and PRS layers on top. To adequately model their impacts, two capacitors and one inductor C_t, C_c, and L_c are added to the original model of the patch antenna. According to the circuit model of the structure shown in Fig. 6.9(d), it is evident that the added elements, due to the effect of PRS, and HIS, influence the antenna matching, and since the HIS and PRS dimensions are fixed and calculated for the gain enhancement, only patch antenna parameters (i.e. W_p, L_p, S_f, L_f, and W_f) are available for impedance matching. Obviously, the values of these parameters are totally different from those obtained for the proximity patch antenna in isolation (without the HIS and PRS layers).

To investigate the effect of PRS and HIS layers, we first designed a proximity patch antenna alone. The effect of integrating the PRS and HIS layers on top of the patch antenna is shown in Fig. 6.10(a). As indicated, the MEFSS cover deteriorates the matching and shifts the resonant frequency. However, after tuning the antenna parameters, the resonance can be adjusted to happen at 10 GHz with a good reflection coefficient and acceptable bandwidth. Fig. 6.10(b)

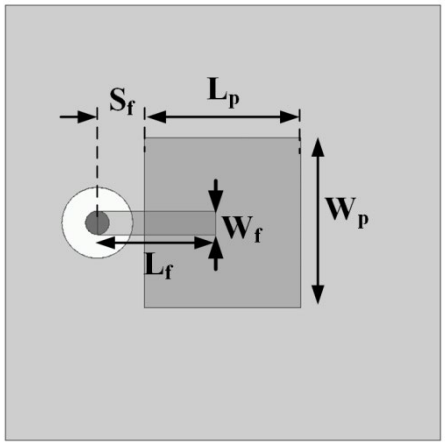

(a)

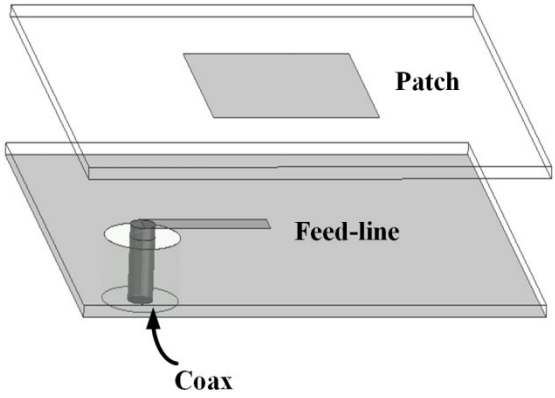

(b)

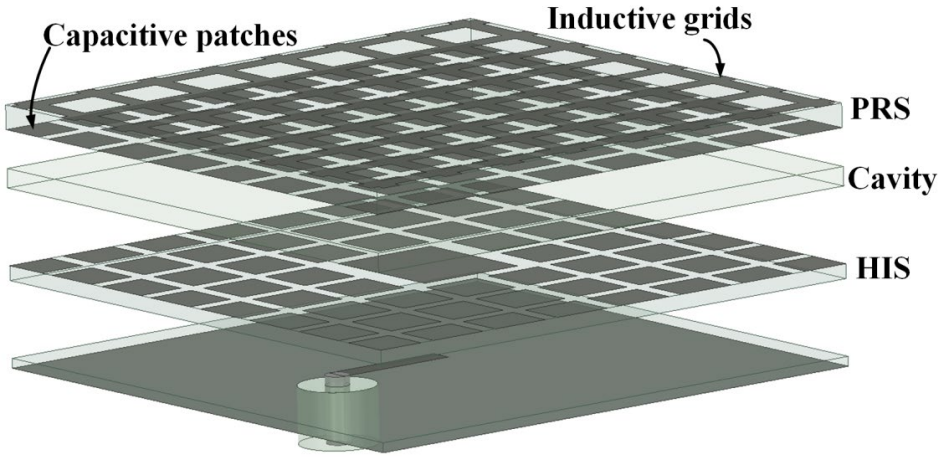

(c)

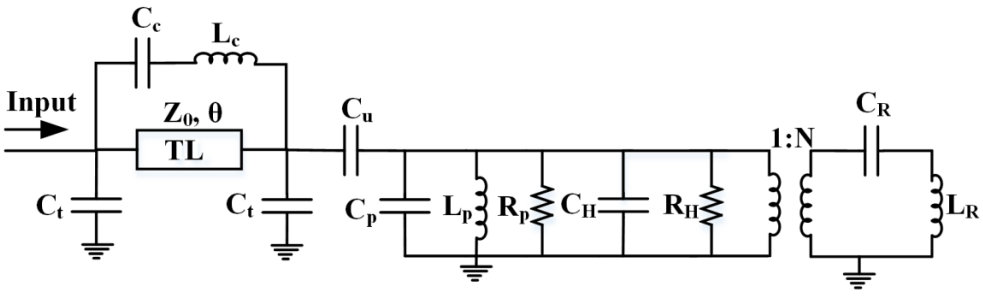

(d)

Fig. 6.9. Patch antenna integrated inside the MEFSS layer, (a) top view and, (b) exploded view of the antenna, (c) the antenna integrated with MEFSS layer, and (d) its equivalent impedance circuit model.

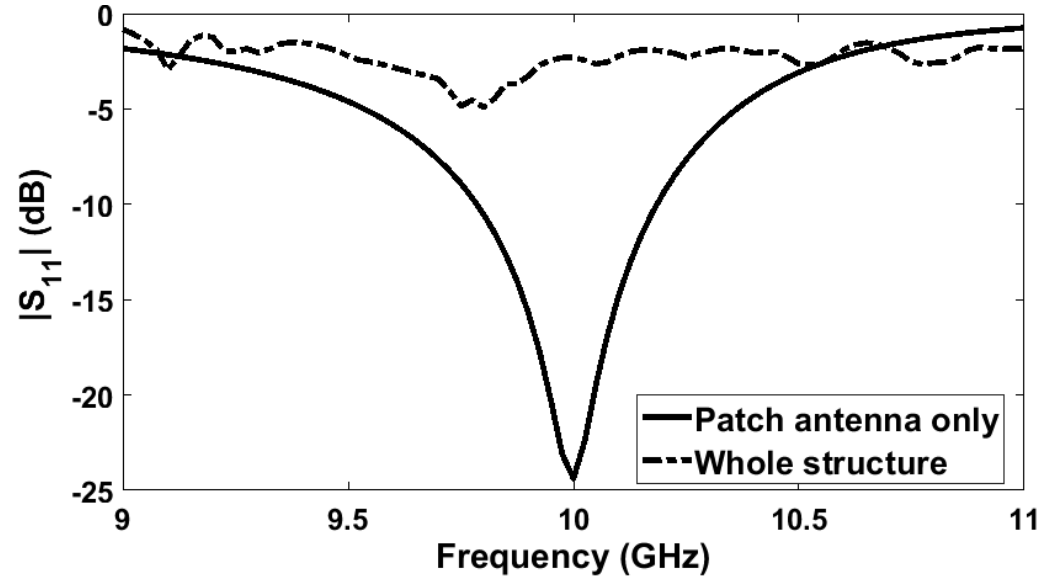

(a)

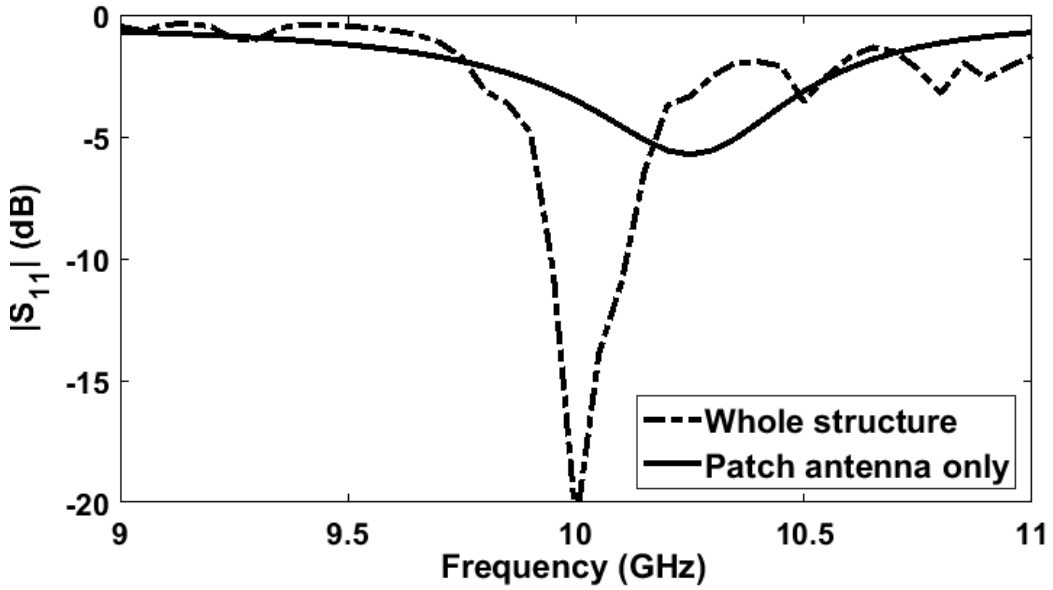

(b)

Fig. 6.10. Matching response of MEFSS-antenna and patch antenna alone when (a) the patch antenna matching is optimum with parameters W_p= 6.4 mm, L_p= 7 mm, L_f= 4.5 mm, S_f= 0.7, W_f= 0.8mm and (b) the whole structure matching is optimum with parameters W_p= 6mm, L_p= 7.3 mm, L_f= 7.1 mm, S_f= 2.9, W_f= 1mm.

shows the MEFSS-antenna matching after tuning the antenna parameters. It is also shown that these tuned parameters do not yield a matched condition for the proximity patch antenna alone.

6.3.3 Measurement Results and Discussion

A MEFSS layer and the embedded proximity patch antenna are designed and optimized at the center frequency of 10 GHz with parameters P= 4mm, W= 1.1 mm, L= 3.6 mm, and S= 0.5 mm, W_p= 6mm, L_p= 7.3 mm, L_f= 7.1 mm, S_f= 2.9, W_f= 1mm. Since the cavity height was needed to be as small as possible, it was selected to be 1 mm. A porotype of the MEFSS layer with the integrated patch antenna is fabricated. Fig. 6.11 shows the fabricated MEFSS cover (an array of 24 × 24) and its different layers. The dimension of the MEFSS structure is 96 mm × 96 mm. As demonstrated in TABLE 6.1, the passivation and antenna layers are very thin and can be easily deformed during the fabrication process. To prevent these layers from deformation, we stuck them on top of a thick support layer as shown in Fig. 6.11. The support layer does not affect the performance of the antenna since it is placed beneath the ground plane.

Fig. 6.12 shows the reflection coefficient of the antenna and MEFSS cover. As shown, the resonant frequency of the whole structure is shifted up to 10.15 GHz (1.5% shift) due to the fabrication errors and misalignment between layers in the assembly process, as well as the tolerance of the laminate boards. In addition, the results show that a measured impedance bandwidth of 1.1% is achieved over 10.08-10.19 GHz which is somewhat narrower than the simulated one (1.7% from 9.94 GHz to 10.11 GHz). It is worth mentioning that a wider impedance bandwidth can be achieved by introducing other resonant frequencies, which will be investigated later. More important factors are the gain enhancement and the gain bandwidth. The simulated and measured gains are shown in Fig. 6.13. Maximum measured realized gain of 14.14 dBi (aperture efficiency of 20%) is obtained which is 0.9 dBi lower than the simulated one. The measured 3 dB gain bandwidth is about 0.3 GHz from 9.94 GHz to 10.24 GHz which corresponds to a fractional bandwidth of 2.97%. It is worth mentioning that the simulated maximum realized gain of the patch antenna alone is 6 dBi, while it is 15.05 dBi for the antenna with MEFSS cover demonstrating a gain improvement of around 9 dBi. To have a wider 3 dB gain bandwidth, multi-layer MEFSS covers can be used.

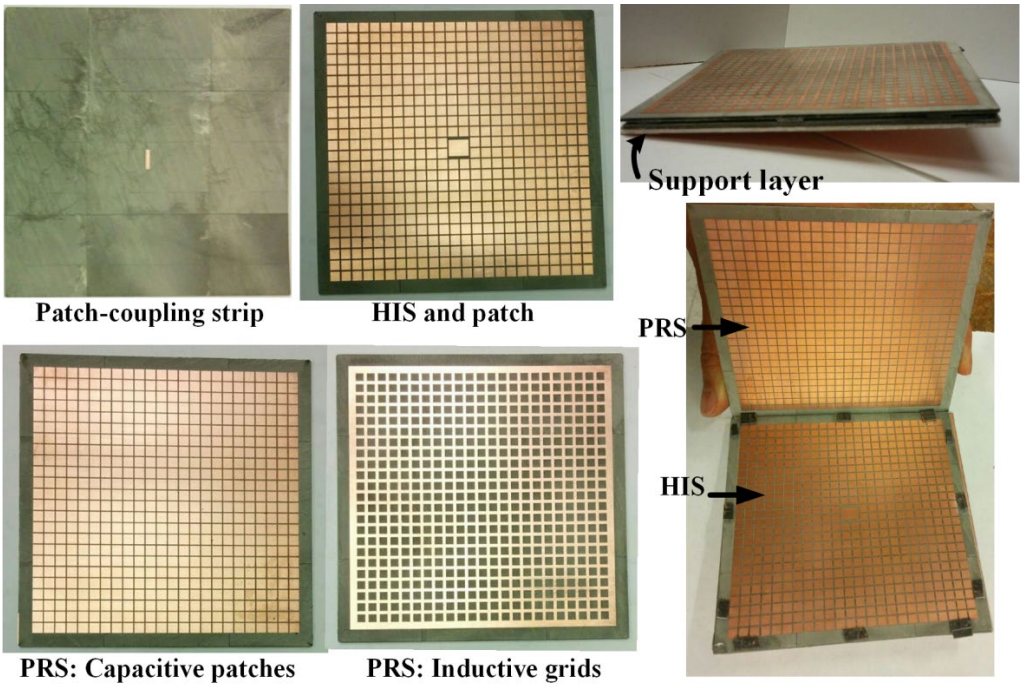

Fig. 6.11. Fabricated MEFSS cover with the feed antenna.

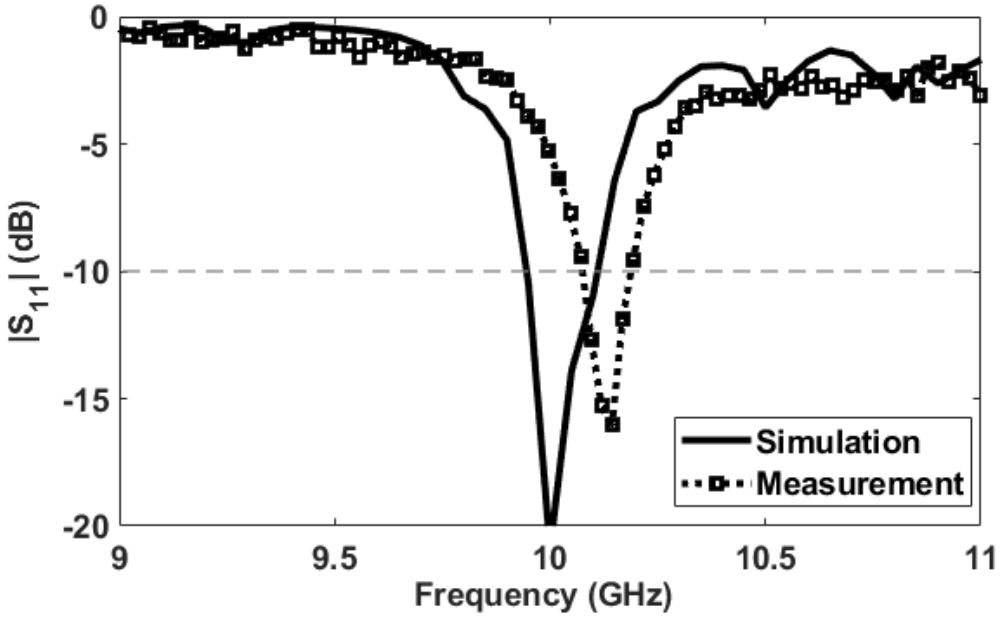

Fig. 6.12. Reflection coefficient of the antenna with MEFSS cover.

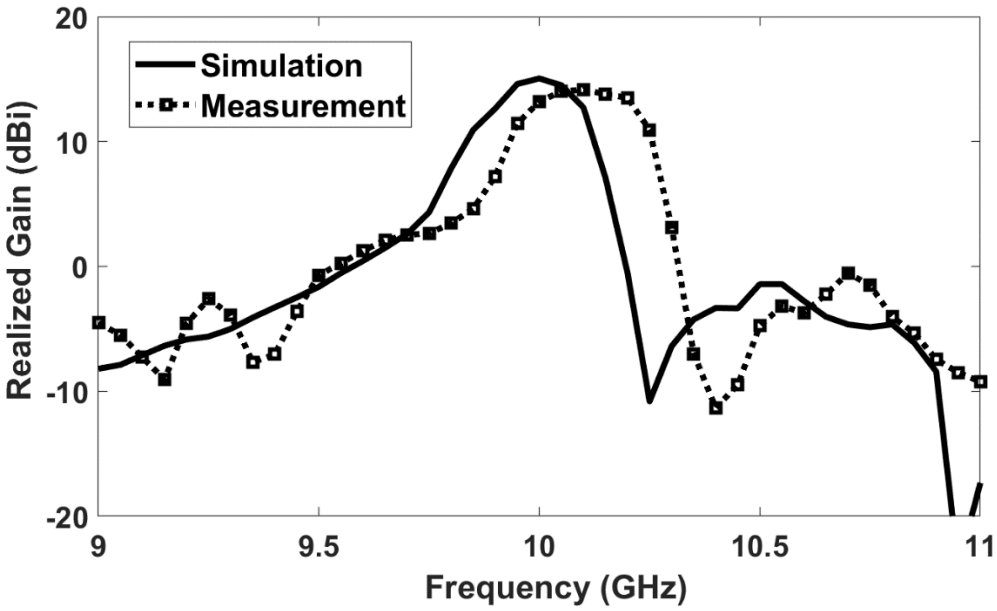

Fig. 6.13. Realized gain of antenna with MEFSS cover.

Fig. 6.14 depicts the E- and H-plane radiation patterns of the antenna structure. Since the resonant frequency of the fabricated antenna is shifted, the measured radiation patterns are for 10.15 GHz, while the simulated radiation patterns are depicted at 10 GHz. An acceptable agreement is achieved between the simulated and measured results, especially around the broadside. The antenna polarization is linear as the cross-polarization levels are at least 24 dB under the co-polarization ones for both E- and H-plane at boresight. As shown in Fig. 6.14(a), the measured side-lobe-level in E-plane is better than -10 dB at the center frequency. Besides, the measured half power beamwidths are 18^{o} and 26^{o} in E- and H-plane, respectively.

6.4 Wideband PFC Antennas

Since the resonance condition in the FPC antenna discussed in previous section happens at a single frequency, as shown in Fig. 6.7, the operational bandwidth achieved was somewhat limited. There are techniques to increase the bandwidth in antennas with FSS structures. For example, several FSS layers can be used to create close resonances to increase the bandwidth. In

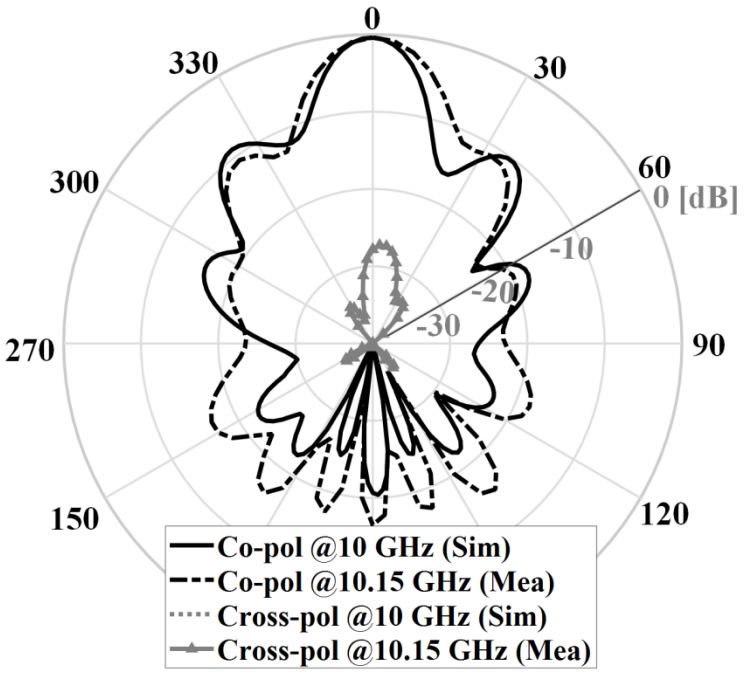

(a)

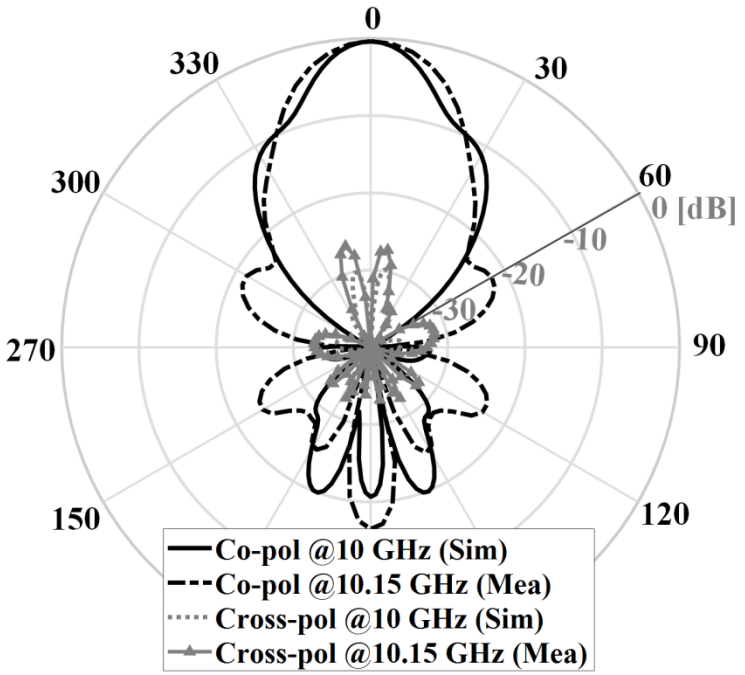

(b)

Fig. 6.14. Radiation patterns of the antenna with MEFSS cover, (a) E-plane, and (b) H-plane.

fact, multi-layer FSS structures create a positive phase gradient and increase the frequencies that satisfy the resonance condition. In this section, our goal is to design wideband FPC antenna with very low height compared with wavelength for on-chip applications.

6.4.1 Wideband MEFSS Antenna Geometry and Principles of Operation

Due to the issues of antenna-on-chip such as low efficiency, the antenna is designed as a part of MEFSS cover and then top metal layer of chip is used to excite the antenna. Slot and patch antennas are used as radiator at the bottom layer of wideband MEFSS structure. As a result, the parallel plate waveguide modes are propagating between the bottom layer of MEFSS structure and top layer of chip. To suppress these modes, electromagnetic bandgap (EBG) structures are utilized on the top layer of chip as displayed in Fig. 6.15. Furthermore, for a wideband gain enhancement, a multi-layer MEFSS cover with N layers of PRS structures and separation layers is employed. The feed line on the chip excites the slot antenna embedded in MEFSS cover. Fig. 6.15(b) shows the aforementioned coupling mechanism in more detail. For a wider bandwidth, the shape of feed line, slot antenna, and microstrip patch must be designed in a way that two adjacent resonances happen over the operating impedance bandwidth. The structure can be optimized for a good impedance matching over the band of interest.

Fig. 6.16 shows exploded and top views of unit-cell structure of the PRS layers in MEFSS cover. These N layers of PRS structures are separated by thin layers of dialectic materials. Each PRS layer consists of inductive and capacitive elements etched on each side of a dielectric layer. Each PRS layer and the intermediate substrate constitute a transmission-line resonator. If those resonances are tailored correctly, a wideband gain enhancement can be achieved. Depending on the desired bandwidth, a few PRS layers are selected for the MEFSS structure. The values for inductors and capacitors of grids and patches of each layer can be calculated by (6.1) and (6.2), respectively.

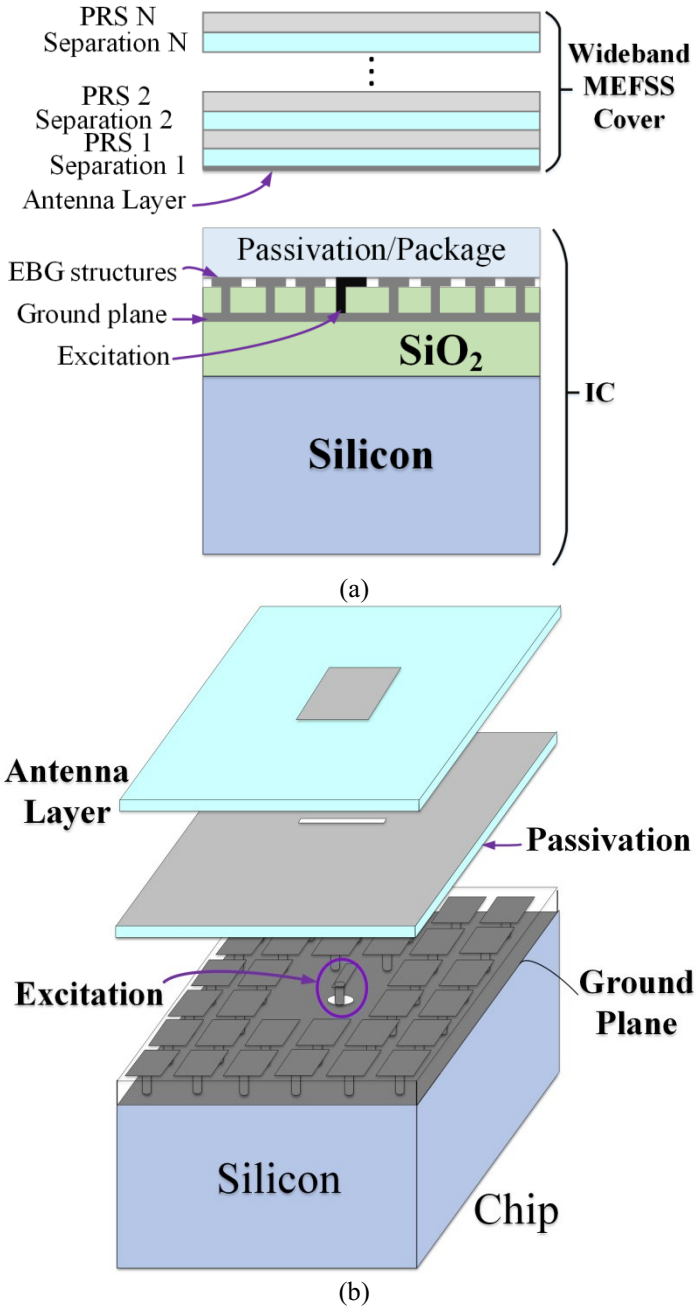

Fig. 6.15. Stacked view of (a) chip with the feed and EBG structures and wideband MEFSS cover, and (b) excitation of slot antenna by a feed line in chip.

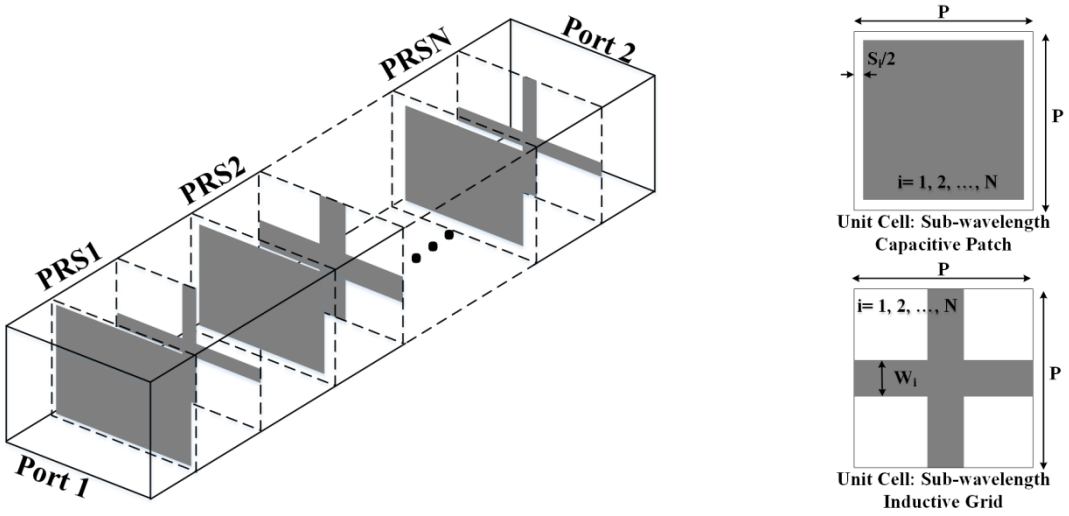

(a) (b)

Fig. 6.16. Unit-cell of PRS layers in MEFSS cover, (a) exploded view and (b) top view.

Fig. 6.17(a) depicts the geometry of the PRS layers of the wideband MEFSS. The number of unit-cells should be enough for a great wideband performance. The permeability/permittivity of ith PRS layer and ith separation layer are shown with $\mu_{PRSi}/\varepsilon_{PRSi}$ and $\mu_{Si}/\varepsilon_{Si}$, respectively, where i=1,2,…,N. The equivalent transmission line model of one unit-cell of these PRS layers is depicted in Fig. 6.17(b). In the model, the PRS and separation layers are modeled by transmission lines with characteristic impedances of $Z_{PRSi}= Z_0\ \eta_{PRSi}$ and $Z_{Si}= Z_0\ \eta_{Si}$, respectively, where $\eta_{PRSi} = \sqrt{\mu_{PRSi}/\varepsilon_{PRSi}}$, $\eta_{Si} = \sqrt{\mu_{Si}/\varepsilon_{Si}}$, and *i=1,2,...,N*.

The PRS layers and the ground plane on which the slot antenna is etched establish a FPC which may increase the antenna gain. In this mechanism, the PRS layers reflect the majority of the propagating wave back to the ground plane. The first separation layer and antenna layer, drawn in Fig. 6.15, constitute the cavity. The transmission line model of the wideband MEFSS cover is shown in Fig. 6.18 in which the PRS layers are substituted by their two-port equivalent network. The infinite transmission line with the characteristic impedance Z_0 models the free-space area above the structure. Also, Z_{S1} and Z_a are the characteristic impedance of the first separation layer and antenna layer, respectively.

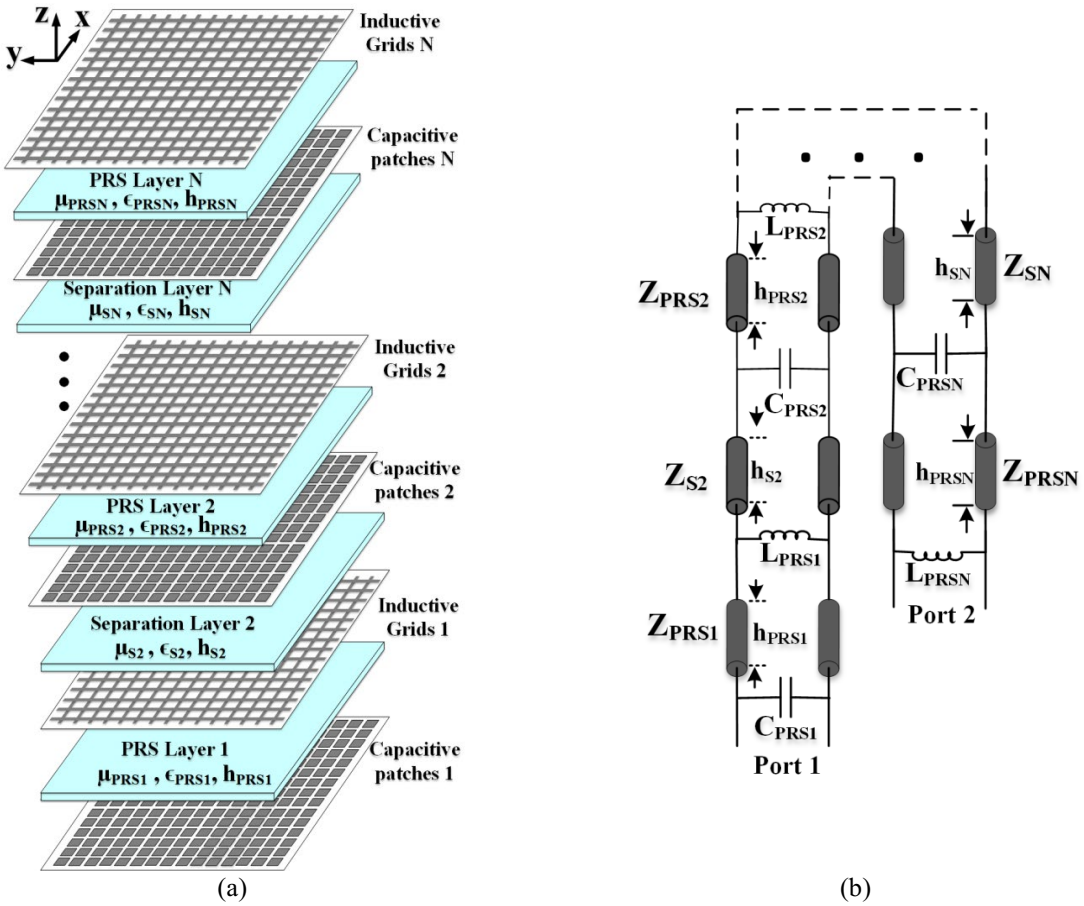

(a) (b)

Fig. 6.17. Wideband MEFSS cover (a) geometry, and (b) its equivalent transmission line model.

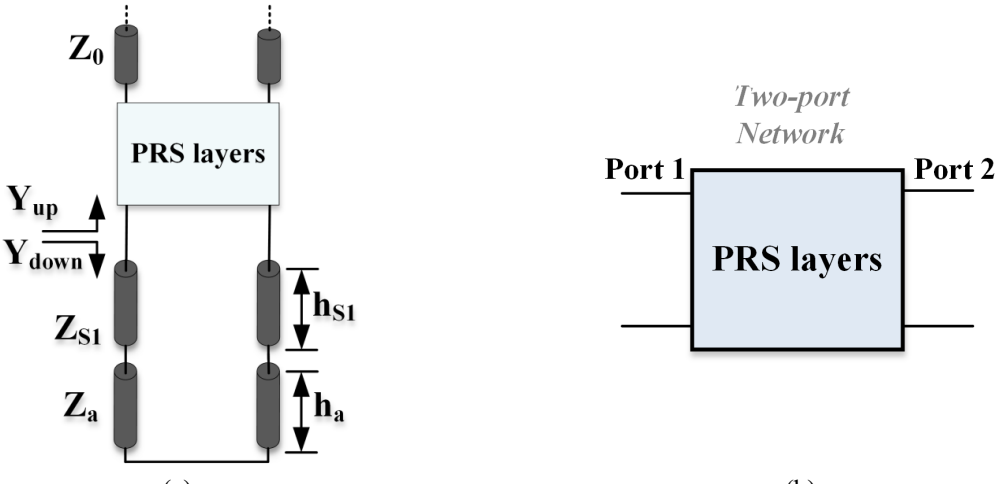

(a) (b)

Fig. 6.18. Transmission line model of the wideband MEFSS cover stablishing a FPC, and (b) Two-port equivalent network of the PRS layers.

The resonances of FPC in Fig. 6.18, which provide the maximum broadside gain, happen when $Im\ (Y_{up}+Y_{down})= 0$, where Y_{up} and Y_{down} are upward and downward admittances, respectively, indicated in Fig. 6.18(a). For a wideband gain enhancement, the resonance condition must happen in several frequencies close enough to each other. For certain substrate layers with certain thickness, the values of inductors and capacitors of PRS layers can be obtained by imposing $Im\ (Y_{up})= -Im(Y_{down})$ at desired resonant frequencies close to each other. Afterward, by using (6.1) and (6.2), the approximate physical dimensions of the PRS layers are calculated. This step provides good initial values for MEFSS dimensions for optimizing the structure with the goal of achieving wideband gain enhancement.

6.4.2 Wideband MEFSS Cover Design

For prototyping purposes, a wideband MEFSS cover consisting of two PRS layers is designed at the center frequency of 10 GHz. The patch antenna, PRS1, and PRS2 are designed on Rogers 5880 with permittivity of 2.2, loss tangent of 0.0009 and with thicknesses of 0.79 mm, 1.57 mm, and 1.57 mm, respectively.

The two-port equivalent network of MEFSS cover is shown in Fig. 6.19. The inductors and capacitors of the equivalent model are selected in a way that three resonant frequencies occur around 10 GHz. Using ANSYS HFSS simulator, a unit-cell of the MEFSS structure can be designed to have three resonances around 10 GHz. The dimensions of inductor grids and capacitive patches of PRS1 and PRS2, and the separation layers 1 and 2 are obtained. Note that the materials of separation layers can be chosen arbitrary; however, since substrate boards with required thickness may not be commercially available, we selected separation layer 2 with the thickness of h_{S2} to be air with permittivity of 1.

Fig. 6.20 shows the obtained resonances around 10 GHz for the MEFSS structure with dimensions S_1= 0.2 mm, S_2= 0.8 mm, W_1=0.8 mm, W_2= 0.6 mm, h_{S1}= 1.1 mm and h_{S2}= 1.5 mm. As shown, the resonance condition happens at three close frequencies resulting in a wideband gain enhancement.

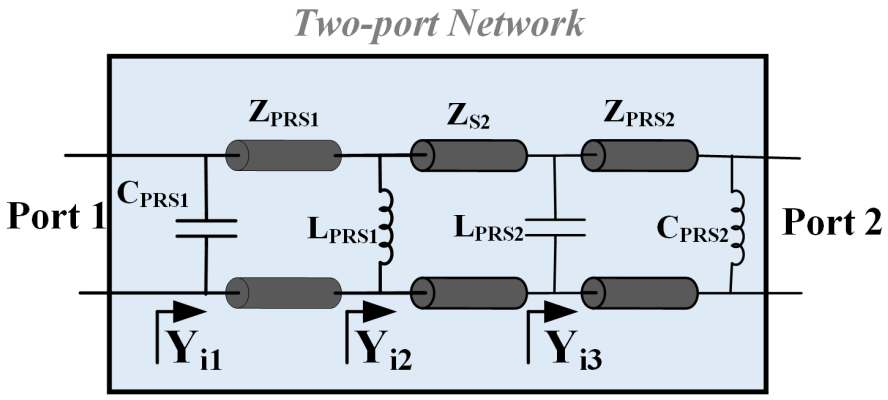

Fig. 6.19. Two-port equivalent network of the MEFSS cover with two PRS layers.

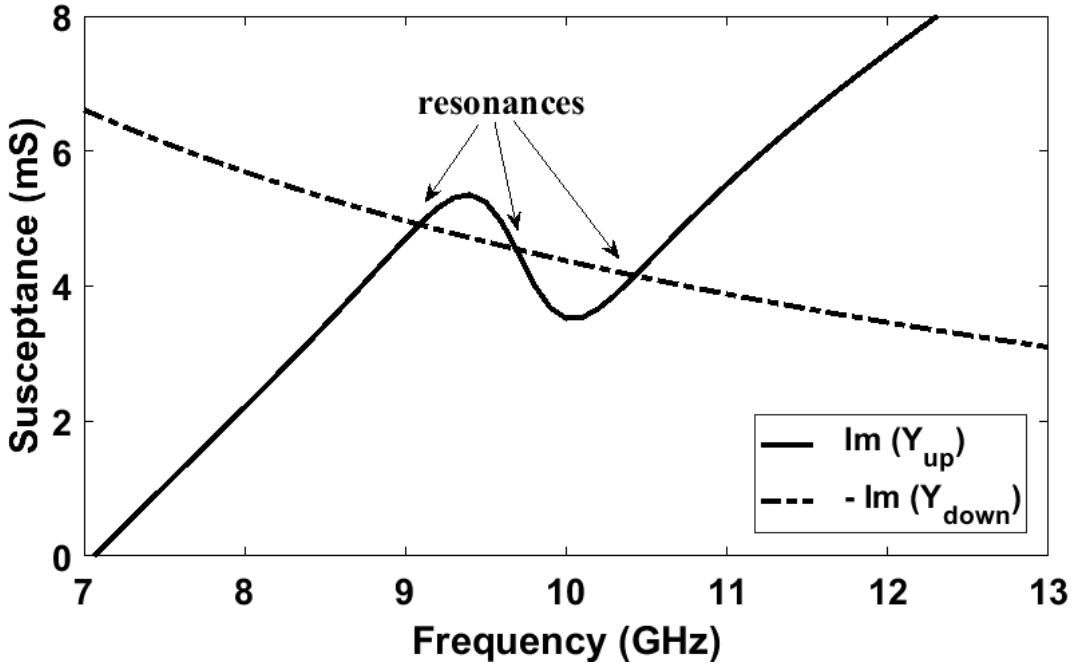

Fig. 6.20. Upward and downward susceptance values of the unit-cell designed for the resonant frequency of 10 GHz (unit-cell dimensions are P= 5.5mm, S_1= 0.2 mm, W_1= 0.8 mm, S_2= 0.8 mm, W_2= 1 mm, and h_{S2}= 1.5 mm).

6.4.3 Antenna Feed Design and Results

By coupling mechanism, the power from patch is coupled through the passivation layer to the antenna embedded inside the MEFSS layer. A trace inside the chip feeds the slot and patch in the MEFSS layer which is placed on top of the chip. Both passivation and feed layers are selected to be Rogers 5880 with the thickness of 1.57 mm, and 0.508 mm, respectively. Due to the existence of parallel plate modes between the shielding conductor inside the chip (feed layer) and the conductor on which the slot is etched (slot layer), antenna efficiency drops. To suppress those parallel plate modes, mushroom-type electromagnetic bandgap (EBG) structure is used. Fig. 6.21 shows the antenna integrated with MEFSS layer and the exploded view of the entire antenna. The MEFSS layer includes 13 unit-cells and its overall height is just 6.54 mm (~λ/5) which is very small compared to the height of conventional FPC geometries with two FSS layers (~λ) for wideband operation.

The unit-cell of the EBG is designed in a way that a bandgap is created in the desired bandwidth. Fig. 6.22 shows the dispersion diagram of the EBG structure for the unit-cell dimensions W_{EBG}= 5.5 mm, P_{EBG}= 6 mm. As shown, between the first two modes, a bandgap from 8.45 GHz to 11.8 GHz is created. Therefore, this EBG structure guarantees that no parallel plate mode is propagated between feed layer and slot layer around the bandwidth of interest.

The simulated reflection coefficient and realized gain of the proposed on-chip antenna with wideband MEFSS cover are plotted in Fig. 6.23. As shown, an impedance bandwidth of 8.5% from 9.55 GHz to 10.4 GHz is obtained for $|S_{11}|$<-10 dB. Over the frequencies 9.4-10.45 GHz, a realized gain of more than 12.6 is achieved. Furthermore, the maximum realized gain of 17.5 dBi happens at 10.3 GHz. The radiation pattern of the proposed on-chip antenna with wideband MEFSS cover is shown in Fig. 6.24. As shown, a side-lobe-level better than 15 dB is achieved. Also the cross-polarizations of both E-plane and H-plane are at least less than 20 dB less than their co-polarizations indicating the antenna polarization is linear.

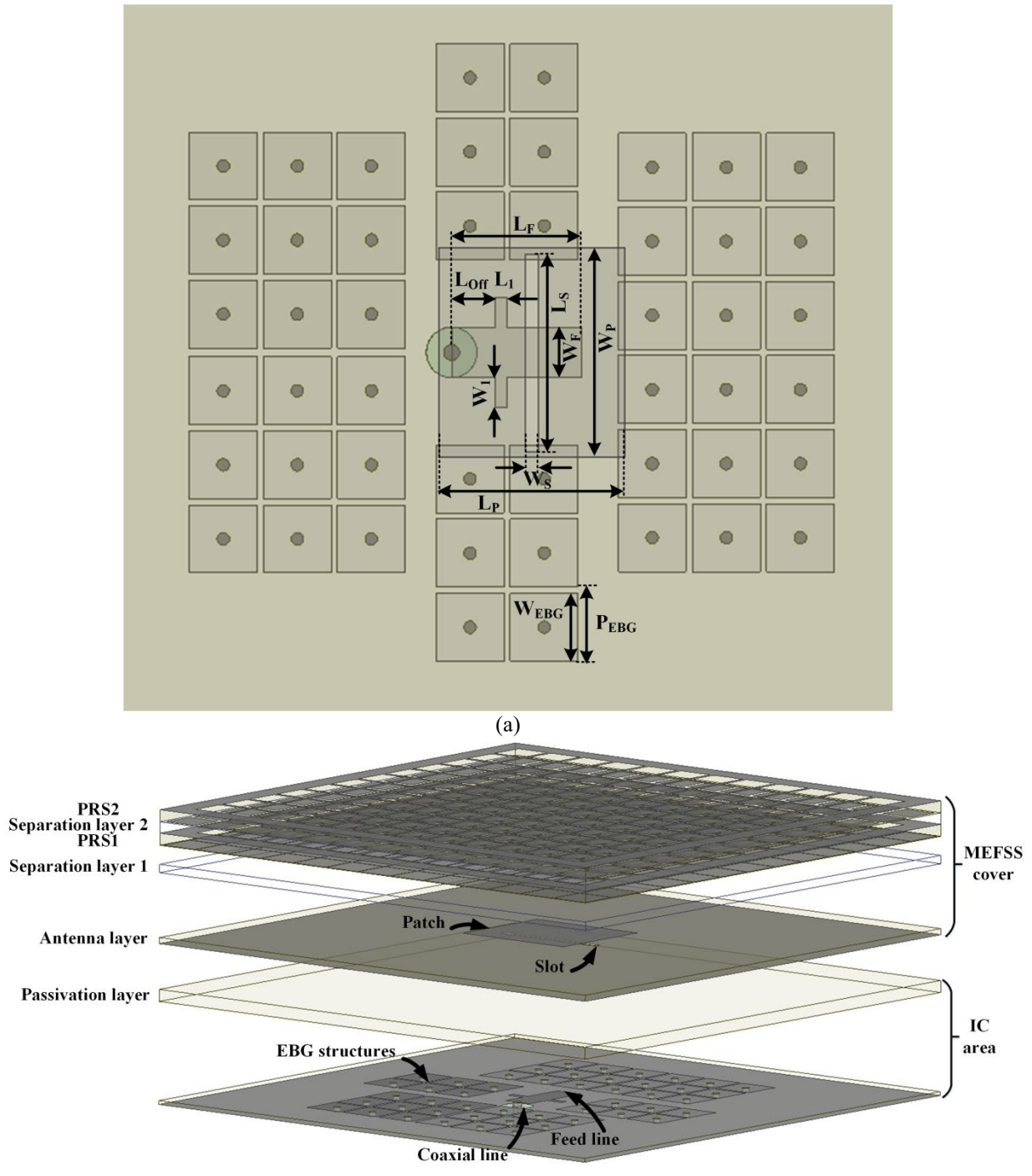

Fig. 6.21. (a) Top View of antenna integrated inside the MEFSS layer, and (b) exploded view of the entire structure. The design parameters are L_P= 15 mm, W_P= 17 mm, L_S= 16 mm, W_S= 1 mm, L_F= 10.5 mm, W_F= 4 mm, L_{Off}= 2.5 mm, W_1= 2.5 mm, L_1= 0.5 mm, W_{EBG}= 5.5 mm, P_{EBG}= 6 mm.

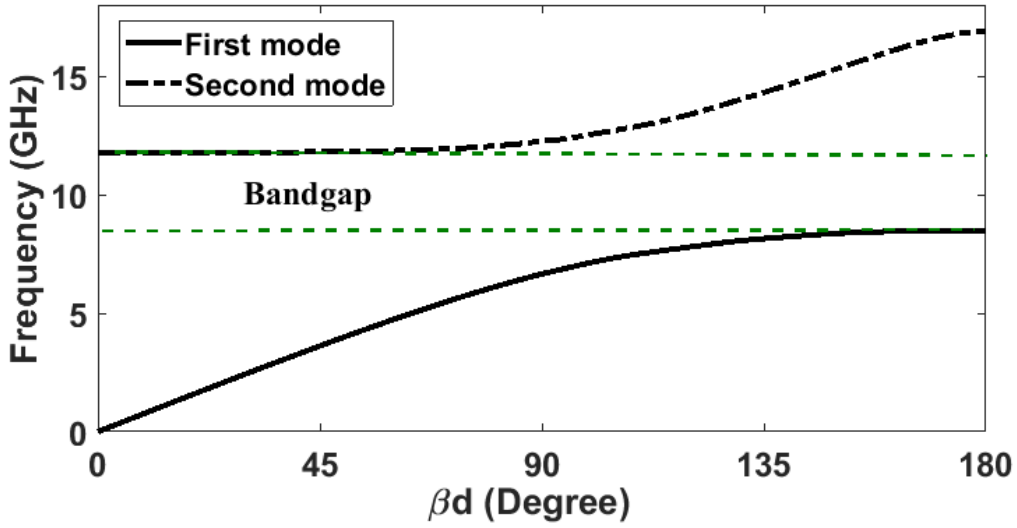

Fig. 6.22. Dispersion diagram of the EBG structure used in the on-chip antenna.

Using MEFSS structures for radiation enhancement of on-chip antenna, two main advantages are achieved: First, the MEFSS cover can be separately added on top of the chip and works based on coupling mechanism and second, this technique makes the thickness of the structure very small which is important in RFIC applications.

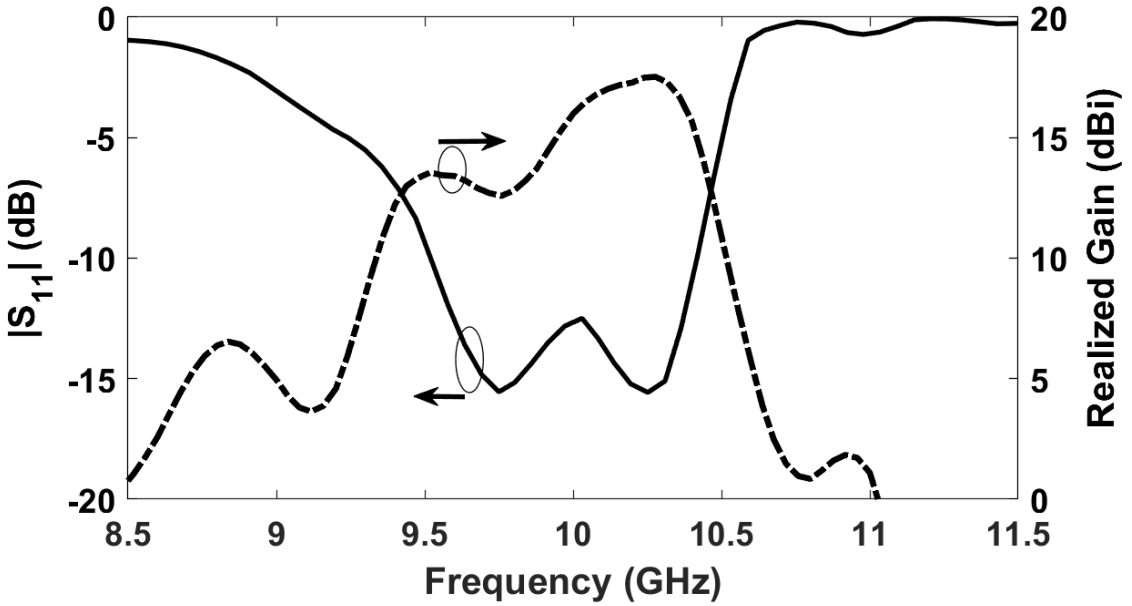

Fig. 6.23. Reflection coefficient and realized gain of the proposed on-chip antenna with wideband MEFSS cover.

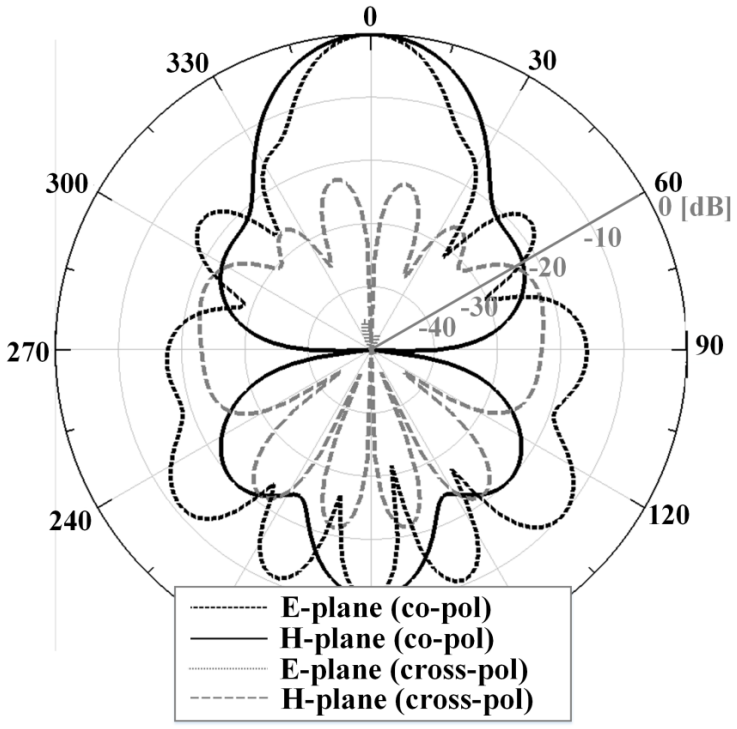

Fig. 6.24. Radiation pattern of the proposed on-chip antenna with wideband MEFSS cover at 10 GHz.

Chapter 7
Conclusion and Future Directions

In this chapter, we summarize all the contribution of this work and conclude the materials presented. Then, the possible future developments are suggested.

7.1 Overall Contributions

Even though the conventional corrugated and FPC antennas are known since many years ago, new technologies and applications stimulate the research on these types of antennas with more details, as described in this thesis.

In particular, the main goal of this work has been the design and analysis of two classes of high-gain planar antennas for the possible applications in radar, space, and satellite communications. The antennas were designed to be integrated with the rest of circuit on PCB or IC, and to be compact and high-efficient. Different TM_{01} to TE_{11} mode converters for high-power applications, high-gain single- and dual-band corrugated antennas, and high-gain narrowband and wideband MEFSS covers for RFICs were proposed, fabricated, and measured in this work.

In the case of high-power applications, TM_{01} to TE_{11} mode converters are required to convert the TM_{01} mode of high power source to TE_{11} mode necessary to feed corrugated antennas. Three categories of TM_{01} to TE_{11} mode converters were designed for the maximum conversion efficiency over a wide bandwidth, printed using 3D printing technology, and measured.

A technique to fabricate corrugated antennas on PCBs using SIW technology was proposed. Using this technique, a corrugated antenna was designed and fabricated on PCBs. All parts of the antenna such as feed line, cavity, and corrugations were fabricated with regular PCB manufacturing. The experimental results showed the reliability of this technique. To minimize the

time of simulation and optimization process in designing large-size corrugated antennas, a fast approach for estimating the radiation performance of corrugated antennas based on analyzing a unit-cell of corrugated structure was proposed. The resonant frequency, spectral bandwidth, and directivity were estimated using the surface susceptance of corrugated structure. The effect of corrugations' width, height, and the materials' permittivity inside corrugations was parametrically studied. A corrugated antenna based on the unit-cell analysis was designed and fabricated and measured to verify the proposed approach.

Two dual-band corrugated antennas were proposed using two different corrugations' dimensions to create dual-band operation. To solve the problem of high front-to-back ratio of transmission line feed, two dual-band feeder antennas were proposed which could feed the corrugated antennas from inside the cavity. These feeder antennas could provide a close-to-TE_{11} mode, which is necessary for constructive radiation pattern, on the output aperture of the cavity. The dual-band corrugated structure was integrated with the dual-band feeder antenna to create the dual-band high-gain corrugated antenna. The dual-band operation of all antennas was verified experimentally.

The radiation performance of an on-chip antenna can be improved off of the chip by placing a MEFSS cover on top of it. Using the TEN model of the structure, it was shown that the MEFSS structure can be designed in a way that the resonance condition happens. This would improve the gain of single antenna embedded in the chip. A scaled prototype of MEFSS cover and the on-chip antenna was fabricated and measured. The measured results showed the reliability of the proposed technique for gain enhancement off of RFICs. A wideband MEFSS cover was proposed and designed to solve the problem of very narrowband gain enhancement of single-layer MEFSS structure.

7.2 Future Directions

Chapter 3 proposed several TM_{01} to TE_{11} mode converters. All those converters were designed and printed with 100% filling percentage. However, being capable of 3D printing with different filling percentages, TM_{01} to TE_{11} mode converters with better conversion efficiency and wider bandwidth may be designed. On the other hand, the 3D printer used in this work could just print dielectric materials. The assembly process of TM_{01} to TE_{11} mode converters may be eliminated by employing a better 3D printer that could print both conductor and dielectric all-in-one process.

Chapter 4 proposed a fast approach for performance estimation of corrugated antennas by using a unit-cell of corrugated structure. By using the proposed approach, wideband, and dual-band corrugated unit-cell may be designed on multi-layer PCBs. Using these unit-cells, wideband, and dual-band corrugated antennas may be designed. Moreover, the analysis performed in chapter 4 was for corrugated antennas with high-gain at broadside. However, the similar analysis can be performed for corrugated antennas with off-axis radiation pattern. One of the limitation of corrugated antennas discussed in chapter 4, was the low aperture efficiency. The reason for this problem is the direction propagation of the cavity into free space. By placing a surface wave launcher that could convert the TE_{11} mode of the cavity to surface waves efficiently, the efficiency of corrugated antenna will be significantly improved. Moreover, sensors and sensor antennas have found many applications in smart homes and cities [118-122], recently. The corrugated antennas can be used as sensor antennas in several application.

The dual-band high-gain antenna corrugated antenna designed in chapter 5 may find many other applications rather than satellite communication. There is still a possibility to increase the gain of this antenna. Using soft corrugated structure around the edge of the antenna may decrease the edge diffraction and enhance the antenna gain. Integrating both soft corrugated structures and the regular corrugations may be considered in future works.

In chapter 6, the off chip methods were proposed to enhance the radiation characteristics of on-chip antennas. Using MEFSS structures, narrow-band and wideband antenna mechanisms were designed. As a further work for chapter 6, MEFSS covers with beamforming or beam-

switching capabilities may be proposed. Using varactor diodes, the phase of PRS structures can be changed in order to have a beamforming over a desired range of frequencies. This may have many applications such as radar instruments. All these designs can be performed for RFICs at higher frequencies. In fact, using low-loss materials such as Parylene membranes, the fabrication of MEFSS covers with different functionality is feasible.

7.3 List of Publications

In this section, the contributions made out of this work during the last four years including both journal and conference papers are listed.

7.3.1 Journal Papers

[J1] M. M. Honari, P. Mousavi, and K. Sarabandi "Wideband Radiation Enhancement of RFICs Using Multi-layer Miniaturized-Element Frequency Selective Surface Covers," Prepared to be submitted to *IEEE Transactions on Antennas and Propagation.*

[J2] M. M. Honari, K. Sarabandi and P. Mousavi, "Dual-Band High-Gain Planar Corrugated Antennas with Integrated Feeding Structure," Prepared to be submitted to *IEEE Transactions on Antennas and Propagation.*

[J3] M. M. Honari, K. Sarabandi, A. Grbic, and P. Mousavi, "Design and Analysis of Corrugated Antennas Based on Corrugations' Surface Susceptance," Prepared to be submitted to *IEEE Transactions on Antennas and Propagation*.

[J4] M. M. Honari, P. Mousavi, and K. Sarabandi " Miniaturized-Element Frequency Selective Surface Metamaterials: A Solution to Enhance Radiation Off of RFICs," Major Revision in *IEEE Transactions on Antennas and Propagation.*

[J5] M. M. Honari, R. Mirzavand, S. Aslanzadeh, H. Saghlatoon, and P. Mousavi, "Wideband Printed TM_{01} to TE_{11} Mode Converters," Accepted in *IEEE Access*.

[J6] M. M. Honari, R. Mirzavand, J. Melzer, A. K. Iyer and P. Mousavi, "Dual-Band Open-Ended Waveguide Feeder Antennas with Collinear Feed Design," *IEEE Transactions on Antennas and*

Propagation, vol. 66, no. 11, pp. 6358-6363, Nov. 2018.

[J7] M. M. Honari, R. Mirzavand and P. Mousavi, "A High-Gain Planar Surface Plasmon Wave Antenna Based on Substrate Integrated Waveguide Technology with Size Reduction," *IEEE Transactions on Antennas and Propagation*, vol. 66, no. 5, pp. 2605-2609, May 2018.

[J8] M. M. Honari, R. Mirzavand, J. Melzer and P. Mousavi, "A New Aperture Antenna Using Substrate Integrated Waveguide Corrugated Structures for 5G Applications," *IEEE Antennas and Wireless Propagation Letters*, vol. 16, pp. 254-257, 2017.

[J9] M. M. Honari, R. Mirzavand, H. Saghlatoon and P. Mousavi, "A Dual-Band Low-Profile Aperture Antenna With Substrate-Integrated Waveguide Grooves," *IEEE Transactions on Antennas and Propagation*, vol. 64, no. 4, pp. 1561-1566, April 2016.

7.3.2 Conference Papers

[C1] M. M. Honari, K. Sarabandi and P. Mousavi, "A Low-Profile Bull's-eye Antennas for Dual-Band Application," Accepted in *2019 IEEE International Symposium on Antennas and Propagation (APSURSI).*

[C2] M. M. Honari, P. Mousavi, and K. Sarabandi, "Gain Enhancement of On-Chip Antennas Using Miniaturized-Element Frequency Selective Surfaces," Accepted in *2019 IEEE International Symposium on Antennas and Propagation (APSURSI).*

[C3] M. M. Honari, R. Mirzavand, H. Saghlatoon and P. Mousavi, "A compact substrate integrated waveguide cavity backed antenna with stable radiation patterns for dual-band applications," *12th European Conference on Antennas and Propagation (EuCAP 2018)*, London, 2018, pp. 1-3.

[C4] M. M. Honari, R. Mirzavand and P. Mousavi, "Low-profile dual-band corrugated SIW antenna," *2016 IEEE International Symposium on Antennas and Propagation (APSURSI)*, Fajardo, 2016, pp. 1225-1226.

Bibliography

[1] C. J. Vourch and T. D. Drysdale, "V-band “bull's eye” antenna for cubesat applications," *IEEE Antennas and Wireless Propagation Letters,* vol. 13, pp. 1092-1095, 2014.

[2] C.-W. Yuan and Q. Zhang, "Design of a TM_{01}-TE_{01} Transmission Line for High-Power Microwave Applications," *IEEE Transactions on Plasma Science,* vol. 37, no. 10, pp. 1908-1915, 2009.

[3] D. Y. Na, J. H. Kim, Y. B. Park, and K.-Y. Jung, "Enhanced and directional transmission through a slit surrounded with grooves in a conducting plane," *IET Microwaves, Antennas & Propagation,* vol. 7, no. 10, pp. 843-850, 2013.

[4] S. Steshenko, M. Zhadobov, R. Sauleau, A. A. Kirilenko, and A. V. Boriskin, "Beam-forming capabilities of waveguide feeds assisted by corrugated flanges," *IEEE Transactions on Antennas and Propagation,* vol. 63, no. 12, pp. 5548-5560, 2015.

[5] X. Gao, S. M. Li, W. P. Cao, Q. Cheng, H. F. Ma, and T. J. Cui, "A highly directive slot antenna with sidewall corrugated structure," *IEEE Antennas and Wireless Propagation Letters,* vol. 12, pp. 1582-1585, 2013.

[6] R. Han, Y. Zhang, Y. Kim, D. Y. Kim, H. Shichijo, and E. Afshari, "Active terahertz imaging using Schottky diodes in CMOS: Array and 860-GHz pixel," *IEEE Journal of Solid-State Circuits,* vol. 48, no. 10, pp. 2296-2308, 2013.

[7] W. T. Khan *et al.*, "A D-band micromachined end-fire antenna in 130-nm SiGe BiCMOS technology," *IEEE Transactions on Antennas and Propagation,* vol. 63, no. 6, pp. 2449-2459, 2015.

[8] Y. P. Zhang, M. Sun, and L. Guo, "On-chip antennas for 60-GHz radios in silicon technology," *IEEE Transactions on Electron Devices,* vol. 52, no. 7, pp. 1664-1668, 2005.

[9] S. Pan, F. Caster, P. Heydari, and F. Capolino, "A 94-GHz extremely thin metasurface-based BiCMOS on-chip antenna," *IEEE Transactions on Antennas and Propagation,* vol. 62, no. 9, pp. 4439-4451, 2014.

[10] M. Nafe, A. Syed, and A. Shamim, "Gain-enhanced on-chip folded dipole antenna utilizing artificial magnetic conductor at 94 GHz," *IEEE Antennas and Wireless Propagation Letters,* vol. 16, pp. 2844-2847, 2017.

[11] H. Chu, Y.-X. Guo, T.-G. Lim, Y. M. Khoo, and X. Shi, "135-GHz micromachined on-chip antenna and antenna array," *IEEE Transactions on Antennas and Propagation,* vol. 60, no. 10, pp. 4582-4588, 2012.

[12] A. Babakhani, X. Guan, A. Komijani, A. Natarajan, and A. Hajimiri, "A 77-GHz phased-array transceiver with on-chip antennas in silicon: Receiver and antennas," *IEEE Journal of Solid-State Circuits,* vol. 41, no. 12, pp. 2795-2806, 2006.

[13] J. M. Edwards and G. M. Rebeiz, "High-efficiency elliptical slot antennas with quartz superstrates for silicon RFICs," *IEEE Transactions on Antennas and Propagation,* vol. 60, no. 11, pp. 5010-5020, 2012.

[14] Y.-C. Ou and G. M. Rebeiz, "Differential microstrip and slot-ring antennas for millimeter-wave silicon systems," *IEEE Transactions on Antennas and Propagation,* vol. 60, no. 6, pp. 2611-2619, 2012.

[15] P. Bijumon, Y. Antar, A. Freundorfer, and M. Sayer, "Dielectric resonator antenna on silicon substrate for system on-chip applications," *IEEE Transactions on Antennas and Propagation,* vol. 56, no. 11, pp. 3404-3410, 2008.

[16] M.-R. Nezhad-Ahmadi, M. Fakharzadeh, B. Biglarbegian, and S. Safavi-Naeini, "High-efficiency on-chip dielectric resonator antenna for mm-wave transceivers," *IEEE Transactions on Antennas and Propagation,* vol. 58, no. 10, pp. 3388-3392, 2010.

[17] A. Hessel, "General Characteristics of Traveling-Wave Antennas, Antenna Theory-Part 2, Chapter 19, Appendix B, 1969," ed: McGraw-Hill Book Company, New York.

[18] R. Anwar, L. Mao, and H. Ning, "Frequency selective surfaces: a review," *Applied Sciences,* vol. 8, no. 9, p. 1689, 2018.

[19] A. Pirhadi, M. Hakkak, F. Keshmiri, and R. K. Baee, "Design of compact dual band high directive electromagnetic bandgap (EBG) resonator antenna using artificial magnetic conductor," *IEEE Transactions on Antennas and Propagation,* vol. 55, no. 6, pp. 1682-1690, 2007.

[20] A. Abbaspour-Tamijani, K. Sarabandi, and G. M. Rebeiz, "Antenna-filter-antenna arrays as a class of bandpass frequency-selective surfaces," *IEEE Transactions on Microwave Theory and Techniques,* vol. 52, no. 8, pp. 1781-1789, 2004.

[21] F. Khosravi, H. Moghadas, and P. Mousavi, "A GNSS antenna with a polarization selective surface for the mitigation of low-angle multipath interference," *IEEE Transactions on Antennas and Propagation,* vol. 63, no. 12, pp. 5287-5295, 2015.

[22] M. U. Afzal and K. P. Esselle, "A low-profile printed planar phase correcting surface to improve directive radiation characteristics of electromagnetic band gap resonator antennas," *IEEE Transactions on Antennas and Propagation,* vol. 64, no. 1, pp. 276-280, 2016.

[23] M. N. Jazi, M. R. Chaharmir, J. Shaker, and A. R. Sebak, "Broadband transmitarray antenna design using polarization-insensitive frequency selective surfaces," *IEEE Transactions on Antennas and Propagation,* vol. 64, no. 1, pp. 99-108, 2016.

[24] A. Edalati and K. Sarabandi, "Reflectarray antenna based on grounded loop-wire miniaturised-element frequency selective surfaces," *IET Microwaves, Antennas & Propagation,* vol. 8, no. 12, pp. 973-979, 2014.

[25] K. Sarabandi and N. Behdad, "A frequency selective surface with miniaturized elements," *IEEE Transactions on Antennas and Propagation,* vol. 55, no. 5, pp. 1239-1245, 2007.

[26] A. Edalati and K. Sarabandi, "Wideband, wide angle, polarization independent RCS

reduction using nonabsorptive miniaturized-element frequency selective surfaces," *IEEE Transactions on Antennas and Propagation,* vol. 62, no. 2, pp. 747-754, 2014.

[27] M. Gao, S. M. A. M. H. Abadi, and N. Behdad, "A dual-band, inductively coupled miniaturized-element frequency selective surface with higher order bandpass response," *IEEE Transactions on Antennas and Propagation,* vol. 64, no. 8, pp. 3729-3734, 2016.

[28] M. Kashanianfard and K. Sarabandi, "Metamaterial inspired optically transparent band-selective ground planes for antenna applications," *IEEE Transactions on Antennas and Propagation,* vol. 61, no. 9, pp. 4624-4631, 2013.

[29] N. Guérin, S. Enoch, G. Tayeb, P. Sabouroux, P. Vincent, and H. Legay, "A metallic Fabry-Perot directive antenna," *IEEE Transactions on Antennas and Propagation,* vol. 54, no. 1, pp. 220-224, 2006.

[30] A. Hosseini, F. Capolino, and F. De Flaviis, "Gain enhancement of a V-band antenna using a Fabry-Pérot cavity with a self-sustained all-metal cap with FSS," *IEEE Transactions on Antennas and Propagation,* vol. 63, no. 3, pp. 909-921, 2015.

[31] G. V. Trentini, "Partially reflecting sheet arrays," *IRE Transactions on Antennas and Propagation,* vol. 4, no. 4, pp. 666-671, 1956.

[32] H. A. Bethe, "Theory of diffraction by small holes," *Physical review,* vol. 66, no. 7-8, p. 163, 1944.

[33] T. W. Ebbesen, H. J. Lezec, H. Ghaemi, T. Thio, and P. A. Wolff, "Extraordinary optical transmission through sub-wavelength hole arrays," *Nature,* vol. 391, no. 6668, p. 667, 1998.

[34] R. W. Wood, "On a remarkable case of uneven distribution of light in a diffraction grating spectrum," *Proceedings of the Physical Society of London,* vol. 18, no. 1, p. 269, 1902.

[35] L. Rayleigh, "Note on the remarkable case of diffraction spectra described by Prof. Wood (from Philosophical Magazine 1907)," *SPIE MILESTONE SERIES MS,* vol. 83, pp. 291-291, 1993.

[36] F. J. Garcia-Vidal, L. Martin-Moreno, T. Ebbesen, and L. Kuipers, "Light passing through subwavelength apertures," *Reviews of Modern Physics,* vol. 82, no. 1, p. 729, 2010.

[37] D. E. Grupp, H. J. Lezec, T. Thio, and T. W. Ebbesen, "Beyond the Bethe Limit: Tunable Enhanced Light Transmission Through a Single Sub - Wavelength Aperture," *Advanced materials,* vol. 11, no. 10, pp. 860-862, 1999.

[38] F. Garcia-Vidal and L. Martin-Moreno, "Transmission and focusing of light in one-dimensional periodically nanostructured metals," *Physical Review B,* vol. 66, no. 15, p. 155412, 2002.

[39] H. J. Lezec *et al.*, "Beaming light from a subwavelength aperture," *Science,* vol. 297, no. 5582, pp. 820-822, 2002.

[40] F. García-Vidal, H. Lezec, T. Ebbesen, and L. Martin-Moreno, "Multiple paths to enhance optical transmission through a single subwavelength slit," *Physical Review Letters,* vol. 90, no. 21, p. 213901, 2003.

[41] M. Beruete, I. Campillo, J. Dolado, J. Rodríguez-Seco, E. Perea, and M. Sorolla, "Enhanced microwave transmission and beaming using a subwavelength slot in corrugated plate," *IEEE Antennas and Wireless Propagation Letters,* vol. 3, no. 16, pp. 328-331, 2004.

[42] M. Beruete, M. Sorolla, I. Campillo, and J. Dolado, "Subwavelength slotted corrugated plate with enhanced quasioptical millimeter wave transmission," *IEEE microwave and wireless components letters,* vol. 15, no. 4, pp. 286-288, 2005.

[43] D. Jackson, J. Chen, R. Qiang, F. Capolino, and A. Oliner, "The role of leaky plasmon waves in the directive beaming of light through a subwavelength aperture," *Optics Express,* vol. 16, no. 26, pp. 21271-21281, 2008.

[44] D. Jackson, A. Oliner, T. Zhao, and J. Williams, "Beaming of light at broadside through a subwavelength hole: Leaky wave model and open stopband effect," *Radio science,* vol. 40, no. 06, pp. 1-12, 2005.

[45] D. Jackson, T. Zhao, J. Williams, and A. Oliner, "Leaky surface-plasmon theory for dramatically enhanced transmission through a sub-wavelength aperture, Part II: Leaky-wave antenna model," in *IEEE Antennas and Propagation Society International Symposium. Digest. Held in conjunction with: USNC/CNC/URSI North American Radio Sci. Meeting (Cat. No. 03CH37450)*, 2003, vol. 2, pp. 1095-1098: IEEE.

[46] A. Sutinjo and M. Okoniewski, "A simple leaky-wave analysis of 1-D grooved metal structure for enhanced microwave radiation," *IEEE Transactions on Antennas and Propagation,* vol. 60, no. 6, pp. 2719-2726, 2012.

[47] A. P. Hibbins, J. R. Sambles, and C. R. Lawrence, "Gratingless enhanced microwave transmission through a subwavelength aperture in a thick metal plate," *Applied Physics Letters,* vol. 81, no. 24, pp. 4661-4663, 2002.

[48] H. Raether, *Surface plasmons on smooth and rough surfaces and on gratings*. Springer-Verlag Berlin An, 2013.

[49] M. Guglielmi and D. Jackson, "Broadside radiation from periodic leaky-wave antennas," *IEEE Transactions on Antennas and Propagation,* vol. 41, no. 1, pp. 31-37, 1993.

[50] G. Lovat, P. Burghignoli, and D. R. Jackson, "Fundamental properties and optimization of broadside radiation from uniform leaky-wave antennas," *IEEE Transactions on Antennas and Propagation,* vol. 54, no. 5, pp. 1442-1452, 2006.

[51] F. Monticone and A. Alu, "Leaky-wave theory, techniques, and applications: from microwaves to visible frequencies," *Proceedings of the IEEE,* vol. 103, no. 5, pp. 793-821, 2015.

[52] B. G. Cai, Y. B. Li, H. F. Ma, W. X. Jiang, Q. Cheng, and T. J. Cui, "Leaky-wave radiations by modulating surface impedance on subwavelength corrugated metal structures," *Scientific reports,* vol. 6, p. 23974, 2016.

[53] U. Beaskoetxea, S. Maci, M. Navarro-Cía, and M. Beruete, "3-D-printed 96 GHz Bull's-Eye antenna with off-axis beaming," *IEEE Transactions on Antennas and Propagation,* vol. 65, no. 1, pp. 17-25, 2017.

[54] H. Caglayan, I. Bulu, and E. Ozbay, "Off-axis beaming from subwavelength apertures," *Journal of Applied Physics,* vol. 104, no. 7, p. 073108, 2008.

[55] B. H. Fong, J. S. Colburn, J. J. Ottusch, J. L. Visher, and D. F. Sievenpiper, "Scalar and tensor holographic artificial impedance surfaces," *IEEE Transactions on Antennas and Propagation,* vol. 58, no. 10, pp. 3212-3221, 2010.

[56] C. Huang, C. Du, and X. Luo, "A waveguide slit array antenna fabricated with

subwavelength periodic grooves," *Applied Physics Letters,* vol. 91, no. 14, p. 143512, 2007.

[57] M. Beruete *et al.*, "Low-profile corrugated feeder antenna," *IEEE Antennas and Wireless Propagation Letters,* vol. 4, pp. 378-380, 2005.

[58] M. Beruete *et al.*, "Very low-profile" Bull's Eye" feeder antenna," *IEEE Antennas and Wireless Propagation Letters,* vol. 4, pp. 365-368, 2005.

[59] M. B. Díaz *et al.*, "Dual-band low-profile corrugated feeder antenna," *IEEE Transactions on antennas and propagation,* vol. 54, no. 2, pp. 340-350, 2006.

[60] M. Beruete *et al.*, "Very low profile and dielectric loaded feeder antenna," *IEEE Antennas and Wireless Propagation Letters,* vol. 6, pp. 544-548, 2007.

[61] H. Shi, X. Wei, Z. Zhao, X. Dong, Y. Lu, and C. Du, "A new surface wave antenna - based spoof surface plasmon mechanism," *Microwave and Optical Technology Letters,* vol. 52, no. 10, pp. 2179-2183, 2010.

[62] H. d. Lu, X. Lv, Z. j. Gao, and Y. Liu, "Experimental radiation characteristics of micromachined terahertz low - profile corrugated horn antenna," *Microwave and Optical Technology Letters,* vol. 57, no. 2, pp. 364-367, 2015.

[63] U. Beaskoetxea *et al.*, "77-GHz high-gain Bull's-Eye antenna with sinusoidal profile," *IEEE Antennas and Wireless Propagation Letters,* vol. 14, pp. 205-208, 2015.

[64] M. Beruete *et al.*, "Terahertz corrugated and bull's-eye antennas," *IEEE Transactions on Terahertz Science and Technology,* vol. 3, no. 6, pp. 740-747, 2013.

[65] S. Alkaraki, Y. Gao, and C. Parini, "Dual-layer corrugated plate antenna," *IEEE Antennas and Wireless Propagation Letters,* vol. 16, pp. 2086-2089, 2017.

[66] C. Huang, Z. Zhao, Q. Feng, and X. Luo, "A high-gain antenna consisting of two slot elements with a space larger than a wavelength," *IEEE Antennas and Wireless Propagation Letters,* vol. 9, pp. 159-162, 2010.

[67] U. Beaskoetxea and M. Beruete, "High aperture efficiency wide corrugations bull's-eye antenna working at 60 GHz," *IEEE Transactions on Antennas and Propagation,* vol. 65, no. 6, pp. 3226-3230, 2017.

[68] Y. Zhang, J. Von Hagen, M. Younis, C. Fischer, and W. Wiesbeck, "Planar artificial magnetic conductors and patch antennas," *IEEE Transactions on Antennas and Propagation,* vol. 51, no. 10, pp. 2704-2712, 2003.

[69] D. Sievenpiper, L. Zhang, R. F. Broas, N. G. Alexopolous, and E. Yablonovitch, "High-impedance electromagnetic surfaces with a forbidden frequency band," *IEEE Transactions on Microwave Theory and techniques,* vol. 47, no. 11, pp. 2059-2074, 1999.

[70] A. P. Feresidis, G. Goussetis, S. Wang, and J. C. Vardaxoglou, "Artificial magnetic conductor surfaces and their application to low-profile high-gain planar antennas," *IEEE Transactions on Antennas and Propagation,* vol. 53, no. 1, pp. 209-215, 2005.

[71] Y. Ge, K. P. Esselle, and T. S. Bird, "The use of simple thin partially reflective surfaces with positive reflection phase gradients to design wideband, low-profile EBG resonator antennas," *IEEE Transactions on Antennas and Propagation,* vol. 60, no. 2, pp. 743-750, 2012.

[72] K. Konstantinidis, A. P. Feresidis, and P. S. Hall, "Multilayer partially reflective surfaces

for broadband Fabry-Perot cavity antennas," *IEEE Transactions on Antennas and Propagation,* vol. 62, no. 7, pp. 3474-3481, 2014.

[73] X. Zhang and S. Li, "Compact circular waveguide TM_{02}-TE_{11} mode converter," *IET Microwaves, Antennas & Propagation,* vol. 11, no. 3, pp. 346-353, 2016.

[74] X. Yu, J. Deng, W. Cao, S. Li, X. Gao, and Y. Jiang, "Method for Synthesis of TE_{01}-TE_{11} Mode Converter for Gyrotron by the NURBS Technique," *IEEE Transactions on Microwave Theory and Techniques,* vol. 63, no. 2, pp. 326-330, 2015.

[75] X. Zhao, C. Yuan, L. Liu, S. Peng, H. Zhou, and D. Cai, "Solution to GW TEM-circular polarized TE_{11} mode converter design for high frequency bands," *IEEE Transactions on Microwave Theory and Techniques,* vol. 65, no. 2, pp. 432-437, 2017.

[76] B. M. Lee, W. S. Lee, Y. J. Yoon, and J. H. So, "X-band TM_{01}-TE_{11} mode converter with short length for high power," *Electronics Letters,* vol. 40, no. 18, pp. 1126-1127, 2004.

[77] W. Lawson, M. R. Arjona, B. P. Hogan, and R. Ives, "The design of serpentine-mode converters for high-power microwave applications," *IEEE Transactions on Microwave Theory and Techniques,* vol. 48, no. 5, pp. 809-814, 2000.

[78] S. Peng, C. Yuan, H. Zhong, and Y. Fan, "Design and experiment of a cross-shaped mode converter for high-power microwave applications," *Review of Scientific Instruments,* vol. 84, no. 12, p. 124703, 2013.

[79] A. Tribak, J. Zbitou, A. Mediavilla Sanchez, and N. Amar Touhami, "Ultra-broadband high efficiency mode converter," *Progress In Electromagnetics Research,* vol. 36, pp. 145-158, 2013.

[80] C.-W. Yuan, H.-H. Zhong, Q.-X. Liu, and B.-L. Qian, "A Novel TM_{01}–TE_{11} Circularly Polarized (CP) Mode Converter," *IEEE microwave and wireless components letters,* vol. 16, no. 8, pp. 455-457, 2006.

[81] R. A. Koslover, C. D. Cremer, W. P. Geren, D. E. Voss, and L. M. Miner, "Circular TM_{01} to TE_{11} waveguide mode converter," ed: Google Patents, 1991.

[82] A. Chittora, S. Singh, A. Sharma, and J. Mukherjee, "A Tapered Metallic Baffle TM_{01} to TE_{11Y} Mode Converter With TE_{11X} Mode Transmission Capability," *IEEE Microwave and Wireless Components Letters,* vol. 25, no. 10, pp. 633-635, 2015.

[83] C.-W. Yuan, Q.-X. Liu, H.-H. Zhong, and B.-L. Qian, "A novel TEM-TE_{11} mode converter," *Ieee Microwave and wireless components letters,* vol. 15, no. 8, pp. 513-515, 2005.

[84] A. Chittora, S. Singh, A. Sharma, and J. Mukherjee, "A Novel TM_{01} to TE_{11} Mode Converter Designed With Radially Loaded Dielectric Slabs," *IEEE Transactions on Microwave Theory and Techniques,* vol. 64, no. 4, pp. 1170-1175, 2016.

[85] A. Chittora, J. Mukherjee, S. Singh, and A. Sharma, "Dielectric loaded TM_{01} to TE_{11} mode converter for S-band applications," *IEEE Transactions on Dielectrics and Electrical Insulation,* vol. 22, no. 4, pp. 2057-2063, 2015.

[86] S.-H. Min *et al.*, "Mode conversion of high-power electromagnetic microwave using coaxial-beam rotating antenna in relativistic backward-wave oscillator," *IEEE Transactions on Plasma Science,* vol. 38, no. 6, pp. 1391-1397, 2010.

[87] M. M. Honari, R. Mirzavand, H. Saghlatoon, and P. Mousavi, "Investigation of the 3D

Printing Roughness Effect on the Performance of a Dielectric Rod Antenna," *IEEE Antennas and Wireless Propagation Letters,* vol. 17, no. 11, pp. 2075-2079, 2018.

[88] M. Zandvakili, M. M. Honari, D. Sameoto, and P. Mousavi, "Microfluidic liquid metal based mechanically reconfigurable antenna using reversible gecko adhesive based bonding," in *2016 IEEE MTT-S International Microwave Symposium (IMS)*, 2016, pp. 1-4: IEEE.

[89] S. Aslanzadeh, H. Saghlatoon, M. M. Honari, R. Mirzavand, C. Montemagno, and P. Mousavi, "Investigation on electrical and mechanical properties of 3D printed nylon 6 for RF/microwave electronics applications," *Additive Manufacturing,* vol. 21, pp. 69-75, 2018.

[90] M. Zandvakili, M. M. Honari, P. Mousavi, and D. Sameoto, "Gecko - Gaskets for Multilayer, Complex, and Stretchable Liquid Metal Microwave Circuits and Antennas," *Advanced Materials Technologies,* vol. 2, no. 11, p. 1700144, 2017.

[91] A. Kumar *et al.*, "A highly deformable conducting traces for printed antennas and interconnects: silver/fluoropolymer composite amalgamated by triethanolamine," *Flexible and Printed Electronics,* vol. 2, no. 4, p. 045001, 2017.

[92] X. Li *et al.*, "Self-reinforcing graphene coatings on 3D printed elastomers for flexible radio frequency antennas and strain sensors," *Flexible and Printed Electronics,* vol. 2, no. 3, p. 035001, 2017.

[93] M. M. Honari, R. Mirzavand, S. Aslanzadeh, H. Saghlatoon, and P. Mousavi, "Wideband Printed TM_{01} to TE_{11} Mode Converters," *IEEE Access,* vol. 7, pp. 35438-35448, 2019.

[94] D. Wang *et al.*, "A compact radiation system for L band magnetically insulated transmission line oscillator," *AIP Advances,* vol. 3, no. 5, p. 052128, 2013.

[95] X.-Y. Wang, Y.-W. Fan, T. Shu, C.-w. Yuan, and Q. Zhang, "A high-efficiency tunable TEM-TE_{11} mode converter for high-power microwave applications," *Aip Advances,* vol. 7, no. 3, p. 035012, 2017.

[96] A. Chittora, S. Singh, A. Sharma, and J. Mukherjee, "Design of wideband coaxial-TEM to circular waveguide TM_{01} mode transducer," in *2016 10th European Conference on Antennas and Propagation (EuCAP)*, 2016, pp. 1-4: IEEE.

[97] D. Wang, F. Qin, S. Xu, and M. Shi, "A metallic photonic crystal high power microwave mode converter," *Applied Physics Letters,* vol. 102, no. 24, p. 244107, 2013.

[98] M. M. Honari, R. Mirzavand, J. Melzer, and P. Mousavi, "A new aperture antenna using substrate integrated waveguide corrugated structures for 5G applications," *IEEE Antennas and Wireless Propagation Letters,* vol. 16, pp. 254-257, 2017.

[99] M. M. Honari, A. Abdipour, G. Moradi, R. Mirzavand, and P. Mousavi, "Design and Analysis of a Series-Fed Aperture-Coupled Antenna Array With Wideband and High-Efficient Characteristics," *IEEE Access,* vol. 6, pp. 22655-22663, 2018.

[100] M. M. Honari, A. Abdipour, and G. Moradi, "Bandwidth and gain enhancement of an aperture antenna with modified ring patch," *IEEE Antennas and Wireless propagation letters,* vol. 10, pp. 1413-1416, 2011.

[101] M. M. Honari, A. Abdipour, and G. Moradi, "Aperture-coupled multi-layer broadband ring-patch antenna array," *IEICE Electronics Express,* vol. 9, no. 4, pp. 250-255, 2012.

[102] A. Hosseini, F. De Flaviis, and F. Capolino, "Design formulas for planar fabry–pérot cavity

antennas formed by thick partially reflective surfaces," *IEEE Transactions on Antennas and Propagation,* vol. 64, no. 12, pp. 5487-5491, 2016.

[103] P. Burghignoli, G. Lovat, and D. R. Jackson, "Analysis and optimization of leaky-wave radiation at broadside from a class of 1-D periodic structures," *IEEE Transactions on Antennas and Propagation,* vol. 54, no. 9, pp. 2593-2604, 2006.

[104] A. Hosseini, F. Capolino, F. De Flaviis, P. Burghignoli, G. Lovat, and D. R. Jackson, "Improved bandwidth formulas for Fabry-Pérot cavity antennas formed by using a thin partially-reflective surface," *IEEE Transactions on Antennas and Propagation,* vol. 62, no. 5, pp. 2361-2367, 2014.

[105] A. Hosseini, F. De Flaviis, and F. Capolino, "A 60 GHz simple-to-fabricate single-layer planar Fabry–Pérot cavity antenna," *IET Microwaves, Antennas & Propagation,* vol. 9, no. 4, pp. 313-318, 2014.

[106] C. A. Balanis, *Antenna theory: analysis and design*. John wiley & sons, 2016.

[107] F. Scire-Scappuzzo and S. N. Makarov, "A low-multipath wideband GPS antenna with cutoff or non-cutoff corrugated ground plane," *IEEE transactions on antennas and propagation,* vol. 57, no. 1, pp. 33-46, 2009.

[108] M. M. Honari, R. Mirzavand, and P. Mousavi, "A high-gain planar surface plasmon wave antenna based on substrate integrated waveguide technology with size reduction," *IEEE Transactions on Antennas and Propagation,* vol. 66, no. 5, pp. 2605-2609, 2018.

[109] M. M. Honari, R. Mirzavand, H. Saghlatoon, and P. Mousavi, "A dual-band low-profile aperture antenna with substrate-integrated waveguide grooves," *IEEE Transactions on Antennas and Propagation,* vol. 64, no. 4, pp. 1561-1566, 2016.

[110] G. Minatti, E. Martini, and S. Maci, "Efficiency of metasurface antennas," *IEEE Transactions on Antennas and Propagation,* vol. 65, no. 4, pp. 1532-1541, 2017.

[111] S. M. Saad, "A more accurate analysis and design of coaxial-to-rectangular waveguide end launcher," *IEEE transactions on microwave theory and techniques,* vol. 38, no. 2, pp. 129-134, 1990.

[112] M. Honari, R. Mirzavand, J. Melzer, A. Iyer, and P. Mousavi, "Dual-Band Open-Ended Waveguide Feeder Antennas With Collinear Feed Design," *IEEE Transactions on Antennas and Propagation,* vol. 66, no. 11, pp. 6358-6363, 2018.

[113] J. Rubio, M. González, and J. Zapata, "Analysis of cavity-backed microstrip antennas by a 3-D finite element/segmentation method and a matrix Lanczos-Padé algorithm (SFELP)," *IEEE antennas and wireless propagation letters,* vol. 1, pp. 193-195, 2002.

[114] M. Simeoni, C. I. Coman, and I. E. Lager, "Compact colinear end-launcher for rectangular waveguides," in *IEEE MTT-S International Microwave Symposium Digest, 2005.*, 2005, pp. 1199-1202: IEEE.

[115] M. Simeoni, C. I. Coman, and I. E. Lager, "Patch end-launchers-a family of compact colinear coaxial-to-rectangular waveguide transitions," *IEEE transactions on microwave theory and techniques,* vol. 54, no. 4, pp. 1503-1511, 2006.

[116] M. Moallem and K. Sarabandi, "Miniaturized-element frequency selective surfaces for millimeter-wave to terahertz applications," *IEEE Transactions on Terahertz Science and technology,* vol. 2, no. 3, pp. 333-339, 2012.

[117] H. Sharifi, R. R. Lahiji, H.-C. Lin, D. Y. Peide, L. P. Katehi, and S. Mohammadi, "Characterization of Parylene-N as flexible substrate and passivation layer for microwave and millimeter-wave integrated circuits," *IEEE Transactions on Advanced Packaging,* vol. 32, no. 1, pp. 84-92, 2009.

[118] H. Saghlatoon, R. Mirzavand, M. M. Honari, and P. Mousavi, "Sensor Antenna Transmitter System for Material Detection in Wireless-Sensor-Node Applications," *IEEE Sensors Journal,* vol. 18, no. 21, pp. 8812-8819, 2018.

[119] R. Mirzavand, M. Honari, B. Laribi, B. Khorshidi, M. Sadrzadeh, and P. Mousavi, "An unpowered sensor node for real-time water quality assessment (humic acid detection)," *Electronics,* vol. 7, no. 10, p. 231, 2018.

[120] R. Mirzavand, M. M. Honari, and P. Mousavi, "High-resolution dielectric sensor based on injection-locked oscillators," *IEEE Sensors Journal,* vol. 18, no. 1, pp. 141-148, 2018.

[121] R. Mirzavand, M. M. Honari, and P. Mousavi, "High-resolution balanced microwave material sensor with extended dielectric range," *IEEE Transactions on Industrial Electronics,* vol. 64, no. 2, pp. 1552-1560, 2017.

[122] R. Mirzavand, M. M. Honari, and P. Mousavi, "Direct-conversion sensor for wireless sensing networks," *IEEE Transactions on Industrial Electronics,* vol. 64, no. 12, pp. 9675-9682, 2017.

[123] T. Tamir and A. Oliner, "Guided complex waves. Part 2: Relation to radiation patterns," in *Proceedings of the Institution of Electrical Engineers*, 1963, vol. 110, no. 2, pp. 325-334: IET.

Appendix A

Splitting Condition of Two-Sided Leaky-Wave Structures

The splitting condition of one-sided/two-sided leaky-wave structures is investigated in [1]. Fig. A.1 shows a horizontal line-source excitation. In this case, there is a TE_{yz} leaky mode propagating in Y-direction. Here, the splitting condition, in which two beams off broadside can establish a single beam with a peak at broadside, is considered. In Fig. A.1., the electric field on the plane Z=0 is given by:

$$E_x^{LW}(y) = E_0 e^{-jk_{yLW}|y|} \tag{A.1}$$

where E_0 is the amplitude of electric field, and

$$k_{yLW} = \beta - j\alpha \tag{A.2}$$

The radiated electric far-field in spherical coordinate system can be calculated using the Fourier transform of (A.1), calculated at $k_y=k_0 \sin\theta$ as [123]:

$$E_x(r,\theta) = E_x^{ff}(\theta)\frac{e^{-jk_0 r}}{\sqrt{r}} = \cos\theta\sqrt{\frac{jk_0}{2\pi}}\frac{2jk_{yLW}E_0}{k_0^2\sin^2\theta - k_{yLW}^2}\frac{e^{-jk_0 r}}{\sqrt{r}} \tag{A.3}$$

The angular power density is then given by:

$$P(\theta) = \frac{|E_x^{ff}(\theta)|^2}{2\eta_0} \propto \frac{|E_0|^2(\beta^2+\alpha^2)\cos^2\theta}{(k_0^2\sin^2\theta - \beta^2 + \alpha^2) + 4\alpha^2\beta^2} \tag{A.4}$$

Assuming $\sin\theta \approx \theta$, and $\cos\theta \approx 1$, for the angles close to broadside, the stationary points of $P(\theta)$ can be found as:

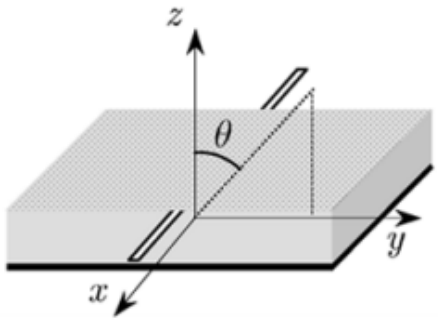

Fig. 0. 1. Dispersion diagram of the EBG structure used in the on-chip antenna.

$$\theta = 0, \pm \frac{\sqrt{\beta^2 - \alpha^2}}{k_0} \tag{A.5}$$

In (A.5), θ=0 is a local minimum if β>α, and the other two angles are the maximum radiation angles. If β≤α, the beam is pointing exactly at broadside. Therefore, the condition β=α is the splitting condition, where two peaks close to broadside start to appear. It can be proved that at the splitting condition, the maximum antenna gain happens.